Modelling High Speed Multistage Compressor Stability

by

Laurent Paul Bonnaure

Ingénieur des Arts et Manufactures, Ecole Centrale de Paris, 1989
Diplôme d'Etudes Approfondies d'Energétique, 1989

Submitted to the Department of Aeronautics and Astronautics in Partial Fulfillment of the Requirements for the Degree of

Master of Science in Aeronautics and Astronautics

at the

Massachusetts Institute of Technology

September 1991

Signature of Author _____
Department of Aeronautics and Astronautics
July 1991

Certified by _____
Professor Alan H. Epstein
Professor of Aeronautics and Astronautics
Thesis Supervisor

Approved by _____
Professor Harold Y. Wachman
Chairman, Department Graduate Committee

MODELLING HIGH SPEED MULTISTAGE COMPRESSOR STABILITY

by

Laurent P. Bonnaure

Submitted to the Department of Aeronautics and Astronautics
on July 1991 in partial fulfillment of
the requirements for the Degree of Master of Science
in Aeronautics and Astronautics

Abstract

A two-dimensional compressible flow analysis of high speed multistage axial compression system stability has been developed. This includes a mean flow prediction model, a linearized stability analysis for both rotating stall and surge-like perturbations, as well as a travelling wave prediction model for flow regimes prior to the instability. Computational implementation of this model allows prediction and investigation of neutral stability operating conditions and instability precursors in a wide range of low and high speed multistage compressors.

Several effects of compressibility of the unsteady flow and stability for the compressor were investigated, including the axial distribution of the stall and pre-stall perturbations. For long compressors at part speed, an (axial) lobed pattern is predicted to occur within the compressor in the neutral stability regime. For the compressors examined, the effects of compressibility on the unsteady perturbations had a stronger influence on the instability onset point than did the mean flow stage mismatching, although the latter was still important.

Inclusion of a simple model of unsteady losses and deviations tended to have a modest stabilizing effect, and reduced the stall frequency as did the inclusion of inter-blade row gaps.

Thesis Supervisor: Professor Alan H. Epstein
Title: Professor of Aeronautics and Astronautics

Acknowledgements

I am greatly indebted to many people for their assistance and support during the course of this work:

Dr. John P. Longley, for his help and patience as well as for his stimulating (and numerous...) remarks. Without his guidance, much of the work in this thesis would not have been possible. I am most grateful (I think I actually improved *some* of my Fortran and I ended up reading *all* your thesis, John ...).

Professor Alan H. Epstein, for his help and guidance as well as for keeping both the morale and the perspectives high.

Professor Edward M. Greitzer, for his insights and encouragements as well as his very useful guidance and supervision all along this research.

Dr. Choon S. Tan, for his friendly remarks and insights on my research.

Fred Newman, for his nice guidance on the NASA 74B compressor data.

Eric Strang, for the numerous and critical discussions during the two years we spent in the same office. I probably learnt and appreciated more about the American culture and the American language (!) from you than from any one else.

John Simon, Jim Paduano, Joel Haynes, Dan Gysling are acknowledged for many fruitful discussions as well as for their friendliness.

I would like to thank also many people during my stay at MIT. Their friendship will be unforgettable:

All the GTL crowd: Eric, Seun Jing, Pete, Dan, Knox, Earl, William, Dave, Victor, John, Jim, Dilip, Fred... A special thanks to my friends Teodore and Franck.

The French crowd: Christophe and Joel. Apart from sharing a car, your friendship will be my best memory from MIT. Eric, for being a real friend. Anna Maria, for the Mac and the friendship. The rest of the French softball team, and the sailors...

The crowd of friends and people I met in the US: Thank you for the good time.

I would like to thank my father as well as my brothers and sisters for their help and support during my stay in the US.

Finally, my fiancée Christine is certainly the person to whom I am mostly indebted. Her love, her constant support, patience and forgiveness made it all worthwhile. With all my love.

This thesis is dedicated to the memory of my mother.

Financial support for this work was provided by Pratt and Whitney Aircraft. The interest and support of Dr. Steve Koff, technical monitor, was very much appreciated.

Table of Contents

List of Figures

Nomenclature

u	velocity in the relative frame
c	velocity in the absolute frame
V_x	axial velocity in the relative frame
V_θ	tangential velocity in the relative frame
W	velocity in the blade passage
U	mean blade velocity
α	absolute flow angle
β	relative flow angle
T	temperature
P	pressure
a	local sound velocity
R	perfect gas constant
γ	adiabatic coefficient
ρ	density
μ	viscosity
$\dot{m}$	mass flow
η_{ac}	adiabatic efficiency
δ	ratio of the compressor inlet total pressure to standard pressure of 14.7 psia
θ	ratio of the compressor inlet total tempature to standard temperature of 518.7 ^oR
N	design rotational speed

Ω	engine frequency
ϕ	flow coefficient
ψ	total to static pressure rise
S	Sutherland's constant
Re	blade relative Reynolds Number
ω	frequency
t	time
n	harmonic number
B	Greitzer's B parameter
λ,μ	inertia parameters
τ	time lag for losses and deviations
x	axial position
θ	angular position
X	generic flow quantity
$\overline{X}$	mean flow quantity
δX	perturbation of the flow quantity
$\omega, \overline{\omega}, \omega_{Loss}$	loss
c	blade chord
s	pitch
ξ	blade stagger
θ^*	camber
R	radius of camber
d	throat
γ	throat angle
t	blade thickness
σ	solidity = $\frac{c}{s}$

β_1^*	leading edge blade metal angle
β_2^*	trailing edge blade metal angle
h	blade height
A	area
V_{plenum}	plenum volume

Subscripts:

t	relative total (stagnation) quantity
rel	relative quantity
abs	absolute quantity
crit	critical value
loss	loss quantity
ND	non-dimensionalized quantity
1	leading edge of the blade
2	trailing edge of the blade
o	reference quantity
ξ	quantity in the blade passage
B	blade quantity
ml	minimum loss quantity
mls	quantity from which the proximity to stall starts to be sensitive
mlc	quantity from which the proximity to choke starts to be sensitive
c	choked quantity

Superscripts:

o	reference quantity
*	critical quantity

Chapter 1

Introduction

1.1 DESCRIPTION OF THE PROBLEM

In most aircraft gas turbine engines, the compression system is composed of several aerodynamically coupled axial flow multistage compressors. Without stable aerodynamic operating conditions, the compression system cannot deliver to the combustion chamber the desired pressure and density rise. Unfortunately, flow field instabilities occur where the pressure and the efficiency of the compressor are close to maximum (figure 1.1). Hence, the motivation for the past forty years to understand the physics involved in these instabilities with the underlying objective to prevent their appearance.

There are two kinds of instabilities in axial flow multistage compressors. The most violent of these instabilities is called surge. It is a global one-dimensional instability that includes the whole compression system, i.e. the compressor, the exit duct, the plenum (which represents the combustion chamber) and the throttle. The mass flow

undergoes large amplitude oscillations where the entire compression system depressurizes and repressurizes, forming the surge cycle (figure 1.2). A typical frequency range for surge is 5 to 15 Hz in a large gas turbine. In high speed machines, these pressure perturbations induce high mechanical stresses and can damage the engine. These flow perturbations can also disturb the combustion chamber operation.

Emmons et al [1] showed that for low speed machines (i.e. machines in which the flow can be assumed to be incompressible), surge can be considered as a Helmholtz resonator kind of oscillation where the neck and the volume of the resonator are respectively the compressor and the plenum.

The second kind of instability is called rotating stall. It is a less violent instability but can be very damaging to the engine operation. It is a local two or three-dimensional instability that is local to the compressor blades.

The physics of this phenomenon has been identified by Emmons et al [1]: when a portion of the circumferential compressor annulus is stalled by some destabilizing effects (local inlet low-pressure region, local inlet change of angle of attack...), the flow separation at the leading edge of the cell causes the angle of attack of the adjacent blades to increase and therefore stalls them. However, since the initial stalled cell creates a significant flow blockage, the streamlines redistribute and reduce the exit flow angle at the exit of the stalled cell, causing it to unstall. The stall cells therefore propagate from one blade passage to the other, in the direction of the rotor typically at 1/4 to 1/2 of the rotor speed. We now understand that end wall boundary layers play an important part in this process.

Unlike surge, rotating stall is a steady phenomenon in a sense that the globally averaged flow field quantities are constant in time. However, operating conditions are much lower than the normal pre-stall ones. Consequently, an engine cannot operate for a long time in the stall regime: the engine thrust is highly reduced, the blades experience

cyclical mechanical stress, acoustic resonance and stall flutter may occur, the combustion chamber can go off, and the turbine inlet temperature increases dramatically due to lower mass flow.

Rotating stall can be very difficult to recover from a large hysteresis (figure 1.3). On a compressor test rig, recovery can be easily obtained by opening the throttle. On an engine, this is not longer possible. Moreover, the combustion effects reduce the turbine flow, which appears as a throttle to the compressor. Therefore, stall is often called "nonrecoverable" and the only way to recover from it is to stop and restart the engine.

Depending on the compressor, either rotating stall or surge can develop first, or both can occur together. Rotating stall may "trigger" surge after a few cycles.

Therefore, aero-engine are operated away from regions where these flow instabilities exist. A limiting operating range beyond which it is considered safe to operate the engine is set. This is often referred to as "surge margin" or "stall margin". Since these instabilities tend to develop near maximum efficiency and pressure rise, this threshold is a balance between security and power.

Recently, precursors to the onset of instability have been identified. Advanced warning of the incipient instability enables the operator to move the operating point away from the unstable operating condition, and therefore allow to safely operate closer to the stall line. This precursor information can also be used as an input to an active control device (Epstein et al [2], Ffowcs Williams et al [3]) : the compressor could then be artificially operated in naturally unstable regions, where the efficiency and the pressure are optimal.

The goal of the present investigation is to identify the structure of flow field instabilities in high-speed multistage compressors, especially in their incipient stages. This is fundamental to the understanding of aero-engine stability, as well as required for the study of active control of their flow instabilities.

1.2 PREVIOUS MODELLING WORK

The majority of both the experimental and the theoretical work carried out on the onset of instability as well as in-stall performance prediction has been done on low-speed, low-pressure ratio compression systems. We designate by low-speed compression systems machines where the blade Mach number is less than 0.3. The emphasis on the low-speed machines is due to two reasons: (i) experience has shown that simple low-speed compressor models capture much of the essence of the onset of instability, and (ii) the proper inclusion of the compressibility effects greatly increases the complexity of the analysis. Also, the testing of low-speed axial compressors is much less complex and expensive than the testing in high speed machines.

1.2.1 Modelling techniques for low-speed multistage compressor instabilities

1.2.1.1 Rotating stall

Currently, rotating stall models are two dimensional and incompressible. They typically consist of three components:

(i) An inlet flow field model:

The inlet flow field is most often considered as being in a two-dimensional, constant annulus area, infinite upstream duct (Dunham [4] proposed however a three dimensional perturbation model). The flow is inviscid, incompressible, irrotational. This latter assumption is true when there is uniform flow coming into the compressor and no backflow. The inlet boundary condition used is the disappearance of the disturbances far upstream.

(ii) A downstream flow field model:

The downstream flow field is most often considered as a two dimensional inviscid, incompressible flow field convecting the vorticity originating in the compressor. The downstream boundary conditions most often used are a constant exit flow angle with

pressure perturbations decaying downstream. The downstream flow is then linearized which leads to a Laplace equation for the static pressure in the downstream duct.

(iii) A compressor blade row model:

This region is where most models differ. Blade rows are most often modelled as actuator disk or semi-actuator disks. The boundary conditions linking the upstream and the downstream flow field across the compressor are usually the following:

- mass conservation,
- an exit flow angle relation,
- a momentum relation in one of the following forms:
  - static pressure rise coefficient as a function of the inlet flow angle (Dunham [4], Wood [5], Stenning [6])
  - total pressure loss coefficient as a function of the inlet flow angle (Tanaka and Nagano [7])
  - vorticity equation with friction losses as a function of the inlet flow angle (Nenni [8])

In any of these models, the unsteady behavior of the bladerow must be determined. In the early works, the local bladerow performance was assumed to be quasi-steady. Later, inertia models were introduced as a correction to the performance of a compressor to account for the acceleration and the deceleration of the fluid in the blade passage, therefore recognizing a finite time response of the blade rows to the flow field. These inertia models take the form:

$$\tau \frac{dX}{dt} = X_{\text{steady state}} - X$$

where: $X_{\text{steady state}}$ is the steady value of the flow field quantity,

X is the instantaneous value of the flow field quantity,

τ is a time constant associated to the process.

1.2.1.2 Surge

Surge is essentially an unsteady axisymmetric flow disturbance in the compression system as a whole. The compression system must be modelled with a downstream plenum and an exit throttle regulating the mass flow through the system. An original one-dimensional "lumped parameter" model was developed by Greitzer [9]. More recently Moore and Greitzer [10,11] have developed a more elaborate model which combines rotating stall and surge and show how the two phenomena are linked.

Once the set of equations modelling the fluid mechanics of the problem are established, they must to solved. One approach is a linearization of these equations where a small perturbation is added to the mean quantity. This has been performed by Stenning [6], Nenni and Ludwig [8], Moore and Greitzer [10,11]. Hynes and Greitzer [12] and Longley [13] used this kind of model for distorted flow stability calculations. The solution of this linearized set of equations corresponds, for rotating stall, to waves travelling around the compressor annulus in the rotor direction. These waves have an exponential decay with axial distance as well as an exponential growth or decay with time. A condition at which these waves are neutrally stable (neither growing nor decaying) can be established, as well as a disturbance travelling speed. This linearized theory gives a good insight of the stall inception phenomenon: a small amplitude wave travelling around the annulus growing in time and with little negative damping.

The instability onset was typically found to be either at the peak of the pressure rise versus mass flow function characteristic of the compressor or at a pressure rise corresponding to a positive slope of this characteristic.

However, this class of linearized model cannot provide any information on the behavior of the once developed stall (propagation speed, number, size) due to the non-linearity of their propagation.

Experimental work supporting the existence of such travelling waves has been

done by McDougall [14] and Garnier [15,21]

An other way to look at this problem is to compute a numerical solution of the fully non-linear problem. This was done by Takata and Nagano [7], Orner [16], Pandolfi and Colusardo [17], Greitzer [9]. They predicted the inception, the stall cell growth (limited by the nonlinear nature of the total pressure losses), the final stall cell size and speed, as well as the hysteresis of the inception point.

1.2.2 Modelling techniques for high-speed multistage compressor instabilities

The modelling work described in the previous section was based on the fundamental assumption of incompressible flow. Experimental work on high speed compression systems however show that instability occurs at a mass flow where the pressure ratio characteristic is still negatively sloped (figure 1.1). Classical low-speed stability calculations failed to explain this type of system instability. Instability features appear to be therefore totally different for high-speed compressors.

Only few experimental studies in the open literature have been carried out on the investigation of rotating stall and surge on high speed compressors: Small and Lewis [18], Hosney and Steenken [19], Newman [20].

Stall transient experiments on a three stage machine performed by Pratt & Whitney Government Engines Business, West Palm Beach, Florida and analyzed by Garnier [21] showed that the stall inception process appears to be qualitatively the same as in low-speed machines, i.e. a small amplitude wave growth. However, these waves behavior were somewhat different to the one observed in the low-speed case. Indeed, both the first and the second harmonics were of significant importance. Moreover, the travelling waves observed appeared to propagate in different directions, depending on the harmonic and the axial location along the compressor axis.

Tesh and Steenken [22], Elder and Gill [23], Davis and O'Brien [24] developed

one-dimensional "lumped parameters" models of high speed surge and rotating stall. Each stage of the compressor were modelled in order to allow accurate interaction between all the elements of the compression system. These models permitted disturbances a finite time to propagate along the compressor axis as well as a strong mismatching of the stages. Hosny et al [44] very recently used the model developed by Tesh and Steenken [22] to study analytically the active control of high-speed axial compressor surge. Modelling an eight-stage compressor, they found out that active control was much more effective on a mismatched compressor than on a matched compressor. Experimental testing is yet to be performed in order to validate these analytical results.

Mazzawy [25] and Cargill and Freeman [26] modelled high speed surge with the concern that some experimental observations indicated that surge might begin with a high amplitude wave travelling down the compressor. In such a case, "lumped parameters" do not adequately describe the initial stages of high-speed surge. The models proposed rather present the initial stages of surge as a "blast wave" or as a forward propagating shock wave.

Mc Kenzie [27] suggested that the point of maximum static density ratio seems to give a good approximation of the experimentally determined surge point. Lavrich [28] investigated quantitatively this suggestion, using a simple one-dimensional model: a positive density slope indeed reduced the amount the total pressure ratio slope must be positive to turn the system unstable. However, Lavrich points out that high-speed compressors are not able to provide a positive density slope large enough to move the instability point on the negative sloped side of the characteristic as observed in actual high speed, high pressure ratio compressors.

1.3 CONCLUSIONS OF THE PREVIOUS WORK AND SCOPE OF THE PRESENT WORK

The key fluid dynamical features of low-speed multistage compressor stability and stability precursors seem to have been so far relatively well captured in existing two-dimensional incompressible models.

The same does not apply to high-speed multistage compressors: neither neutral stability operating conditions assessments nor precursor predictions have been so far successful. Moreover, little has been done so far to evaluate the differences between the high-speed and the low-speed machines. To what extent is a low-speed axial-flow compressor different from a high-speed one? An analytical model including compressibility effects could be a very useful tool in studying this question. Moreover, in the long run scope of active control of high-speed multistage compressor instabilities, a model of such high-speed instability inceptions will be of some considerable use.

Described here is the development of a two-dimensional compressible model of the entire high speed compression system - inlet duct, blade rows, inter blade gaps, exit duct, plenum, throttle. A linear stability analysis as well as a travelling wave prediction technique will then be proposed.

Using this theoretical model, an investigation of the compressibility effects on the stability margin and on the neutral stability propagation frequency will be conducted. The effects of unsteady losses, unsteady deviations and inter blade row gaps will be also evaluated in high speed compressors. The key point to the implementation of active control on high speed machines being an adequate location of sensors in the compressor, the axial distribution of the flow field perturbations at and around the neutral stability operating condition will then be investigated.

The model will also be tested and used as a prediction tool on existing low-speed and high-speed compressors operating around their instable regime.

Chapter 2

Meanflow Prediction

2.1 INTRODUCTION

A necessary part of the design of any aero-engine is the estimation of its compressor characteristics. For the current investigation of the high-speed multistage compressor stability, the knowledge of the meanflow quantities at the considered operating point is essential. Both experimental or analytical programs can be used to provide this information.

The most accurate source of information is of course experimental data. However, as will be seen in Chapter 3, considerable meanflow information is required by the extensive model developed in this thesis. Such data is seldom available in sufficient detail for high speed multistage axial compressors because of the difficulty and expense of a high-speed rig. Also, the computational algorithm requires such extensive meanflow information for many operating points. Moreover, most of the meanflow data is required near the neutral stability operating point: this includes unstable flows as well as flows on

the verge of instability. As seen in Chapter 1, this region is very difficult to both measure and model. At last, the data will only be valid for one particular compressor configuration operating at one particular speed.

Since the purpose of this thesis is to get a physical understanding of the general fluid mechanics phenomena involved with high-speed compressors instability, one cannot restrict oneself to a particular set of observations.

Consequently, since the detailed steady mean flow quantities in the blade rows and in the inter blade row gaps are required for the stability analysis later performed, an analytical meanflow calculation needs to be performed. This internal flow modelling and the accurate estimation of the off-design compressor characteristics is an issue for any gas turbine engines company. However, for the purpose of this work, only the level of sophistication required to capture the flow phenomenon essential for the stability investigated is included in order to minimize the complexity of the fluid equations and to get the best computational efficiency.

For this purpose, we develop here a mean line off-design prediction model using a stage-stacking method [30]. This involves constructing loss and deviation models applicable to high speed axial compressor blade rows. Such models rely on empirical correlations from experimental data. The method developed will be tested on a range of compressors and it is our belief that the degree of accuracy achieved will be adequate to capture the main meanflow phenomena that are important in actual high-speed multistage axial flow compressors. The purpose is not to design an extremely accurate speedline generator, but rather to get a general and adequate mean flow prediction. This trade-off will be discussed often in this thesis.

The accuracy clearly depends on the correlation used: thus, the more experimental data used to derive the correlations, the better the prediction will be ([30] versus [32]). Improved predictions of the compressor characteristic can often be done by tuning the

empirical parameters of the model. Actually, most of today's compressor performance prediction tools are developed for one particular set of compressors, and the performance of similar compressors is extrapolated from it.

Another way of looking at this method is to consider that it generates a fictitious compressor map, that is realistic enough to behave like a real compressor.

The computerized method developed here requires as inputs the compressor blade geometries at meanline, as well as the design rotational speed, Reynolds Number and inlet flow angle [29]. This chapter will discuss the highlights of the method developed for the mean flow prediction.

2.2 COMPRESSOR GEOMETRY

The compressor is modelled as a succession of blade rows and inter-blade row gaps, where the inter-blade row gaps have a constant area and where the compressor area changes only take place within the blade passages. This assumption is adopted for consistency with the compressor stability analysis model. Also, the compressor is assumed to have a constant meanline. The entire compressor model is shown in figures (2.1.a) and (2.1.b).

2.2.1 Sign convention adopted

Angles and tangential velocities are positive in the direction of the rotor speed. The velocity triangles used are shown on Diagram (2.1):

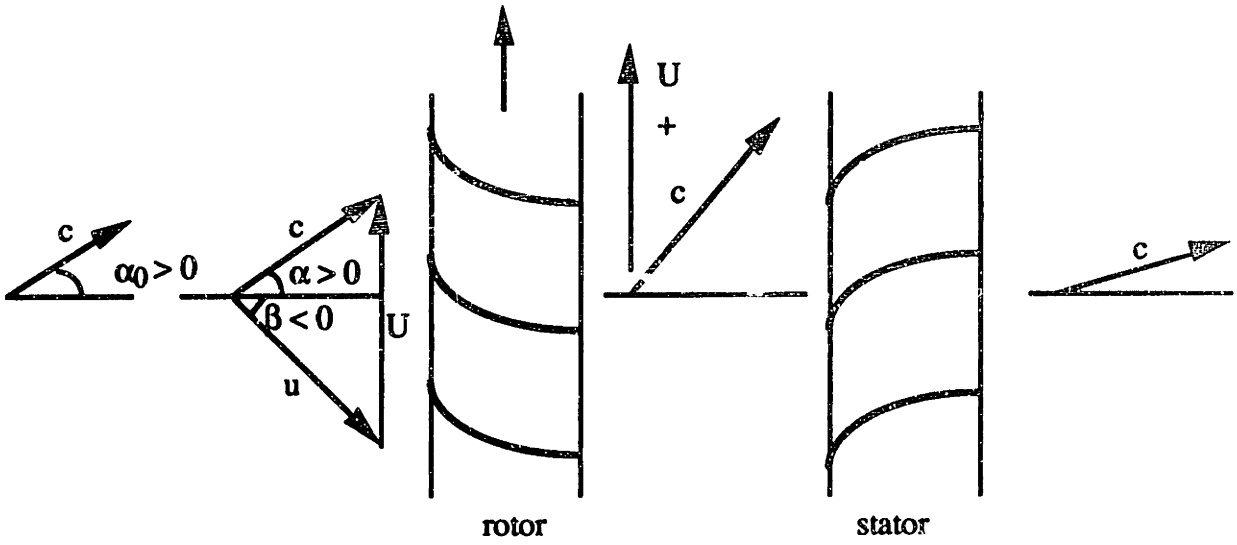

$$\theta_{abs} = \theta_{rel} + \frac{U}{r} t$$

$$u_\theta = c_\theta - U$$

Diagram (2.1): Velocity triangles

Camber is therefore positive for a rotor and negative for a stator, whereas stagger is negative for a rotor and positive for a stator.

2.2.2 Blade row geometry

It is essentially described on Diagram (2.2). The blade metal angles are classically derived by:

$$\beta_1^* = \xi + \frac{\theta^*}{2} \qquad (2.1)$$

$$\beta_2^* = \xi - \frac{\theta^*}{2} \qquad (2.2)$$

$\beta_{1\,gas} = \beta_1^*$ + incidence angle

$\beta_{2\,gas} = \beta_2^*$ + deviation angle (negative for a rotor and positive for a stator)

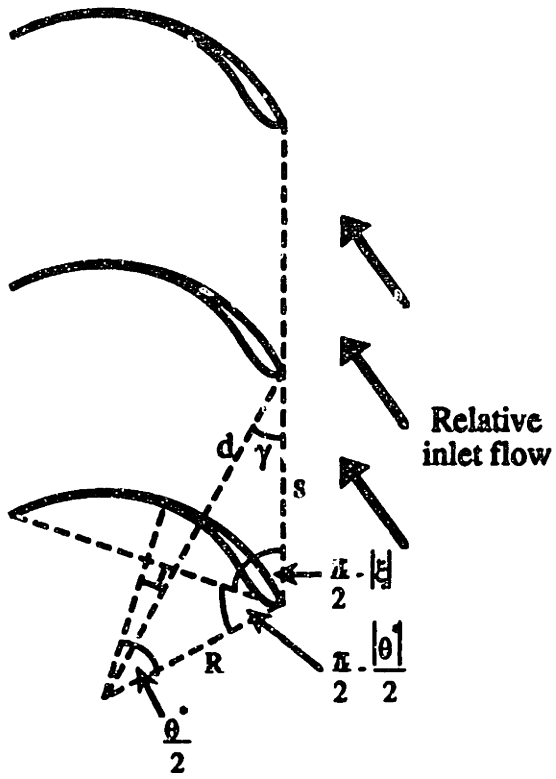

Diagram (2.2): Blade row geometry

If the blade camber is not zero, the curvature radius, the throat, and the throat turning are defined in the following way:

$$\frac{R}{c} = \frac{1}{2\sin\left(\frac{\theta^*}{2}\right)} \tag{2.3}$$

$$\frac{d}{c} = \sqrt{\left(\frac{s}{c}\right)^2 + \left(\frac{R}{c}\right)^2 + 2\left(\frac{s}{c}\right)\left(\frac{R}{c}\right)\cos\left(\xi + \frac{\theta^*}{2}\right)} - \left(\frac{R}{c}\right) - \frac{1}{2}\left(\frac{t}{c}\right) \tag{2.4}$$

$$\gamma = \text{Arcsin}\left(\frac{R}{d+R}\sin\left(\xi + \frac{\theta^*}{2}\right)\right) \tag{2.5}$$

and: throat turning= throat angle - leading edge metal angle

$$= \gamma - \beta_1^* \tag{2.6}$$

If the blade camber is zero, we get:

$$\gamma = \xi \tag{2.7}$$

$$\frac{d}{c} = \left(\frac{s}{c}\right) \cos\xi - \frac{1}{2}\left(\frac{t}{c}\right) \tag{2.8}$$

and: throat turning= 0 (2.9)

We therefore get expressions for the throat area, the throat height and the mean radius (figure 2.1.b):

$$x_{throat} - x_{leading\ edge} = \frac{1}{2}\, d\, \sin\gamma \tag{2.10}$$

$$A_{throat} = \left(\frac{d}{s}\right) \cdot \left(\begin{matrix} A_{leading\ edge} \\ + \left(A_{trailing\ edge} - A_{leading\ edge} \right) \dfrac{x_{throat} - x_{leading\ edge}}{x_{trailing\ edge} - x_{leading\ edge}} \end{matrix} \right) \tag{2.11}$$

$$\frac{h_{throat}}{h_{leading\ edge}} = 1 + \frac{1}{2}\left(\frac{d}{c}\right) \frac{\sin\gamma}{\cos\left(\theta^*\right)} \left(\frac{R_{tip_{trailing\ edge}} - R_{hub_{trailing\ edge}}}{R_{tip_{leading\ edge}} - R_{hub_{leading\ edge}}} - 1 \right) \tag{2.12}$$

$$R_{mean} = \text{constant} = \sqrt{\frac{R^2_{hub_{leading\ edge}} + R^2_{tip_{leading\ edge}}}{2}} = \sqrt{\frac{R^2_{hub_{trailing\ edge}} + R^2_{tip_{trailing\ edge}}}{2}} \tag{2.13}$$

The B parameter is classically defined as:

$$B = \frac{U}{2\,a} \sqrt{\frac{V_{plenum}}{A_{duct}\, L_{total}}} \tag{2.14}$$

2.3 NON-DIMENSIONALIZATION

The reference quantities used to non-dimensionalize the flow quantities are the inlet stagnation quantities:

P_t^o inlet stagnation pressure

T_t^o inlet stagnation temperature

$V^o = \sqrt{\gamma R T_t^o}$ inlet stagnation speed of sound

$$l^o = \sqrt{\frac{R_{hub}^2 + R_{tip}^2}{2}}$$ mean radius

$$t^o = \frac{l^o}{V^o}$$

2.4 MODEL OUTLINE

2.4.1 Model assumptions

Raw and Weir [30] showed that the shape and the slope of a speed line can be reproduced quite accurately - for the cases they considered - by only looking at the velocity triangles at the inlet and at the exit of the blades at their mean-radius, i.e. the triangles along the streamline that divides the flow into two equal halves. Therefore, for the purpose of the analysis, a one-dimensional compressible flow is considered along the meanline assumed to be of constant radius. The compressor geometry has been described in section 2.2. Losses are assumed to take place within the blade row passages only and no meanflow redistribution is assumed to take place with the inter-blade row passages.

It is important to note that empirical loss and deviation models are being used in this model and that they do not claim to capture every meanflow phenomenon in the compressor. Also, they are highly dependent on the blade geometry used in the

compressor. The models used [30,31,32] were chosen because they are the simplest ones available in the open literature that consider a large range of compressor configurations and parameters.

Furthermore, the losses and deviations that are associated with the meanline in this model represent some average over the blade span. This will be of considerable interest to the current investigation.

2.4.2 Stage-stacking method

The individual blade rows are represented by velocity triangles at their inlet and outlet which are simply stacked in series down the compressor flow path. Once the overall compressor inlet flow conditions are known, they are used as the inlet flow conditions for the first blade. The corresponding loss coefficient and deviation are specified at the considered speed for the incident Mach Number, and incident relative flow angle. This determines, with the mass conservation, the exit flow quantities. Because no change is assumed to take place between the blades, these exit flow quantities are used as inlet flow quantities for the following blade row.

The performance of each stage (mass flow, pressure ratio, adiabatic efficiency) are therefore determined and stacked to get the whole compressor characteristics. As pointed out by Steinke [33], the meanflow quantities obtained do not represent just the blade performance at the meanflow radius, but the performance integrated along the bladespan and therefore the overall compressor performance.

2.4.3 Semi-actuator mean flow quantities

For the purpose of the investigation of high speed compressor stability, the blade rows are modelled as semi-actuator disks (see figure 3.2). In this model [34], the blade passages are replaced by straight channels inclined to the axis at the stagger angle. It will be of some use to know the mean flow quantities satisfying the semi-actuator disk

assumptions within the blade passage at the leading and trailing edges of the blades. As will be justified in Chapter 3, the assumption is made that the losses are incurred at the leading edge of the blade. Continuity and the knowledge of the total pressure within the blade therefore provides the required meanflow information within the blade passages.

2.5 EMPIRICAL CORRELATIONS USED

2.5.1 Basic assumptions

The empirical correlations used to develop this flow field prediction tool are mainly derived from Raw and Weir [30] and NASA SP-36 [31,32]. They rely on the following assumptions:

a) The mean total pressure losses at minimum loss incidence, namely the cascade losses and the secondary losses, are lumped together and are assumed to depend on the diffusion factor and on the blade chord Reynolds number.

The empirical correlation between total pressure loss parameter and diffusion factor developed by Raw and Weir [30] is an extension of that of Lieblein et al [31] to diffusion related losses and secondary losses. Besides, it has been extended to large diffusion factors where the cascade would be fully stalled even at minimum loss incidence. It is shown on figure 2.2. Figure 2.2 actually shows:

$$\frac{\omega_{ml}\, s}{2\, c} \cos \beta_2 = f(\mathrm{DFAC}) \tag{2.15}$$

where ω_{ml} represents the losses at minimum loss incidence and where DFAC represents the diffusion factor.

$$\mathrm{DFAC} = 1 - \frac{u_2}{u_1} + \frac{1}{2 \,.\, \mathrm{solidity}} \left(\sin \beta_1 - \frac{u_2}{u_1} \sin \beta_2 \right) \tag{2.16}$$

This total pressure loss parameter is modified as a function of the blade chord Reynolds number. It is shown on figure 2.3. The viscosity is taken from the

Sutherland law:

$$\frac{\mu}{\mu_o} = \left(\frac{T}{T_o}\right)^{3/2} \left(\frac{T_o+S}{T+S}\right) \qquad (2.17)$$

for air: $T_o = 491.6\ ^oR$

S = Sutherland's constant= 199 ^oR

$\mu_o = 0.1716$ mP

b) The shock losses are a function of the incident Mach number and of the total turning of the flow on the suction surface of the blade up to the throat. It is interesting to notice that the shock losses have been interpolated to high subsonic inlet Mach number. It is shown on figure 2.4.

c) The deviation correlations are derived from Carter's rule for an airfoil with circular arc camber lines. These deviations are function of the diffusion factor as well as the camber of the airfoil, as shown on figure 2.5. It indeed shows the rapid rise of the deviation as the cascade starts to stall (diffusion factor above 0.55). Figure 2.5 actually gives F_1 and F_2 such that:

$$\beta_2 = \left(m_c \frac{1}{\sqrt{\text{solidity} \cdot \left(1 - \frac{J}{C}\right)}} + F_1 + F_2\right) \cdot \theta^* + \beta_2^* \quad \text{for an inlet guide vane} \qquad (2.18)$$

$$\beta_2 = \left(m_c \frac{1}{\text{solidity} \cdot \left(1 - \frac{J}{C}\right)} + F_1 + F_2\right) \cdot \theta^* + \beta_2^* \quad \text{for a rotor or a stator} \qquad (2.19)$$

m_c is the Carter parameter defined on figure 2.6. This distinction between rotor, stator and IGV was not made by Raw and Weir.

d) The blades considered are originally double circular arc (D.C.A.) airfoils or so called 'J' blades that are straight on a length J then followed by a double circular arc section. However, for non-standard camber line shape, an equivalent 'J' blade is calculated from:

$$\frac{J}{C} = \frac{\sin\left(\xi - \frac{\left(\beta_1^* + \beta_2^*\right)}{2}\right)}{\sin\left(\frac{\theta^*}{2}\right)} \qquad (2.20)$$

where is ξ the actual stagger and β_1^* and β_2^* the actual inlet and exit metal angles of the blade.

2.5.2 Construction of the loss-bucket model

The loss-bucket model represents the variation of the loss parameter with incidence angle as a function of the incidence Mach number. It is therefore the essential basis for the off-design performance prediction of the axial flow compressor.

The loss bucket is obtained from five basic lines shown on figure 2.7. A loss bucket model can be expressed in terms of incidence flow angle and incidence Mach number, or in terms of area ratio (up to throat) and incidence Mach number [30]. The area ratio is used to evaluate the amount of acceleration of the incidence flow area $A_{\text{leading edge}}$ up to the cascade throat area A_{throat}. Indeed:

$$\frac{A_{\text{throat}}}{A_{\text{leading edge}}} = \frac{d\, h_{\text{throat}}}{s\, h_{\text{leading edge}} \cos\beta_1} \qquad (2.21)$$

The incidence flow angle β_1 will be the quantity used for the loss bucket construction. A typical loss bucket is shown on figure 2.7:

(i) Line 1 corresponds to the relative inlet flow angle (on the stall side) β_{1mls} where the loss coefficient starts to increase because of the separation of the flow due to positive incidence and the proximity to full stall. It is to be noted that, as the

Mach number increases, this increase of loss arises closer to the minimum loss incidence because of the effects of the shock-induced separation on the suction surface of the blade row. The onset of blade stall (originally suggested by Lieblein [31]) is commonly taken at a diffusion loading level characterized by a diffusion factor of 0.55.

(ii) Line 2 corresponds to the relative inlet flow angle for minimum loss β_{1ml}. It has been previously referred to as the minimum loss incidence angle.

It is defined from NASA SP-36 [31,32] as:

$$\beta_{1ml} = (i_c - i_{2D}) + \beta_1^* + K_i \, . \, i_o + n \, . \, \theta^* \qquad (2.22)$$

$i_c - i_{2D}$ is referenced as the reference incidence angle- 2D cascade rule incidence. It is a function of the relative inlet Mach Number and the percentage of the blade height from compressor tip as shown on figure 2.8.

K_i is referenced as the correction factor. It is a function of blade maximum thickness ratio as shown on figure 2.9.

i_o is referenced as the zero camber incidence angle. It is a function of the solidity and of the relative inlet flow angle as shown in figure 2.10.

n is referenced as the slope factor. It is a function of the solidity and of the relative inlet flow angle as shown on figure 2.11.

(iii) Line 3 corresponds to the relative inlet flow angle (on the choke side) β_{1mlc} where the loss coefficient starts to increase because of the proximity to choke. This line exists only up to the critical Mach number where the blade can no longer operate at a previously defined minimum loss. In other words, at and beyond the critical Mach number, stall induced losses or shock induced losses become significant at the same incidence. The current investigation showed that a relevant position of this line can be determined by a interpolated choke margin between

1.02 (at critical Mach number) and the choke margin at Mach 0.4 (see Appendix 5).

(iv) Line 4 corresponds to the relative inlet flow angle β_{1ml} for "minimum" loss for a Relative Mach Number greater than the critical Mach Number. According the assumptions of Raw and weir [30], it occurs at a constant choke margin of 1.02, i.e. $\frac{A_{throat}}{A^*} = 1.02$.

(v) Line 5 corresponds to the relative inlet flow angle β_{1c} necessary to choke the blade row. It is a unique function of the Mach number for isentropic flow, determining by the analytical choking condition. For Mach number higher than the critical Mach number, the flow is no longer isentropic and the shock losses modify this choked line as shown on figure 2.7. These shock losses are assumed to take place just behind the leading edge of the blade. We get:

$$\cos \beta_{1c} = \frac{Q_t(1)}{Q_t(M_1)} \frac{h_{throat}}{h_{leading\ edge}} \frac{d}{c} \frac{1}{\left(\frac{s}{c}\right)} \frac{P_{t_{throat}}}{P_{t_{leading\ edge}}} \qquad 2.23)$$

$$\text{where } \frac{P_{t_{throat}}}{P_{t_{leading\ edge}}} \text{ represents the shock losses}$$

The numerical implementation of these five lines is described in Appendix 5. It has to be stressed that this is an empirically based model dependent on data such as the critical Mach number, the minimum loss choke margin for incident Mach Number greater than the critical Mach number, and the entire position of lines 1,2,3 on figure 2.7. The current model uses a construction technique for all these parameters, somewhat generalizing the prediction technique. This generalization of course can somewhat reduce the accuracy of the predictions (less experimental inputs), but the inputs of the model are now just the compressor geometry and the inlet flow conditions.

In Chapter 4 will be seen that using this self-consistent model, the main flow field

phenomena are well captured and the predicted characteristics are still relevant. The numerical implementation of this meanflow model will be discussed in Chapter 4.

As shown on figure 2.7, once these five lines have been positioned, three expressions are needed: the minimum loss coefficient, the shape of the loss rise due to stall, and the shape of the loss rise due to choke.

(i) Minimum loss coefficient:

It is determined by the empirical correlation defined at the beginning of section 2.5.1.

(ii) Loss rise on the stall side of minimum loss:

Raw and Weir found a good agreement with test data achieved by modelling this loss rise as:

$$K\left(\beta_1 - \beta_{1mls}\right)^N \tag{2.25}$$

where K=0.007, N=1.27, and β_1 in degrees

This value of K might need to be increased when the meanline incident Mach number exceed 1.0.

(ii) Loss rise on the choke side of minimum loss:

Raw and Weir found a good agreement with test data achieved by modelling this loss rise by:

$$f\left(\frac{\beta_{1mlc} - \beta_1}{\beta_{1mlc} - \beta_{1c}}\right)$$

An interpolation of their data showed that :

$$f(x) = 0.1\left(\left(\frac{1}{1-x}\right)^{0.05} - 1\right) \tag{2.26}$$

gave some relevant value for this loss rise.

As a summary, the complete loss in each blade row is expressed as:

(i) a minimum loss (defined in Equation 2.15 and Equation 2.22)

(ii) a multiplicative factor due to the blade Reynolds number (defined on Figure 2.3)

(iii) an additional loss due to the proximity of choke or stall (defined in Equation 2.25 and Equation 2.26)

(iv) a shock loss (defined on Figure 2.4)

2.6 SPEEDLINE GENERATION TECHNIQUE

2.6.1 Unchoked case

The choking mass flow is first established for the considered rotational speed and inlet operating conditions. The speedline is then generated as a series of operating points from a specified percentage of the calculated choked mass flow. The calculation stops when the pressure ratio falls below one.

2.6.2 Choked case

When one blade row is choked, the calculation cannot proceed by incrementing the mass flow since it is fixed. However, once a blade passage is choked, the exit static pressure must be specified, since the choking condition only defines an upper bound for the exit static pressure.

In order to calculate the flow on the choked part of the characteristic, the static pressure at the exit of a choked blade is decreased from this critical static pressure. This is equivalent to adding an expansion loss to this choked blade row. The blade row is now operating in a "more choked" regime. However, adding this expansion loss changes the inlet conditions to the downstream blade rows. One consequence might be to unchoke the choked blades downstream of the calculated blade row. However, because of the nature of choking, the aerodynamic conditions of the rows upstream of the choked row remain constant during these calculations.

This provides more calculation points to the speedline and more insight on the vertical part of the characteristic where the mass flow is fixed because of a choked blade somewhere in the compressor.

These incremental steps in expansion loss are applied progressively starting from the choked blades at the rear of the compressor in moving towards the front. The choked blades downstream of the choked blade being calculated are progressively unchoked by incrementing the expansion losses of this blade. Then, the closest upstream choked blade expansion loss is increased, which reduces its exit static pressure and might unchoke the blade.

Chapter 3

Compression System Model

3.1 Introduction

A number of incompressible models have been developed to study the internal unsteady flow of axial compressors. The current investigation however requires a accurate model that captures the nature of the unsteady, compressible flow field in the whole compression system, in order to address the stability issue of high-speed multistage compressors.

Cumpsty and Marble [35] developed a two dimensional compressor model, with blade rows replaced by compressible actuator disks, to trace the passage of total pressure perturbation through high hub-to-tip ratio machines. The problem with the use of actuator disks is, however, that the fluid mechanics inside the blade passage are not captured. Moreover, modelling the capacitance and inertia effects accurately lead to a somewhat unrealistic representation of the circumferential cross flow as discussed by Hynes [36].

Kaji and Okazaki [37] developed an interesting analysis based on the semi-actuator disk theory to study the propagation of sound waves through a blade row. However, they did not included entropy perturbations.

Hynes [36] addressed the issue of the use of actuator and semi-actuator disk models in the study of inlet distortion, showing through examples how disturbances interact with the system components.

The model developed in this chapter is based on a similar approach of the flow field modelling as Hynes. A compressible semi-actuator disk model is developed with a corresponding set of boundary conditions. From this model, the issue of stability in high-speed multistage compression systems is addressed, both in the choked and the unchoked case.

3.1.1 Compressor geometry

The compression system is modelled as a series of an inlet duct, a compressor, an exit duct, a plenum (considered to model a combustion chamber) and a throttle, as shown on figure 3.1.

The inlet duct of the compressor is taken as the first volume and the compressor itself has one volume to represent each of the inter blade row gaps as well as one volume to represent the fluid in the blade row. The final volume represents the exit duct of the compressor. These volumes have a constant area (straight cylindrical channels) with the compressor area changing only within the blade passages. The compressor is assumed to have a constant meanline. The compressor geometry and the nomenclature are shown on figure 2.1.

The blade passages are assumed to be straight channels, inclined to the axis at stagger angle ξ, as shown in figure 3.2.

3.1.2 Assumptions

(i) The model developed is actually specific to the geometrical assumptions developed in the previous section.

(ii) The compressor is of high hub-to tip ratio so that radial variations of the flow quantities are insignificant. The only significant radial variation assumed to take place is actually the one in the mean pressure, in order to just balance the mean radial equilibrium equation. However, all the perturbations are assumed to be independent of the radius.

It has to be pointed out that this certainly is the most serious limitation of this model. Hawthorne et al [42] showed that in steady, incompressible, distorted flow two-dimensional disturbances will develop into three-dimensional ones if there is a specific distance in which the flow is allowed to swirl.

(iii) Viscosity and heat transfer are considered of little influence on the dynamics of the compressor. These are not currently but could be included in the boundary conditions in the compressor and some heat addition could be added in the plenum.

(iv) The amplitude of the perturbations of the flow quantities is assumed to be sufficiently small so that the flow equations can be linearized around their mean uniform and steady values. These values can be from design program (Chapter 2) or from experimental data. We therefore get:

$$X = \overline{X} + \delta X$$

3.2 OVERALL DESCRIPTION OF THE MODEL ISSUES

In order to address the stability issues associated with the compression system, a stability analysis is conducted in a similar way to the usual hydrodynamic stability analysis where a most general unsteady disturbance is added to the mean quantity. The flow equations of the compression system are then linearized so that the stability issue involves the examination of the growth of such disturbances. By expressing these

unsteady disturbances as a harmonic series in time, the governing equation yields a dispersion relation between the steady state compressor characteristics, the geometry, the harmonic and the growth rate. This dispersion equation is then solved for the growth rate: if it is positive, then the system is unstable, if it is negative, then the system is stable. A neutral stability operating point can then be determined, as a growth rate of zero. Moreover, the governing equations can be integrated, giving the transient behavior of the flow field instability phenomena. They can also be integrated at operating regions close to this neutral stability point, giving the behavior of the onset of these instability phenomena.

3.3 INTER-BLADE ROW ANALYSIS

Under these assumptions described in section 3.1.2, the linearized equations determining the two-dimensional flow field in the inter-blade row gaps and in the inlet and exit ducts, can be expressed in the following way:

Mass continuity:

$$\frac{\partial \delta\rho}{\partial t} + \rho \frac{\partial \delta V_x}{\partial x} + V_x \frac{\partial \delta\rho}{\partial x} + \frac{1}{r}\left(\rho \frac{\partial \delta V_\theta}{\partial \theta} + V_\theta \frac{\partial \delta\rho}{\partial \theta}\right) = 0 \qquad (3.1)$$

Axial momentum:

$$\rho \frac{\partial \delta V_x}{\partial t} + \rho V_x \frac{\partial \delta V_x}{\partial x} + \rho \frac{1}{r} V_\theta \frac{\partial \delta V_x}{\partial \theta} = -\frac{\partial \delta P}{\partial x} \qquad (3.2)$$

Circumferential momentum:

$$\rho \frac{\partial \delta V_\theta}{\partial t} + \rho V_x \frac{\partial \delta V_\theta}{\partial x} + \rho \frac{1}{r} V_\theta \frac{\partial \delta V_\theta}{\partial \theta} = -\frac{1}{r} \frac{\partial \delta P}{\partial \theta} \qquad (3.3)$$

Energy equation:

$$\frac{\partial \delta S}{\partial t} + V_x \frac{\partial \delta S}{\partial x} + \frac{1}{r} V_\theta \frac{\partial \delta S}{\partial \theta} = 0$$

For a perfect gas, this equation becomes:

$$\frac{\partial \delta P}{\partial t} + V_x \frac{\partial \delta P}{\partial x} + \frac{V_\theta}{r} \frac{\partial \delta P}{\partial \theta} = a^2 \left[\frac{\partial \delta \rho}{\partial t} + V_x \frac{\partial \delta \rho}{\partial x} + \frac{V_\theta}{r} \frac{\partial \delta \rho}{\partial \theta} \right] \tag{3.4}$$

These equations apply separately to each inter-blade row volume and to the region upstream and downstream of the compressor (inlet and exit duct).

These equations are first solved for the static pressure. Differentiating equation (3.1) with respect to x and equation (3.2) with respect to θ, and using equation (3.3), we obtain:

$$\frac{\partial^2 \delta P}{\partial x^2} + \frac{1}{r^2} \frac{\partial^2 \delta P}{\partial \theta^2} = \frac{1}{a^2} \left[\frac{\partial .}{\partial t} + V_x \frac{\partial .}{\partial x} + \frac{V_\theta}{r} \frac{\partial .}{\partial \theta} \right]^2 \delta P \tag{3.5}$$

The solution of this equation is of the form:

$$\delta P = \sum_n A(x) e^{i \omega t + i n \theta}$$

Indeed, equation (3.5) is a wave equation which is solved using a spectral method for a time dependence of disturbances of the form: $e^{i\omega t}$. Each spatial harmonic can be solved independently and the general time dependence is obtained by Fourier superposition since the problem is linear.

The substitution of this form of δP into equation (3.5) leads to a second order linear differential equation in A(x):

$$\left(1 - M_x^2\right) \frac{d^2 A}{dx^2} - 2 i M_x \left(\frac{\omega r}{a} + n M_\theta \right) \frac{dA}{dx} + \left[\left(\frac{\omega r}{a} + n M_\theta \right)^2 - n^2 \right] A = 0 \tag{3.6}$$

This equation is then solved for δP. Having δP, basic algebra yields expressions for the other perturbations.

We get, as a solution for a disturbance with time dependence $e^{i\omega t}$:

Static pressure:

$$\frac{\delta P}{P} = \sum_{n \neq 0}^{\infty} \left[\gamma \left(\frac{\omega r}{a} + r \alpha \frac{V_x}{a} + n \frac{V_\theta}{a} \right) B_n e^{i\varphi} + \gamma \left(\frac{\omega r}{a} + r \beta \frac{V_x}{a} + n \frac{V_\theta}{a} \right) C_n e^{i\psi} \right] \qquad (3.7)$$

Density:

$$\frac{\delta \rho}{\rho} = \sum_{n \neq 0}^{\infty} \left[\left(\frac{\omega r}{a} + r \alpha \frac{V_x}{a} + n \frac{V_\theta}{a} \right) B_n e^{i\varphi} + \left(\frac{\omega r}{a} + r \beta \frac{V_x}{a} + n \frac{V_\theta}{a} \right) C_n e^{i\psi} + E_n e^{i\chi} \right] \qquad (3.8)$$

Axial velocity:

$$\frac{\delta V_x}{a} = \sum_{n \neq 0}^{\infty} \left[- \alpha r B_n e^{i\varphi} - \beta r C_n e^{i\psi} + \frac{n V_x}{a} D_n e^{i\chi} \right] \qquad (3.9)$$

Tangential velocity:

$$\frac{\delta V_\theta}{a} = \sum_{n \neq 0}^{\infty} \left[- n B_n e^{i\varphi} - n C_n e^{i\psi} + \left(\frac{\omega r}{a} + \frac{n V_\theta}{a} \right) D_n e^{i\chi} \right] \qquad (3.10)$$

Total pressure:

$$\frac{\delta P_t}{P_t} = \sum_{n \neq 0}^{\infty} \left[\begin{array}{l} \dfrac{\gamma}{1 + \dfrac{\gamma - 1}{2} M^2} \dfrac{\omega r}{a} B_n e^{i\varphi} + \dfrac{\gamma}{1 + \dfrac{\gamma - 1}{2} M^2} \dfrac{\omega r}{a} C_n e^{i\psi} \\ + \dfrac{\gamma}{1 + \dfrac{\gamma - 1}{2} M^2} \left[n \dfrac{V_x^2}{a^2} + \left(\dfrac{\omega r}{a} + \dfrac{n V_\theta}{a} \right) \dfrac{V_\theta}{a} \right] D_n e^{i\chi} + \dfrac{\gamma}{1 + \dfrac{\gamma - 1}{2} M^2} \dfrac{M^2}{2} E_n e^{i\chi} \end{array} \right] \qquad (3.11)$$

Total temperature:

$$\frac{\delta T_t}{T_t} = \sum_{n\neq 0}^{\infty} \left[\begin{array}{c} \left[\frac{\gamma - 1}{1 + \frac{\gamma - 1}{2} M^2} \frac{\omega r}{a} B_n e^{i\varphi} + \frac{\gamma - 1}{1 + \frac{\gamma - 1}{2} M^2} \frac{\omega r}{a} C_n e^{i\psi} \right. \\ \left. + \frac{\gamma - 1}{1 + \frac{\gamma - 1}{2} M^2} \left[n \frac{V_x^2}{a^2} + \left(\frac{\omega r}{a} + \frac{n V_\theta}{a} \right) \frac{V_\theta}{a} \right] D_n e^{i\chi} - \frac{1}{1 + \frac{\gamma - 1}{2} M^2} E_n e^{i\chi} \right] \end{array} \right] \quad (3.12)$$

Flow angle:

$$\frac{\delta \tan \alpha}{\tan \alpha} = \sum_{n\neq 0}^{\infty} \left[\left(- \frac{n a}{V_\theta} + \frac{\alpha r a}{V_x} \right) B_n e^{i\varphi} + \left(- \frac{n a}{V_\theta} + \frac{\beta r a}{V_x} \right) C_n e^{i\psi} + \frac{\omega r}{V_\theta} D_n e^{i\chi} \right] \quad (3.13)$$

with:

$$\varphi = \omega t + n\theta + \alpha x \quad (3.14)$$

$$\psi = \omega t + n\theta + \beta x \quad (3.15)$$

$$\chi = \omega t + n\theta - \frac{\omega + n \frac{V_\theta}{r}}{V_x} x \quad (3.16)$$

and:

$$\alpha = \frac{\left(\frac{\omega V_x}{a^2} + \frac{n V_x V_\theta}{r a^2} \right) - i \left[- \left(\frac{\omega}{a} + \frac{n V_\theta}{r a} \right)^2 + \frac{n^2}{r^2} \left(- \frac{V_x^2}{a^2} + 1 \right) \right]^{\frac{1}{2}}}{1 - \frac{V_x^2}{a^2}} \quad (3.17)$$

$$\beta = \frac{\left(\frac{\omega V_x}{a^2} + \frac{n V_x V_\theta}{r a^2} \right) + i \left[- \left(\frac{\omega}{a} + \frac{n V_\theta}{r a} \right)^2 + \frac{n^2}{r^2} \left(- \frac{V_x^2}{a^2} + 1 \right) \right]^{\frac{1}{2}}}{1 - \frac{V_x^2}{a^2}} \quad (3.18)$$

The perturbed flow quantities in the inter-blade row gaps have been set as a function of the four complex coefficients B_n, C_n, D_n and E_n which will be determined through boundary conditions at the edges of the control volumes defining the inter-blade row

gaps. These complex coefficients are constants which are determined partly by the inlet amplitude of disturbance and partly by the interaction with the other system components. Any change in these two settings will result only in a change in B_n, C_n, D_n and E_n. In other words, these four coefficients univoquely characterize both the perturbations in the inter-blade row gaps of the compressor and the compressor setting.

Physical interpretation can be associated with the above four coefficients. B_n and C_n represent the potential modes. They are also referred to as the pressure modes. B_n is the upstream decaying mode and C_n the upstream growing mode. They are found in the incompressible models. The terms associated with them indeed reduce to the incompressible form when the Mach number is low enough (Appendix 3). These terms are the only ones that can have an influence in the upstream direction, and in particular that can be felt upstream of the compressor. These terms strongly effect the way in which the blade rows are coupled. Indeed, the strength of any coupling is influenced by the rate at which these decay with axial distance. In particular, in the upstream and downstream ducts, these terms directly determine the coupling with upstream and downstream components that might eventually be included in the compressor system (dual spool compressors, etc.). At some critical distance (which depends on the frequency, the harmonic and the operating condition), the influence of the compressor can be neglected.

D_n represents the vortical mode. The terms involving D_n are also found in incompressible versions of this model and are unaltered by the inclusion of compressibility. They can be interpreted as vorticity terms which are convected with the mean flow. Unlike, B_n and C_n, D_n only exert an influence in the downstream direction, since it is of convective nature.

E_n represents the entropy mode. It is also referred to as the density mode. The terms associated with E_n are absent from incompressible models. They indeed represent

density inhomogeneities which again are convected with the mean flow. They alone of the four coefficients contribute to a perturbation in entropy and do not contribute to any perturbation in static pressure or axial velocity. Unlike, B_n and C_n, E_n only exert an influence in the downstream direction, since it is of convective nature.

In summary, we get:

$$\delta X = \sum_n \begin{bmatrix} A_n\ e^{in\theta}\ e^{ik_A x}\ e^{i\omega t} \\ +B_n\ e^{in\theta}\ e^{ik_B x}\ e^{i\omega t} \\ +C_n\ e^{in\theta}\ e^{ik_C x}\ e^{i\omega t} \\ +D_n\ e^{in\theta}\ e^{ik_D x}\ e^{i\omega t} \end{bmatrix} \begin{matrix} \longrightarrow \text{ Potential mode} \\ \longrightarrow \text{ Potential mode} \\ \longrightarrow \text{ Vortical mode} \\ \longrightarrow \text{ Entropy mode} \end{matrix} \qquad (3.19)$$

where ω, k_A, k_B, k_C, k_D are complex numbers functions of ω and of the operating point.

Therefore, if we consider each spatial harmonic and each mode, we get:

$$\delta X = A \exp[-\mathrm{Im}(k_A(\omega))\, x - \mathrm{Im}(\omega)\, t] \cdot \exp[i n \theta + i\, \mathrm{Re}(k_A(\omega))\, x + i\, \mathrm{Re}(\omega)\, t] \qquad (3.20)$$

axial damping — damping — harmonic — wave frequency

The second exponential represents a travelling wave whereas the first exponential actually represents the wave amplitude, axially growing or decaying. This relates to the observations of Garnier et al [15].

If the Mach number is chosen to be small enough, the compressible flow solutions reduce to the incompressible ones, which are derived in Appendix 3.

The case ω=0 reduces to the steady-state case, very clearly derived by Ham and Williams [39]. It should however be pointed out that, at steady state, the potential modes no longer contribute to perturbations in total pressure and total temperature.

3.4 BLADE ROW ANALYSIS

The blade passages are assumed to be straight channels, inclined to the axis at stagger angle ξ, as shown in figure 3.2. The effects due to the thickness of the blades and their camber are neglected. This is the semi-actuator disk_modelling technique [34]. The

model of a blade row is similar to the one developed by Kaji and Okazaki [37]. The flow in the blade relative reference frame is considered one-dimensional. This insures that blade rows inhibit crossflow. Therefore, circumferential flow redistribution is only possible in the inter-blade row spaces.

Similarly to section 3.3, the following equations determining the one-dimensional flow in the blade row space are derived in blade reference frame:

Mass continuity:

$$\frac{\partial \delta\rho}{\partial t} + w\frac{\partial \delta\rho}{\partial \xi} = -\rho\frac{\partial \delta w}{\partial \xi} \tag{3.21}$$

Momentum:

$$\frac{\partial \delta w}{\partial t} + w\frac{\partial \delta w}{\partial \xi} = -\frac{1}{\rho}\frac{\partial \delta P}{\partial \xi} \tag{3.22}$$

Energy equation:

$$\frac{\partial \delta P}{\partial t} + w\frac{\partial \delta P}{\partial \xi} = a^2\left(\frac{\partial \delta\rho}{\partial t} + w\frac{\partial \delta\rho}{\partial \xi}\right) \tag{3.23}$$

A solution for a disturbance with time dependence $e^{i\omega t}$ is obtained in a similar way to section 3.3, the general time dependence being obtained by Fourier superposition since the problem is linear. It has to be pointed out that, in the blade reference frame, for the circumferential harmonic n, the disturbance frequency will now be $\omega + n\,\Omega$, where Ω is the blade revolution frequency.

$$\left(\frac{\partial .}{\partial t} + w\frac{\partial .}{\partial \xi}\right)^2 \delta P = a^2\frac{\partial^2 \delta P}{\partial \xi^2} \tag{3.24}$$

with $\delta P = \sum_n A(\xi)\, e^{i(\omega + n\Omega)t}$ Ω: engine rotation frequency

We get, solving for $A(\xi)$, the following flow quantities:

Static pressure:

$$\frac{\delta P}{P} = \sum_{n=-\infty}^{\infty} \left[\gamma \tilde{B}_n e^{i\tilde{\varphi}} + \gamma \tilde{C}_n e^{i\tilde{\psi}} \right] \tag{3.25}$$

Density:

$$\frac{\delta \rho}{\rho} = \sum_{n=-\infty}^{\infty} \left[\tilde{B}_n e^{i\tilde{\varphi}} + \tilde{C}_n e^{i\tilde{\psi}} + \tilde{E}_n e^{i\tilde{\chi}} \right] \tag{3.26}$$

Velocity:

$$\frac{\delta w}{a} = \sum_{n=-\infty}^{\infty} \left[- \tilde{B}_n e^{i\tilde{\varphi}} + \tilde{C}_n e^{i\tilde{\psi}} \right] \tag{3.27}$$

Total pressure:

$$\frac{\delta P_t}{P_t} = \sum_{n=-\infty}^{\infty} \left[\begin{array}{c} \dfrac{\gamma}{1 + \dfrac{\gamma - 1}{2} M_\xi^2} (1 - M_\xi) \tilde{B}_n e^{i\tilde{\varphi}} + \dfrac{\gamma}{1 + \dfrac{\gamma - 1}{2} M_\xi^2} (1 + M_\xi) \tilde{C}_n e^{i\tilde{\psi}} + \\ \dfrac{\gamma}{1 + \dfrac{\gamma - 1}{2} M_\xi^2} \dfrac{M_\xi^2}{2} \tilde{E}_n e^{i\tilde{\chi}} \end{array} \right] \tag{3.28}$$

Total temperature:

$$\frac{\delta T_t}{T_t} = \sum_{n=-\infty}^{\infty} \left[\begin{array}{c} \dfrac{\gamma - 1}{1 + \dfrac{\gamma - 1}{2} M_\xi^2} (1 - M_\xi) \tilde{B}_n e^{i\tilde{\varphi}} + \dfrac{\gamma - 1}{1 + \dfrac{\gamma - 1}{2} M_\xi^2} (1 + M_\xi) \tilde{C}_n e^{i\tilde{\psi}} \\ - \dfrac{1}{1 + \dfrac{\gamma - 1}{2} M_\xi^2} \tilde{E}_n e^{i\tilde{\chi}} \end{array} \right] \tag{3.29}$$

These solutions are expressed in the relative frame. To simplify the matching problem at the each boundary of each control volume, expressions (3.4) to (3.8) can be expressed in stationary coordinates:

$$\tilde{\varphi} = \omega t + n\theta - n \tan \xi \frac{x}{r} - \frac{(\omega + n\Omega)}{W - a} \frac{x}{\cos \xi} \tag{3.30}$$

$$\tilde{\psi} = \omega t + n\theta - n \tan\xi \frac{x}{r} - \frac{(\omega + n\Omega)}{W + a} \frac{x}{\cos\xi} \tag{3.31}$$

$$\tilde{\chi} = \omega t + n\theta - n \tan\xi \frac{x}{r} - \frac{(\omega + n\Omega)}{W} \frac{x}{\cos\xi} \tag{3.32}$$

In these expressions, the term $n \tan\xi\left(\frac{x}{r}\right)$ represents a shift opposite to the rotation direction because the staggering of the blade. The term $\frac{\Omega x}{W \cos\xi}$ represents a shift in the rotation direction due to the movement of the blade. Therefore, the sign convention adopted in Chapter 2, where angle are measured positive in the direction of the rotor rotation, now becomes clear (rotor stagger are thus usually negative).

The perturbed flow field quantities within the blade passage depend on three coefficients $\tilde{B_n}$, $\tilde{C_n}$, $\tilde{E_n}$. $\tilde{B_n}$ and $\tilde{C_n}$ correspond to the potential modes and are similar to B_n and C_n in the inter-blade row gaps. Similarly, $\tilde{E_n}$ is the entropy mode. Due to the one-dimensionality of the model within the blade passage, there is no vortical mode.

3.5 BOUNDARY CONDITIONS IN THE UNCHOKED CASE

As seen previously, the Fourier coefficients defined in the bladed and unbladed regions are coupled via boundary conditions. Two sets of boundary conditions need to be specified: one at the leading edge of the blade, one at the trailing edge, in order to track these Fourier coefficient from the inlet of the compression system to the exit.

3.5.1 Leading edge boundary conditions

In the upstream gap, four Fourier coefficients are specified. Three boundary conditions are therefore required to define the three Fourier coefficients within the blade passage. These conditions are to be applied in the blade reference frame.

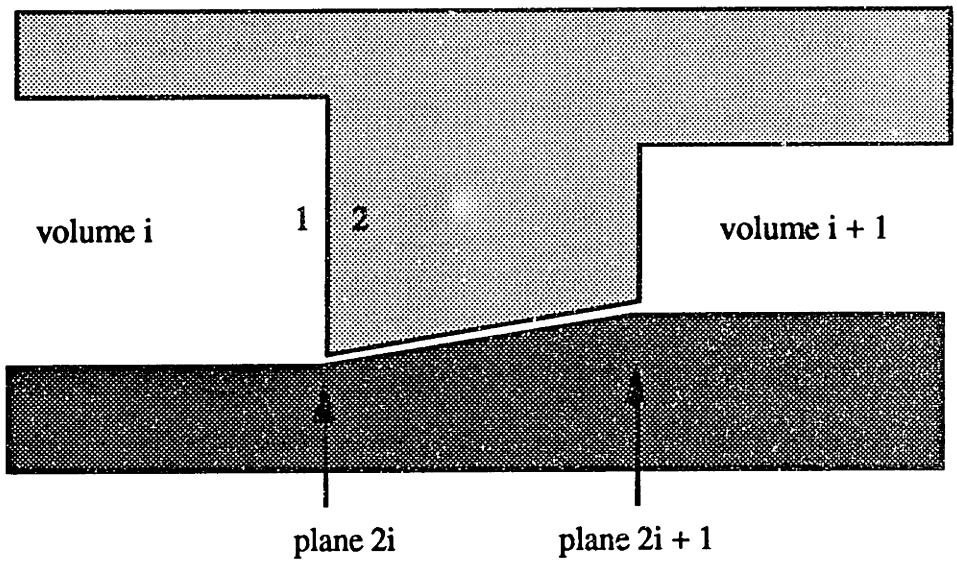

Diagram (3.1): Leading edge boundary conditions notations

(i) Continuity

$$\frac{\delta\rho_1}{\rho_1} + \frac{\delta V_{x_1}}{V_{x_1}} = \frac{\delta\rho_2}{\rho_2} + \frac{\delta V_{x_2}}{V_{x_2}} \tag{3.33}$$

The subscript 1 denotes quantity at the leading edge to be evaluated in the upstream volume and subscript 2 quantity at the leading edge to be evaluated in the blade passage, as shown in Diagram (3.1).

(ii) Relative total temperature conservation

$$\delta T_{t_1} = \delta T_{t_2} \tag{3.34}$$

(iii) Total pressure losses

They are assumed to occur at the leading edge of the blade. Indeed, the influence of the blade curvature is important at the leading edge. Also, this is relevant to the mean flow calculation (Chapter 2).

In order to capture the loss characteristic of the blade row in unsteady flow, the model originally suggested by Emmons et al [1] for unsteady losses is applied:

$$\tau_{Loss} \frac{d\,Loss}{dt} = \text{Quasi-steady Loss} - \text{Loss} \tag{3.35}$$

where τ_{Loss} is a boundary layer delay time, which is typically of the order of magnitude of the time it takes to an eddy to convect down through the blade passage.

Therefore, for a disturbance with time dependence $e^{i\omega t}$, we get:

$$\text{Loss} = \frac{\text{Quasi-steady Loss}}{1 + i\,\omega\,\tau_{Loss}} \tag{3.36}$$

where the loss is defined by the loss coefficient ω_{Loss}:

$$\omega_{Loss} = -\frac{P_{t2} - P_{t1}}{P_{t1} - P_{s1}} = \omega_{Loss}\left(\tan\beta_1 , M_{r1}\right) \tag{3.37}$$

We get, in terms of the perturbed quantities:

$$\delta P_{t_2} = \delta P_{t_1} + \frac{1}{1 + i\,\omega\,\tau_{Loss}} \begin{bmatrix} -\left(\delta P_{t_1} - \delta P_{S_1}\right)\omega_{Loss} \\ -\left(P_{t_1} - P_{S_1}\right)\left[\dfrac{\partial \omega_{Loss}}{\partial \tan\alpha_1}\,\delta\tan\alpha_1 + \dfrac{\partial \omega_{Loss}}{\partial M_{R_1}}\,\delta M_{R_1}\right] \end{bmatrix} \tag{3.38}$$

In equation (3.37) and (3.38), ω represents the frequency of the perturbation whereas ω_{Loss} represents the loss coefficient. Here again, it must be pointed out that in case of a rotor, this boundary condition has to be applied in the relative frameso that ω is replaced by $(\omega + n\,\Omega)$.

3.5.2 Trailing edge boundary conditions

In the upstream blade row, three Fourier coefficients are specified. Four boundary conditions are therefore required to define the four Fourier coefficients in the downstream volume. These conditions are, here again, to be applied in the blade reference frame.

(i) Continuity

$$\frac{\delta\rho_1}{\rho_1} + \frac{\delta V_{x_1}}{V_{x_1}} = \frac{\delta\rho_2}{\rho_2} + \frac{\delta V_{x_2}}{V_{x_2}} \tag{3.39}$$

The subscript 1 denotes quantity at the trailing edge to be evaluated in the upstream blade row and subscript 2 quantity at the trailing edge to be evaluated in the blade passage, as shown in Diagram (3.2).

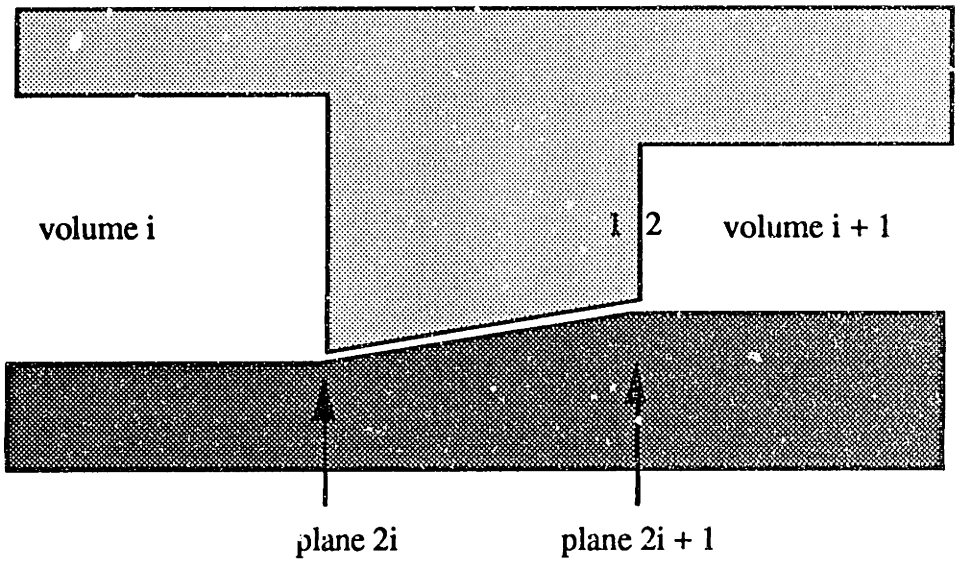

Diagram (3.2): Trailing edge boundary conditions notations

(ii) Relative total temperature conservation

$$\delta T_{t_1} = \delta T_{t_2} \tag{3.40}$$

(iii) Relative total pressure conservation

All the losses are assumed to take place at the leading edge.

$$\delta P_{t_1} = \delta P_{t_2} \tag{3.41}$$

(iv) Deviation condition

Here again, in order to capture the deviation characteristic of the blade row in unsteady situation, a similar model to the unsteady losses is applied to the unsteady deviations :

$$\tau_{Deviation} \frac{d\,\beta_2}{d\,t} = \beta_{2_{Steady\text{-}state}} - \beta_2 \tag{3.42}$$

where $\tau_{Deviation}$ has the same physical features as τ_{Loss}.

Therefore, for a disturbance with time dependence $e^{i\omega t}$, we get:

$$\text{Deviation} = \frac{\text{Quasi-steady Deviation}}{1 + i\,\omega\,\tau_{\text{Deviation}}} \tag{3.43}$$

Since $\beta_2 = \beta_2\,(\beta_{1\,\text{inlet}}, M_{r\,\text{inlet}})$, we get, in terms of the perturbed quantities:

$$\delta\beta_2 = \frac{1}{1 + i\,\omega\,\tau_{\text{Deviation}}}\left[\frac{\partial\beta_2}{\partial\beta_1}\,\delta\beta_1 + \frac{\partial\beta_2}{\partial M_{R_1}}\,\delta M_{R_1}\right] \tag{3.44}$$

Here again, it has to be pointed out that in case of a rotor, since this boundary condition has to be applied in the relative frame, ω has to be replaced by $\omega + n\,\Omega$.

3.6 STACKING METHOD

Since we are only interested in the undistorted flow case, there is no coupling between each spatial harmonic. We will therefore restrict our consideration to a particular n.

As discussed in section 3.5, there are four unknown constants in the description of the flow field in each of the control volumes upstream and downstream of the blade row and three in the description of the flow within the blade row itself. If the upstream flow constants are known, then the leading edge boundary conditions are just sufficient to determine the blade row flow and the four trailing edge determine the downstream flow constants.

This is expressed analytically as:

$$M\,V_{2i}\begin{pmatrix} B_{n_i} \\ C_{n_i} \\ D_{n_i} \\ E_{n_i} \end{pmatrix} = M\,B_{2i}\begin{pmatrix} \tilde{B}_{n_i} \\ \tilde{C}_{n_i} \\ \tilde{E}_{n_i} \end{pmatrix} \tag{3.45}$$

(leading edge boundary conditions)

$$M\,B_{2i+1}\begin{pmatrix} \tilde{B}_{n_i} \\ \tilde{C}_{n_i} \\ \tilde{E}_{n_i} \end{pmatrix} = M\,V_{2i+1}\begin{pmatrix} B_{n_{i+1}} \\ C_{n_{i+1}} \\ D_{n_{i+1}} \\ E_{n_{i+1}} \end{pmatrix} + M\,VC_{2i+1}\begin{pmatrix} B_{n_i} \\ C_{n_i} \\ D_{n_i} \\ E_{n_i} \end{pmatrix} \tag{3.46}$$

(trailing edge boundary conditions)

where:

- MV_{2i} is the 3*4 matrix associated with the modes of volume i at the leading edge of blade i
- MB_{2i} is the 3*3 matrix associated with the modes of blade i at the leading edge of blade i
- MB_{2i+1} is the 4*3 matrix associated with the modes of blade i at the trailing edge of blade i
- MV_{2i+1} is the 4*4 matrix associated with the modes of volume i+1 at the trailing edge of blade i
- MVC_{2i+1} is the 4*4 matrix associated with the modes of volume i at the trailing edge of blade i

The expression of the above matrices is defined is Appendix 4.

Some elementary algebra leads to:

$$\begin{pmatrix} B_{n_{i+1}} \\ C_{n_{i+1}} \\ D_{n_{i+1}} \\ E_{n_{i+1}} \end{pmatrix} = M V_{2i+1}^{-1} \left(- M VC_{2i+1} + M B_{2i+1} M B_{2i}^{-1} M V_{2i} \right) \begin{pmatrix} B_{n_i} \\ C_{n_i} \\ D_{n_i} \\ E_{n_i} \end{pmatrix} \qquad (3.47)$$

$$\begin{pmatrix} B_{n_{i+1}} \\ C_{n_{i+1}} \\ D_{n_{i+1}} \\ E_{n_{i+1}} \end{pmatrix} = A_i(\omega) \begin{pmatrix} B_{n_i} \\ C_{n_i} \\ D_{n_i} \\ E_{n_i} \end{pmatrix} \qquad (3.48)$$

Finally,

$$\begin{pmatrix} B_{n_{N+1}} \\ C_{n_{N+1}} \\ D_{n_{N+1}} \\ E_{n_{N+1}} \end{pmatrix} = A_N(\omega)\, A_{N-1}(\omega) \cdots A_1(\omega) \begin{pmatrix} B_{n_1} \\ C_{n_1} \\ D_{n_1} \\ E_{n_1} \end{pmatrix} = A\ (\omega) \begin{pmatrix} B_{n_1} \\ C_{n_1} \\ D_{n_1} \\ E_{n_1} \end{pmatrix} \qquad (3.49)$$

3.7 STABILITY ANALYSIS FORMULATION

The inlet flow field of the compression system is assumed to be clean and

undistorted. Neither vorticity nor entropy perturbations are convected down the inlet duct. An upstream growing pressure mode is physically non-existent. Therefore, the only mode present at the inlet of the compressor is an upstream decaying one.

In terms of vector modes, we get, for am arbitrary amplitude:

$$\begin{pmatrix} B_{n_1} \\ C_{n_1} \\ D_{n_1} \\ E_{n_1} \end{pmatrix} = \begin{pmatrix} 1 \\ 0 \\ 0 \\ 0 \end{pmatrix} \tag{3.50}$$

3.7.1 Non-zeroth harmonic (rotating stall-like perturbations)

The exit duct cannot physically contain any upstream growing pressure mode. In terms of vector mode, this means:

$$\begin{pmatrix} B_{n_{N+1}} \\ C_{n_{N+1}} \\ D_{n_{N+1}} \\ E_{n_{N+1}} \end{pmatrix} = \begin{pmatrix} 0 \\ x \\ y \\ z \end{pmatrix} \tag{3.51}$$

Therefore, the compression system operating conditions is determined by:

$$\begin{pmatrix} 0 \\ x \\ y \\ z \end{pmatrix} = A\ (\omega) \begin{pmatrix} 1 \\ 0 \\ 0 \\ 0 \end{pmatrix} \tag{3.52}$$

where $A\ (\omega)$ is the combination of matrices defined in Equation 3.49

This leads to the dispersion equation:

$$A\ (\omega)\ (1,1) = 0 \tag{3.53}$$

This, of course, is a function of the operating point, of the compressor geometry and of the disturbance frequency. This formulation of the compression system operating conditions defines a non-standard eigenvalue problem.

It should be pointed out that the downstream components do not interfere with this matching condition. Indeed, the flow field in the plenum and downstream is

axisymmetric.

This matching condition concerns only the compressor for the non-zeroth harmonics. This is not the case however for the zeroth harmonic.

3.7.2 Zeroth harmonic (surge-like perturbations)

The perturbations at the exit of the compressor must be matched with the downstream components of the compression system. Further modelling is therefore required:

(i) Plenum

The plenum is assumed to respond isentropically to its density changes:

$$\frac{\delta P_{plenum}}{P_{plenum}} = \gamma \frac{\delta \rho_{plenum}}{\rho_{plenum}} \tag{3.54}$$

(ii) Throttle

The throttle is assumed to act as a quasi -steady choked orifice. This will exist from a one-dimensional point of view if:

$$\frac{P_{ex}}{P_o} \leq \left(1+\frac{\gamma-1}{2} \right)^{\frac{\gamma}{\gamma-1}} \cong 1.893 \tag{3.55.a}$$

Since we are usually considering high-speed machines with pressure ratio greater than two, this seems to be a reasonable assumption. We can therefore assume that the corrected flow is constant.

$$\frac{\dot{m}_{throttle}\sqrt{T_{plenum}}}{P_{plenum}\, A_{throttle}} = \sqrt{\frac{\gamma}{R}}\, D(M) = \text{constant} \qquad \text{if choked} \tag{3.55.b}$$

$$\text{where} \qquad D(M) = M\left(1+\frac{\gamma-1}{2}M^2\right)^{-\frac{\gamma+1}{2(\gamma-1)}} \tag{3.56}$$

$D(1) = 0.5787$ for γ taken to be 1.4

$$\dot{m}_{throttle} = \sqrt{\gamma}\, D\, (M)\, A_{throttle} \sqrt{P_{plenum}\, \rho_{plenum}} \tag{3.57}$$

By linearizing, we get:

$$\frac{\delta \dot{m}_{throttle}}{\dot{m}_{throttle}} = \frac{1}{2}\left(\frac{\delta P_{plenum}}{P_{plenum}} + \frac{\delta \rho_{plenum}}{\rho_{plenum}} \right) \tag{3.58}$$

The continuity equation for the plenum leads to:

$$\dot{m}_{exit\ compressor\ duct} - \dot{m}_{throttle} = V_{plenum} \frac{d\, \rho_{plenum}}{d\, t} \tag{3.59.a}$$

$$\delta \dot{m}_{throttle} = \delta \dot{m}_{exit\ compressor\ duct} - V_{plenum} \frac{d\, \delta \rho_{plenum}}{d\, t} \tag{3.59.b}$$

since $\dfrac{\delta \dot{m}_{exit\ compressor\ duct}}{\dot{m}_{exit\ compressor\ duct}} = \dfrac{\delta \rho_{exit\ compressor\ duct}}{\rho_{exit\ compressor\ duct}} + \dfrac{\delta V_{x\ exit\ compressor\ duc}}{V_{x\ exit\ compressor\ duct}}$,

we get Equation 3.60:

$$\frac{\delta \rho_{exit\ compressor\ duct}}{\rho_{exit\ compressor\ duct}} + \frac{\delta V_{x\ exit\ compressor\ duct}}{V_{x\ exit\ compressor\ duct}}$$

$$- \gamma \frac{V_{plenum}\, P_{exit\ compressor\ duct}}{a^2\, \dot{m}_{exit\ compressor\ duct}} \frac{d}{dt}\left(\frac{\delta\, P_{plenum}}{P_{plenum}} \right) - \frac{\gamma + 1}{2\, \gamma} \frac{\delta\, P_{plenum}}{P_{plenum}} = 0 \tag{3.60}$$

This equation must be satisfied for the 0th harmonic. This leads to the matching condition specific to the 0th harmonic:

$$\frac{\omega r}{V_x}\frac{1}{1-\frac{V_x}{a}}\left[\begin{array}{c}\left(\frac{V_x}{a}-1\right)e^{i\left(\frac{\omega}{a}\frac{1}{1-\frac{V_x}{a}}L_{duct}\right)}\\ +\frac{V_x}{a}\left[i\,\omega\,\gamma^2\frac{V_{plenum}\,P_{exit\ comp\ duct}}{a^2\,\dot{m}_{exit\ comp\ duct}}-\frac{\gamma+1}{2}\right]e^{i\left(\frac{\omega}{a}\frac{1}{1-\frac{V_x}{a}}L_{duct}\right)}\end{array}\right]B_{0_{N+1}}$$

$$+\frac{\omega r}{V_x}\frac{1}{1+\frac{V_x}{a}}\left[\begin{array}{c}\left(\frac{V_x}{a}+1\right)e^{i\left(-\frac{\omega}{a}\frac{1}{1+\frac{V_x}{a}}L_{duct}\right)}\\ +\frac{V_x}{a}\left[i\,\omega\,\gamma^2\frac{V_{plenum}\,P_{exit\ comp\ duct}}{a^2\,\dot{m}_{exit\ comp\ duct}}-\frac{\gamma+1}{2}\right]e^{i\left(-\frac{\omega}{a}\frac{1}{1+\frac{V_x}{a}}L_{duct}\right)}\end{array}\right]C_{0_{N+1}}$$

$$+E_{0_{N+1}}e^{-i\frac{\omega}{V_x}L_{duct}}=0 \tag{3.61}$$

In a more condensed form:

$$b(\omega)\,B_{0_{N+1}}+c(\omega)\,C_{0_{N+1}}+E_{0_{N+1}}=0 \tag{3.62}$$

We therefore get from:

$$\begin{pmatrix}B_{0_{N+1}}\\ C_{0_{N+1}}\\ D_{0_{N+1}}\\ E_{0_{N+1}}\end{pmatrix}=A_0(\omega)\begin{pmatrix}1\\0\\0\\0\end{pmatrix} \tag{3.63}$$

$$b(\omega)\,B_{0_{N+1}}+c(\omega)\,C_{0_{N+1}}+E_{0_{N+1}}=0 \tag{3.64}$$

In other terms, we get a dispersion equation of the form:

$$b(\omega)A_0(\omega)(1,1)+c(\omega)A_0(\omega)(2,1)+A_0(\omega)(4,1)=0 \tag{3.65}$$

This is a function of the operating point, of the compressor geometry and of the disturbance frequency. This formulation of the compression system operating conditions defines a non-standard eigenvalue problem, in a similar way to the non-zeroth harmonic case.

Unfortunately, as can be seen, the dispersion equation $f(\omega, \dot{m}) = 0$ cannot be solved analytically for both the zeroth and non-zeroth harmonic cases. A specific numerical approach will be exposed in Chapter 4.

3.8 CHOKED CASE

A choked blade row allows all the perturbations to travel downstream, but none can travel upstream. Indeed, for a choked nozzle, perturbations in the inlet total pressure are still found downstream, but no downstream perturbations can propagate upstream.

The choking condition implies that the mass flow function at the leading edge of the choked blade remains constant:

$$\dot{m}\frac{\sqrt{T_t}}{A\,P_t\cos\alpha} = \sqrt{\frac{\gamma}{R}}\,M\left(1+\frac{\gamma-1}{2}M^2\right)^{-\frac{\gamma+1}{2(\gamma-1)}} = \text{constant} \qquad (3.66)$$

This actually specifies an additional constraint to the previously defined set of equations. Since such a constraint is to be applied at each choked blade row, this specified the allowed perturbations. This set of equation is sufficient to conduct a stability analysis for the blade rows upstream of and including the choked blade: here, the compressor actually decouples.

Since at the choked row all perturbations pass freely downstream, the problem is to choose the additional perturbations to be added at the exit the choked blade (inlet of the sub-compressor) in order to conduct a sub-stability analysis. However, as will be seen in Chapter 6, as one operates closer and closer to a choked operating point, the perturbations in static pressure become larger and larger. Moreover, when one operates on the choked part of the speedline, an additional expansion loss is defined (Chapter 2) specifing the exit static pressure of the blade row. It seems therefore reasonable to add at the exit of the choked blade rows an additional perturbation in static pressure (potential perturbation) to the ones coming from upstream of this blade, to conduct a sub-stability analysis of the

sub-compressor downstream of this blade.

It should be pointed that the perturbation in static pressure at the trailing edge of a choked blade can be large enough to unchoke the blade. This case will not be considered in this study, for the main reason that the linearization is not valid any more - the perturbated quantity is now large enough to change the operating mean quantity which violates the approach of this study. However, this limitation does not change the validity of the formulation of the next sections.

3.8.1 Boundary conditions

Boundary conditions across an unchoked blade row within a choked compressor are obviously unchanged.

3.8.1.1 Leading edge of a choked blade boundary conditions

(i) Continuity

$$\frac{\delta\rho_1}{\rho_1} + \frac{\delta V_{x_1}}{V_{x_1}} = \frac{\delta\rho_2}{\rho_2} + \frac{\delta V_{x_2}}{V_{x_2}} \tag{3.67}$$

(ii) Relative total temperature conservation

$$\delta T_{t_1} = \delta T_{t_2} \tag{3.68}$$

(iii) Total pressure losses

The expansion loss, as defined in Chapter 2, is not to be included in these losses. It actually takes place within the blade passage, between the throat and the trailing edge.

$$\delta P_{t_2} = \delta P_{t_1} + \frac{1}{1 + i\,\omega\,\tau_{Loss}} \left[\begin{array}{l} -\left(\delta P_{t_1} - \delta P_{S_1} \right) \omega_{Loss} \\ -\left(P_{t_1} - P_{S_1} \right) \left[\dfrac{\partial \omega_{Loss}}{\partial \tan \alpha_1} \delta \tan \alpha_1 + \dfrac{\partial \omega_{Loss}}{\partial M_{R_1}} \delta M_{R_1} \right] \end{array} \right] \tag{3.69}$$

These three boundary conditions are exactly similar to the one applied in the unchoked case. However, as pointed out previously, since the blade is choked, an extra boundary

condition arises at the leading edge:

(iv) Choking condition

$$\frac{\rho V_x \sqrt{T_t}}{P_t \cos \alpha} = \text{constant} \tag{3.70}$$

$$\frac{\delta\rho}{\rho} + \frac{\delta V_x}{V_x} + \frac{1}{2}\frac{\delta T_t}{T_t} - \frac{\delta P_t}{P_t} - \frac{\delta \cos\alpha}{\cos\alpha} = 0 \tag{3.71}$$

In terms of vector modes, we get:

$$\left(M^2 - 1\right)\left[\frac{\frac{\gamma - 1}{2}}{1 + \frac{\gamma - 1}{2}M^2}\frac{\omega r}{a} + \left(r\alpha\frac{V_x}{a} + n\frac{V_\theta}{a}\right)\frac{1}{M^2}\right]B_n e^{i\varphi}$$

$$+\left(M^2 - 1\right)\left[\frac{\frac{\gamma - 1}{2}}{1 + \frac{\gamma - 1}{2}M^2}\frac{\omega r}{a} + \left(r\beta\frac{V_x}{a} + n\frac{V_\theta}{a}\right)\frac{1}{M^2}\right]C_n e^{i\psi}$$

$$+\frac{1 - M^2}{M^2\left(1 + \frac{\gamma - 1}{2}M^2\right)}\left[n\frac{V_x^2}{a^2} + \frac{V_\theta}{a^2}\left(r\omega + n V_\theta\right)\right]D_n e^{i\chi}$$

$$+\frac{1 - M^2}{2\left(1 + \frac{\gamma - 1}{2}M^2\right)}E_n e^{i\chi} = 0 \tag{3.72}$$

or: $$\alpha(\omega)B_n + \beta(\omega)C_n + \gamma(\omega)D_n + \delta(\omega)E_n = 0 \tag{3.73}$$

3.8.1.2 Trailing edge of a choked blade boundary conditions

(i) Continuity

$$\frac{\delta\rho_1}{\rho_1} + \frac{\delta V_{x_1}}{V_{x_1}} = \frac{\delta\rho_2}{\rho_2} + \frac{\delta V_{x_2}}{V_{x_2}} \tag{3.74}$$

(ii) Relative total temperature conservation

$$\delta T_{t_1} = \delta T_{t_2} \tag{3.75}$$

(iii) Total pressure losses

The expansion loss, occuring within the throat and the trailing edge, is assumed to take place at the trailing edge.

$$\delta P_{t_2} = \delta P_{t_1} + \begin{bmatrix} -\left(\delta P_{t_1} - \delta P_{S_1}\right) \omega_{\text{Expansion Loss}} \\ -\left(P_{t_1} - P_{S_1}\right)\left[\dfrac{\partial \omega_{\text{Expansion Loss}}}{\partial \tan \alpha_1} \delta \tan \alpha_1 + \dfrac{\partial \omega_{\text{Expansion Loss}}}{\partial M_{R_1}} \delta M_{R_1}\right] \end{bmatrix} \tag{3.76}$$

(iv) Deviation condition

This is still valid in the choked case: a change in the inlet flow angle can move the shock position and still affect the exit flow angle.

$$\delta \beta_2 = \frac{1}{1 + i\ \omega \tau_{\text{Deviation}}} \left[\frac{\partial \beta_2}{\partial \beta_1} \delta \beta_1 + \frac{\partial \beta_2}{\partial M_{R_1}} \delta M_{R_1}\right] \tag{3.77}$$

Conditions (i), (ii), (iv) are similar to the ones in the unchoked case.

3.8.2 Stability analysis formulation

As seen above, the compressor actually decouples at the choked blades. However, an extra constraint as well as a new variable corresponding to the exit static pressure must be introduced. Since the problem is linear, we will investigate the actions of the inlet potential perturbations and of the additional static pressure perturbations at the exit of each choked blade.

In the following formulation, i_{C_m} represents the number of the mth choked blade row, whereas a_m represents the amplitude of the static pressure perturbation at the exit of the $i_{C_{m-1}}$th blade. This is illustrated on Diagram 3.3.

In this section, the formulation will be explicitely done for the first choked blade row. The extension to n choked blade rows is relatively simple but requires some algebra. The overall result will however be presented.

(i) First choked blade row

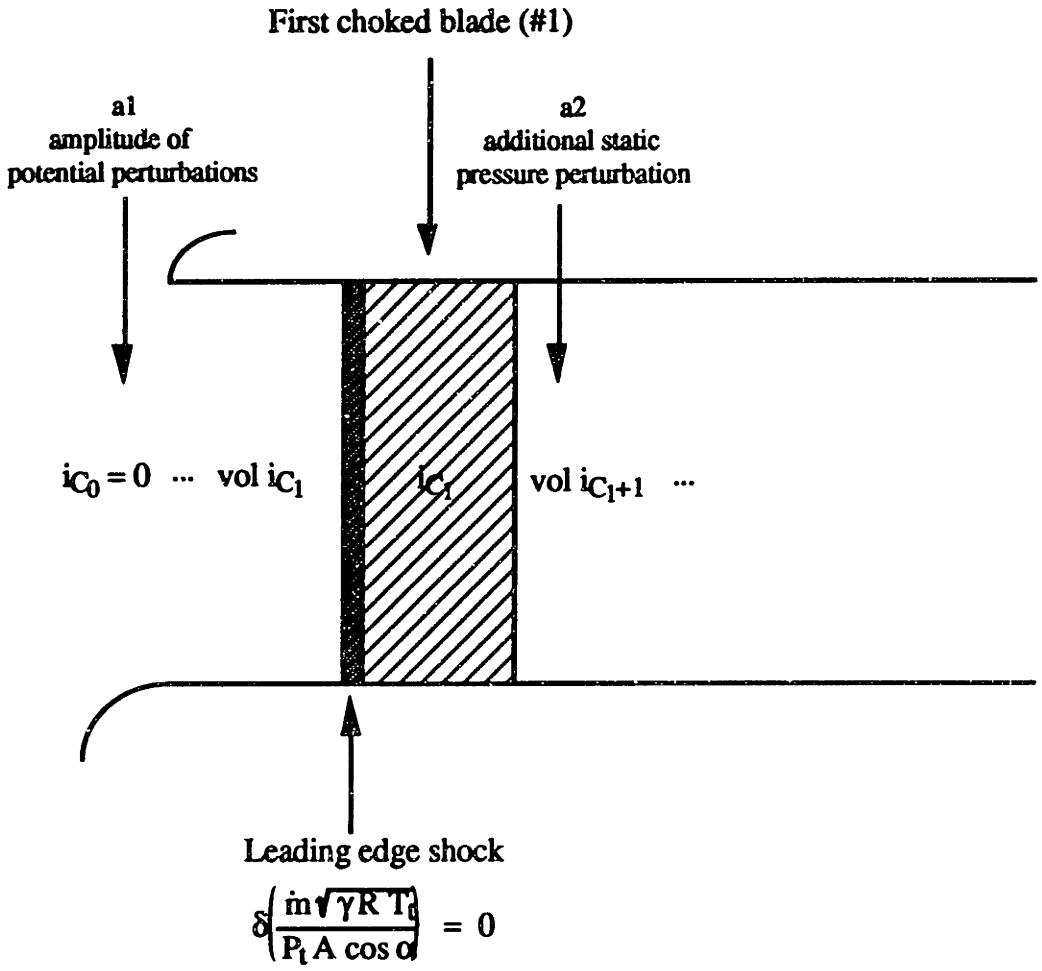

Diagram (3.3): First choked blade

We get up to the first choked blade:

$$\begin{pmatrix} B_{n_{iC1}} \\ C_{n_{iC1}} \\ D_{n_{iC1}} \\ E_{n_{iC1}} \end{pmatrix} = \prod_{k=1}^{i_{C1}-1} A_k(\omega) \cdot \begin{pmatrix} 1 \\ 0 \\ 0 \\ 0 \end{pmatrix} \cdot a_1 = A(\omega)_{i \to i_{C1}-1} \cdot \begin{pmatrix} 1 \\ 0 \\ 0 \\ 0 \end{pmatrix} \cdot a_1 \qquad (3.78)$$

The additional choking condition of this choked blade can be written, using the same conventions as in section (3.8.1.1):

$$\alpha_{iC1}(\omega)\, B_{n_{iC1}} + \beta_{iC1}(\omega)\, C_{n_{iC1}} + \gamma_{iC1}(\omega)\, D_{n_{iC1}} + \delta_{iC1}(\omega)\, E_{n_{iC1}} = 0 \qquad (3.79)$$

Putting together the previous expressions leads to:

$$\left[\begin{array}{l} \alpha_{iC1}(\omega)\, A(\omega)_{i \to iC1-1}(1,1) + \beta_{iC1}(\omega)\, A(\omega)_{i \to iC1-1}(2,1) + \\ \gamma_{iC1}(\omega)\, A(\omega)_{i \to iC1-1}(3,1) + \delta_{iC1}(\omega)\, A(\omega)_{i \to iC1-1}(4,1) \end{array}\right] a_1 = 0 \qquad (3.80)$$

$$F_{11}(\omega) \cdot a_1 = 0 \qquad (3.81)$$

At the exit of the first blade row, an additional static pressure perturbation of amplitude a_2 is added:

$$\begin{pmatrix} B_{n_{iC1}+1} \\ C_{n_{iC1}+1} \\ D_{n_{iC1}+1} \\ E_{n_{iC1}+1} \end{pmatrix} = A_{iC1}(\omega) \begin{pmatrix} B_{n_{iC1}} \\ C_{n_{iC1}} \\ D_{n_{iC1}} \\ E_{n_{iC1}} \end{pmatrix} + \begin{pmatrix} 1 \\ 0 \\ 0 \\ 0 \end{pmatrix} \cdot a_2 \qquad (3.82)$$

(iii) Last choked row (i_{C_n})

After some algebra, we have similarly:

$$F_{n1}(\omega)\, a_1 + \ldots + F_{nn}(\omega)\, a_n = 0 \qquad (3.83)$$

And the additional static pressure perturbation:

$$\begin{pmatrix} B_{n_{N+1}} \\ C_{n_{N+1}} \\ D_{n_{N+1}} \\ E_{n_{N+1}} \end{pmatrix} = A(\omega)_{1 \to N} \begin{pmatrix} 1 \\ 0 \\ 0 \\ 0 \end{pmatrix} \cdot a_1 + A(\omega)_{iC1+1 \to N} \begin{pmatrix} 1 \\ 0 \\ 0 \\ 0 \end{pmatrix} \cdot a_2 + \ldots$$

$$\ldots + A(\omega)_{iCn+1 \to N} \begin{pmatrix} 1 \\ 0 \\ 0 \\ 0 \end{pmatrix} \cdot a_{n+1} \qquad (3.84)$$

In summary, we get:

$$
\begin{aligned}
&F_{11}(\omega)\,a_1 &&= 0\\
&F_{21}(\omega)\,a_1 + F_{22}(\omega)\,a_2 &&= 0\\
&\qquad\vdots\\
&F_{n1}(\omega)\,a_1 + &&+ F_{nn}(\omega)\,a_n = 0
\end{aligned}
\tag{3.85}
$$

where:

$$
\begin{aligned}
F_{pq}(\omega) = {} & \alpha_{iC_p}(\omega).A(\omega)_{iC_{q-1}+1 \to iC_p-1}(1,1)\\
& + \beta_{iC_p}(\omega).A(\omega)_{iC_{q-1}+1 \to iC_p-1}(2,1)\\
& + \gamma_{C_p}(\omega).A(\omega)_{iC_{q-1}+1 \to iC_p-1}(3,1)\\
& + \delta_{iC_p}(\omega).A(\omega)_{iC_{q-1}+1 \to iC_p-1}(4,1)
\end{aligned}
\tag{3.86}
$$

with: $A(\omega)_{\alpha \to \beta} = \prod_{k=\alpha}^{\beta} A_k(\omega)$ (3.87)

This latter expression now needs to be linked with an exit stability condition (surge/stall), in order to fully define the stability analysis formulation.

1) <u>$n \neq 0$ (rotating stall)</u>

As seen previously, we need for the non-zeroth harmonic to get:

$$
\begin{pmatrix} B_{nN+1} \\ C_{nN+1} \\ D_{nN+1} \\ E_{nN+1} \end{pmatrix} = \begin{pmatrix} 0 \\ .. \\ .. \\ .. \end{pmatrix}
\tag{3.88}
$$

This can be expressed in terms of matrices as:

$$
\begin{aligned}
&A(\omega)_{1 \to N}(1,1).a_1 + A(\omega)_{iC1+1 \to N}(1,1).a_2 + \cdots\\
&\cdots + A(\omega)_{iCn+1 \to N}(1,1).a_{n+1} = 0
\end{aligned}
\tag{3.89}
$$

or: $F_{n+1\,1}(\omega)\,a_1 + \cdots + F_{n+1\,n+1}(\omega)\,a_{n+1} = 0$ (3.90)

with: $F_{n+1\,q}(\omega) = A(\omega)_{iC_{q-1}+1 \to N}(1,1) \qquad n \neq 0$ (3.91)

2) n = 0 (surge)

As seen previously, we need for the zeroth harmonic to get:

$$b(\omega)\,B_{N+1} + c(\omega)\,C_{N+1} + E_{N+1} = 0 \tag{3.92}$$

This can be expressed in terms of matrices as:

$$F_{n+1\,1}(\omega)\,a_1 + \cdots + F_{n+1\,n+1}(\omega)\,a_{n+1} = 0 \tag{3.93}$$

where:

$$\begin{aligned} F_{n+1\,q}(\omega) = {} & b(\omega)\,A(\omega)_{iC_{q-1}+1 \to N}(1,1) \\ & + c(\omega)\,A(\omega)_{iC_{q-1}+1 \to N}(2,1) \\ & + A(\omega)_{iC_{q-1}+1 \to N}(4,1) \end{aligned} \tag{3.94}$$

3) Conclusion

We get, for both the surge-like and the stall-like stability analysis, the following formulation:

$$\begin{bmatrix} F_{1\,1}(\omega) & 0 & 0 & 0 & 0 \\ F_{2\,1}(\omega) & F_{2\,2}(\omega) & 0 & 0 & 0 \\ \vdots & \vdots & \ddots & 0 & 0 \\ F_{n\,1}(\omega) & F_{n\,2}(\omega) & \cdots & F_{n\,n}(\omega) & 0 \\ F_{n+1\,1}(\omega) & F_{n+1\,2}(\omega) & \cdots & \cdots & F_{n+1\,n+1}(\omega) \end{bmatrix} \cdot \begin{bmatrix} a_1 \\ a_2 \\ \vdots \\ a_n \\ a_{n+1} \end{bmatrix} = \begin{bmatrix} 0 \\ \vdots \\ \vdots \\ \vdots \\ 0 \end{bmatrix} \tag{3.95}$$

which can be written as:

$$[M(\omega)] \cdot \begin{bmatrix} a_1 \\ a_2 \\ \vdots \\ a_n \\ a_{n+1} \end{bmatrix} = \begin{bmatrix} 0 \\ \vdots \\ \vdots \\ \vdots \\ 0 \end{bmatrix} \tag{3.96}$$

The stability analysis therefore consists of solving the following dispersion equation for ω :

$$\mathrm{Det}\,[M(\omega)] = 0 \tag{3.97}$$

Chapter 4

Computational Description of the Model

4.1 INTRODUCTION

A computational tool [29] has been developed to solve the compression system flow fields in order to predict the steady compressor performance, as well as the neutral stability operating conditions and the operating conditions around this neutrally stable point. The calculation consists of three parts. The first part solves the governing equations for a undistorted steady flow. The second and third parts add a most general unsteady disturbance to the previously calculated solution of the mean flow. They determine the growth rate of the perturbations, indicating the stability of the compression system. The second part determines the stability operating point, whereas the third part solves for the structure of the travelling waves about this operating point. This chapter dicusses detatils of each of these calculations.

4.2 MEANFLOW CALCULATION

The meanflow calculation uses a classical stage-stacking method explained in Chapter 2. An empirical model for losses and deviations have been deferred in this chapter. However, the major computational problems come from the fact that most of the correlations used to the meanline performance deviation and losses prediction are defined through implicit relations, as stated in Chapter 2. Most computational algorithms are therefore iterative schemes with some adaptative relaxation included.

In the stacking process, when all the conditions at the inlet of a blade are known, an iteration is performed on the density ratio across the blade. Once the exit density is assumed, the exit axial velocity and the diffusion factor are specified. An iteration is done for get the exit flow angle from the diffusion factor. Then, the minimum loss operating conditions are determined and the loss bucket is constructed, which leads to the loss coefficient, and to a new density. An original construction of the loss bucket is developed in Appendix 5.

Some speedlines generated by this model are shown on figures 4.1.a to 4.1.e. for low speed machines, and on figures 4.2.a to 4.2.f for high speed machines. Both pressure characteristics and adiabatic efficiencies can be evaluated. In both cases, predictions and experimental data are in reasonable agreement. The geometry inputted to these mean flow calculations are included in Appendix 1.

4.3 NEUTRAL STABILITY CALCULATION

In Chapter 3, the formulation of the unsteady compression system operating conditions was set. Basically, for a given geometry, the only valid disturbances are determined in order for both their frequency and the operating point to meet the dispersion equation:

$$f(\omega, \dot{m}) = 0 \tag{4.1}$$

The above formulation defines a non-standard eigenvalue problem, where the eigenmodes of the compressor are determined by the values of ω for which there exists a flowfield perturbation at the specified operating point $\dot{m}$.

If the operating point is fixed, we get:

$$f(\omega, \dot{m}_{fixed}) = g(\omega) = 0 \tag{4.2}$$

From Equation (4.2), the neutral stability point is obtained for a zero growth rate of the disturbances, i.e. Im (ω) = 0. A positive imaginary part would indicate a stable mode and a negative imaginary part an unstable mode. This condition on ω defines the operating point at neutral stability. Therefore, the stability analysis consists of solving Equation (4.1) with the stability condition Im (ω) = 0. This determines a specific neutral stability operating point and a corresponding specific eigenvalue of the system, ω, the neutral stability frequency. From these values, the modes and the perturbed flow field quantities can be determined everywhere in the compressor, as stated in Chapter 3. This leads to the transient behavior of the flow field instabilities at neutral stability.

A convenient way to solve this problem is to use the Nyquist criterion.

4.3.1 Nyquist criterion

Let g (ω) be some single-valued function analytic in a given region of the complex plane except at a finite number of points. According to this criterion [38], given a closed contour C (C oriented anticlockwise) in the complex plane so that g (ω) is analytic at every point on C, we get:

$$\frac{1}{2\pi} \Delta_C \mathrm{Arg} (g(\omega)) = N_{zeros} - N_{poles} \tag{4.3}$$

where $\Delta_C \mathrm{Arg} (g(\omega))$ represents the change in argument of g(ω) around C and where N_{poles} and N_{zeros} are the number of poles and zeros inside the contour C

This criterion is illustrated in Figures 4.3.a and 4.3.b. This criterion is very efficient in a sense that the evaluation of g (ω) around a contour gives insight on the behavior of this function inside this contour: instead of scanning through the whole complex plane, one only needs to evaluate g (ω) around a contour.

4.3.2 Neutral stability algorithm

For the neutral stability analysis, since the boundary is set by Im (ω) = 0, a Nyquist contour of a shape similar to the one on Diagram (4.1) is used (see section 4.3.3).

For a fixed mass flow, the function considered is the dispersion function g (ω) as defined in equation (4.2) and the Nyquist criterion leads to the number of zeros minus the number of poles within the above contour. The zeros of g(ω) cannot be determined analytically, but its poles can. Indeed, if one looks at the stacked matrices shown in section 3.6, two matrices must be inverted at each blade:

(i) MB_{2i} which is always invertible

(ii) MV_{2i+1} which is not invertible, but of which we can analytically compute the determinant:

$$\det (MV_{2i+1}) = A\left(r^2 \omega^2 + 2 n r V_\theta \omega + n^2 \left(V^2 - a^2\right)\right) \left(r^2 \omega^2 + 2 n r V_\theta \omega + n^2 V^2 \right) \tag{4.4.a}$$

where A is a constant depending on the mean flow.

This yields to the following poles for each blade row:

$$\frac{r \omega}{n a} = - M_\theta \pm \sqrt{1 - M_x^2} \tag{4.4.b}$$

These poles actually correspond to Im (α) = Im (β) = 0, where α and β are defined in section 3.3. This corresponds to a pure oscillatory mode in the inter-blade row gaps.

$$\frac{r\omega}{n\,a} = -M_\theta \pm i\,M_x \qquad (4.5)$$

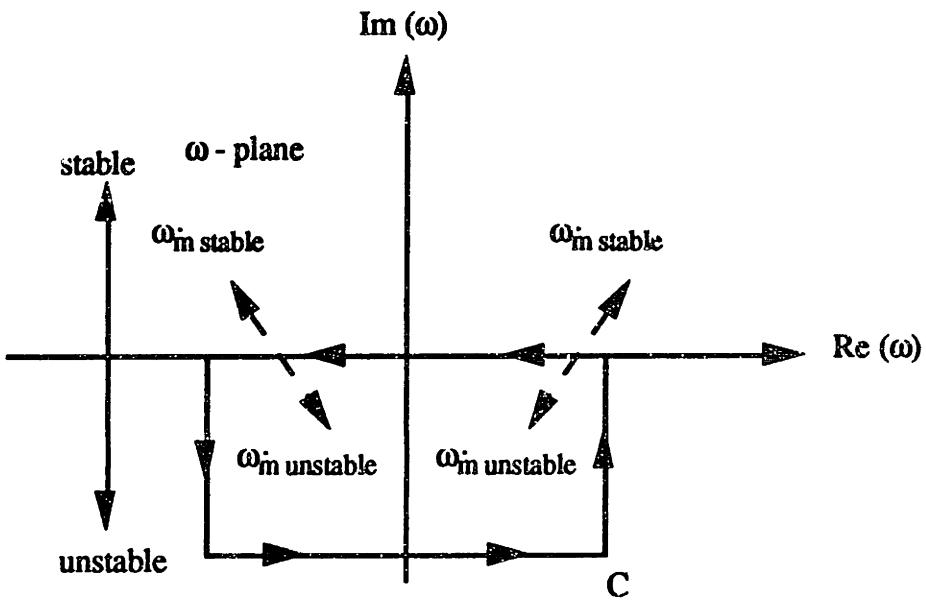

Diagram (4.1): Nyquist contour (Neutral stability prediction)

The poles of the dispersion function g (ω) are therefore known and their number within the Nyquist contour specified. By evaluating g (ω) along this contour, the number of unstable zeros at this operating point is determined. An iteration can be conducted on the mass flow in order to determine the neutral stability mass flow at which the zeros lie exactly on the real axis. Once this mass flow is determined, the eigenvalues are set such that Equation (4.2) is satisfied. This sets the neutral stability frequencies.

At this operating point and at this neutral stability frequency, the modes as well as the perturbed flowfield quantities are predicted along the compressor axis.

4.3.3 Nyquist contour and computational techniques

A reasonable investigation width for the Nyquist contour is set for the harmonic considered, in order to improve the computational efficiency. For non-zeroth harmonic, the zeros are excepted to lay between -n and +n. For the zeroth harmonic, a reasonable

width is half of the Helmholtz frequency of the compression system:

$$\omega_{Helmholtz} = \frac{U}{2 L B} \tag{4.6}$$

A reasonable depth for the Nyquist is to be chosen too, for practical numerical consideration.

As stated in section 4.3.2, the poles of g (ω) corresponding to the oscillatory modes lay on the real axis and are therefore most likely to be on the Nyquist contour. In order to meet the hypothesis of the Nyquist criterion that g (ω) must be analytic at every point of the contour, the Nyquist contour must adapted in order to circle these poles. A similar check is done for the other poles so that they do not lay on the contour.

As seen in Chapter 3, the dispersion function is derived from the expressions of the pertubations of the flow field quantities within the blade rows and within the inter-blade rows passages. However, the two potential modes in the inter-blade gaps are expressed as a function of two coefficients α and β of the form:

$$\alpha = \alpha (\omega) = u (\omega) - i (v (\omega))^{1/2} \tag{4.7}$$

$$\beta = \beta (\omega) = u (\omega) + i (v (\omega))^{1/2} \tag{4.8}$$

where u (ω) and v (ω) are complex functions of the complex frequency ω and of the operating point (see section 3.3). α is indeed set so that Im (α) is negative in order to characterize the upstream decaying potential mode. β similarly characterizes the upstream growing mode. The usual way the complex square root function $s^{1/2}$ is defined leads to a discontinuity where the argument of s is π. If we map the square root function where the values of s scan different contours of the complex plane, we get the patterns on Diagram 4.2:

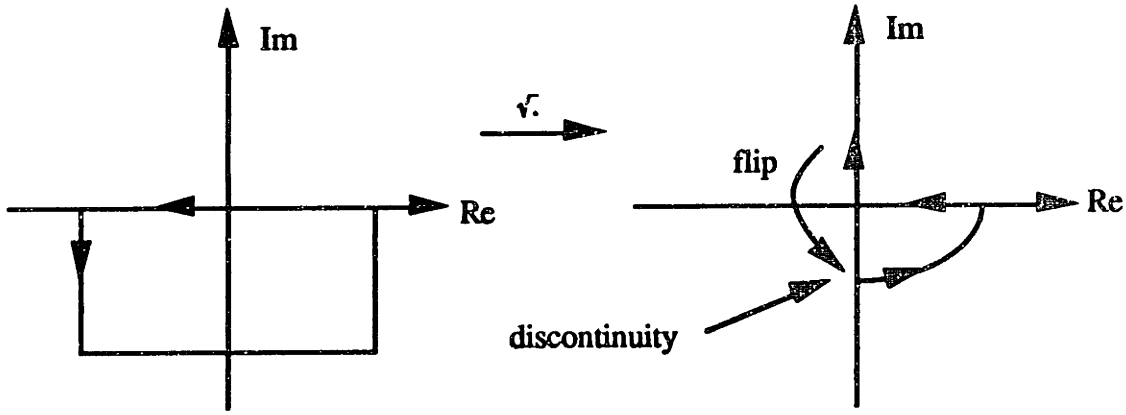

Diagram (4.2): Square root function discontinuity

In order to apply the Nyquist criterion, $\alpha(\omega)$ and $\beta(\omega)$ need to be continuous and single-valued along the contour C. This means that the square root function must be appropriately defined in order not to present the discontinuity where the argument of $v(\omega)$ is π. A "flip" of the usual square root function is specified by inspection of the neighbouring values of $v(\omega)$ along the contour. This is shown on Diagram (4.2).

Another way of performing this calculation would be to adapt the Nyquist contour such that the image of the contour through $v(\omega)$ does not include the discontinuity point of argument π. In other words, this means indenting the Nyquist contour so that frequencies such that:

$$-\left(\frac{\omega}{a}+n\frac{V_\theta}{r\,a}\right)^2+\frac{n^2}{r^2}\left(-\frac{V_x^2}{a^2}+1\right)=R\,e^{i\pi}$$

or rather

$$\omega=-\frac{n\,V_\theta}{r}\pm\left[\frac{n^2}{r^2}\left(1-\frac{V_x^2}{a^2}\right)-R\,e^{i\pi}\right]^{\frac{1}{2}} \qquad (4.9)$$

do not belong to the contour. We get Diagram 4.3:

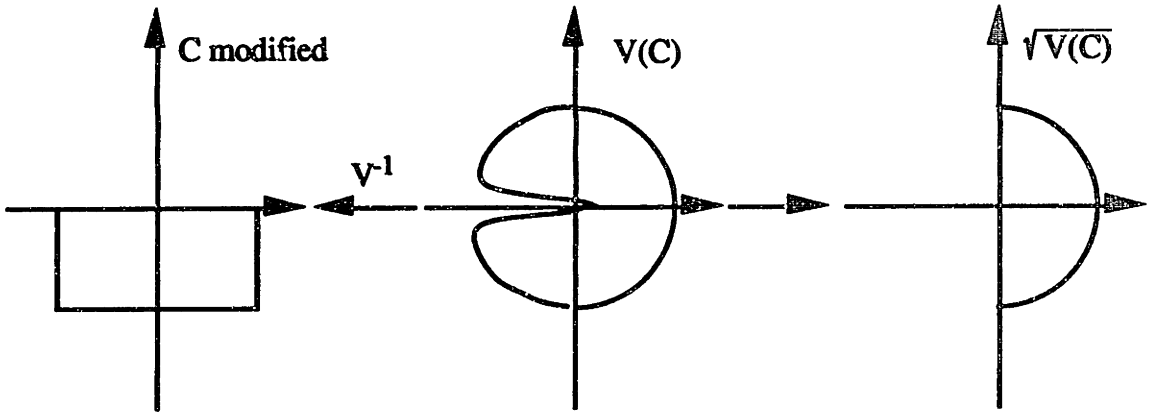

Diagram (4.3): Possible Modified Nyquist Contour

4.4 TRAVELLING WAVE PREDICTION ALGORITHM

Looking back to Equation (4.1), it is of considerable interest to be able to determine, for some specified mass flow, the flow field perturbations along the compressor axis. More specifically, what do these travelling waves look like, what do their frequency and damping look like? The operating point must be close to the neutral stability point in order to such travelling waves be observed, because of the damping term.

Since the operating point is fixed, the eigenvalues of the compression system are now fixed. The Nyquist Criterion is again used to determine them. The same computational techniques as described in section 4.3.3 are used. However, in this case, instead of iterating on the mass flow, an iteration can be performed on the 'upper bound' of the Nyquist Contour to determine the position of the eigenvalues in the complex plane, as shown on Diagram 4.4.

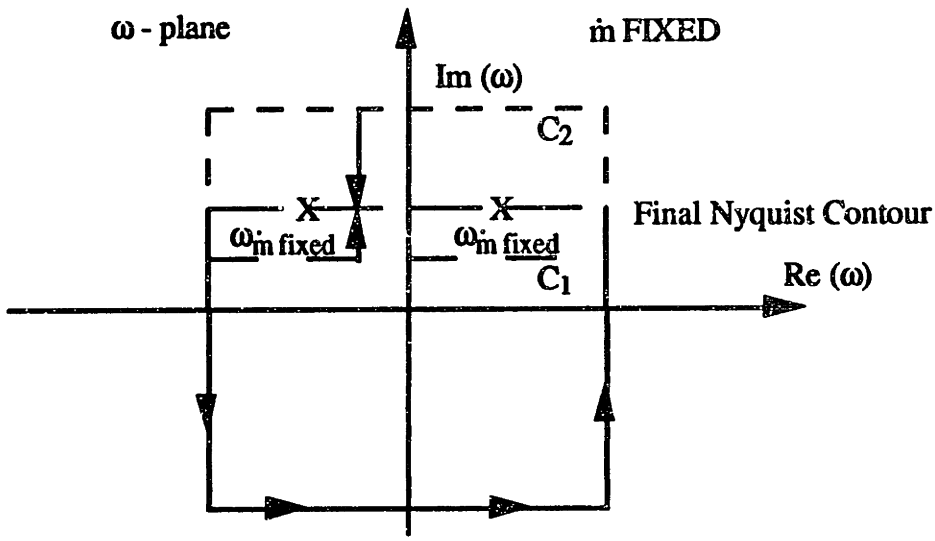

Diagram (4.4): Nyquist contour (travelling wave prediction)

Once the eigenvalues of the system are obtained, the damping, the wave frequency, and the axial damping are known. The travelling waves are consequently fully determined for the considered spatial harmonic. At this point, the global perturbations (including several harmonics) can be tracked along the compressor axis.

Chapter 5

Prediction of low speed compression system stability and comparison between low and high speed model predictions

5.1 INTRODUCTION

The objective of this chapter is to validate the compressible model developed in this thesis with calculations on low-speed compressors. Indeed, (i) experimental results are available and (ii) results can be compared to the ones obtained from simple incompressible models. In low speed machines, the flow is pretty much incompressible so that the incompressible models presented in Chapter 1 capture relatively well the main flow field phenomena. Moreover, such incompressible models lead to an analytical solution for the stability margin. Once the compressible model validated, it would therefore be of considerable interest to assess the range of validity of such incompressible models.

Once these effects quantified, an investigation of the stability margin and of the rotating stall precursors using this detailed compressible model will be conducted.

5.2 COMPARISON BETWEEN THE NEUTRAL STABILITY PREDICTIONS FROM THE LOW AND HIGH SPEED MODELS

An incompressible stability analysis has been performed in Appendix 3 for a low speed axial flow compression system operating with clean inlet flow. It is an extension of the Hynes-Greitzer model to compressors whose pressure rise coefficient and exit flow angle are sensitive to the inlet swirl and that are operating with non-axial inlet mean flow. This extended incompressible model includes a number of compressor features in order to be as close as possible to the actual behavior of axial low speed compressor. However, a analytical solution to the stability analysis can still be obtained.

Such an analysis can be used for (i) testing the validity of the compressible model developed in this thesis on simple low speed incompressible cases, and (ii) comparing the incompressible features of stability margin with the compressible ones.

For the simplicity for the calculations performed in this investigation, an axial inlet mean flow has been assumed. We get, from Equations (A.3.22) and (A.3.23) with $\alpha_1 = 0$, a neutrally stable flow coefficient ϕ_{NS} defined by:

$$\left(\frac{\partial \psi}{\partial \phi}\right)_{\phi_{NS}} = \left(\frac{\partial \alpha_2}{\partial \alpha_1}\right)_{\phi_{NS}} \frac{1}{\cos^2 \alpha_2} \phi_{NS} \tag{5.1}$$

It has to be pointed out that all harmonics become unstable at the same flow coefficient. The corresponding frequency ω_{NS} is therefore:

$$\frac{r\,\omega_{NS}}{n\,U} = - \frac{\lambda - \left(\frac{\partial \psi}{\partial \alpha_1}\right)_{\phi_{NS}} \frac{1}{|n|\,\phi_{NS}} - \left(\frac{\partial \alpha_2}{\partial \phi}\right)_{\phi_{NS}} \frac{\phi_{NS}^2}{|n| \cos^2 \alpha_2}}{\left(\frac{2}{|n|} + \mu\right)} \tag{5.2}$$

Calculations have been performed on the C106 single-stage compressor described by Longley [13] and whose geometry is shown in section (A.1.3). In order to compare the incompressible analytic solution to the compressible stability analysis calculation developed in the previous chapters, the compressor geometry was adjusted in order to

have no inter-blade row gaps. Neither unsteady losses nor deviations were assumed.

Figure 5.1 shows the neutral stability frequencies obtained from both the compressible calculation and the incompressible analytical solution for the first four harmonics for the range of blade Mach number varying from 0.04 to 0.3. As can be seen, the compressible calculation results match exactly the analytical solutions for sufficiently low Mach numbers. The flow coefficients were very similar too (0.5% in relative error at M=0.2).

Shown in figure 5.2 is the relative difference on the neutral stability frequencies obtained from the compressible and incompressible models. It has however to be pointed out that the lower the harmonic is, the higher the relative error is. For blade Mach number up to 0.35, the error is less than 2%. A interpolation using the least square method performed for values obtained for blade Mach numbers of 0.04 to 0.3 shows a very good fit such that:

$$\frac{\omega_{compressible}}{\omega_{incompressible}} = A \frac{1}{\sqrt{1 - M^2_{blade}}} + B \qquad (5.3)$$

where A and B are obtained by the least square method for each harmonic. The form of Equation (5.3) is classical and might be expected by the form of the equations derived in Chapter 3 and Appendix 4. An expansion of Equation (5.3) leads to the classical form:

$$\frac{\omega_{compressible}}{\omega_{incompressible}} = A' M^2_{blade} + B' \qquad (5.4)$$

However, for blade Mach numbers above 0.35, the neutral stability frequency behavior starts to deviate from this interpolation, as shown in figure 5.2. The non-linearities due to the compressibility are becoming significant. Besides, the harmonic behavior is not captured anymore by the interpolation.

5.3) INVESTIGATION OF THE NEUTRAL STABILITY OPERATING CONDITIONS

The compressible model results being in excellent agreement with the theoretical

ones for sufficiently low Mach numbers and for hypothetical compressor geometries, the next step is to investigate the validity of this model on an actual multistage low speed compressor. Apart from the incompressibility assumption relaxed in this model, some other flow features previously not included in stability calculations (unsteady losses, unsteady deviations, inter blade row gaps, finite length blades, etc.) are now taken into account. The current issue is now to evaluate the effectiveness of this model in predicting the stability margin. Calculations on low-speed machines where many experimental observations are available will therefore bring some meaningful insights.

Calculations have been performed on a 3 stage axial compressor at MIT described by Garnier [21] and whose geometry is shown in Section (A.1.2). The staggering is referenced as the build #2. The actual compressor geometry was included in this stability analysis and unsteady losses and deviations were taken into account. Different IGV staggers were tested.

Figure 5.3 shows the experimental speedlines obtained for a range of inlet guide vanes settings varying from -16.9 degrees to +68.1 degrees. Figure 5.4 shows the predicted speedlines as well as the predicted stall point. It has to be pointed out that these speedlines have been obtained through the one-dimensional meanflow prediction algorithm described in Chapter 2 and Chapter 4, using the empirical correlations described in Chapter 2 and Appendix 5. These latter correlations were originally high speed correlations.

The superposition of the predicted and the experimental speedlines shows a very good agreement. The only discrepancy consists in the flow coefficient range: the predicted speedlines reflect the actual compressor behavior but at a flow coefficient of 0.05 to 0.1 higher. This can be seen on figure 5.5 for an IGV setting of + 8.1 degrees. Considering the relative simplicity of the meanflow generation technique and of the generic correlations used, the shape of the characteristic is very satisfying.

Figure 5.6 shows the predicted and the measured stall flow coefficient for the different IGV staggers. The above discrepancy in the mean flow coefficient range can be observed. However, the trends of the stall operating point are well captured by the calculation.

Shown on figure 5.7 is the predicted slope of the pressure rise coefficient at neutral stability. Rotating stall is predicted to happen at a slightly positive slope. As developed in Appendix 3, the slope of the compressor characteristic appears to be a determining factor for the rotating stall inception point. However, the experimental determination of this slope is very inaccurate as can be observed on figure 5.3. This is mainly due to the finite amount of discrete measurements in the immediate proximity of the stall point. However, positive slopes can be seen at neutral stability on figure 5.3 for some IGV settings (+3.1°, +8.1°, +13.1°, +23.1°, +33.1°). As the IGV stagger increases, the slope of the measured pressure rise characteristic at neutral stability appears to be decreasing, which is in agreement with the trend of figure 5.8. Without risking ourselves to plot the measured slopes of the compressor characteristic, it seems as if the neutral stability slopes are somewhat captured by the calculation.

Figure 5.8 shows the predicted rotating stall frequencies for the different IGV settings. A rotating stall (first harmonic-like) frequency of 13.3 Hz was measured for an IGV setting of +8.1° on the actual compressor. The predicted frequency of 14.5 Hz is in very good agreement.

5.4 INVESTIGATION OF TRAVELLING WAVES

5.4.1 Introduction

The good prediction trends of the neutral stability operating conditions for low speed compressor leads us to the investigation of the compressor operating conditions prior to the stall inception. Travelling waves have been quite extensively observed in

such regimes [15, 21]. A good physical understanding as well as an efficient prediction tool can be of considerable interest in the design of an active control device. The modelling of such travelling waves have been exposed in Chapter 3 and 5.

5.4.2 MIT single stage compressor

5.4.2.1 Investigation of the mean flow effects on the stability analysis

The calculations in this section were performed using the MIT single-stage compressor geometry [21]. Garnier [15,21] measured travelling waves in this compressor over a large range of flow coefficient. The rotor blades were highly loaded in order to promote stall there (a diffusion factor of 0.6 was chosen). The geometry used can be found in section A.1.1. The strange behavior of this compressor design , and especially the kink in its speedline was somewhat captured by the meanflow calculations, as shown in figures 5.9 and 5.13.

Figure 5.9 shows the measured speedline as well as the predicted one. The speedline is allowed to go beyond the predicted stall point. As can be seen, the prediction is not very good. However, travelling wave calculations will still be performed based on this meanflow prediction referred to as "case 1". Figure 5.10 indicates the corresponding static pressure pattern along the compressor axis at neutral stability.

Figure 5.11 shows the measured and the predicted travelling wave frequencies as the flow coefficient is increased from its neutral stability value. The predicted pattern is very similar to the measured one, indicating that the correct fluid mechanics of such travelling waves are indeed captured by the model. However, the stall points differ by 10%. The frequencies range also differ by approximately 15%.

The measured and predicted damping is shown on figure 5.12. The discrepancy in flow coefficient is still present. Moreover, the predicted damping increases faster than the measured one. However, close enough to stall, both behaviors are very similar.

In order to assess the influence of the mean flow on this prediction, the empirical correlations used to predict the meanflow have been reset in order to achieve a better fit with the experimental measurements. This mean flow prediction, referred to as "case 2", is shown on figure 5.13. The corresponding static pressure pattern along the compressor axis at neutrtal stability is shown on figure 5.14. The comparison of figure 5.9 to figure 5.13 shows an increased static pressure rise across the rotor and the stator.

However, the travelling wave frequencies and damping predicted with this mean flow do not differ significantly from case 1. This is shown on figures 5.15 and 5.16.

The discrepancy of the damping prediction can be accounted for by the relatively poor meanflow prediction. The losses and deviations correlations used were derived from high speed machines, and may not perform very well on a low speed compressor. The analytical incompressible stability analysis can however give some insight on the departure of the prediction. From Equation (A.3.22), the damping frequency is determined by:

$$\frac{r\,\omega_i}{U} = -\frac{\left(\frac{\partial\psi}{\partial\phi}\right) - \left(\frac{\partial\alpha_2}{\partial\alpha_1}\right)\phi\frac{1}{\cos^2\alpha_2}}{\left(\frac{2}{|n|}+\mu\right)} \tag{5.5}$$

Once the neutral stability point is predicted, the slope of the predicted characteristic remains very small, and fails to capture the strong negative slope at the kink of the experimental characteristic shortly after stall. Therefore, the measured damping sharply increases. Once the predicted slope gets a value close to the experimental one, the predicted damping starts to increase, but the damping rates are still very different. As the flow coefficient increases, the damping is expected to increase as $\left(\frac{\partial\alpha_2}{\partial\alpha_1}\right)\phi\ \frac{1}{\cos^2\alpha_2}$. However, the predicted slope remains constant, which is characteristic of low turning and therefore of a low $\left(\frac{\partial\alpha_2}{\partial\alpha_1}\right)$. This term is much lower in the prediction than it is in the

actual compressor, which explains the discrepancy in the damping prediction, even when the value of the slope of the characteristic is in agreement. This latter term is usually very small for multistage compressors but might be quite important for a single stage compressor.

The accuracy of the characteristic shape prediction appears to be the keystone for an accurate stability calculation. Since "case 1" and "case 2" characteristics have very similar shapes, and since the behavior of this single stage.compressor is unusual, the above calculations did not capture well the precursor behavior, but this does not necessarily question the validity of the stability model. The mean flow prediction requires improvement .

One reason for running this case was the availability of data, even though it was known that the behavior of single stage compressors (and especially of this one) is generally more difficult to predict than that of multistage compressors.

5.4.2.2 Investigation of the axial distribution of the travelling waves amplitude

In high speed machines, as indicated by Garnier [21] and by Cargill and Freeman [26], the axial position of the sensors is very important for the precursor wave detection. Figures 5.17 and 5.18 show the amplitude of the first harmonic of the static pressure and axial velocity perturbations at 0.1% of the stall point. These perturbations actually correspond to a travelling wave observable in the machine, since the damping is low. The static pressure perturbations cover a wide range (+20% to -80% of the inlet perturbation) and their amplitude is maximum in the IGV-rotor gap. The axial velocity perturbations cover a smaller range and are mostly seen at the stator inlet.

Figure 5.19 is of some interest since it shows the perturbations in mass flow along the compressor axis. An incompressible model would not allow such a perturbation to vary along the compressor. Here, the perturbation amplitude grows as the

Mach number rises, increasing up to 4.5% of its inlet value at the compressor exit. This range makes sense since the mean blade Mach number is 0.23.

Garnier [21] measured the mean amplitude of the first harmonic of the velocity peturbations at six stations along the compressor axis. This is shown on figure 5.19.b along with the model predictions. The trend of the velocity perturbations is well captured. It must be pointed out that this calculation was made very close of stall so that the predicted travelling wave frequency and damping are close to the actual one. Besides, "case 2" was used to get a better approximation of the mean flow quantities. However, as pointed out by Garnier, this distribution might not be the best to consider for active control of actual compressors, but rather the signal to noise ratio. No noise model has been implemented so far on this model to assess the effects of noise on the quality of travelling wave measurements.

5.4.3 MIT three stage compressor

Calculations have been done on the MIT three-stage compressor used by Garnier [21]. This is actually the same compressor as the one used in section 5.3. A inlet guide vane setting of +8.1° was chosen.

As shown on figure 5.20, the travelling wave frequency decreases from 14.5 Hz at stall to 3 Hz at 110% of the stall flow coefficient and then increases back. This behavior differs from the one observed on the single stage compressor where the frequency would remain approximately constant over a large range of flow coefficient. However, for higher flow coefficients, the frequency would similarly start to drop.

As shown on figure 5.21, the damping sharply increases as we move away from stall, which is expected. Its behavior is however similar to the one found in the single stage case.

Experimental measurements of such travelling waves characteristics in this

compressor are currently being performed at the MIT Gas Turbine Laboratory.

5.4.4 Summary

The travelling wave predictions performed on both single stage and multistage compressors show that the key fluid mechanics are well captured by the model. However, the fidelity of the meanflow prediction (slopes, deviations) appears to be a key point in the accuracy of the calculation. More experimental data, especially on multistage compressors, are therefore required in order to assess the validity of the model in predicting rotating stall precursors.

5.5 Conclusions

The effect of relieving the assumption of incompressibility in previous stability models has been investigated. For blade Mach numbers up to 0.35, the error is less than 2 % and is classically a function of the square of the Mach number. For higher Mach numbers, the departure of this square interpolation is significant, and the incompressible models fail to capture adequately the stability features of axial compressors.

The two-dimensional model developed in this thesis has then been used to efficiently predict the stability margin of different low speed compressor configurations.

The travelling wave behavior prediction has been less satisfactory, although all the fluid mechanics trends are correctly predicted. However, the only comparison done so far has been on one singular low-speed compressor. The key point appears to be the effectiveness of the mean flow calculation. More test calculations will have to be conducted, as soon as experimental measurements are available, in order to make a adequate statement of the validity of this prediction tool.

Chapter 6

Investigation into compressibility effects and prediction of high speed compression system stability

6.1 INTRODUCTION

The model developed in this thesis has been so far evaluated in low speed compressors, where a lot of information is available, both theoretically and experimentally.

The purpose of this chapter is to investigate the stability attributes of high speed multistage compressors as well to give some insight on how, where and when the instability occurs. This is quite challenging since very little information is available on such machines to compare the predictions with. Since it is very difficult to experimentally investigate high speed compressor stability for reasons previously presented, the model developed is all the more useful in understanding the key features of rotating stall and surge in such machines.

Two phenomena, due to the compressibility of the flow going through the machine, seem to affect the stability margin of high speed compressors. The first effect is the stage mismatching - this could be qualified as a *static* compressible effect. The

second effect of compressibility is that the perturbations leading to the instability are of compressible nature - this could be qualified as a *dynamic* compressible effect. The main objective of this chapter is to assess the role these two phenomena play in the determination of the stability margin. The accuracy of the mean flow calculation will also be adressed in terms of the effectiveness of the stability attributes.

Pre-stall travelling waves behavior will then be investigated. The effects of unsteady losses, unsteady deviations and inter blade row gaps will finally be assessed.

6.2 EVALUATION OF THE EFFECTS OF COMPRESSIBLE PERTURBATIONS ON NEUTRAL STABILITY

6.2.1 NACA eight-stage compressor

Calculations using the compressible model developed in this thesis were done on the NACA 8 stage high speed compressor, which is described in Appendix 1. As can be seen on figure 6.1, the predicted and the experimental characteristics as well as the instability points are in reasonable agreement (5% to 10 % error for the stall point). For the 50%, 60% and 70% speedlines, the instability occur at approximately zero slope. However, at 90% speed, both the predicted and the experimental stall points occur at a strongly negative slope.

The second harmonic is predicted to stall first, as stated in tables 6.1 to 6.3. The range of frequency at neutral stability varies between 43% and 53% of the rotor frequency. However, the higher the harmonic is, the higher the stall frequency is.

At 50% speed, the mean blade Mach number is 0.56. The flow field is therefore definitely compressible. The compressibility of the perturbations can therefore be assessed by:

$$\frac{\delta \dot{m}_{\text{local}}}{\delta\left(\overline{\rho}\,\overline{A}\,\overline{u_x}\right)_{\text{inlet}}} = \frac{\delta u_{x\,\text{local}}\;\overline{\rho}_{\text{local}}\overline{A}_{\text{local}}}{\delta\left(\overline{\rho}\,\overline{A}\,\overline{u_x}\right)_{\text{inlet}}} + \frac{\delta \rho_{\text{local}}\;\overline{A}_{\text{local}}\overline{u_x}_{\text{local}}}{\delta\left(\overline{\rho}\,\overline{A}\,\overline{u_x}\right)_{\text{inlet}}} \qquad (6.1)$$

It must be pointed out that, in the low speed case, the mass flow perturbations are the same everywhere along the compressor axis and therefore equation (6.1) is constant and equates to one everywhere in the compressor.

The amplitude of each of the above terms along the compressor axis at neutral stability for the first three harmonics are shown at 50% speed on figures 6.2.a to 6.2.c and at 90% speed on figures 6.3.a to 6.3.c. As can be seen, the perturbation in axial velocity is the preponderant term. However, the mass flow perturbation is no longer constant along the compressor axis. For the first harmonic (figures 6.2.a and 6.3.a), the perturbations are smaller inside the compressor than they are at the inlet, proving a storage of the perturbations within the compressor. This is no longer the case for the higher harmonics, for which the mass flow perturbations oscillate around their inlet values. Besides, the amplitude of these perturbations increases with the Mach number. At 90% speed, they reach four times their inlet value at the third stage.

Shown on figures 6.4.a to 6.4.c are the amplitudes of the perturbations along the compressor axis at neutral stability for each harmonic at 50% speed. These amplitudes are scaled with their value at the inlet of the compressor. These data are of considerable importance for the design of active control devices. Indeed, if one knows where the instability is expected to develop, sensors and actuators can be located consequently.

Densities and static pressures (shown in figures 6.5.a to 6.5.c) behave similarly and are out of phase with the axial velocities and mass flows. Moreover, a lobed pattern can clearly be seen along the compressor axis, the number of lobes being set by the number of the harmonic considered. This could already be observed on figures 6.2.a to 6.2.c. This standing wave phenomenon within the compressor was observed for rotational speeds varying from 50% to 70% of the design speed, but is much harder to capture at higher speeds. Besides, it was not observed for shorter compressors (see section 6.3). It therefore appears that instability appears at some resonance mode for

sufficiently long compressors.

Figures 6.5.a to 6.6.c are an effort to quantify the relative amplitude of the perturbations of the various flow quantities with one another. The inlet static pressure perturbation was chosen as a reference quantity. Indeed, measuring velocities is not easy in high-speed compressors, whereas static pressure is a much easier quantity to obtain in such machines with instruments such as Kulite high response pressure transducers. Density and axial velocity perturbations were classically scaled with the static pressure perturbations, as indicated on the figures.

Figures 6.5.a to 6.5.c show the same lobed pattern as in figures 6.4.a to 6.4.c. However, the static pressure perturbations appear to be the most important quantities in terms of relative amplitude. It must be pointed out that the pressure and the density perturbations amplitude are, here again, very much in phase, but the axial velocity perturbations clearly peaks when these two perturbations are decreasing (figure 6.5.b). This is also observed at 90% speed in figures 6.6.a to 6.6.c.

6.2.2 NASA three-stage compressor (74 A)

Calculations have been performed on the first three stages of a NASA five-stage high speed compressor referred to as 74 A. Three compressor geometries were tested at 80% design rotational speed: (i) at the design setting, (ii) at "reset 1", (iii) at reset 2" for maximum adiabatic efficiency at 80% speed. Details of these geometries are given in Appendix 1.

The predicted and the experimental characteristics as well as the stall points for several harmonics are shown on figures 6.7 to 6.9 for these three geometries. The first harmonic stalls first but the second and higher harmonics stall points are quite different. The agreement between the experimental and the predicted stall points is good. Details of the operating conditions at neutral stability for each harmonic is given on tables 6.4 to 6.6.

It must be pointed out that the neutral stability frequencies are much higher for the design setting than for the other two. Besides, the neutrally stable operating conditions for the two resets are very close, although their mean characteristics differ significantly.

As seen on the NACA 8 stage compressor, the neutral stability frequencies appear to be very much proportional to the harmonic number. This result is consistent with the low speed analytical results developed in Appendix 3.

The axial distributions of the flow field perturbations at the neutrally stable operating conditions for the first four harmonics are shown on figures 6.10.a to 6.10.d. It appears that the four harmonics behave similarly at their stability point. However, the higher the harmonic is, the stronger the amplitude of the perturbations are. The static pressure perturbations appear to be the more significant. This will be confirmed in figures 6.26.a to 6.26.c. No standing wave within the compressor can be seen. It is believed that the total length of the compressor is too short to allow such waves to develop.

6.3 EVALUATION OF THE MISMATCHING EFFECTS ON NEUTRAL STABILITY

6.3.1 NASA three-stage compressor (74 A)

As seen in section 6.2.2, the frequency behavior at neutral stability for the two resets of the 74 A compressor was very similar, although their mean characteristics were different. We tried in this section to evaluate the influence of the restaggering of the compressor on the stability attributes.

The total pressure losses and deviations for both IGV-stator settings are shown on figures 6.11.a to 6.12.b. The distances are measured from the leading edge of the inlet guide vane. For the first reset, the first rotor as well as the stators are operating in a more stalled regime than in the second reset. However, the last rotor is close to choke in the second reset. Actually, the mass flow is higher too.

The amplitude of the flow perturbations for the first two harmonics at their neutral stability points are shown on figures 6.13.a to 6.15.b for both resets. The static pressure perturbations are very much alike. The axial velocity and mass flow perturbations are larger and the harmonics are more separated for the second reset. Unlike reset 1, the first harmonic has a larger amplitude than the second harmonic at their neutral stability point.

Nonetheless, the neutral stability *unsteady* perturbations are very similar although the *steady* mean flow characteristics are quite different. It therefore appears that the stability margin is mainly determined by the perturbed flow quantities - or rather by their inner features (such as compressibility, inter-blade row redistribution, unsteady losses and deviations) - rather than by the mean flow quantities. However, as was seen in chapter 3, these perturbed flow quantities do depend on the mean flow, but the neutral stability conditions are much more affected by the features of the perturbations than by the steady effects of mismatching. This will be confirmed in section 6.5. However, stage mismatching still affects the stability boundary (cf design setting of the 74 A compressor).

As suggested by Tan [45], a effective way to prove this would be to perform a similar calculation where the mean flow would be compressible but the perturbations incompressible. However, as seen in figures 6.15.a and 6.15.b, the stability margin prediction would be affected by the assumption of incompressibility: the perturbations in mass flow are found to be as high as 6 times their inlet values at some axial locations in the compressor. Moreover. the validity of the expansion:

$$X = \underset{\text{compressible}}{\overline{X}} + \underset{\text{incompressibl}}{\delta X}$$

would be questionable.

6.3.2 NASA three-stage compressor (74 B)

Calculations have been performed on the first three stages of a NASA five-stage high speed compressor referred to as 74 B. Stability attributes for four different IGV-stator settings are shown in this section. Details of the geometry for the different resets are given in Appendix 1. This compressor is actually quite similar to the 74 A, but results are presented because some experimental data were available. Assessing the validity of the model developed in this thesis on different settings of an actual high speed compressor is therefore the main objective of this section.

The predicted and the experimental pressure ratio and adiabatic efficiency characteristics as well as the stall points are shown on figures 6.16.a-b, 6.17.a-b, 6.18.a-b, 6.19.a-b. The predictions are quite accurate. The individual stage characteristics obtained were also in good agreement with unpublished NASA experimental results. The frequency range varies between 35% and 57% of the rotor frequency for the different resets. A comparison similar to the one in the previous section is not performed because the rotational speeds are different for the four calculations.

Experimental measurements of the post-stall frequencies were available from NASA and are shown on tables 6.7 and 6.8, along with the predicted at-stall frequencies. It must be pointed out that the predicted and the measured frequencies are not exactly the same: the measurements are post-stall unstable measurements, whereas the predictions are neutral stability predictions. Even though the mass flow where the post-stall measurements were made is very close to the neutrally stable mass flow, the frequencies are however expected to be somewhat different. The post-stall measurements were obtained in an unstable regime where the non-linear effects are very large. Such regime cannot be predicted with the linear model developed in this thesis.

The predicted instability frequencies are about 15% below the measured values. We do not know at this time whether this trend is due to the difference between the

operating points (stability onset versus post stall) or a systematic problem in the calculation.

6.4 INVESTIGATION OF THE TRAVELLING WAVES

Calculations of travelling wave structure have been performed on the two resets of the NASA 74 A compressor at 80% design rotational speed. The first four harmonics behavior was investigated at 1% in mass flow function from the stall point for the first reset, as well as the first two harmonics at 0.5% and 1% of the stall point for the second reset. The corresponding flow perturbations - actually corresponding to a travelling wave behavior - are shown in figures 6.20.a to 6.23.b. In both resets, the first harmonic would stall first. Both resets present a similar precursor behavior. It can be seen that only the first two harmonics are of significant magnitude. The first harmonic amplitude is the largest at the front of the compressor, as expected since it is the one that triggers the instability. However, the second harmonic amplitude becomes clearly preponderant from the third stage on.

The travelling wave amplitudes predicted for the second reset are stronger than for the first reset. The first harmonic amplitude however is more affected by the restaggering than the second one. The difference between the first two harmonics is also larger for the second reset.

This second harmonic behavior, not expected in low speed machines, was experimentally observed in a Pratt & Whitney three-stage high-speed compressor [21]. The distribution of the travelling wave amplitudes for the first two harmonics are shown for two settings of this compressor in figure 6.24 and 6.25. They are indeed of similar amplitude, and their axial distribution is not in contradiction with the ones predicted for the NASA 74 A compressor.

Shown on figures 6.26.a to 6.26.c are the relative amplitude of the perturbed flow

quantities at 1% of the stall point. Here again, it appears that the static pressure is the flow quantity whose perturbations are comparatively the largest. At stall inception, static pressure data for the second harmonic at the exit of compressor are indicators of the proximity to stall. However, the best location to look at would be the exit of the inlet guide vanes or the inlet of the first rotor where the static pressure perturbations are the largest before stall for the first harmonic: the compressor physically stalls there.

Although no experimental measurements were available, the behavior of the travelling waves damping and frequency was investigated. This is shown on figures 6.27 and 6.28 for mass flow functions up to 8% of the stall point. Calculations of travelling wave at higher mass flow failed because of computational accuracy. The precursor frequency decreases at 3% of the stall point and then rises again. This shape is similar to the one obtained for the MIT three-stage low speed compressor (figure 5.20). The damping sharply increases up to 3% of the stall point then decreases to finally sharply increase again as expected.

6.5 EVALUATION OF THE EFFECTS OF UNSTEADY LOSSES, UNSTEADY DEVIATIONS AND INTER BLADE ROW GAPS ON THE STABILITY MARGIN

As seen in section 6.3, the attributes of the flow field perturbations are preponderant in the determination of the stability margin. The significant influence of the compressible effects being demonstrated, the present model also accounts for the effects of unsteady losses, unsteady deviations and inter blade row flow redistribution. The purpose of the section is to evaluate the effects of these flow features on high speed compressor stability margin.

This is shown on figures 6.29 and 6.30 for the first and second harmonics for the second reset of the NASA 74 A compressor at 80% design rotational speed. The unsteady losses, the unsteady deviations and the inter blade row gaps were varied from their original value in the actual compressor down to a value of zero. The following

conclusions can be drawn:

(i) The influence of the above features on the stability margin are much more sensitive for the second harmonic than for the first harmonic.

(ii) The inter-blade row gap inclusion appears to have a destabilizing effect, i.e. increases the neutral stability mass flow. The redistribution of the perturbations between the blades has a negative effect on the stability margin. Gaps tend also to reduce the stall frequency. It must be pointed out that the current high speed multistage compressor designs have their inter stage spacings kept as small as possible.

(iii) Both the unsteady losses and the unsteady deviations have a stabilizing effect. But the influence of the unsteady deviations can be felt only with the presence of the unsteady deviations. Indeed, a stalled blade being highly loaded, the deviation across this blade is very much constant and the unsteady part of this deviation is minimal. However, if unsteady losses are taken into account, the unsteady deviation has significant influence on the next blade, because of the large slope of the loss bucket at this incidence: a small change in the (unsteady) incidence has a large consequence on the (unsteady) loss of the next blade Another way to look at this phenomenon is to consider deviations as a consequence of the total pressure losses.

(iv) Unsteady losses tend to significantly reduce the stall frequency. A similar statement cannot be made for the unsteady deviations.

The significance of such effects confirms the preponderance of the flow field perturbations and of their attributes on the stability margin of high speed multistage compressors. The mean flow effects appear to be secondary, but still important.

6.6 CONCLUSIONS

The two-dimensional compressible model developed in this thesis has been used to efficiently predict the stability margin of eight different high speed compressor configurations. Axial distribution of the compressible flow field perturbations was investigated. For sufficiently long compressors, standing waves along the compressor axis have been found at neutral stability operating conditions. An investigation of travelling waves prior to stall also confirmed the observed importance of the second harmonic.

The relaxation of the assumption of the incompressibility of the perturbations was found to be fundamental for the understanding of high speed multistage compressor stability. The influence of the compressible unsteady perturbations turned out to be more important than the steady compressible meanflow mismatching effect on the stability margin. The inclusion of unsteady losses, unsteady deviations and inter-blade row redistributions was also investigated. All these effects tend to reduce the stall frequency, but unsteady losses and unsteady deviations have a stabilizing effect on the stability margin whereas inter blade row gaps tend to destabilize the compressor. It also confirms the importance of the unsteady flow field perturbations on the stability of high speed multistage compressors. This however does not mean that the mean stage mismatching within a compressor has no influence on the stability boundary.

Chapter 7

Conclusions

7.1 SUMMARY

A two-dimensional compressible model for high speed multistage compressor stability has been developed. This includes a mean flow prediction model, a linearized stability analysis model for both rotating stall and surge-like perturbations as well as a travelling wave prediction model for flow regimes prior to the instability. Computational implementation of this model has allowed the investigation of neutral stability operating conditions and instability precursors in a wide range of both low-speed and high-speed multistage compressors. One particular focus of this analysis was the evaluation of the compressibility effects on the stability margin of high speed machines.

As a result, a more accurate appreciation and prediction of the stability and of the instability precursors in multistage compressors has been established.

7.2 CONCLUSIONS

The proposed mean flow prediction model gives good results for a range of low-speed and high-speed multistage compressors. The purpose of this calculation is not to generate a highly accurate speedline generator, but rather to capture the correct trends of the mean flow field in the actual compressor using a tool deliberately designed to be as general as possible. It must be pointed out that this is a generic calculation, where the losses and the deviations are evaluated from general high speed empirical correlations, which therefore inherently contain some inaccuracy. However, the results obtained are satisfactory.

The two-dimensional stability analysis developed in this thesis includes an extensive range of fluid dynamic effects intrinsic to the compression system flow fields (compressibility, inter blade row flow redistribution, blade row flow redistribution using a semi-actuator disk method, unsteady losses, unsteady deviations, swirl sensitivity). In simple cases, it reduces to classical stability models.

A computational implementation of this whole model has been used for the investigation of stability and instability precursors attributes on low-speed and high-speed compressors.

7.2.1 Low-speed compressors investigations

The compressibility impacts on the stability margin have been evaluated via comparison with simple analytical incompressible stability models. For blade Mach numbers up to 0.35, simple incompressible models capture well the stability attributes (less than 2% difference). The correction due to compressibility effects is a classical function of the square root of the blade Mach number. For higher Mach numbers, the compressibility influence becomes preponderant.

The model was used to successfully capture the stability features of different compressors. As far as travelling waves predictions are concerned, trends are adequately captured. However, the accuracy of predictions are dependant on the accuracy of the meanflow speedline shape.

In any cases, the accuracy of the mean flow calculation is a key factor to an effective prediction of the stability margin and of the stall precursors. More experimental measurements - and corresponding test calculations - are still necessary to evaluate the range of validity of the model, as well as to get more insight on all the fluid dynamic phenomena that actually occur within the compressor in such regimes.

7.2.2 High-speed compressors investigations

The model reasonably captures the stability margin of different high speed compressors. Axial distribution of the stall and pre-stall perturbations was investigated. For long compressors, an (axial) lobed pattern is found within the compressor. Both the first and the second harmonics have a dominant effect on the neutral stability and on the precursors.

The influence of the compressible unsteady perturbations was found to be more important to the stability margin than the effects of the steady compressible meanflow mismatching. However, stage mismatching still influences the compressor stability. The use of a fully compressible model is therefore a requirement for the investigation of high speed multistage compressor stability.

Unsteady losses and deviations have a stabilizing impact on the compressor, but tend to reduce the predicted stall frequency. Unsteady deviations effects seem to be a consequence of the unsteady losses effects. Inter blade row gaps have a destabilizing impact on the stability margin but similarly reduce the compressor stall frequency.

7.3 RECOMMENDATIONS FOR FUTURE WORK

The theoretical model and the associated computational method developed [29] represent a preliminary step in the investigation of high speed multistage compressor stability. Two directions should be considered fo future work:

(i) Improvement of the model as a prediction tool:

The efficiency of the model as a prediction tool has been demonstrated. However, the accuracy of the stability attributes clearly requires a improvement of the mean flow prediction. In particular, most of the calculations predict slightly higher mass flows than the ones observed in the actual compressors. A better calculation of the blade passage blockage (boundary layer effects, endwall interactions) will certainly improve significantly this calculation. Besides, better predictions can definitely be obtained with the inclusion of correlation models specific to the compressor. The inclusion of noise in the model would then enable a better understanding of the stall precursors in actual high speed machines. Finally, the use of this model in an active control loop would be the first step to an actual implementation of active control on high speed machines.

(ii) Use and development of the model for further investigations of the fluid dynamic effects in high speed compression systems:

Although improvements have been made in this research on the modelling and the understanding of high speed compressor stability, additional work is required to get a more thorough appreciation of the fluid mechanics involved in the present model. This is in particular valid for the choked stability analysis, and for parametric studies on the influence of the mean flow on the stability margin. Further understanding of standing waves patterns within the compressor at neutral stability is required. An extension of this model to inlet distorted flow would then be of significant interest.

Finally, further comparisons and testing with experimental measurements on real compressors are essential to assess the range of validity of the model (three-dimensional effects..), as well as to get a better understanding of the actual fluid dynamics involved in high speed multistage compressor stability.

References

1. Emmons, H.W., Pearson, C.E., and Grant, H.P. "Compressor Surge and Stall Propagation", ASME Transactions, Vol. 79 pp 455-469, April 1955.

2. Epstein, A. H., Ffowcs Williams, J.E., and Greitzer, E.M., 1986, " Active Suppression of Aerodynamic instabilities in Turbomachines", AIAA Paper No. 86-1994.

3. Ffowcs Williams, J.E., and Huang, X.Y., 1989, "Active Stabilization of Compressor Surge", Journal of Fluid Mechanics, Volume 2045, pages 245-269.

4. Dunham, J., "Non-Axisymmetric Flows in Axial Compressors", Mechanical Engineering Science, Monograph No. 3, Institution of Mechanical Engineers, October 1965.

5. Wood, M.D., "Theoritical and Experimental Studies of Stall Propagation in Rows of Axial Flow Compressor Blades", The Aeronautical Quarterly, November 1959.

6. Stenning, A.H., "Rotating Stall and Surge", ASME Journal of Fluids Engineering, Volume 102, March 1980.

7. Takata, H., and Nagano, S., "Nonlinear Analysis of Rotating Stall", ASME Paper No. 72-GT-3, October 1972.

8. Nenni, J.P., and Ludwig, G.R., "A Theory to Predict the Inception of Rotating Stall in Axial Flow Compressors", AIAA Paper No. 74-528, June 1974.

9. Greitzer, E.M., "Surge and Rotating Stall in Axial Compressors, Part 1: Theoritical Compression System Model", and "Part 2: Experimental Results and Comparison with Theory", ASME Journal of Engineering for Power, April 1976.

10. Moore, F.K., and Greitzer, E.M., "A Theory of Post-Stall Transients in Axial Compressors, Part 1: Development of the Equations", ASME Journal of Engineering for Gas Turbine and Power, Vol 108, pp 68-76, January 1986.

11. Greitzer, E.M., and Moore, F.K., "A Theory of Post-Stall Transients in Axial Compressors, Part 2: Applications", ASME Journal of Engineering for Gas Turbine and Power, Vol 108, pp 231-239, January 1986.

12. Hynes, T.P., and Greitzer, E.M., "A Method for Assessing Effects of Circumferential Flow Distortion on Compressor Stability", Journal of Turbomachinery, Vol 109, pp 371-379, July 1987.

13. Longley, J.P., "Inlet Distortion and Compressor Stability", PhD Dissertation, Cambridge University Engineering Department, July 1988.

14. McDougall, N.M., Cumpsty, N.A., and Hynes, T.P., "Stall Inception in Axial Compressors", Submitted to 1989 ASME Gas Turbine Conference.

15. Garnier, V.H., Epstein, A.H., Greitzer, E.M., "Rotating Waves as a Stall Inception in Axial Compressors", Journal of Turbomachinery, Paper No. 90-GT-156, April 1991.

16. Orner, N., "Rotating Stall in Axial Flow Compressors", VKI Lecture Series 3: "Unsteady Flow in Turbomachines", 1979.

17. Pandolfi, M., and Colusardo, G., "Numerical investigations on the Generation and Development of Rotating Stalls", ASME Paper No. 78-WA/GT-5, December 1978.

18. Small, C.J., and Lewis, J.T., "High Speed Compressor Rig as a Stall Recovery Research Tool", AIAA Paper No. 85-1428, July 1985.

19. Hosny, W.M., and Steenken, W.G., "Aerodynamic Instability Performance of an Advanced High-Pressure-Ratio Compression Component", AIAA Paper No. 86-1619, June 1986.

20. Newman, F.A., Experimental Vibration Damping Characteristics of the Third-Stage Rotor of a Three-Stage Transonic Axial-Flow Compressor, AIAA Paper No. 88-3229, July 1988.

21. Garnier, V.H., "Experimental Investigation of Rotating Waves as a Rotating Stall Inception Indication in Compressors", MS Thesis, MIT Department of Aeronautics and Astronautics, September 1989.

22. Tesh, W.A., and Steenken, W.G., 1976, "Dynamic blade Row Compression Component Model for Stability Studies", AIAA Paper No. 76-203.

23. Elder, R.L., and Gill, M.E., 1984, "A Surge Prediction Method for Multistage Axial Flow Compressors", IMechE Paper No. C74/84.

24. Davis, M.W., and O'Brien, W.F., 1987, "A Stage-by-Stage Post Stall Compresson System Modelling Technique", AIAA Paper No. 87-2088.

25. Mazzawy, R.S., 1979, "Surge-Induced Loads in Gas Turbines", ASME Journal of Engineering for Power, Volume 106, pagres 313-336.

26. Cargill, A.M., and Freeman, C., "High Speed Compressor Surge with Application to Active Control", Journal of Turbomachinery, Paper No. 90-GT-354, April 1991.

27. McKenzie, A.B., "An Alternative Criterion for Surge ?", Unpublished Rolls Royce Memorandum, 1981.

28. Lavrich, P.L., "Instability and Rotating Stall in High Speed Axial Flow Compression Systems", MS Thesis, MIT Department of Aeronautics and Astronautics, January 1985.

29. Bonnaure, L.P., "Computational Documentation of the High Speed Multistage Compressor Satbility Prediction Code: HSPEED", Unpublished GTL Memorandum, 1991.

30. Raw, J., and Weir, G.C., "The Prediction of Off-Design Characteristics of Axial and Axial/Centrifugal Compressors", SAE Technical Paper 800628, April 1980.

31. NASA SP-36, Chapter VI.

32. NASA SP-36 Chapter VII.

33. Steinke, R.J., "STGSTK A Computer Code for Predicting Multistage Axial-Flow Compressor Performance by a Meanline Stage-Stacking Method", NASA Technical Paper 2020, 1982.

34. Horlock, Actuator Disk Theory, Mc Graw Hill, 1978.

35. Cumpsty, N.A., and Marble F.E., "The Generation of Noise by the Fluctuation in Gas Temperature into a Turbine", Cambridge University, CUED/A TURBO/TR 57, 1974.

36. Hynes, T.P., "Actuator and Semi-Actuator Disk Models of Compression Systems Operating with Inlet Distortion", Cambridge University, CUED/A TURBO/TR 104, 1980.

37. Kaji, S., and Okazaki, T., "Propagation of Sound Waves through a Blade Row, Part 1: Analysis based on the Semi-Actuator Disk Theory", Journal of Sound Vibration II (3), pp 339-353, 1970.

38. Krall, N.A., and Trivelpiece, A.W., Principle of Plasma Physics, Mc Graw Hill, Inc., 1973.

39. Ham, C.J., Williams, D.D., "Some Applications of Actuator and Semi-Actuator Disk Theory to the Problem of Intake/Engine Compatibility", Tokyo International Gas Turbine Congress, 83-Tokyo-IGTC-50, 1983.

40. Steinke, R.J., "Design of 9.271-Pressure-Ratio Five-Stage Core Compressor and Overall Performance for the First Three Stages", NASA Technical Paper 2597, May 1986.

41. Longley, J.P., Private communication

42. Hawthorne, W.R., Mc Cune, J.E., Mitchell, N.A., and Tan C.S., "Non-axisymmetris Flow through Annular Actuator disks: Inlet Distortion Problem", ASME Journal of Engineering for Power, Volume 100, No 14, 1978.

43. Voit, C.H., "Investigation of a High-Pressure Ratio Eigth-Stage Axial-Flow Compressor With Two Transonic Inlet Stages I Aerodynamic Design", NACA RM E53I24, December 1953

44. Hosny, W.M., Leventhal, L., and Steenken, W.G., "Active Stabilization of Multistage Axial-Compressor Aerodynamic System Instabilities", ASME Paper No. 91-GT-403, presented at the International Gas Turbine and Aeroengine Congress and Exposition, Orlando, FL, June 3-6, 1991

45. Tan, C.S., Private communication

Appendix 1

Compressor Geometries

In the following compressor geometry files:

ξ represents the stagger in degrees

θ^* represents the camber in degrees

σ represents the solidity

$\frac{t}{c}$ represents the thickness to chord ratio

c represents the non-dimensionalized chord length

RHLE represents the non-dimensionalized hub radius at the leading edge

RTLE represents the non-dimensionalized tip radius at the leading edge

RHTE represents the non-dimensionalized hub radius at the trailing edge

RTTE represents the non-dimensionalized tip radius at the trailing edge

A.1.1 MIT SINGLE STAGE COMPRESSOR [21]

Blade type	ξ	θ^*	σ	$\frac{t}{c}$	c
IGV	15.0	10.0	0.555	0.190	0.152
Rotor 1	27.9	25.1	0.504	0.106	0.144
Stator 1	45.0	25.5	0.529	0.081	0.148

RHLE = RHTE = 22.38 cm

RTLE = RTTE = 29.85 cm

$l^* = 26.38$ cm

$S^* = 0.664$

$Re^* = 16{,}600{,}080$

Rotational Speed (non-dimensionalized) = 0.214

A.1.2 MIT 3 STAGE COMPRESSOR (BUILD #1, BUILD #2, BUILD #3, BUILD #4) [21]

Blade type	ξ(#1)	ξ(#2)	ξ(#3)	ξ(#4)	θ^*	σ	$\frac{t}{c}$	c
IGV	8.1	8.1	18.1	13.1	11.0	1.442	0.12	0.073
Rotor 1	37.8	42.8	30.3	44.3	17.0	1.353	0.12	0.157
Stator 1	21.0	11.0	31.0	26.0	27.0	1.478	0.12	0.109
Rotor 2	38.5	43.5	31.0	45.5	18.0	1.336	0.12	0.156
Stator 2	23.0	12.0	33.0	28.0	25.0	1.527	0.12	0.109
Rotor 3	39.6	44.6	32.1	46.6	20.0	1.377	0.12	0.177
Stator 3	15.5	5.5	25.5	20.5	53.0	1.565	0.12	0.109

RHLE = RHTE = 0.935

RTLE = RTTE = 1.062

$l^* = 28.7$ cm

$S^* = 0.664$

$Re^* = 18{,}065{,}960$

Rotational Speeds = 1170 rpm, 1800 rpm, 2400 rpm

A.1.3 C106 SINGLE STAGE COMPRESSOR [13]

Blade type	ξ	θ^*	σ	$\frac{t}{c}$	c
IGV	13.5	17.0	1.197	0.112	0.129
Rotor 1	38.5	25.0	1.158	0.108	0.119
Stator 1	28.0	34.0	1.189	0.112	0.128

RHLE = RHTE = 0.849

RTLE = RTTE = 1.131

$l^* = 22.4$ cm

$S^* = 0.664$

$Re^* = 14{,}127{,}060$

Rotational Speed (non-dimensionalized) = 0.203

A.1.4 C106 THREE STAGE COMPRESSOR [13]

- Matched build: The last two stages have the same geometry as the first stage of the C106 one stage compressor
- Mismatched build: The staggers of the two last stages are increased by $+10^o$

A.1.5 C106 FOUR STAGE COMPRESSOR [13]

Blade type	ξ	θ^*	σ	$\frac{t}{c}$	c
IGV	09.5	17.0	1.197	0.112	0.124
Rotor 1	44.2	20.0	1.470	0.110	0.158
Stator 1	23.2	40.0	1.560	0.110	0.160

The last three stages are identical to the first one.

RHLE = RHTE = 0.849

RTLE = RTTE = 1.131

$l^* = 22.4$ cm

$S^* = 0.664$

$Re^* = 14{,}127{,}060$

Rotational Speed (non-dimensionalized) = 0.203

A.1.6 NACA 8 STAGE COMPRESSOR [43]

Blade type	ξ	θ^*	σ	$\frac{t}{c}$	c	RHLE	RTLE	RHTE	RTTE
Rotor 1	46.09	11.77	1.446	0.080	0.393	0.547	1.140	0.657	1.140
Stator 1	23.15	22.00	1.036	0.060	0.217	0.657	1.140	0.720	1.140
Rotor 2	40.50	15.44	1.405	0.058	0.363	0.720	1.140	0.746	1.140
Stator 2	34.80	20.50	1.200	0.060	0.222	0.746	1.140	0.775	1.140
Rotor 3	36.30	26.00	1.134	0.080	0.166	0.775	1.140	0.808	1.140
Stator 3	37.25	32.50	0.897	0.060	0.166	0.808	1.140	0.840	1.140
Rotor 4	35.60	29.00	1.275	0.080	0.162	0.840	1.140	0.869	1.140
Stator 4	37.55	35.50	0.898	0.060	0.162	0.869	1.140	0.895	1.140
Rotor 5	34.70	32.50	1.294	0.070	0.156	0.895	1.140	0.921	1.140
Stator 5	37.30	38.50	0.948	0.060	0.157	0.921	1.140	0.944	1.140
Rotor 6	34.40	37.00	1.232	0.070	0.149	0.944	1.140	0.963	1.140
Stator 6	36.55	41.50	0.979	0.060	0.150	0.963	1.140	0.980	1.140
Rotor 7	35.30	38.00	1.205	0.070	0.146	0.980	1.140	0.996	1.140
Stator 7	36.85	41.50	1.000	0.060	0.146	0.996	1.140	1.008	1.140
Rotor 8	35.30	39.00	1.184	0.070	0.140	1.008	1.140	1.018	1.140
Stator 8	37.15	41.50	1.014	0.060	0.140	1.018	1.140	1.022	1.140

$l^* = 22.3$ cm

$S^* = 1.623$

$Re^* = 8{,}106{,}960$

Design Rotational Speed = 13,380 rpm

A.1.7 NASA 5 STAGE COMPRESSOR (74 A): FIRST THREE STAGES [40]

Blade type	ξ	θ^*	σ	$\frac{t}{c}$	c	RHLE	RTLE	RHTE	RTTE
IGV	00.29	00.00	2.000	0.100	0.299	0.689	1.233	0.689	1.233
Rotor 1	47.48	14.52	1.619	0.049	0.368	0.689	1.233	0.721	1.211
Stator 1	14.70	49.55	1.459	0.064	0.277	0.721	1.211	0.789	1.194
Rotor 2	45.36	16.39	1.468	0.061	0.289	0.789	1.194	0.851	1.179
Stator 2	15.43	51.09	1.417	0.065	0.191	0.851	1.179	0.888	1.173
Rotor 3	41.64	20.10	1.423	0.077	0.222	0.888	1.173	0.919	1.153
Stator 3	15.87	53.68	1.417	0.070	0.164	0.919	1.153	0.943	1.147

$l^* = 20.8$ cm

$S^* = 1.243$

$Re^* = 13{,}665{,}800$

Design Rotational Speed = 16,042 rpm

This compressor has two resets possible for optimum compressor adiabatic efficiency:

Reset 1:		IGV	Stator 1	Stator 2	Stator 3
		+15°	+10°	+10°	+10°

Reset 2:	Speed	IGV	Stator 1	Stator 2	Stator 3
	100%	+15°	+10°	+10°	+10°
	95%	+10°	+8°	+8°	+10°
	90%	+10°	+6°	+5°	+10°
	85%	+10°	+7°	+1°	-7°
	80%	+15°	+6°	-2°	-3°
	70%	+15°	+9°	-4°	-3°
	60%	+12°	+8°	-6°	-4°
	50%	+6°	+10°	-2°	-3°

A.1.8 NASA 5 STAGE COMPRESSOR (74 B): FIRST THREE STAGES [20]

Blade type	ξ	θ^*	σ	$\frac{t}{c}$	c	RHLE	RTLE	RHTE	RTTE
IGV	17.71	00.00	1.252	0.100	0.302	0.689	1.233	0.689	1.233
Rotor 1	48.48	16.37	1.633	0.049	0.371	0.689	1.233	0.721	1.211
Stator 1	24.71	49.57	1.472	0.064	0.279	0.721	1.211	0.789	1.194
Rotor 2	46.48	19.26	1.481	0.060	0.292	0.789	1.194	0.851	1.179
Stator 2	15.42	51.09	1.431	0.065	0.193	0.851	1.179	0.888	1.173
Rotor 3	42.68	26.34	1.436	0.076	0.227	0.888	1.173	0.919	1.153
Stator 3	15.79	53.33	1.428	0.072	0.165	0.919	1.153	0.943	1.147

$l^* = 20.8$ cm

$S^* = 1.243$

$Re^* = 13{,}665{,}800$

Design Rotational Speed = 16,042 rpm

This compressor has one reset possible for optimum compressor adiabatic efficiency:

Speed	IGV	Stator 1	Stator 2	Stator 3
100%	+0°	+10°	+6°	+10°
90%	+15°	+6°	+2°	+0°
80%	+18°	+10°	+0°	+0°
70%	+21°	+10°	+0°	-8°
50%	+29°	+10°	+2°	-8°

Appendix 2

Compressible Flow Relations

The stagnation quantities are defined from:

$$C_p T_t = C_p T_s + \frac{V^2}{2} \tag{A.2.1}$$

where T_t is the total temperature.

$$\frac{T_t}{T_s} = 1 - \frac{\gamma - 1}{2} M^2 \tag{A.2.2}$$

$$\frac{P_t}{P_s} = \left(1 - \frac{\gamma - 1}{2} M^2 \right)^{\frac{\gamma}{\gamma - 1}} \tag{A.2.3}$$

$$\frac{\rho_t}{\rho_s} = \left(1 - \frac{\gamma - 1}{2} M^2 \right)^{\frac{1}{\gamma - 1}} \tag{A.2.4}$$

$$\frac{V}{\sqrt{\gamma R T_t}} = M \left(1 - \frac{\gamma - 1}{2} M^2 \right)^{-\frac{1}{2}} \tag{A.2.5}$$

$$Q_t(M) = \frac{\dot{m} \sqrt{\gamma R T_t}}{P_t A \cos\alpha} = \gamma M \left(1 - \frac{\gamma - 1}{2} M^2 \right)^{\frac{1}{2} - \frac{\gamma}{\gamma - 1}} \tag{A.2.6}$$

Q_t (M) is not a monotonic function but it reaches a maximum at M=1, i.e. at the choking condition. In order to invert this relation and to get the subsonic case ($0 < Q_t(M) < Q_t(1)$), the following algorithm is to be used:

$$M_{old} = 1$$

$$M_{new} = Q_t(M_{old})\,\frac{1}{\gamma}\left(1 - \frac{\gamma - 1}{2} M_{old}^2\right)^{-\frac{1}{2} + \frac{\gamma}{\gamma - 1}}$$

The conversion of Mach number from the rotor relative reference frame is done as:

$$M_{abs}^2 = M_{rel}^2 + \frac{1}{T_{sND}}\left(2\, M_{rel} \sin\beta \sqrt{T_{sND}}\, U_{rowND} + U_{rowND}^2\right) \qquad \text{(A.2.7)}$$

The adiabatic efficiency is classically:

$$\eta_{ad} = \frac{\left(\frac{P_{exit}}{P_{inlet}}\right)^{\frac{\gamma - 1}{\gamma}} - 1}{\frac{T_{exit}}{T_{inlet}} - 1} \qquad \text{(A.2.8)}$$

Appendix 3

Incompressible Undistorted Flow Analytic Stability Analysis of a Compressor

A linear stability is conducted in this appendix, for a low-speed axial-flow compression system. It is actually an extension of the Hynes-Greitzer model, with an non-axial mean flow, and with inlet swirl influence on the pressure rise coefficient and on the exit flow angle.

This analysis consists of two parts: (i) solution and linearization of the 2-D incompressible flow field, (ii) a classical hydrodynamic stability calculation.

The compression system is modelled as in Diagram (A.3.1).

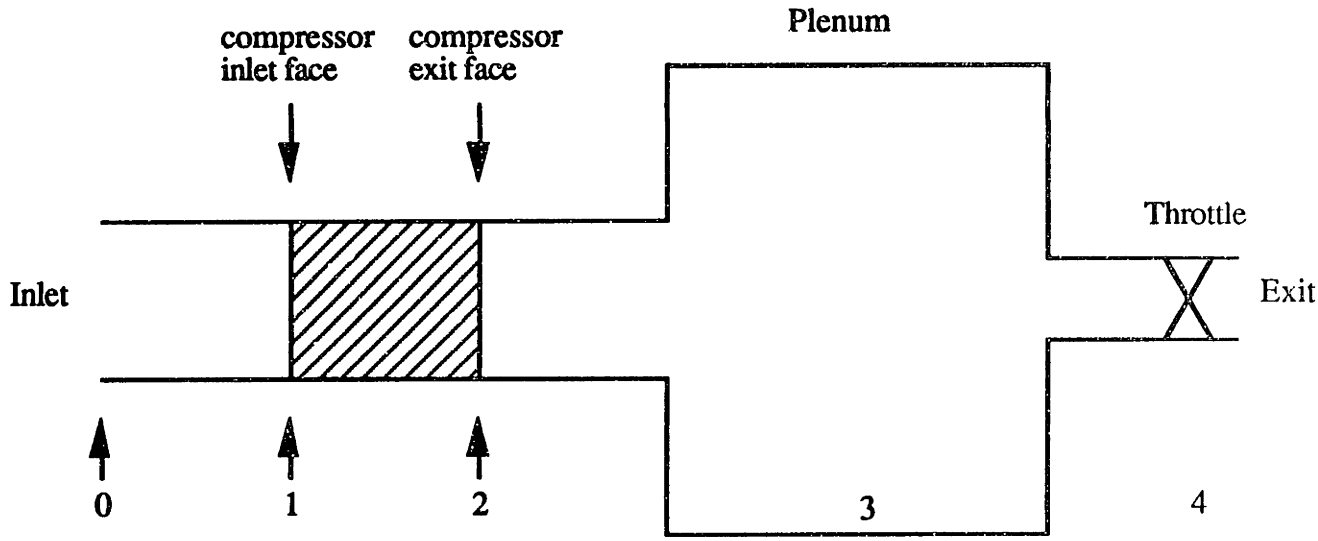

Diagram (A.3.1): Compression system

A circumferentially unrolled piece of the flowfield in the upstream and downstream volumes is shown on Diagram (A.3.2).

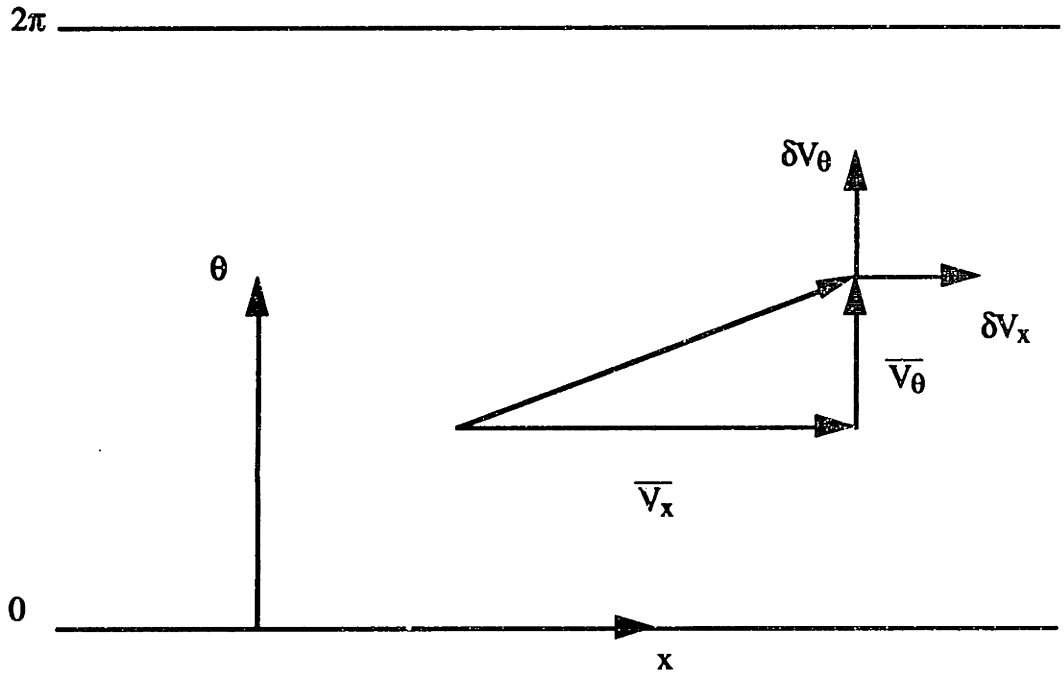

Diagram (A.3.2): Unrolled flowfield

A.3.1 LINEARISED FLOW FIELD EQUATIONS

The notations are defined on Diagram (A.3.2).

The equations of motion for inviscid incompressible fluid flow can be written in the following way:

$$\nabla.\vec{u} = 0$$
$$\frac{\partial \vec{u}}{\partial t} + (\vec{u}.\nabla)\vec{u} = -\frac{1}{\rho}\nabla P_s \qquad \text{(A.3.1)}$$

We define a stream function ψ such that:

$$V_x = \frac{1}{r}\frac{\partial \psi}{\partial \theta}$$
$$V_\theta = -\frac{\partial \psi}{\partial x} \qquad \text{(A.3.2)}$$

where the vorticity is defined as: $\xi = -\nabla^2\psi$

After some algebra found in [13], we get the stream function or vorticity equation:

$$\frac{\partial}{\partial t}(\nabla^2\psi) + \frac{1}{r}\frac{\partial \psi}{\partial \theta}\frac{\partial}{\partial x}(\nabla^2\psi) - \frac{\partial \psi}{\partial x}\frac{1}{r}\frac{\partial}{\partial \theta}(\nabla^2\psi) = 0 \qquad \text{(A.3.3)}$$

We consider the case where the steady mean flow has swirl. The stream function must therefore be of the form:

$$\psi = r\,\overline{V_x}\,\theta - \overline{V_\theta}\,x \qquad \text{(A.3.4)}$$

For small disturbances about this mean flow, we get:

$$\psi = r\,\overline{V_x}\,\theta - \overline{V_\theta}\,x + \delta\psi \qquad \text{(A.3.5)}$$

Linearizing (A.3.1), we get:

$$\frac{\partial}{\partial t}(\nabla^2\delta\psi) + \overline{V_x}\frac{\partial}{\partial x}(\nabla^2\delta\psi) + \frac{\overline{V_\theta}}{r}\frac{\partial}{\partial \theta}(\nabla^2\delta\psi) = 0$$

$$\left(\frac{\partial}{\partial t} + \overline{V_x}\frac{\partial}{\partial x} + \frac{\overline{V_\theta}}{r}\frac{\partial}{\partial \theta}\right)(\nabla^2\delta\psi) = 0 \qquad \text{(A.3.6)}$$

This wave equation indicates that there are one convective vortical mode which convects with the meanflow aa well as two potential modes, one axially growing and the other axially decaying. Moreover, the solution has the classical form:

$$\nabla^2 \delta\psi = f\left(t+kx , \theta \right) \tag{A.3.7}$$

Solving equation (A.3.2) in the Fourier space, we get:

$$\nabla^2 \psi = \sum_{n=-\infty}^{\infty} \alpha_n e^{i n \theta - i \frac{1}{\overline{V_x}} (\omega + \frac{n \overline{V_\theta}}{r}) x + i \omega t} \tag{A.3.8}$$

Integrating, we get equation (A.3.9):

$$\delta \psi = \sum_{n=-\infty}^{+\infty} \frac{-\alpha_n}{\frac{(\omega + n \frac{\overline{V_\theta}}{r})^2}{\overline{V_x}^2} + \frac{n^2}{r^2}} e^{i n \theta - \frac{i}{\overline{V_x}} (\omega + \frac{n \overline{V_\theta}}{r}) x + i \omega t}$$

$$+ \sum_{\substack{n=-\infty \\ n \neq 0}}^{+\infty} \beta_n e^{i n \theta - \frac{|n| x}{r} + i \omega t}$$

$$+ \sum_{\substack{n=-\infty \\ n \neq 0}}^{+\infty} \gamma_n e^{i n \theta + \frac{|n| x}{r} + i \omega t}$$

$$+ (\xi_1 \theta + \xi_2 \theta x + \xi_3 x + \xi_4) e^{i \omega t}$$

$$\text{where } \xi_4 = 0 \text{ and } \xi_2 = 0 \tag{A.3.9}$$

ξ_2 has no physical meaning and is therefore ignored. ξ_4 is ignored too since it does not affect the stream function. ξ_1 and ξ_3 correspond to the zeroth harmonic.

Redefining the constants:

$$\delta\psi = r\overline{V_x}A_0 e^{-i\frac{\omega x}{\overline{V_x}}+i\omega t} + r\overline{V_x}\theta B_0 e^{i\omega t} - x\overline{V_x}C_0 e^{i\omega t}$$

$$+\sum_{\substack{n=-\infty\\ n\neq 0}}^{+\infty} -\frac{ir\overline{V_x}}{n}A_n e^{in\theta-\frac{i}{\overline{V_x}}(\omega+n\frac{\overline{V_\theta}}{r})x+i\omega t}$$

$$+\sum_{\substack{n=-\infty\\ n\neq 0}}^{+\infty} -\frac{ir\overline{V_x}}{n}B_n e^{in\theta-\frac{|n|x}{r}+i\omega t}$$

$$+\sum_{\substack{n=-\infty\\ n\neq 0}}^{+\infty} -\frac{ir\overline{V_x}}{n}C_n e^{in\theta+\frac{|n|x}{r}+i\omega t} \qquad \text{(A.3.10)}$$

In terms of perturbations of the flow field quantities, we get expression (A.3.11) in a matrix form:

$$\begin{bmatrix} \frac{\delta V_x}{\overline{V_x}} \\ \frac{\delta V_\theta}{\overline{V_x}} \\ \frac{\delta P_s}{\rho\overline{V_x}^2} \\ \frac{\delta P_t}{\rho\overline{V_x}^2} \end{bmatrix} = \begin{bmatrix} 0 & 1 & 0 \\ \frac{i\omega r}{\overline{V_x}} & 0 & 1 \\ 0 & -\frac{i\omega x}{\overline{V_x}}-1 & 0 \\ \frac{i\omega r}{\overline{V_x}}\tan\alpha & -\frac{i\omega x}{\overline{V_x}} & \tan\alpha \end{bmatrix} \begin{bmatrix} A_0 e^{-\frac{i\omega x}{\overline{V_x}}+i\omega t} \\ B_0 e^{i\omega t} \\ C_0 e^{i\omega t} \end{bmatrix}$$

$$+\sum_{\substack{n=-\infty\\ n\neq 0}}^{+\infty} \begin{bmatrix} 1 & 1 & 1 \\ \beta_n & -i\frac{|n|}{n} & i\frac{|n|}{n} \\ 0 & \frac{n}{|n|}i\beta_n - 1 & -\frac{n}{|n|}i\beta_n - 1 \\ 1+\beta_n\tan\alpha & \frac{ir\omega}{\overline{V_x}|n|} & -\frac{ir\omega}{\overline{V_x}}|n| \end{bmatrix} \begin{bmatrix} A_n e^{in\theta-i\beta_n\frac{nx}{r}+i\omega t} \\ B_n e^{in\theta-\frac{|n|x}{r}+i\omega t} \\ C_n e^{in\theta+\frac{|n|x}{r}+i\omega t} \end{bmatrix}$$

where $\beta_n = \tan\alpha + \frac{r\omega}{n\overline{V_x}}$

(A.3.11)

A.3.2 CLEAN FLOW STABILITY ANALYSIS

The compressor geometry used is defined in Diagram (A.3.1). The most general unsteady perturbation is of the form:

$$\delta \phi = \sum_{n=-\infty}^{+\infty} a_n e^{i n \theta + i \omega t} \qquad \text{(A.3.12)}$$

Since the undistorted flow case is considered, all harmonics are decoupled, and the stability analysis can be performed for each harmonic independently. We get, for instance, for the nth harmonic:

$$(n \neq 0) \qquad \delta \phi = a_n e^{i n \theta + i \omega t} \qquad \text{(A.3.13)}$$

A.3.2.1 Upstream flow field:

$$C_n = \frac{a_n}{\phi_1}$$

$$\delta V_x = \delta V_\theta = 0 \qquad \text{as } x \text{ goes to } -\infty$$

Therefore, $C_n \neq 0$ and $B_n = 0$.

The upstream flow is potential, therefore no vortical mode can exist and $A_n = 0$. We get:

$$\frac{\delta P_{t_1}}{\rho U^2} = -\frac{r}{|n| U} \frac{\partial}{\partial t} (\delta \phi_1) \qquad \text{(A.3.14)}$$

A.3.2.2 Across the compressor:

We get from Hynes - Greitzer [12]:

$$\frac{P_{s_2} - P_{t_1}}{\rho U^2} = \psi (\phi_1 , \alpha_1) - \lambda \frac{\partial \phi}{\partial \theta} - \frac{r \mu}{U} \frac{\partial \phi}{\partial t} \qquad \text{(A.3.15)}$$

where $\lambda = \sum_{\text{rotors}} \frac{\text{axial chord}}{r \cos^2 (\text{stagger})}$ and $\mu = \sum_{\text{all rows}} \frac{\text{axial chord}}{r \cos^2 (\text{stagger})}$

Linearizing about the mean, we get:

$$\frac{\delta P_{s_2} - \delta P_{t_1}}{\rho U^2} = \frac{\partial \psi}{\partial \phi}(\delta \phi_1) + \frac{\partial \psi}{\partial \alpha_1}(\delta \alpha_1) - \lambda \frac{\partial}{\partial \theta}(\delta \phi_1) - \frac{r \mu}{U}\frac{\partial}{\partial t}(\delta \phi_1)$$

$$\text{with} \quad \delta \alpha_1 = \cos^2 \alpha_1 \frac{1}{|n| \overline{\phi_1}} \frac{\partial(\delta \phi_1)}{\partial \theta} - \frac{\sin \alpha_1 \cos \alpha_1}{\overline{\phi_1}}(\delta \phi_1) \qquad \text{(A.3.16)}$$

A.3.2.3 Compressor exit:

$$\delta V_x = \delta V_\theta = 0 \quad \text{as} \quad x \text{ goes to } +\infty$$

Therefore, $C_n = 0$

$$\frac{\delta P_{s_2}}{\rho U^2} = \frac{n}{|n|} i \left[\frac{\overline{V_{\theta 2}}}{U} \overline{\phi_2} + \frac{r \omega}{n U} \overline{\phi_2} + i \frac{n}{|n|} \overline{\phi_2^2} \right] B_n e^{i n \theta + i \omega t} \qquad \text{(A.3.17)}$$

The problem is now to express B_n as a function of a_n. For this purpose, we use two conditions:

(i) $\alpha_2 (\phi_1 , \alpha_1)$

$$\text{therefore,} \quad \delta \alpha_2 = \left(\frac{\partial \alpha_2}{\partial \phi_1}\right) \delta \phi_1 + \left(\frac{\delta \alpha_2}{\delta \alpha_1}\right) \delta \alpha_1 \qquad \text{(A.3.18)}$$

$$\delta \alpha_2 = \cos^2 \alpha_2 \left[\frac{r \omega}{n \overline{V_{x_2}}} A_n - \left[\tan \alpha_2 + i \frac{n}{|n|} \right] B_n \right] e^{i n \theta + i \omega t} \qquad \text{(A.3.19)}$$

(ii) $\overline{\phi_1} = \overline{\phi_2} = \phi$

$$\delta \phi_1 = \delta \phi_2 \quad \text{therefore,} \quad a_n = \phi (A_n + B_n)$$

System (i) and (ii) enables us to express B_n as a function of a_n which we put in the expression of $\frac{\delta P_{s_2}}{\rho U^2}$, we get:

$$\frac{\delta P_{s_2}}{\rho U^2} = + \frac{1}{|n|} \left[- \frac{\phi^2}{\cos^2 \alpha_2} \left(\left(\frac{\partial \alpha_2}{\partial \phi_1}\right) \frac{\partial \delta \phi_1}{\partial \theta} + \left(\frac{\partial \alpha_2}{\partial \alpha_1}\right) \frac{\partial \delta \alpha_1}{\partial \theta} \right) + \frac{r}{U}\frac{\partial}{\partial t}(\delta \phi_1) \right] \qquad \text{(A.3.20)}$$

A.3.2.4 Summary and conclusion

From sections A.3.2.1 and A.3.2.3, we have the expressions of $\frac{\delta P_{s2}}{\rho U^2}$ and $\frac{\delta P_{t1}}{\rho U^2}$.

The Hynes-Greitzer model, described in section A.3.2.2 provides an expression for $\frac{\delta P_{s2} - \delta P_{t1}}{\rho U^2}$. We get:

$$i\frac{\omega r}{U}\left(\frac{2}{|n|}+\mu\right) = \left(\frac{\partial\psi}{\partial\phi_1}\right) - \frac{\sin\alpha_1\cos\alpha_1}{\phi}\left(\frac{\partial\psi}{\partial\alpha_1}\right) - \frac{\phi\cos^2\alpha_1}{\cos^2\alpha_2}\left(\frac{\partial\alpha_2}{\partial\alpha_1}\right) + i\left[\begin{array}{l}\left(\frac{\partial\psi}{\partial\alpha_1}\right)\frac{n\cos^2\alpha_1}{|n|\phi} - n\lambda + \left(\frac{\partial\alpha_2}{\partial\phi_1}\right)\frac{n}{|n|}\frac{\varphi^2}{\cos^2\alpha_2} \\ - \left(\frac{\partial\alpha_2}{\partial\alpha_1}\right)\frac{n}{|n|}\frac{\phi\sin\alpha_1\cos\alpha_1}{\cos^2\alpha_2}\end{array}\right] \quad \text{(A.3.21)}$$

With $\omega = \omega_r + i\,\omega_i$, we get by equaling real and imaginary parts:

$$\frac{r\,\omega_i}{U} = -\frac{\left(\frac{\partial\psi}{\partial\phi}\right) - \left(\frac{\partial\alpha_2}{\partial\alpha_1}\right)\phi\frac{\cos^2\alpha_1}{\cos^2\alpha_2} - \left(\frac{\partial\psi}{\partial\alpha_1}\right)\frac{\sin\alpha_1\cos\alpha_1}{\phi}}{\left(\frac{2}{|n|}+\mu\right)} \qquad \text{(damping)} \quad \text{(A.3.22)}$$

$$\frac{r\,\omega_r}{n\,U} = -\frac{\lambda - \left(\frac{\partial\psi}{\partial\alpha_1}\right)\frac{\cos^2\alpha_1}{|n|\phi} - \left(\frac{\partial\alpha_2}{\partial\phi}\right)\frac{\phi^2}{|n|\cos^2\alpha_2} + \left(\frac{\partial\alpha_2}{\partial\alpha_1}\right)\frac{\sin\alpha_1\cos\alpha_1\,\phi}{|n|\cos^2\alpha_2}}{\left(\frac{2}{|n|}+\mu\right)} \quad \text{(A.3.23)}$$

(propagation speed)

The denominator is always positive. Therefore, a positive damping implies:

$$\left(\frac{\partial\psi}{\partial\phi}\right) - \left(\frac{\partial\alpha_2}{\partial\alpha_1}\right)\phi\frac{\cos^2\alpha_1}{\cos^2\alpha_2} - \left(\frac{\partial\psi}{\partial\alpha_1}\right)\frac{\sin\alpha_1\cos\alpha_1}{\phi} < 0$$

The neutral stability operating point is obtained by equaling Equation A.3.24 to zero. Equation A.3.23 leads to the neutral stability frequency for this neutrally stable flow

coefficient.

Some remarks can be made on these results:

(i) For $\alpha_1 = 0$, we get the same propagation speed as Longley [41].

(ii) For $\alpha_1 = 0$ and $(\frac{\partial \alpha_2}{\partial \alpha_1}) = 0$, we get the same damping as Longley [13].

(iii) As suggested by Longley [41], the stability limit is affected by a variation in the exit flow angle due to changes in the inlet flow angle. Furthermore, it is altered by the mean inlet swirl.

Appendix 4

Boundary Conditions Matrices

In this appendix is included the analytical expressions of the boundary matrices of Chapter 3. The notations used are the same as the one in that chapter. Subscript 'B' refers to quantities within the blade passage at the leading edge or at the trailing edge.

A.4.1 LEADING EDGE MATRICES

As shown in Chapter 3, we have at the leading edge:

$$M\,V_{2i}\begin{pmatrix} B_{n_i} \\ C_{n_i} \\ D_{n_i} \\ E_{n_i} \end{pmatrix} = M\,B_{2i}\begin{pmatrix} \tilde{B}_{n_i} \\ \tilde{C}_{n_i} \\ \tilde{E}_{n_i} \end{pmatrix} \qquad (A.4.1)$$

Where:

$$M\,V_{2i}\,(1,1) = \left(\frac{\omega r}{a_i} + r\,\alpha_i\left(\frac{V_{x_i}}{a_i} - \frac{a_i}{V_{x_i}}\right) + n\,\frac{V_{\theta_i}}{a_i}\right)e^{i\varphi_i} \qquad (A.4.2)$$

$$M\,V_{2i}\,(1,2) = \left(\frac{\omega r}{a_i} + r\,\beta_i\left(\frac{V_{x_i}}{a_i} - \frac{a_i}{V_{x_i}}\right) + n\,\frac{V_{\theta_i}}{a_i}\right)e^{i\psi_i} \qquad (A.4.3)$$

$$M\,V_{2i}\,(1,3) = n\,e^{i\chi_i} \qquad (A.4.4)$$

$$M V_{2i}(1,4) = e^{i\chi_i} \tag{A.4.5}$$

$$M V_{2i}(2,1) = \frac{T_{t_i}}{1+\frac{\gamma-1}{2}M_i^2}\frac{\omega r}{a_i}(\gamma-1)e^{i\varphi_i} \tag{A.4.6}$$

$$M V_{2i}(2,2) = \frac{T_{t_i}}{1+\frac{\gamma-1}{2}M_i^2}\frac{\omega r}{a_i}(\gamma-1)e^{i\psi_i} \tag{A.4.7}$$

$$M V_{2i}(2,3) = \frac{T_{t_i}}{1+\frac{\gamma-1}{2}M_i^2}\left[n\frac{V_{x_i}^2}{a_i^2} + \left(\frac{\omega r}{a_i}+\frac{n V_{\theta_i}}{a_i}\right)\frac{V_{\theta_i}}{a_i}\right](\gamma-1)e^{i\chi_i} \tag{A.4.8}$$

$$M V_{2i}(2,4) = -\frac{T_{t_i}}{1+\frac{\gamma-1}{2}M_i^2}e^{i\chi_i} \tag{A.4.9}$$

$$M V_{2i}(3,1) = \frac{\gamma P_{t_i}}{1+\frac{\gamma-1}{2}M_i^2}\frac{\omega r}{a_i}e^{i\varphi_i}$$

$$+\frac{e^{i\varphi_i}}{1+i(\omega+n\Omega)\tau_{Loss}}\left[\omega_{Loss}P_{S_i}\gamma\left(\frac{\omega r}{a_i}+r\alpha_i\frac{V_{x_i}}{a_i}+n\frac{V_{\theta_i}}{a_i}\right)-\omega_{Loss}\frac{\gamma P_{t_i}}{1+\frac{\gamma-1}{2}M_i^2}\frac{\omega r}{a_i}\right.$$

$$\left.-(P_{t_i}-P_{S_i})\left[\left(\frac{\partial\omega_{Loss}}{\partial\tan\alpha_i}\right)\tan\alpha_i\left(-\frac{n a_i}{V_{\theta_i}}+\frac{\alpha_i r a_i}{V_{x_i}}\right)\right.\right.$$

$$\left.\left.+\left(\frac{\partial\omega_{Loss}}{\partial M_{R_i}}\right)\left\{-\frac{V_{x_i}}{V_i}\alpha_i r-\frac{V_{\theta_i}}{V_i}n\right.\right.\right.$$

$$\left.\left.\left.\left\{-\frac{M_i}{2}(\gamma-1)\left(\frac{\frac{\omega r}{a_i}}{+r\alpha_i\frac{V_{x_i}}{a_i}+\frac{n V_{\theta_i}}{a_i}}\right)\right\}\right]\right] \tag{A.4.10}$$

$$MV_{2i}(3,2) = \frac{\gamma P_{t_i}}{1+\frac{\gamma-1}{2}M_i^2}\frac{\omega r}{a_i}e^{i\psi_i}$$

$$+\frac{e^{i\psi_i}}{1+i(\omega+n\Omega)\tau_{Loss}}\left[\begin{array}{l}\omega_{Loss}P_{S_i}\gamma\left(\frac{\omega r}{a_i}+r\beta_i\frac{V_{x_i}}{a_i}+n\frac{V_{\theta_i}}{a_i}\right)-\omega_{Loss}\frac{\gamma P_{t_i}}{1+\frac{\gamma-1}{2}M_i^2}\frac{\omega r}{a_i}\\ -(P_{t_i}-P_{S_i})\left[\begin{array}{l}\left(\frac{\partial\omega_{Loss}}{\partial\tan\alpha_i}\right)\tan\alpha_i\left(-\frac{n\,a_i}{V_{\theta_i}}+\frac{\beta_i\,r\,a_i}{V_{x_i}}\right)\\ +\left(\frac{\partial\omega_{Loss}}{\partial M_{R_i}}\right)\left\{\begin{array}{l}-\frac{V_{x_i}}{V_i}\beta_i r-\frac{V_{\theta_i}}{V_i}n\\ -\frac{M_i}{2}(\gamma-1)\left(\begin{array}{l}\frac{\omega r}{a_i}\\ +r\beta_i\frac{V_{x_i}}{a_i}+n\frac{V_{\theta_i}}{a_i}\end{array}\right)\end{array}\right.\end{array}\right]\end{array}\right] \quad \text{(A.4.11)}$$

$$MV_{2i}(3,3) = \frac{\gamma P_{t_i}}{1+\frac{\gamma-1}{2}M_i^2}\left(n\frac{V_{x_i}{}^2}{a_i{}^2}+\left(\frac{\omega r}{a_i}+\frac{n\,V_{\theta_i}}{a_i}\right)\frac{V_{\theta_i}}{a_i}\right)e^{i\chi_i}$$

$$+\frac{e^{i\chi_i}}{1+i(\omega+n\Omega)\tau_{Loss}}\left[\begin{array}{l}-\omega_{Loss}\frac{\gamma P_{t_i}}{1+\frac{\gamma-1}{2}M_i^2}\left(n\frac{V_{x_i}{}^2}{a_i{}^2}+\left(\frac{\omega r}{a_i}+\frac{n\,V_{\theta_i}}{a_i}\right)\frac{V_{\theta_i}}{a_i}\right)\\ -(P_{t_i}-P_{S_i})\left[\begin{array}{l}\left(\frac{\partial\omega_{Loss}}{\partial\tan\alpha_i}\right)\tan\alpha_i\frac{\omega r}{V_{\theta_i}}\\ +\left(\frac{\partial\omega_{Loss}}{\partial M_{R_i}}\right)\left\{\begin{array}{l}\frac{V_{x_i}}{V_i}n-\frac{V_{x_i}}{a_i}\\ +\frac{V_{\theta_i}}{V_i}\left(\frac{\omega r}{a_i}+n\frac{V_{\theta_i}}{a_i}\right)\end{array}\right.\end{array}\right]\end{array}\right] \quad \text{(A.4.12)}$$

$$MV_{2i}(3,4) = \frac{\gamma P_{t_i}}{1+\frac{\gamma-1}{2}M_i^2}\frac{M_i^2}{2}e^{i\chi_i}$$

$$+\frac{e^{i\chi_i}}{1+i(\omega+n\Omega)\tau_{Loss}}\left[\begin{array}{l}-\omega_{Loss}\frac{\gamma P_{t_i}}{1+\frac{\gamma-1}{2}M_i^2}\frac{M_i^2}{2}\\ -(P_{t_i}-P_{S_i})\left(\frac{\partial\omega_{Loss}}{\partial M_{R_i}}\right)\frac{M_i}{2}\end{array}\right] \quad \text{(A.4.13)}$$

$$MB_{2i}(1,1) = \left(1 - \frac{a_{Bi}}{w_{Bi}}\right) e^{i\tilde{\varphi}} \tag{A.4.14}$$

$$MB_{2i}(1,2) = \left(1 + \frac{a_{Bi}}{w_{Bi}}\right) e^{i\tilde{\psi}} \tag{A.4.15}$$

$$MB_{2i}(1,3) = e^{i\tilde{\chi}} \tag{A.4.16}$$

$$MB_{2i}(2,1) = \frac{T_{t_{Bi}}}{1 + \frac{\gamma - 1}{2} M_{\xi_i}^2} \left(1 - M_{\xi_i}\right)(\gamma - 1)\, e^{i\tilde{\varphi}} \tag{A.4.17}$$

$$MB_{2i}(2,2) = \frac{T_{t_{Bi}}}{1 + \frac{\gamma - 1}{2} M_{\xi_i}^2} \left(1 + M_{\xi_i}\right)(\gamma - 1)\, e^{i\tilde{\psi}} \tag{A.4.18}$$

$$MB_{2i}(2,3) = -\frac{T_{t_{Bi}}}{1 + \frac{\gamma - 1}{2} M_{\xi_i}^2} e^{i\tilde{\chi}} \tag{A.4.19}$$

$$MB_{2i}(3,1) = \frac{\gamma P_{t_{Bi}}}{1 + \frac{\gamma - 1}{2} M_{\xi_i}^2} \left(1 - M_{\xi_i}\right) e^{i\tilde{\varphi}} \tag{A.4.20}$$

$$MB_{2i}(3,2) = \frac{\gamma P_{t_{Bi}}}{1 + \frac{\gamma - 1}{2} M_{\xi_i}^2} \left(1 + M_{\xi_i}\right) e^{i\tilde{\psi}} \tag{A.4.21}$$

$$MB_{2i}(3,3) = \frac{\gamma P_{t_{Bi}}}{1 + \frac{\gamma - 1}{2} M_{\xi_i}^2} \frac{M_{\xi_i}^2}{2} e^{i\tilde{\chi}} \tag{A.4.22}$$

A.4.2 TRAILING EDGE MATRICES

As shown in Chapter 3, we have at the trailing edge:

$$M B_{2i+1} \begin{pmatrix} \tilde{B}_{n_i} \\ \tilde{C}_{n_i} \\ \tilde{E}_{n_i} \end{pmatrix} = M V_{2i+1} \begin{pmatrix} B_{n_{i+1}} \\ C_{n_{i+1}} \\ D_{n_{i+1}} \\ E_{n_{i+1}} \end{pmatrix} + M V C_{2i+1} \begin{pmatrix} B_{n_i} \\ C_{n_i} \\ D_{n_i} \\ E_{n_i} \end{pmatrix} \tag{A.4.23}$$

Where:

$$M B_{2i+1}(1,1) = \left(1 - \frac{a_{Bi}}{w_{Bi}}\right) e^{i\tilde{\varphi}} \tag{A.4.24}$$

$$M B_{2i+1}(1,2) = \left(1 + \frac{a_{Bi}}{w_{Bi}}\right) e^{i\tilde{\psi}} \tag{A.4.25}$$

$$M B_{2i+1}(1,3) = e^{i\tilde{\chi}} \tag{A.4.26}$$

$$M B_{2i+1}(2,1) = \frac{T_{t_{Bi}}}{1 + \frac{\gamma-1}{2} M_{\xi_i}^2} \left(1 - M_{\xi_i}\right)(\gamma - 1) e^{i\tilde{\varphi}} \tag{A.4.27}$$

$$M B_{2i+1}(2,2) = \frac{T_{t_{Bi}}}{1 + \frac{\gamma-1}{2} M_{\xi_i}^2} \left(1 + M_{\xi_i}\right)(\gamma - 1) e^{i\tilde{\psi}} \tag{A.4.28}$$

$$M B_{2i+1}(2,3) = -\frac{T_{t_{Bi}}}{1 + \frac{\gamma-1}{2} M_{\xi_i}^2} e^{i\tilde{\chi}} \tag{A.4.29}$$

$$M B_{2i+1}(3,1) = \frac{P_{t_{Bi}}}{1 + \frac{\gamma-1}{2} M_{\xi_i}^2} \left(1 - M_{\xi_i}\right) \gamma e^{i\tilde{\varphi}} \tag{A.4.30}$$

$$M B_{2i+1}(3,2) = \frac{P_{t_{Bi}}}{1 + \frac{\gamma-1}{2} M_{\xi_i}^2} \left(1 + M_{\xi_i}\right) \gamma e^{i\tilde{\psi}} \tag{A.4.31}$$

$$M B_{2i+1}(3,3) = \frac{P_{t_{Bi}}}{1 + \frac{\gamma-1}{2} M_{\xi_i}^2} \frac{M_{\xi_i}^2}{2} \gamma e^{i\tilde{\chi}} \tag{A.4.32}$$

$$M B_{2i+1}(4,1) = 0 \tag{A.4.33}$$

$$M B_{2i+1}(4,2) = 0 \tag{A.4.34}$$

$$M B_{2i+1}(4,3) = 0 \tag{A.4.35}$$

$$M V_{2i+1}(1,1) = \left(\frac{\omega r}{a_{i+1}} + r\,\alpha_{i+1} \left(\frac{V_{x_{i+1}}}{a_{i+1}} - \frac{a_{i+1}}{V_{x_{i+1}}} \right) + n \frac{V_{\theta_{i+1}}}{a_{i+1}} \right) e^{i\varphi_{i+1}} \tag{A.4.36}$$

$$M V_{2i+1}(1,2) = \left(\frac{\omega r}{a_{i+1}} + r\,\beta_{i+1} \left(\frac{V_{x_{i+1}}}{a_{i+1}} - \frac{a_{i+1}}{V_{x_{i+1}}} \right) + n \frac{V_{\theta_{i+1}}}{a_{i+1}} \right) e^{i\psi_{i+1}} \tag{A.4.37}$$

$$M V_{2i+1}(1,3) = n\, e^{i\chi_{i+1}} \tag{A.4.38}$$

$$M V_{2i+1}(1,4) = e^{i\chi_{i+1}} \tag{A.4.39}$$

$$M V_{2i+1}(2,1) = \frac{T_{t_{i+1}}}{1 + \frac{\gamma - 1}{2} M_{i+1}^2} \frac{\omega r}{a_{i+1}} (\gamma - 1)\, e^{i\varphi_{i+1}} \tag{A.4.40}$$

$$M V_{2i+1}(2,2) = \frac{T_{t_{i+1}}}{1 + \frac{\gamma - 1}{2} M_{i+1}^2} \frac{\omega r}{a_{i+1}} (\gamma - 1)\, e^{i\psi_{i+1}} \tag{A.4.41}$$

$$M V_{2i+1}(2,3) = \frac{T_{t_{i+1}}}{1 + \frac{\gamma - 1}{2} M_{i+1}^2} \left(n \frac{V_{x_{i+1}}^2}{a_{i+1}^2} + \left(\frac{\omega r}{a_{i+1}} + \frac{n\, V_{\theta_{i+1}}}{a_{i+1}} \right) \frac{V_{\theta_{i+1}}}{a_{i+1}} \right) (\gamma - 1)\, e^{i\chi_{i+1}} \tag{A.4.42}$$

$$M V_{2i+1}(2,4) = - \frac{T_{t_{i+1}}}{1 + \frac{\gamma - 1}{2} M_{i+1}^2} e^{i\chi_{i+1}} \tag{A.4.43}$$

$$M V_{2i+1}(3,1) = \frac{P_{t_{i+1}}}{1 + \frac{\gamma - 1}{2} M_{i+1}^2} \frac{\omega r}{a_{i+1}} \gamma e^{i\varphi_{i+1}} \tag{A.4.44}$$

$$M V_{2i+1}(3,2) = \frac{P_{t_{i+1}}}{1 + \frac{\gamma - 1}{2} M_{i+1}^2} \frac{\omega r}{a_{i+1}} \gamma e^{i\psi_{i+1}} \tag{A.4.45}$$

$$M V_{2i+1}(3,3) = \frac{P_{t_{i+1}}}{1 + \frac{\gamma - 1}{2} M_{i+1}^2} \left(n \frac{V_{x_{i+1}}^2}{a_{i+1}^2} + \left(\frac{\omega r}{a_{i+1}} + \frac{n\, V_{\theta_{i+1}}}{a_{i+1}} \right) \frac{V_{\theta_{i+1}}}{a_{i+1}} \right) \gamma e^{i\chi_{i+1}} \tag{A.4.46}$$

$$M V_{2i+1}(3,4) = \frac{P_{t_{i+1}}}{1 + \frac{\gamma - 1}{2} M_{i+1}^2} \frac{M_{i+1}^2}{2} \gamma e^{i \chi_{i+1}} \tag{A.4.47}$$

$$M V_{2i+1}(4,1) = -\left(-\frac{n}{V_{\theta_{i+1}}} a_{i+1} + \frac{\alpha_{i+1}\, r\, a_{i+1}}{V_{x_{i+1}}} \right) e^{i \varphi_{i+1}} \frac{\tan \alpha_{i+1}}{1 + \tan^2 \alpha_{i+1}} \tag{A.4.48}$$

$$M V_{2i+1}(4,2) = -\left(-\frac{n}{V_{\theta_{i+1}}} a_{i+1} + \frac{\beta_{i+1}\, r\, a_{i+1}}{V_{x_{i+1}}} \right) e^{i \psi_{i+1}} \frac{\tan \alpha_{i+1}}{1 + \tan^2 \alpha_{i+1}} \tag{A.4.49}$$

$$M V_{2i+1}(4,3) = -\frac{\omega r}{V_{\theta_{i+1}}} e^{i \chi_{i+1}} \frac{\tan \alpha_{i+1}}{1 + \tan^2 \alpha_{i+1}} \tag{A.4.50}$$

$$M V_{2i+1}(4,4) = 0 \tag{A.4.51}$$

$$M VC_{2i+1}(4,1) = \frac{e^{i \varphi_i}}{1 + i(\omega + n\Omega)\tau_{Dev}} \left[\left(\frac{\partial \alpha_{i+1}}{\partial \alpha_i} \right) \frac{\tan \alpha_i}{1 + \tan^2 \alpha_i} \left(-\frac{n\, a_i}{V_{\theta_i}} + \frac{\alpha_i\, r\, a_i}{V_{x_i}} \right) + \left(\frac{\partial \alpha_{i+1}}{\partial M_{R_i}} \right) \left\{ -\alpha_i\, r \frac{V_{x_i}}{V_i} - n \frac{V_{\theta_i}}{V_i} - \frac{M_i}{2}(\gamma - 1) \left(\frac{\omega r}{a_i} + r\, \alpha_i \frac{V_{x_i}}{a_i} + n \frac{V_{\theta_i}}{a_i} \right) \right\} \right] \tag{A.4.52}$$

$$M VC_{2i+1}(4,2) = \frac{e^{i \psi_i}}{1 + i(\omega + n\Omega)\tau_{Dev}} \left[\left(\frac{\partial \alpha_{i+1}}{\partial \alpha_i} \right) \frac{\tan \alpha_i}{1 + \tan^2 \alpha_i} \left(-\frac{n\, a_i}{V_{\theta_i}} + \frac{\beta_i\, r\, a_i}{V_{x_i}} \right) + \left(\frac{\partial \alpha_{i+1}}{\partial M_{R_i}} \right) \left\{ -\beta_i\, r \frac{V_{x_i}}{V_i} - n \frac{V_{\theta_i}}{V_i} - \frac{M_i}{2}(\gamma - 1) \left(\frac{\omega r}{a_i} + r\, \beta_i \frac{V_{x_i}}{a_i} + n \frac{V_{\theta_i}}{a_i} \right) \right\} \right] \tag{A.4.53}$$

$$MVC_{2i+1}(4,3) = \frac{e^{i\chi_i}}{1 + i(\omega + n\Omega)\tau_{Dev}} \left[\left(\frac{\partial \alpha_{i+1}}{\partial \alpha_i} \right) \frac{\tan \alpha_i}{1 + \tan^2 \alpha_i} \frac{\omega r}{V_{\theta_i}} + \left(\frac{\partial \alpha_{i+1}}{\partial M_{R_i}} \right) \left\{ n \frac{V_{x_i}}{a_i} \frac{V_{x_i}}{V_i} + \frac{V_{\theta_i}}{V_i} \left(\frac{\omega r}{a_i} + n \frac{V_{\theta_i}}{a_i} \right) \right\} \right] \quad \text{(A.4.54)}$$

$$MVC_{2i+1}(4,4) = \frac{e^{i\chi_i}}{1 + i(\omega + n\Omega)\tau_{Dev}} \left(\frac{\partial \alpha_{i+1}}{\partial M_{R_i}} \right) \frac{M_i}{2} \quad \text{(A.4.55)}$$

Appendix 5

Computational Construction of the Meanline Loss Bucket

A typical loss bucket is shown on figure (2.7), inspired from Raw and Weir [30]. The loss bucket used in the computational implementation of the model is constructed in the following way:

A.5.1 CRITICAL POINTS POSITIONING

In the proposed construction of the loss bucket, four critical points are needed, as shown on Diagram (A.5.1):

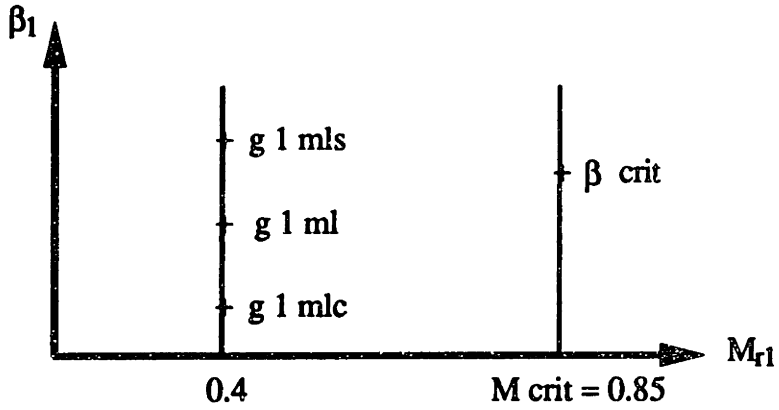

Diagram (A.5.1): Loss bucket construction: critical points

(i) **g_{1ml}: minimum loss relative inlet flow angle at M=0.4.**

This point is evaluated from this empirical correlations described in section 2.5.2, where:

$$\beta_{1ml} = (i_c - i_{2D}) (M_{r1}) + \beta_1^* + K_i \left(\frac{t}{c}\right) . i_o (\sigma,\beta_1) + n (\sigma,\beta_1) . \theta^* \quad (A.5.1)$$

(ii) **g_{1mls}: relative inlet flow angle at which the loss coefficient starts to increase from its minimum loss value due to the proximity of stall at M=0.4.**

This point is evaluated at a diffusion factor of 0.55:

$$DFAC = 1 - \frac{u_2}{u_1} + \frac{1}{2 . \text{solidity}} \left(\sin \beta_1 - \frac{u_2}{u_1} \sin \beta_2\right) \quad (A.5.2)$$

Knowing the diffusion factor, we can evaluate β_2 corresponding to g_{1mls}. From Raw &Weir, this deviation is a function of this DFAC. We need to get u_2.

The iteration scheme is therefore:

initial guess: $\beta_{1_{old}} = \beta_1^*$

$$u_2 = \sqrt{\gamma R T_2}\, Q_t^{-1}\left(\frac{A_1 \cos \beta_{1_{old}}}{A_2 \cos \beta_2} \frac{1}{1 + \Omega\left(1 - \frac{P_{s_1}}{P_{t_1}}\right)} Q_t(M_1)\right)$$

where: $$Q_t(M_1) = \frac{\dot{m} \sqrt{T_t}}{P_{t_1} A_1 \cos \beta_1}$$

$$P_{t_2} = P_{t_1} + \Omega . (P_{t_1} - P_{s_1}) \text{ and } \Omega = \Omega_{ml} + \Omega_{sh}$$

$$\beta_{1_{new}} = \text{Arcsin}\left(2 . \text{solidity} . \frac{u_2}{u_1} . \left(\frac{1}{\cos \beta_2} + \frac{1}{2 . \text{solidity}} \tan \beta_2\right) - 2 . \text{solidity} . 0.45\right)$$

(iii) **g_{1mlc}: relative inlet flow angle at which the loss coefficient starts to increase from its minimum loss value due to the proximity of choke at M=0.4.**

It is computed with: $\overline{g_{1mlc}\, g_{1ml}} = 2\ \overline{g_{1ml}\, g_{1mls}}$ (A.5.3)

From g_{1mlc}, we get the choke margin at M=0.4: chkmrg.

$$Q_t(0.4) = \frac{\dot{m}\sqrt{T_t}}{P_{t_{\text{leading edge}}} \cdot s \cdot h_1 \cdot \cos\beta_{1mlc}}$$

$$Q_t(1) = \frac{\dot{m}\sqrt{T_t}}{P_{t_{\text{throat}}} \cdot \frac{d \cdot h_t}{\text{chkmrg}}}$$

(iv) **β_{crit}: relative inlet flow angle at M_{crit} at which $\beta_{1mls} = \beta_{1ml} = \beta_{1mlc}$ computed using a choke margin of 1.02.**

$$\cos\beta_{crit} = \frac{Q_t(1)}{Q_t(M_{crit})} \cdot \frac{d}{c} \cdot \text{solidity} \cdot \frac{h_h}{h_1} \cdot \frac{1}{1.02} \cdot \frac{P_t}{P_{t_{\text{leading edge}}}} \qquad \text{(A.5.4)}$$

A.5.2 CHOKING LINE

The maximum flow at throat is:

$$Q_t(1) = \frac{\dot{m}\sqrt{\gamma R T_t}}{P_{t_{\text{throat}}} \cdot d \cdot h_t} \qquad \text{(A.5.5)}$$

The flow at the leading edge is:

$$Q_t(M_1) = \frac{\dot{m}\sqrt{\gamma R T_t}}{P_{t_{\text{leading edge}}} \cdot s \cdot h_1 \cdot \cos\beta_{1c}}$$

We therefore get:

$$\cos\beta_{1c} = \frac{Q_t(1)}{Q_t(M_1)} \frac{h_t}{h_1} \frac{d}{c} \frac{1}{\left(\frac{s}{c}\right)} \frac{P_{t_{\text{throat}}}}{P_{t_{\text{leading edge}}}}$$

$$\frac{P_{t_{\text{throat}}}}{P_{t_{\text{leading edge}}}} = 1 - \Omega_{sh}(M_1, \beta_1)\left[1 - \frac{P_{s_{\text{leading edge}}}}{P_{t_{\text{leading edge}}}}(M_1)\right]$$

The iteration scheme is therefore:

initial guess: $\beta_{1_{old}} = \beta_1^*$

$$\beta_{1_{c_{new}}} = \text{Arcos}\left(\frac{Q_t(1)}{Q_t(M_1)} \frac{h_t}{h_1} \frac{d}{c} \frac{1}{\left(\frac{s}{c}\right)} \left[1 - \Omega_{sh}\left(M_1 , \beta_{1_{c_{old}}}\right) \left[1 - \frac{P_{s_{\text{leading edge}}}}{P_{t_{\text{leading edge}}}}(M_1) \right] \right] \right)$$

A.5.3 CONSTRUCTION OF THE LOSS BUCKET

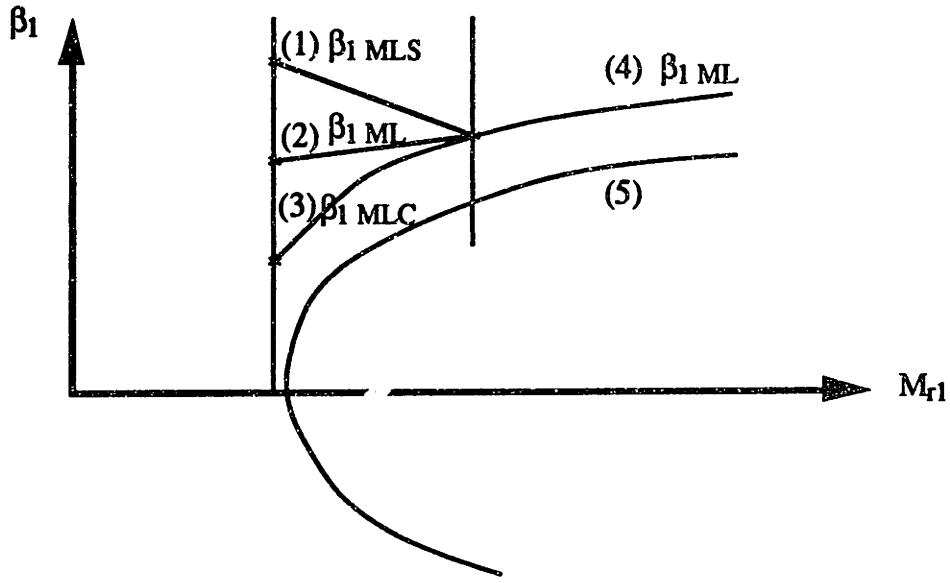

Diagram (A.5.2): Loss bucket construction

Once we have the four critical points, we deduce the lines of Diagram (A.5.2):

- Line (1): simple straight line
- Line (2): simple straight line
- Line (3): Its construction is shown on Diagram (A.5.3)

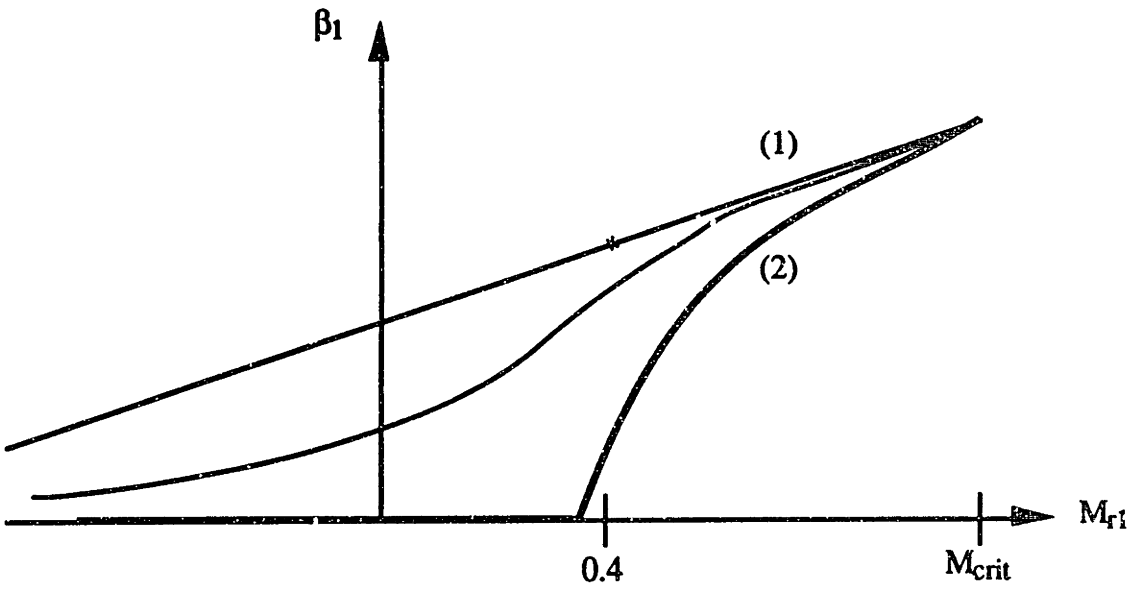

Diagram (A.5.3): Interpolation to get β_{1mlc}

(i) First method:

β_{1mlc} is obtained using a choke margin interpolated between chkmrg and 1.02. This is represented by line (2) on Diagram (A.5.3). If $\beta_{1mlc} < 0$, then $\beta_{1mlc} = 0$.

(ii) Second method:

β_{1mlc} is obtained through a straight line between β_{crit} and $\beta_{1c}(0.4)$.

This is represented by line (1) on Diagram (A.5.3).

(iii) Interpolation:

Finally, we interpolate between these two ideas:

For high Mach Number, the actual β_{1mlc} is close to the result obtained from the second method.

For low Mach Number, the actual β_{1mlc} is close to the result obtained from the first method.

– Line (4) Computed using a constant choke margin of 1.02.

– Line (5) Computed in the section 2 of this appendix.

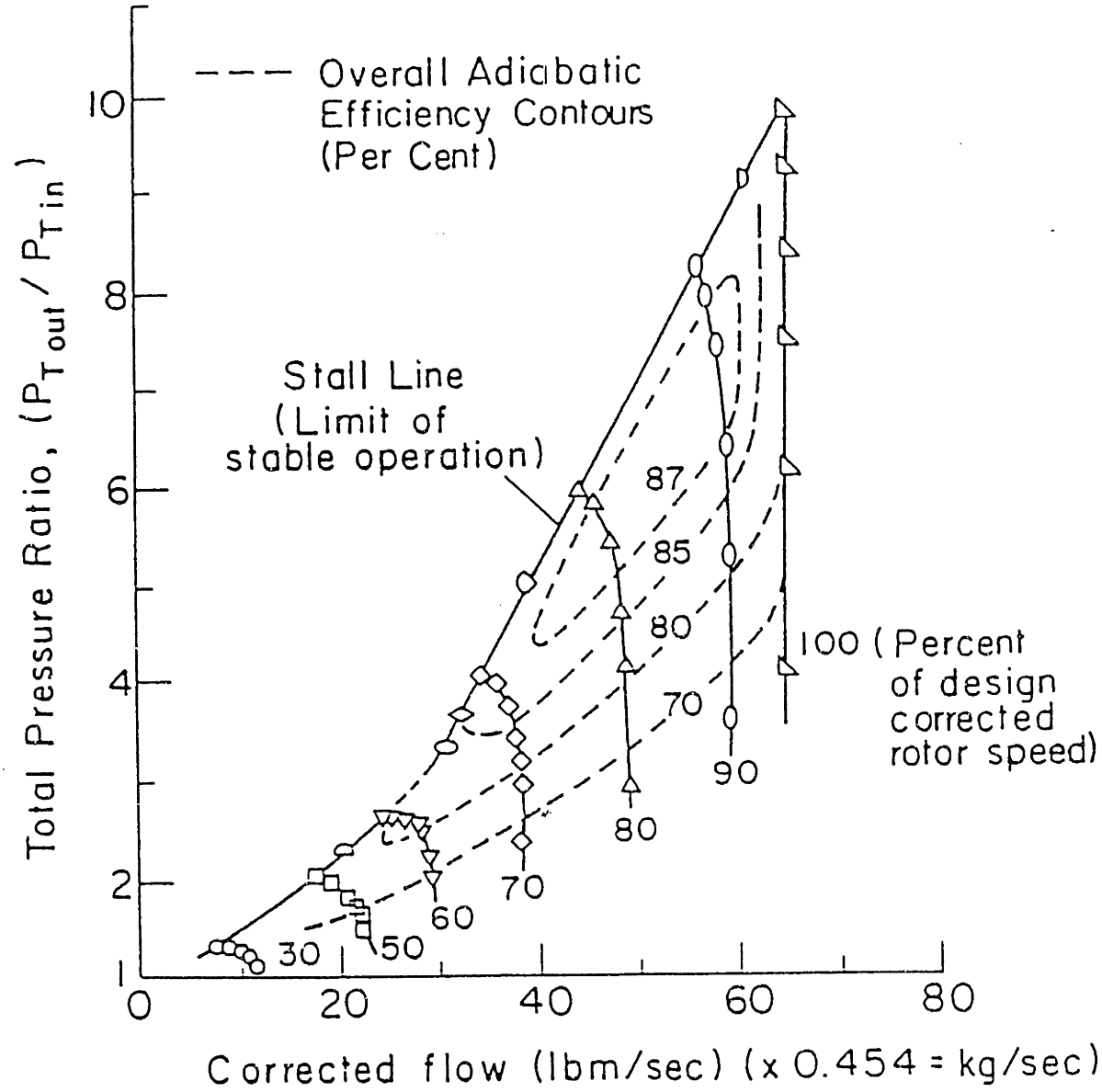

Figure 1.1 Typical high-speed compressor performance map

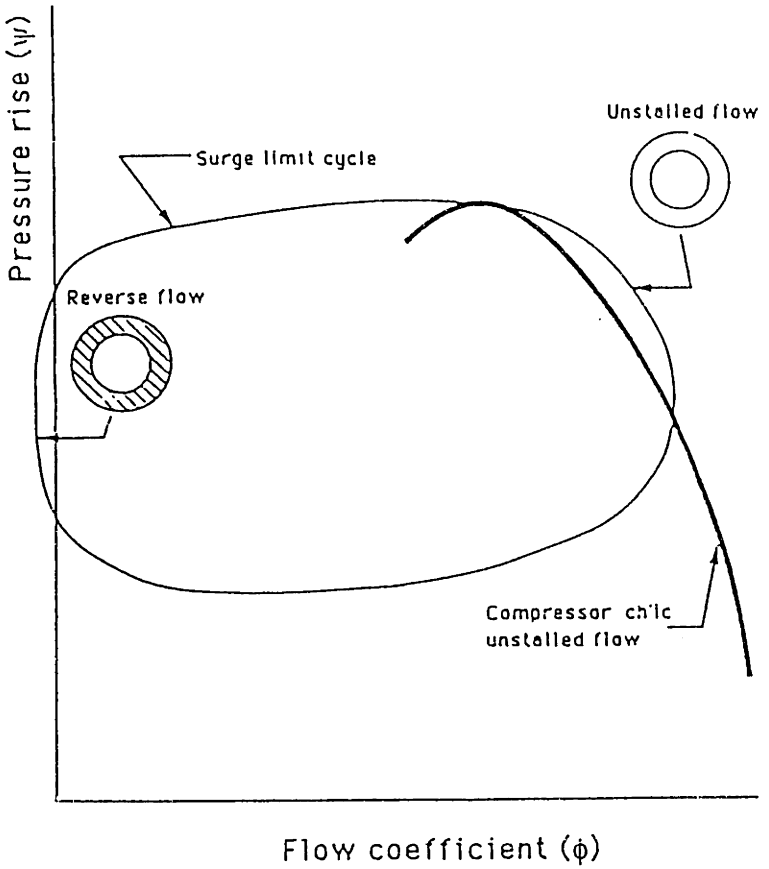

Figure 1.2 Surge limit cycle

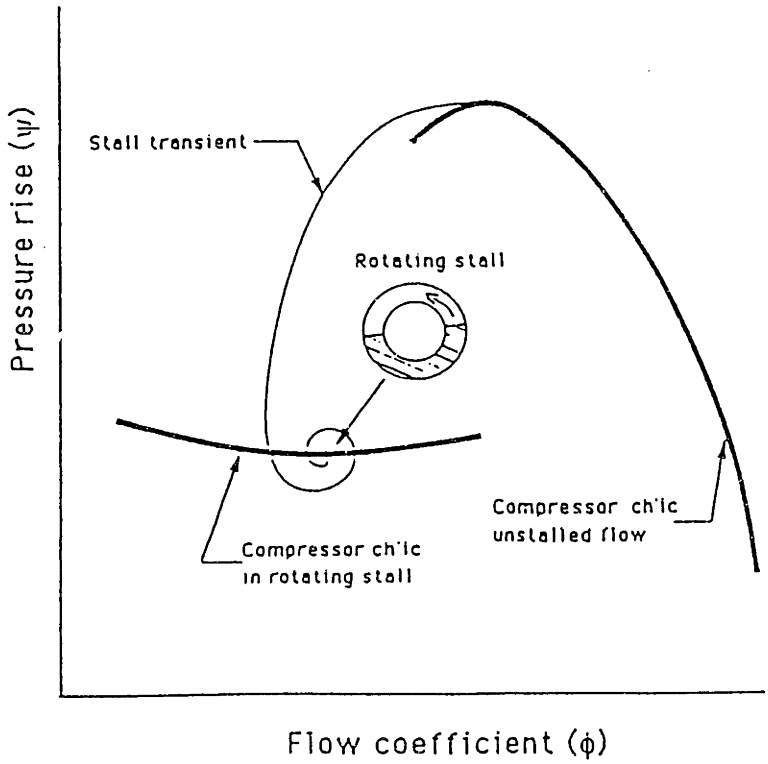

Figure 1.3 Rotating stall

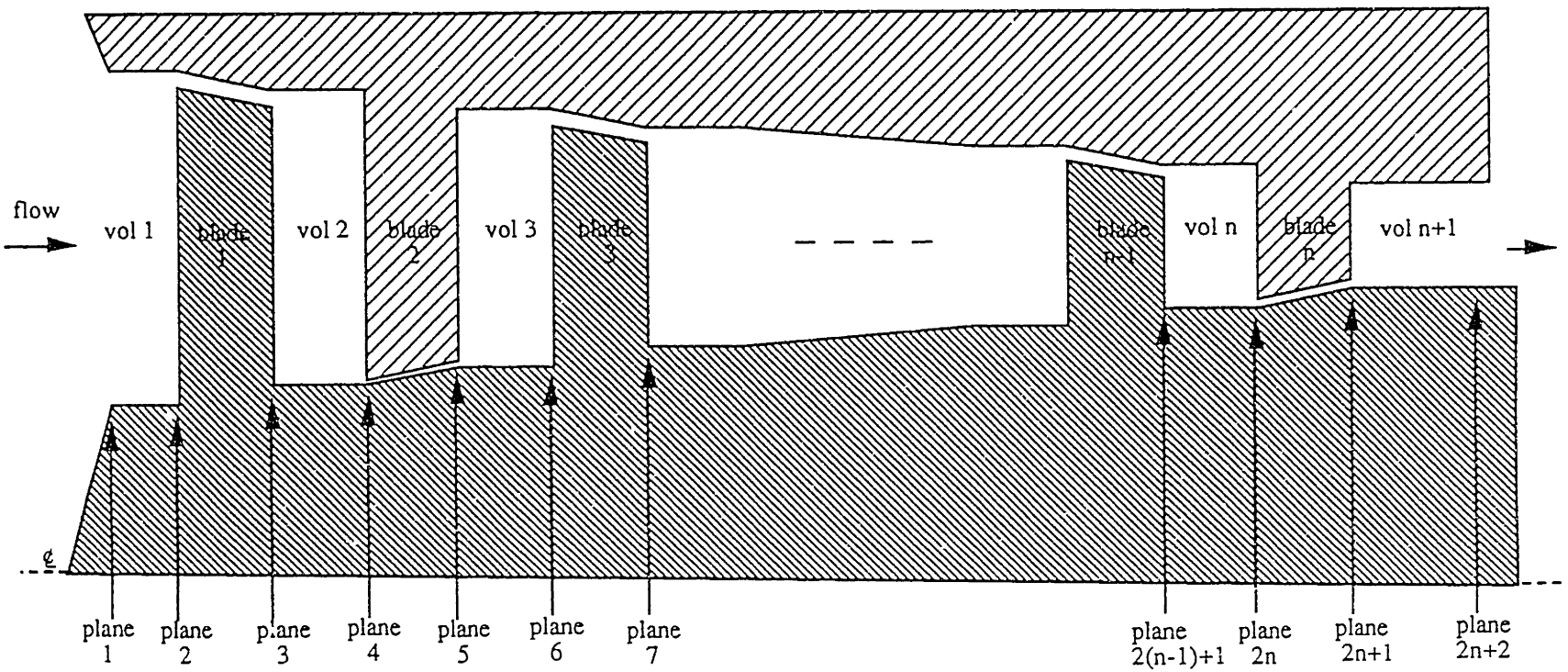

Figure 2.1.a Compressor model

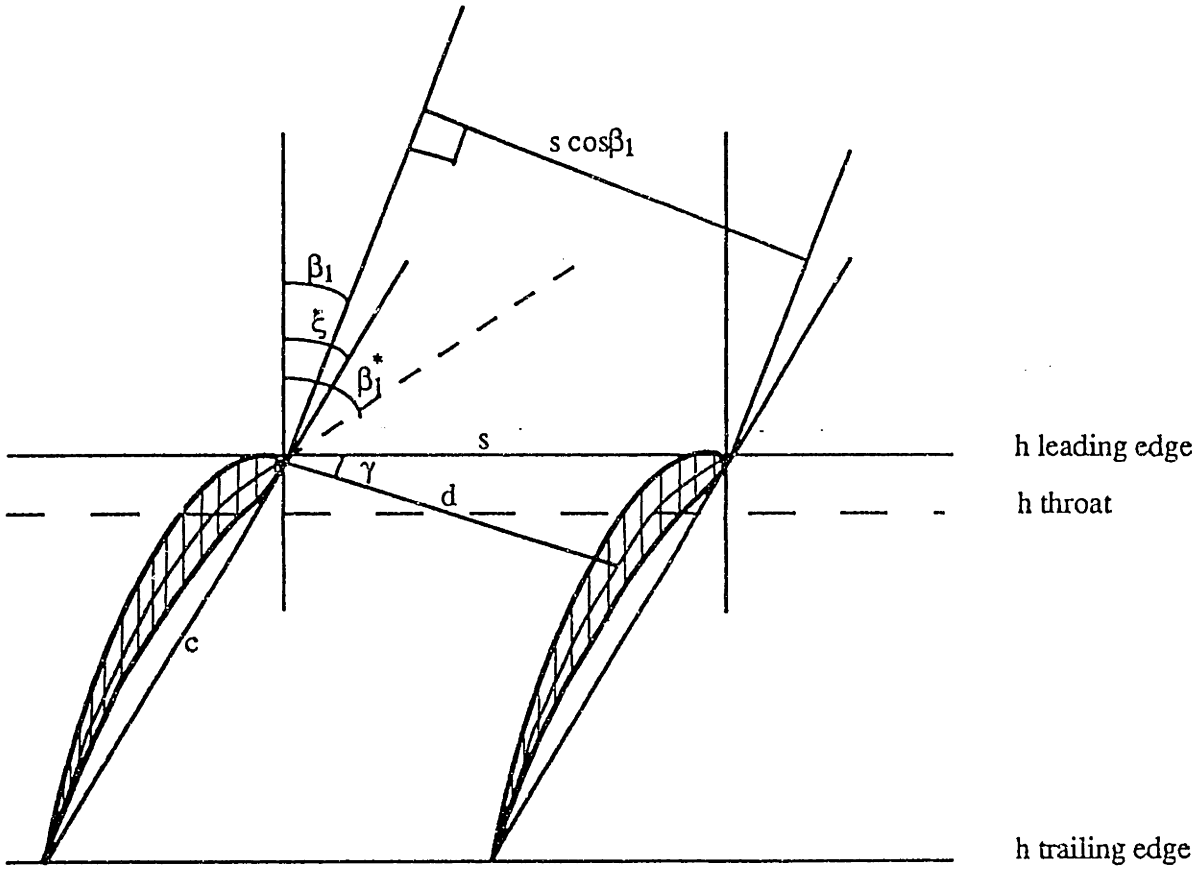

Figure 2.1.b Blade geometry

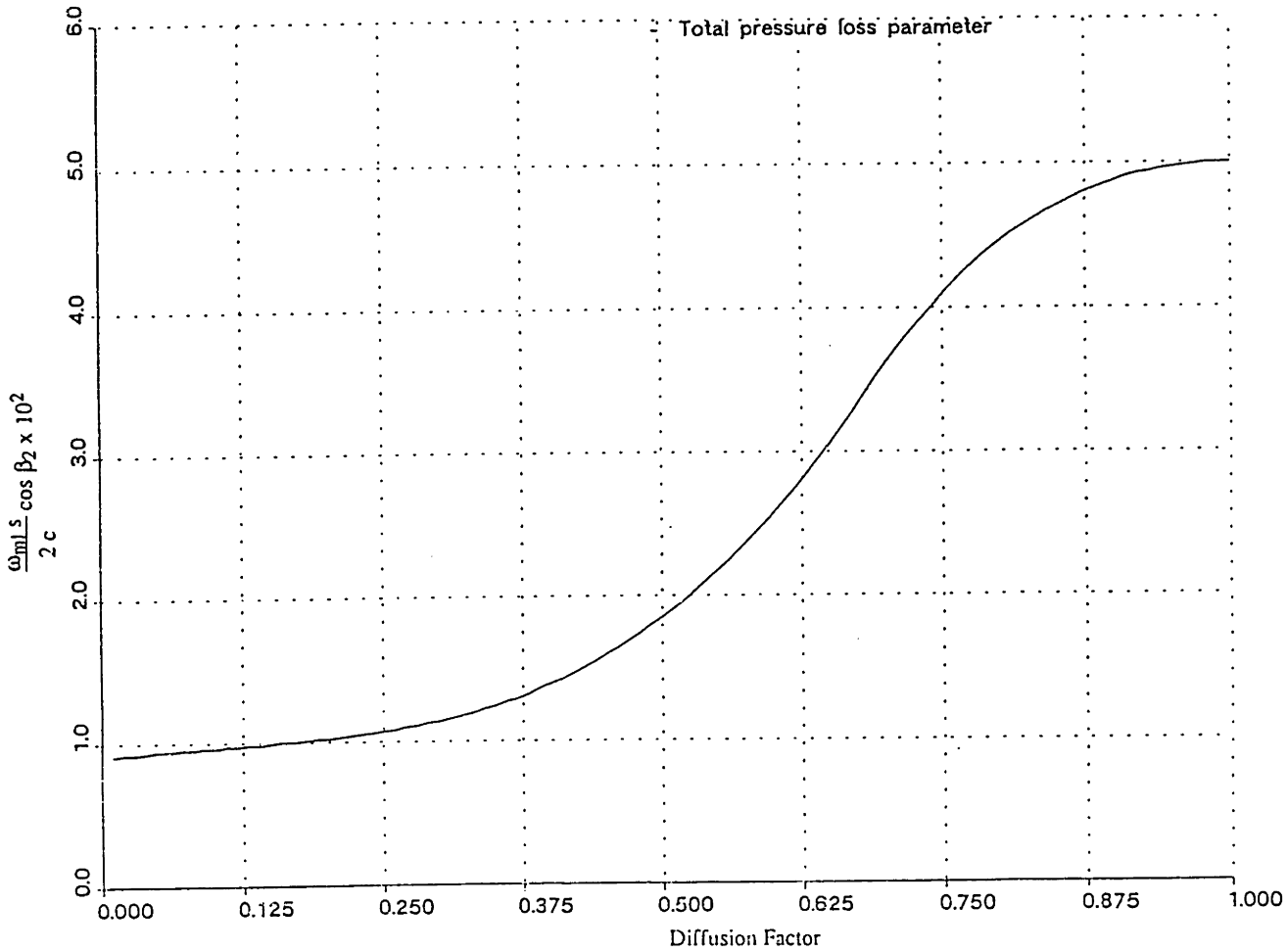

Figure 2.2 Total pressure parameter at minimum-incidence angle as a function of the diffusion factor [30]

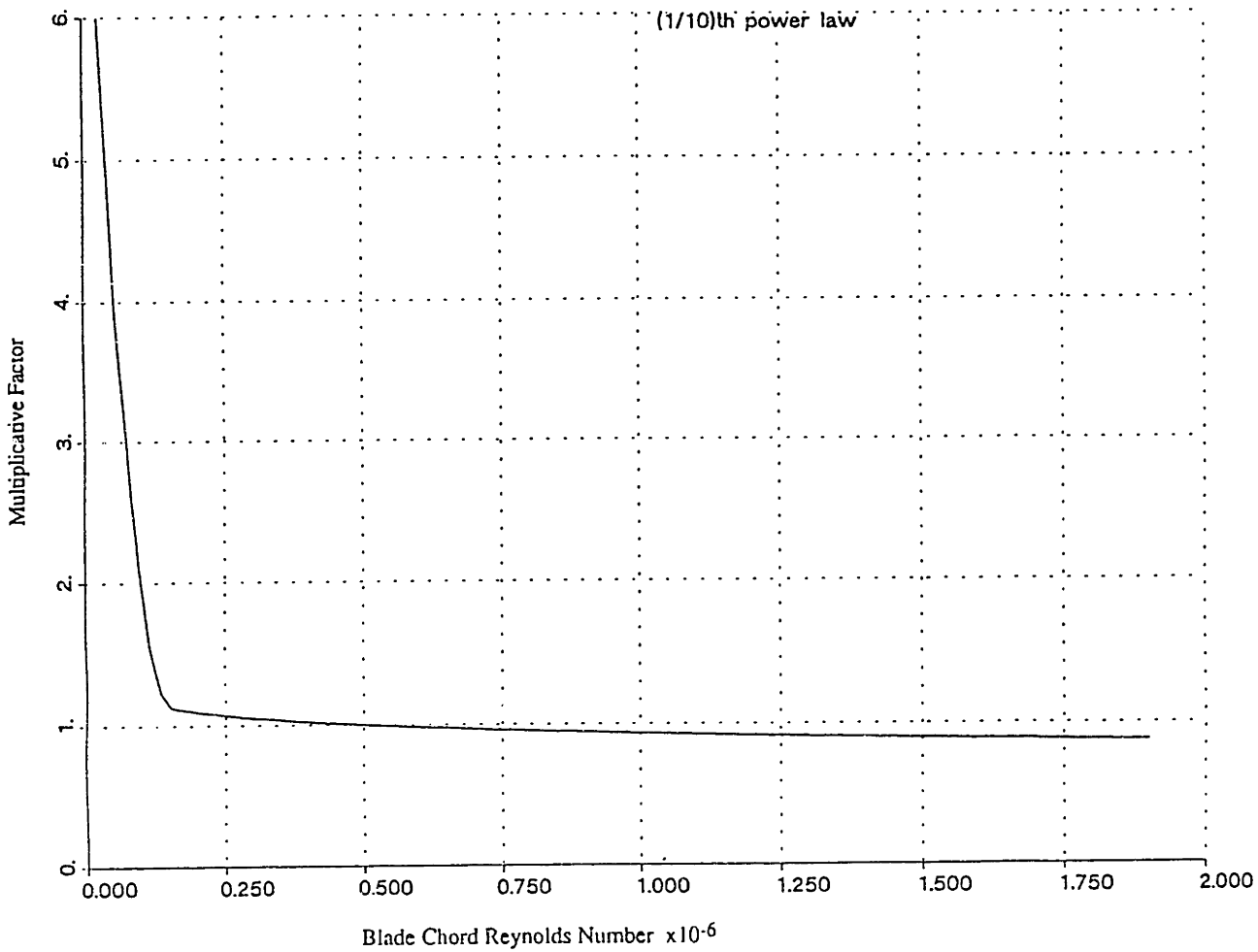

Figure 2.3 Multiplicative factor on the loss coefficient as a function of the blade chord Reynolds Number [30]

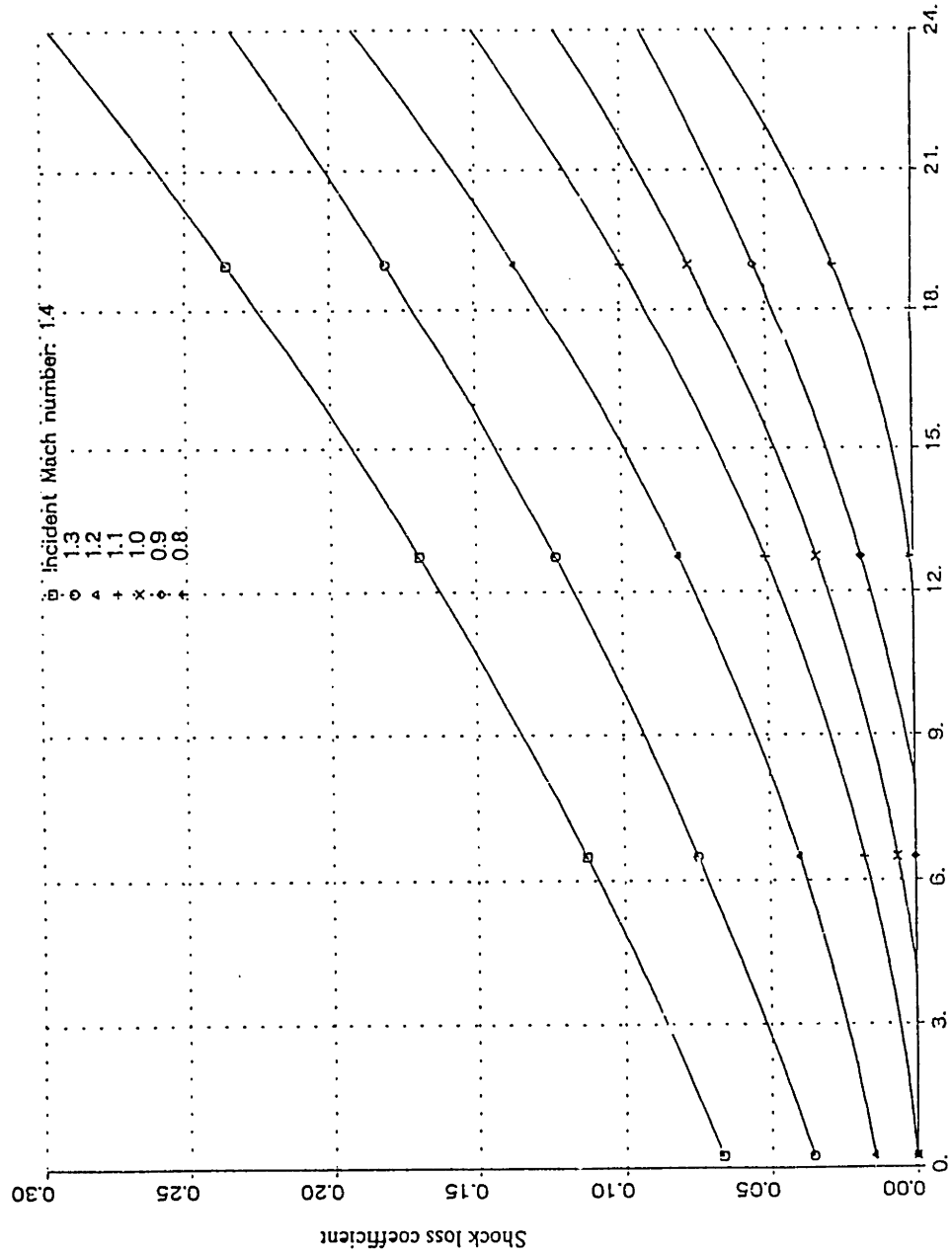

Figure 2.4 Shock losses as a function of the incident Mach number and of the total turning of the flow on the suction surface of the blade up to the throat [30]

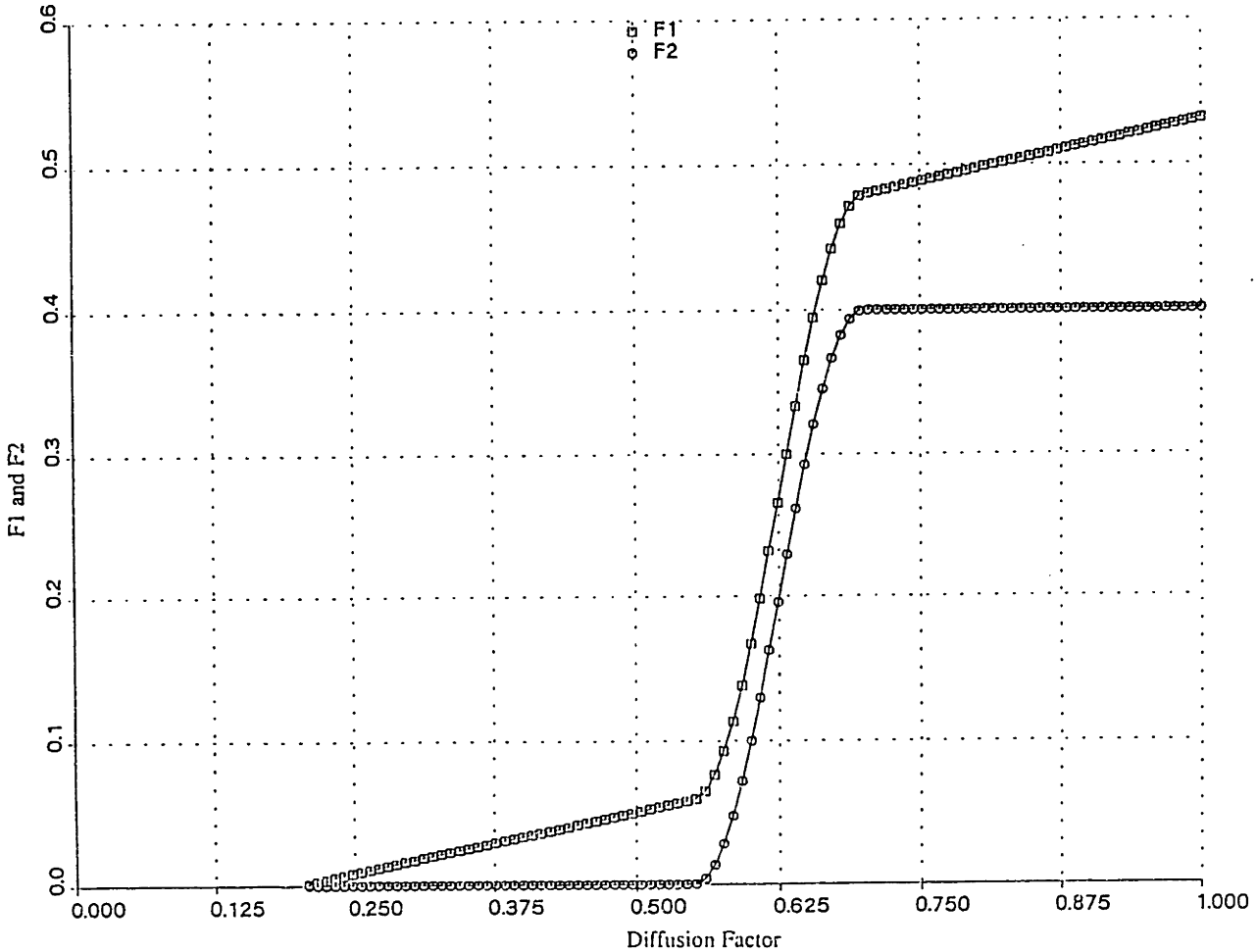

Figure 2.5 Deviation adder applied to Carter's rule as a function of the Diffusion Factor: F1 and F2 [30]

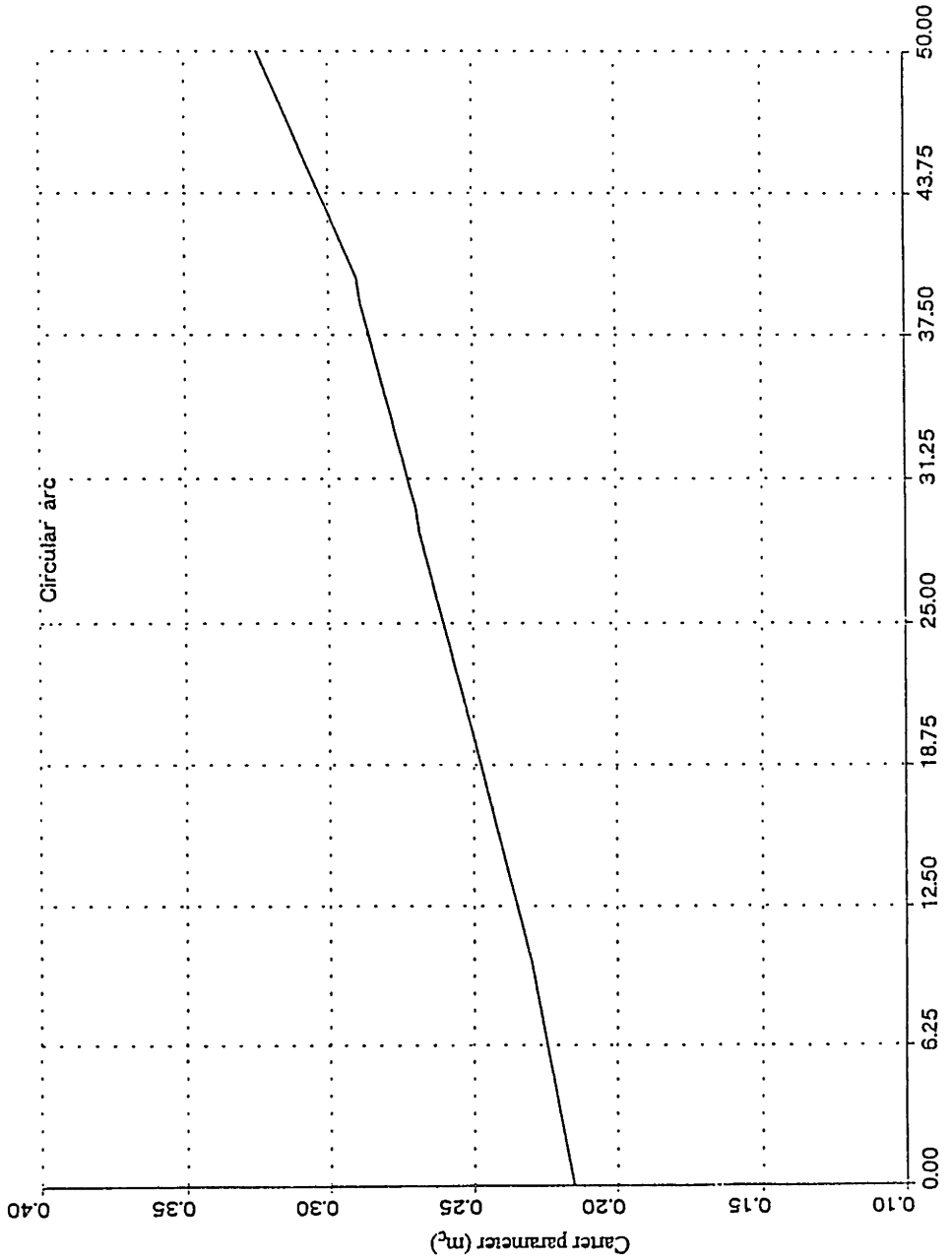

Figure 2.6 Carter parameter as a function of the stagger angle [31,32]

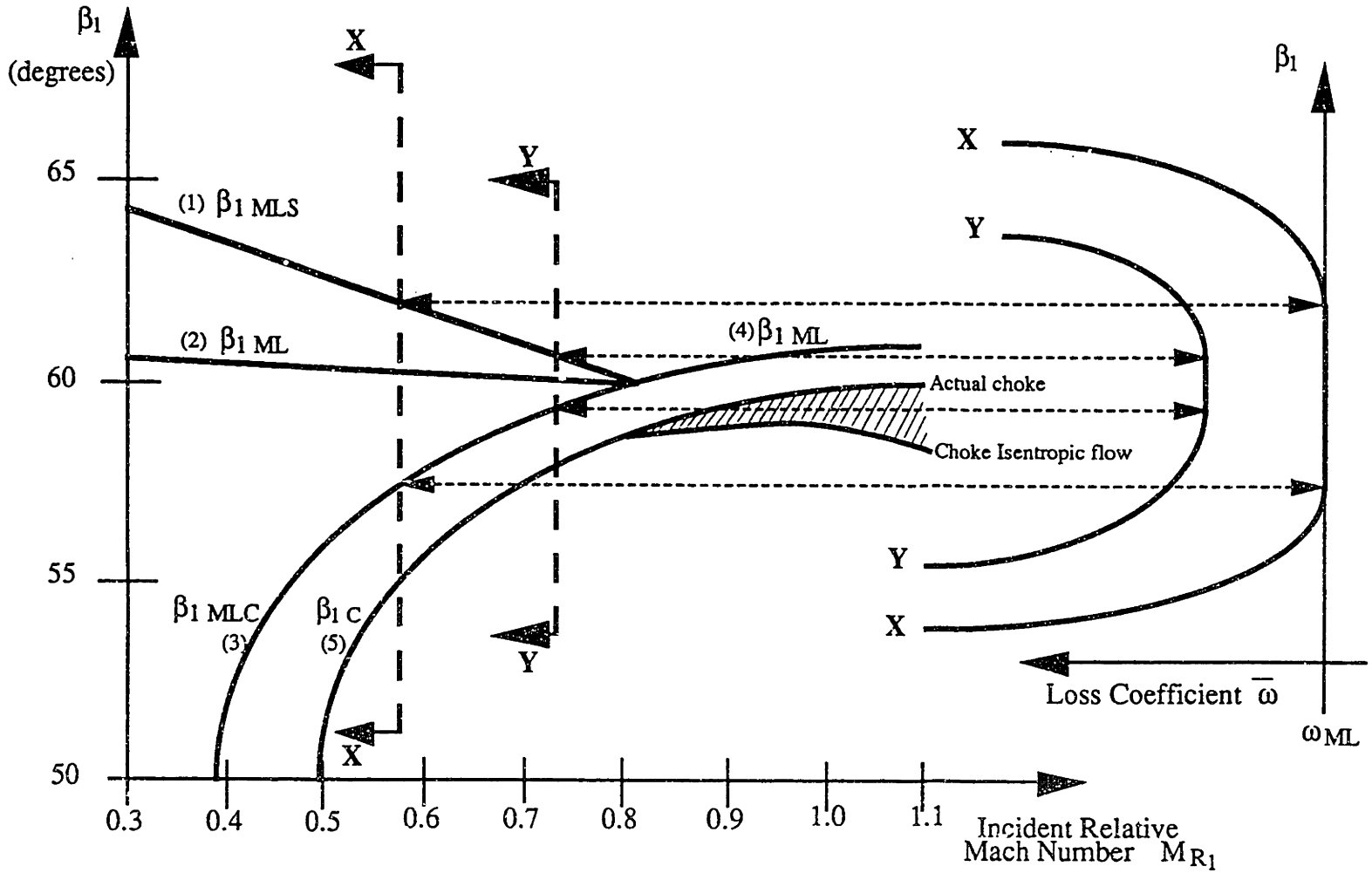

Figure 2.7 Typical Loss bucket

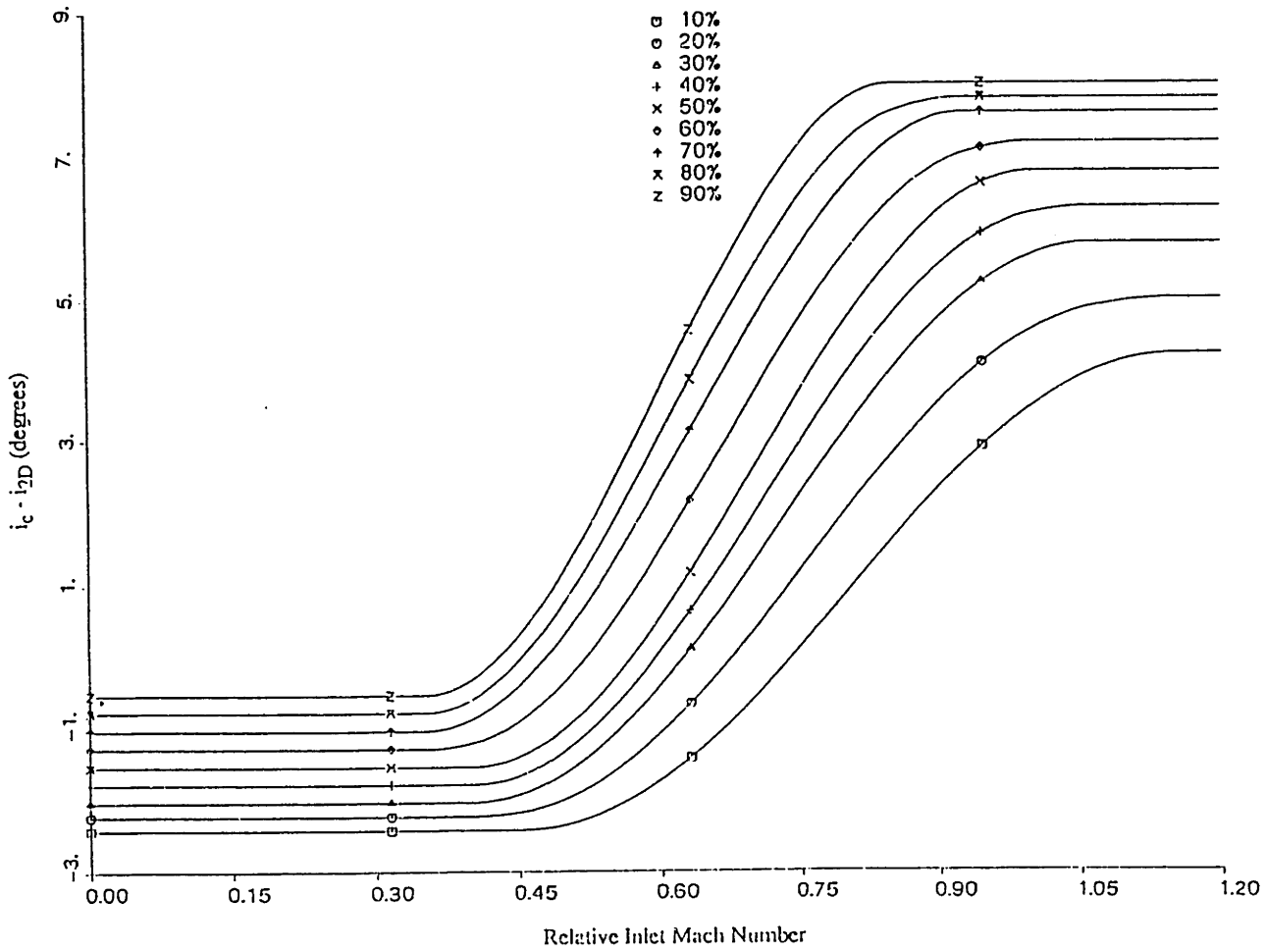

Figure 2.8 Reference incidence angle minus two-dimensional-cascade-rule reference incidence angle as a function of the inlet Mach number and the percent of blade height from compressor tip [31,32]

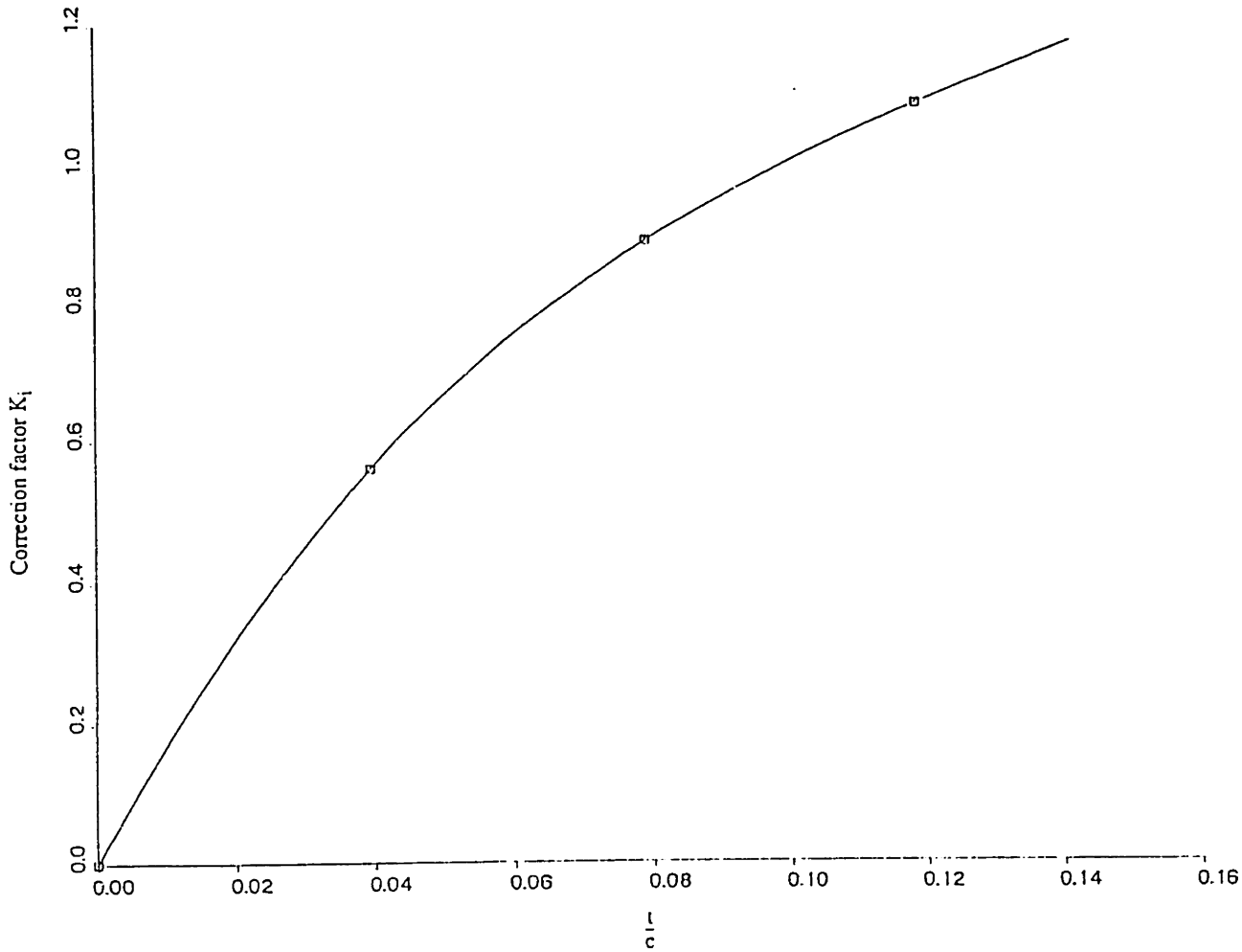

Figure 2.9 Thickness correction for zero-camber reference incidence angle [31,32]

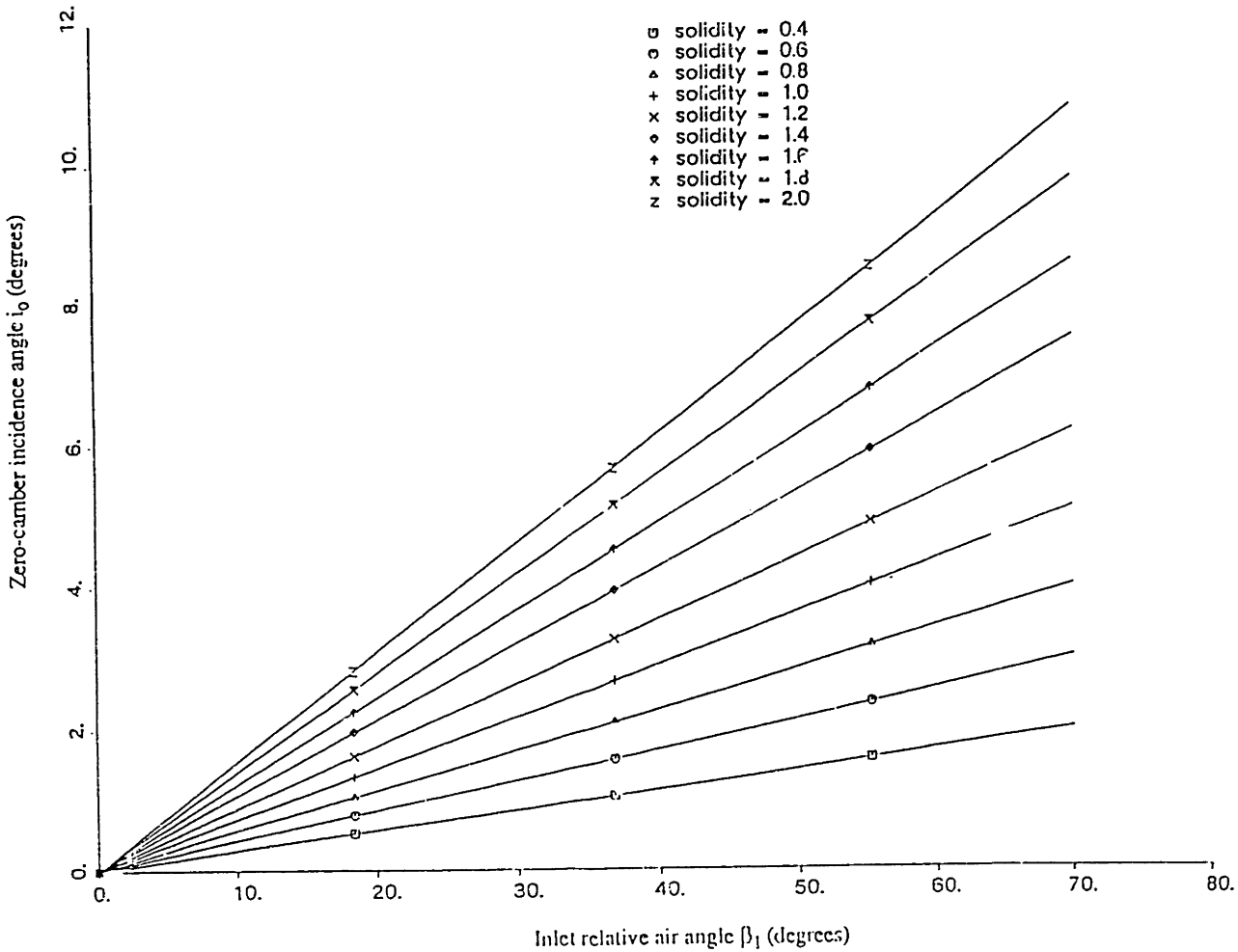

Figure 2.10 Reference minimum-loss incidence angle for zero camber as a function of the inlet relative air angle and the solidity [31,32]

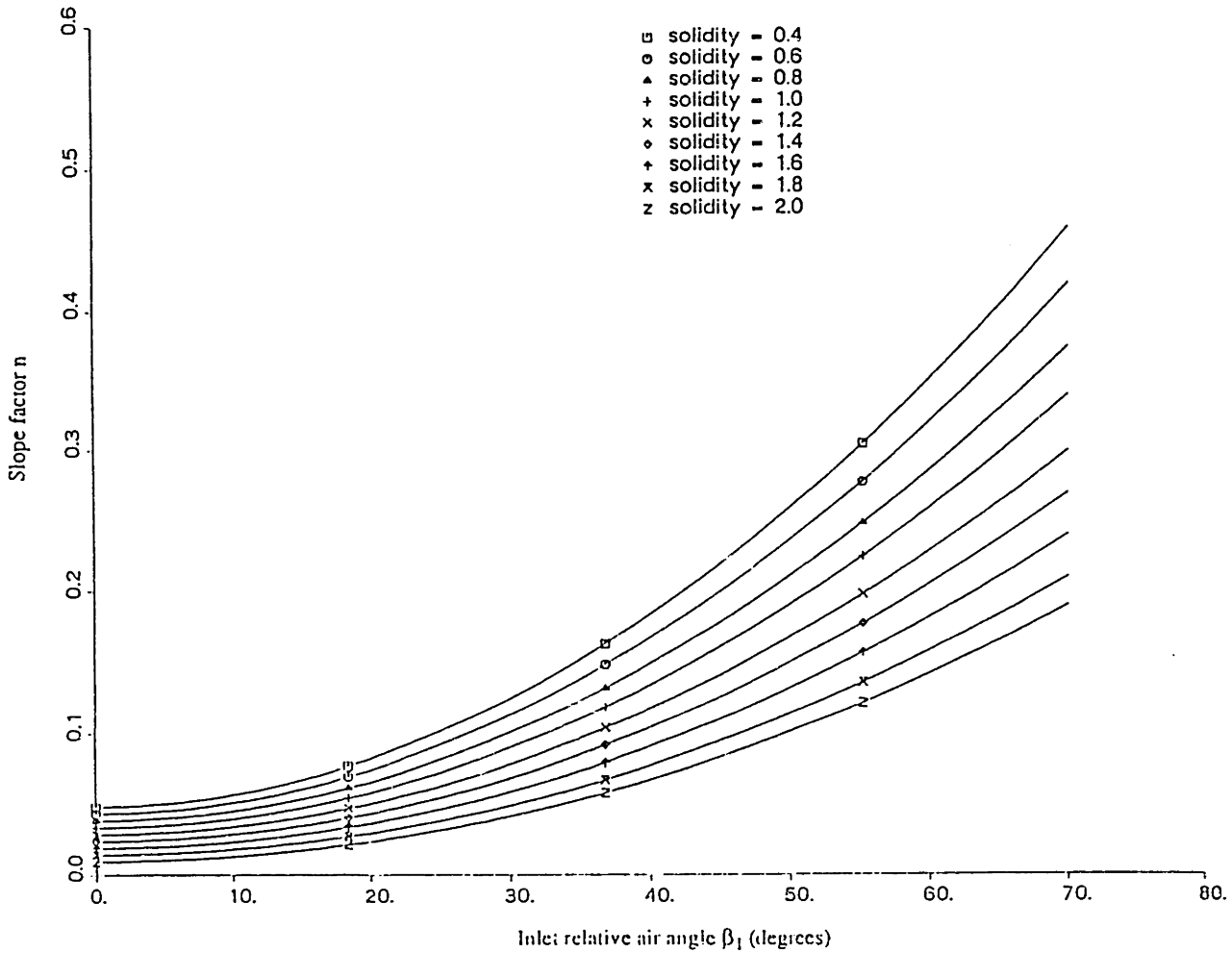

Figure 2.11 Reference minimum-loss incidence angle slope factor as a function of the inlet relative air angle and the solidity [31,32]

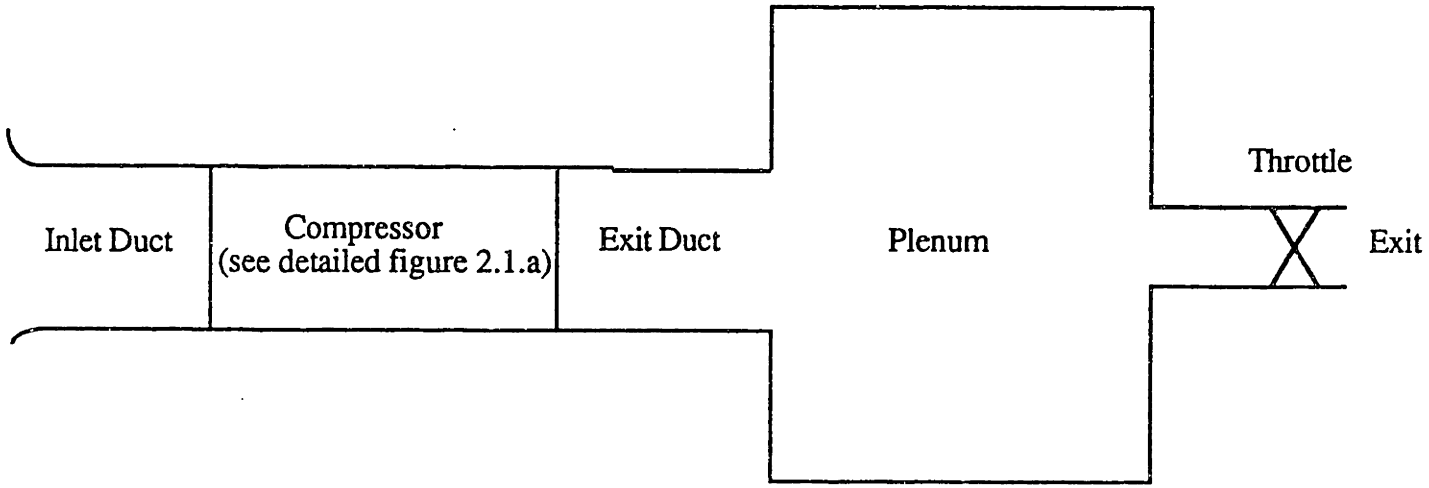

Figure 3.1 Compression System Model

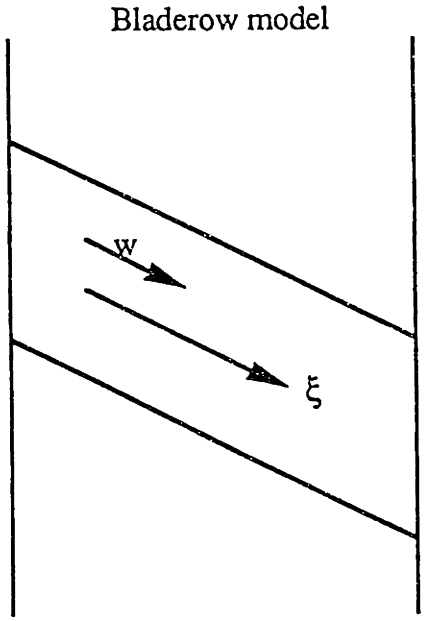

Figure 3.2 Blade row model

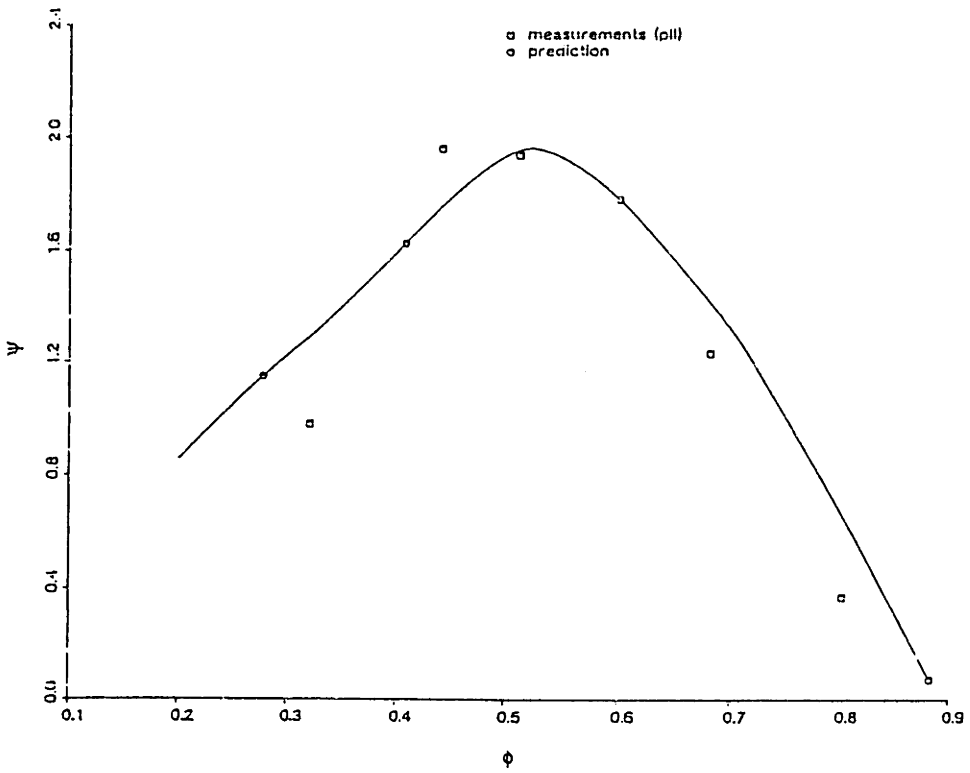

Figure 4.1.a MIT 3 stage compressor (build 2) Total to static pressure characteristic

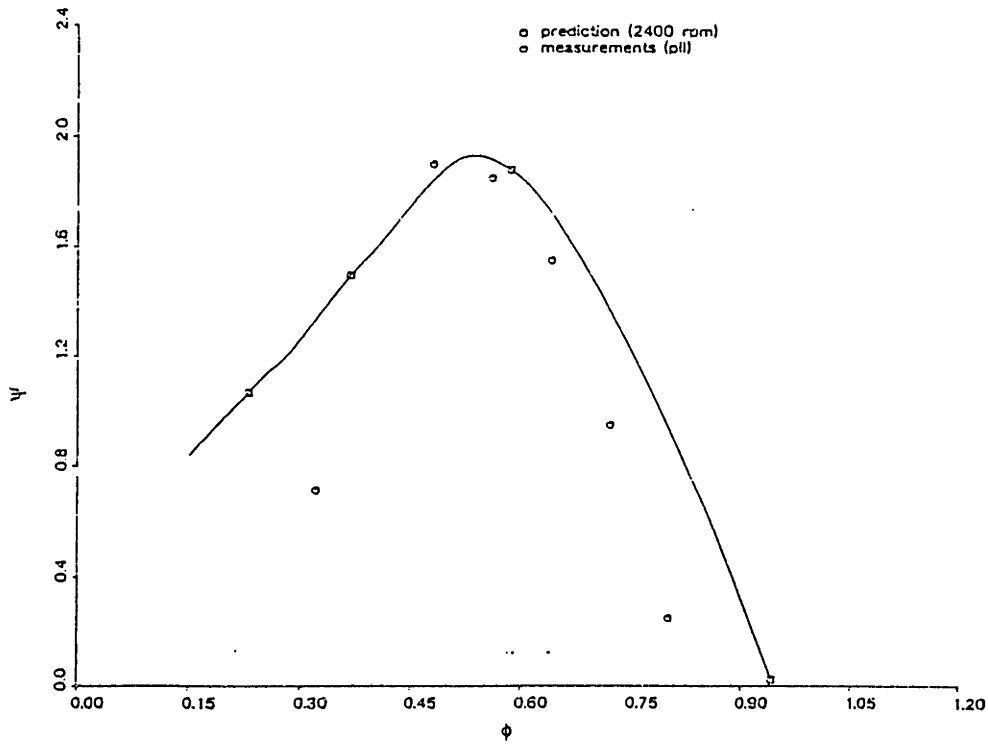

Figure 4.1.b MIT 3 stage compressor (build 3) Total to static pressure characteristic

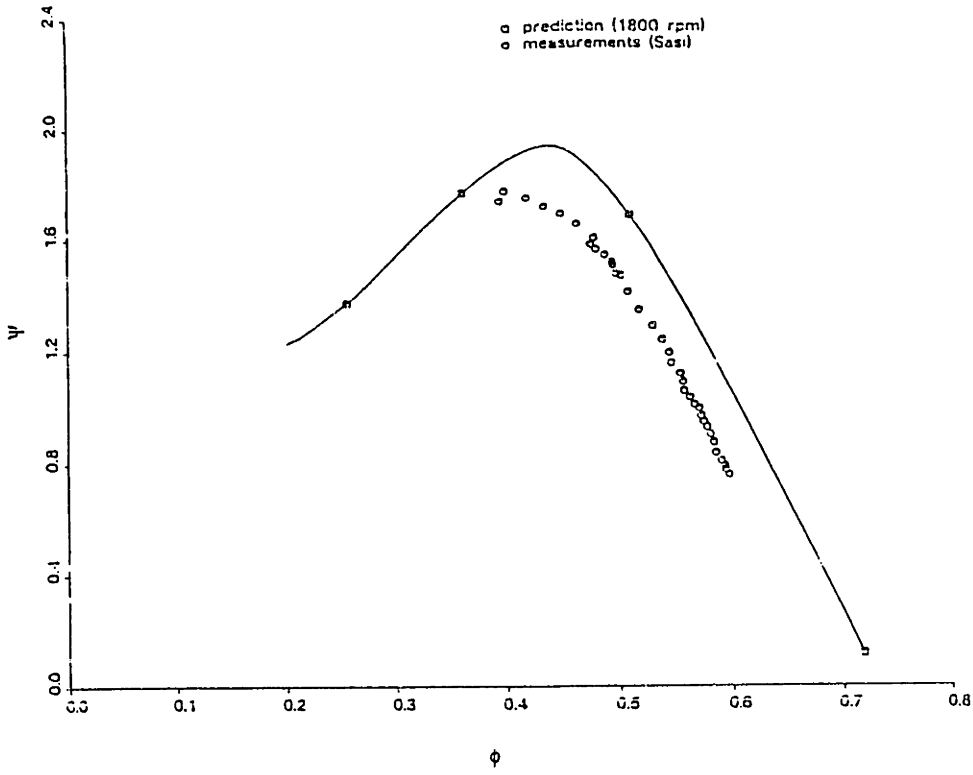

Figure 4.1.c MIT 3 stage compressor (build 4) Total to static pressure characteristic

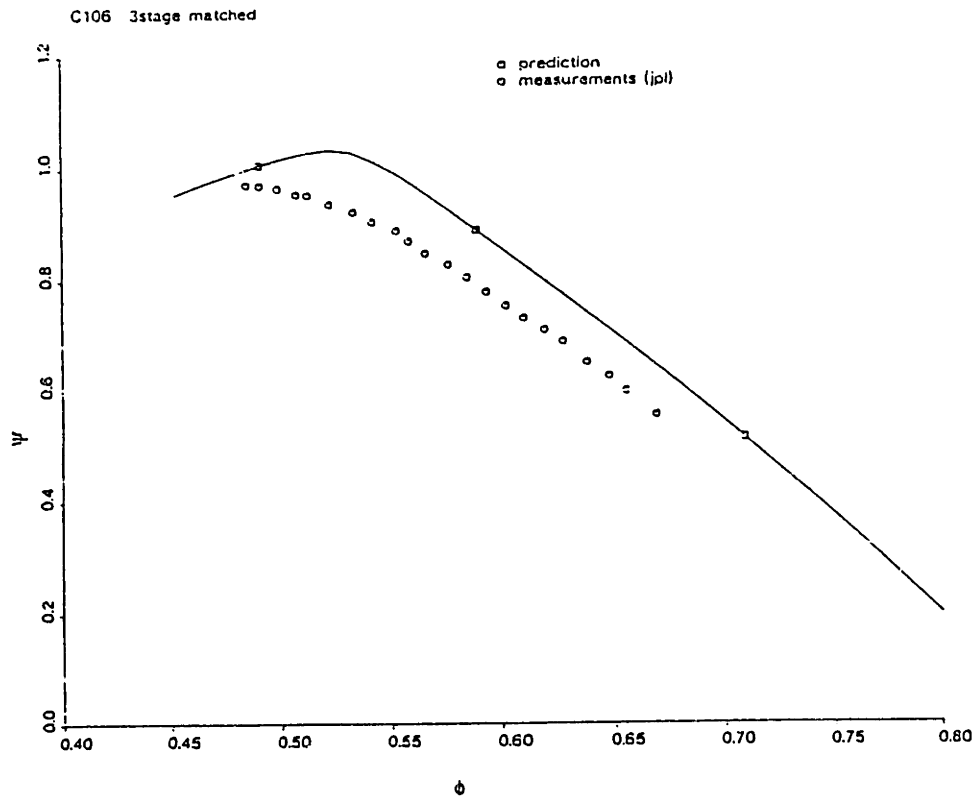

Figure 4.1.d C106 3 stage compressor (matched build) Total to static pressure characteristic

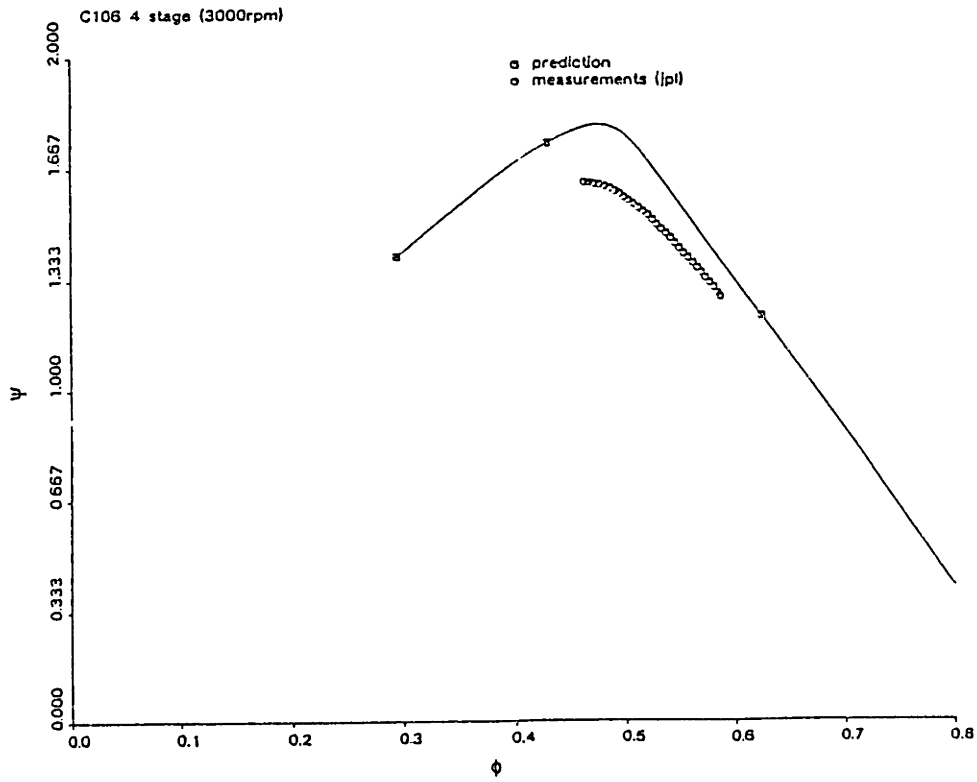

Figure 4.1.e C106 4 stage compressor Total to static pressure characteristic

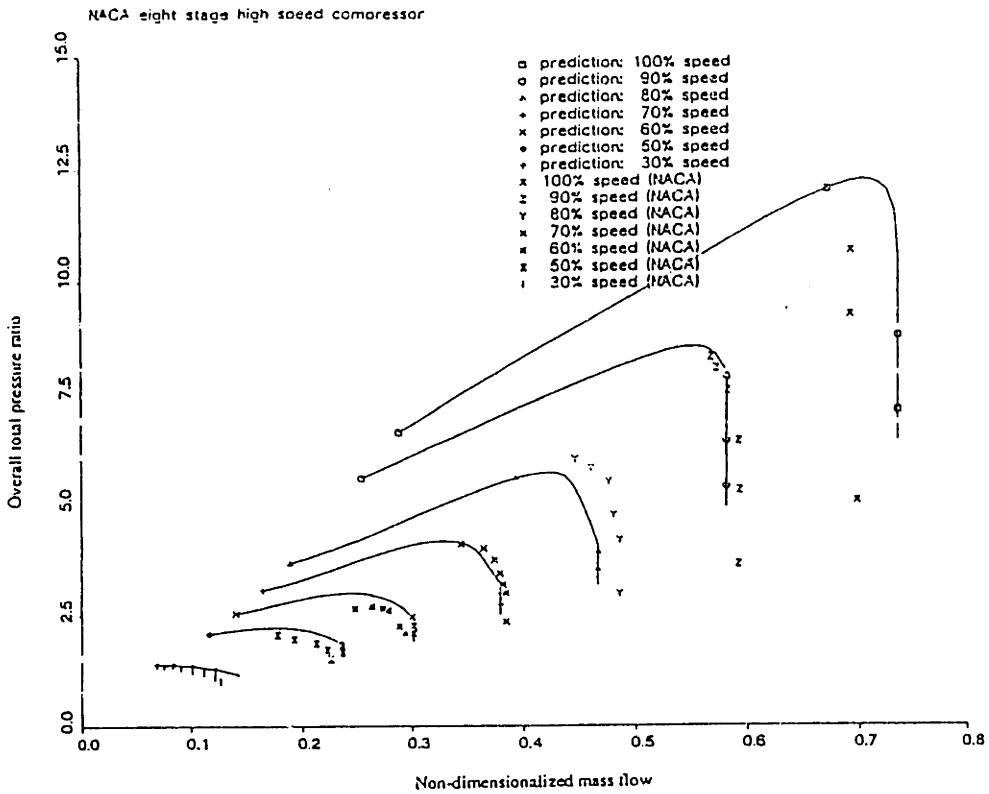

Figure 4.2.a NACA 8 stage compressor pressure ratio characteristic

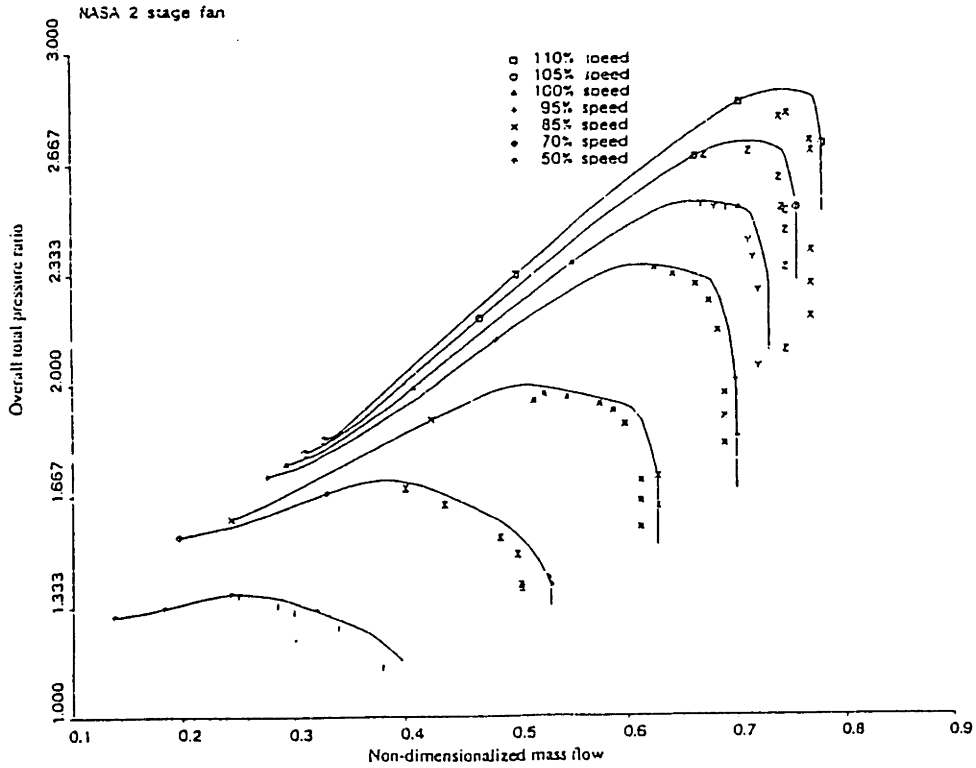

Figure 4.2.b NASA 2 stage fan pressure ratio characteristic

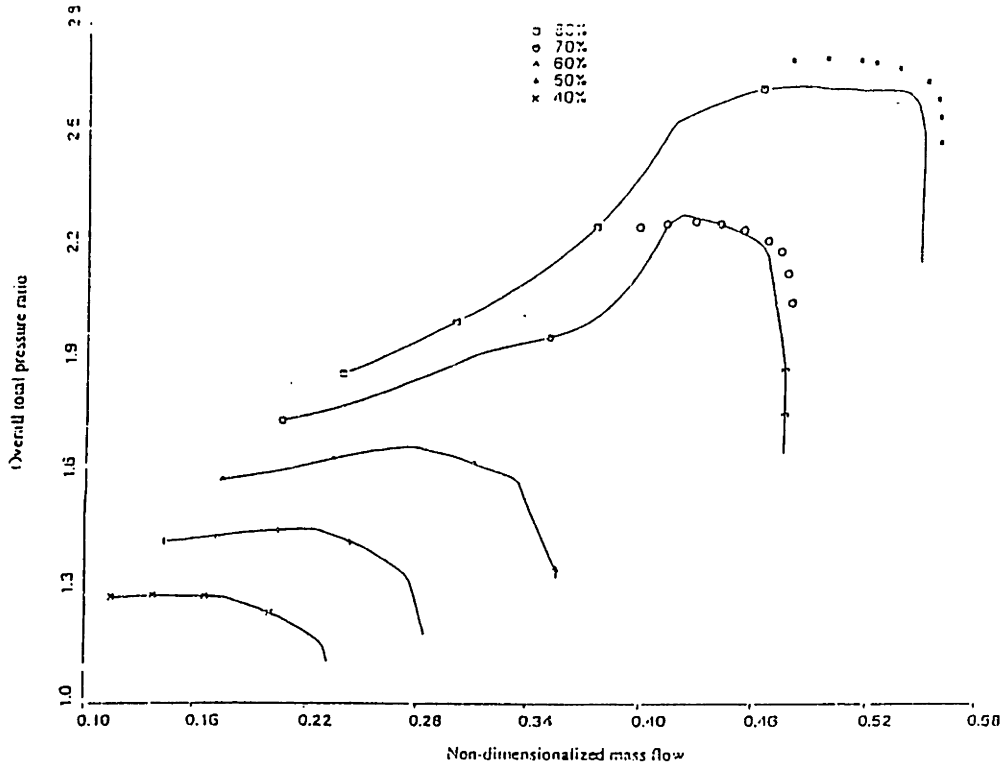

Figure 4.2.c NASA 5 stage compressor (74A design setting) first three stages

Pressure ratio characteristic

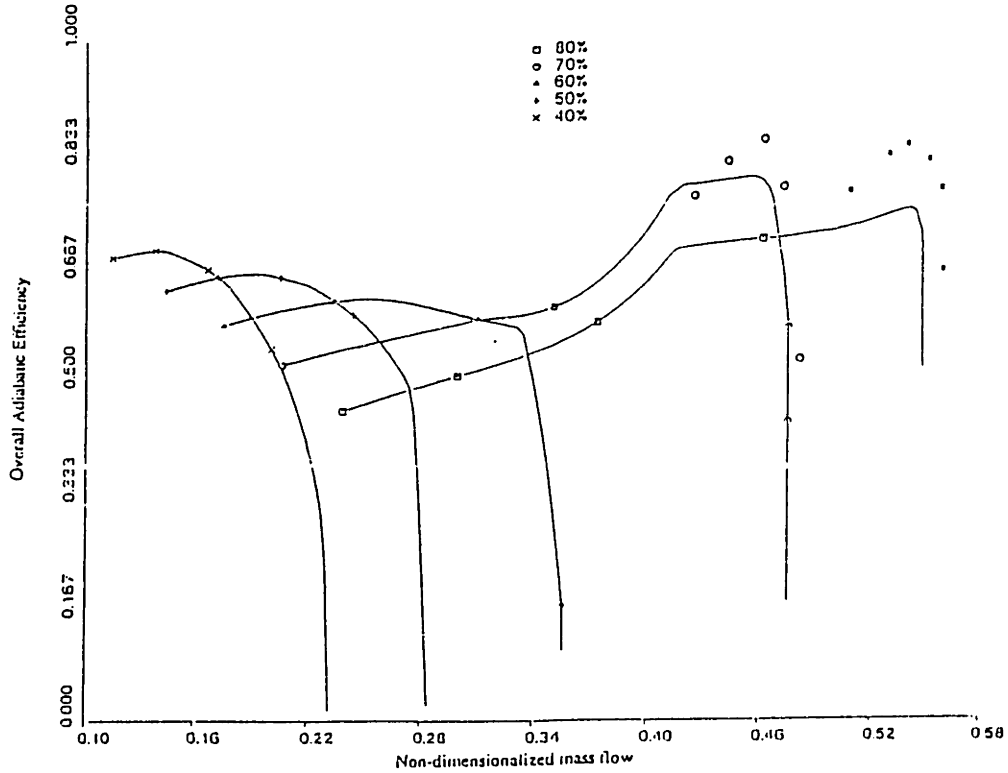

Figure 4.2.d NASA 5 stage compressor (74A design setting) first three stages

Adiabatic efficiency

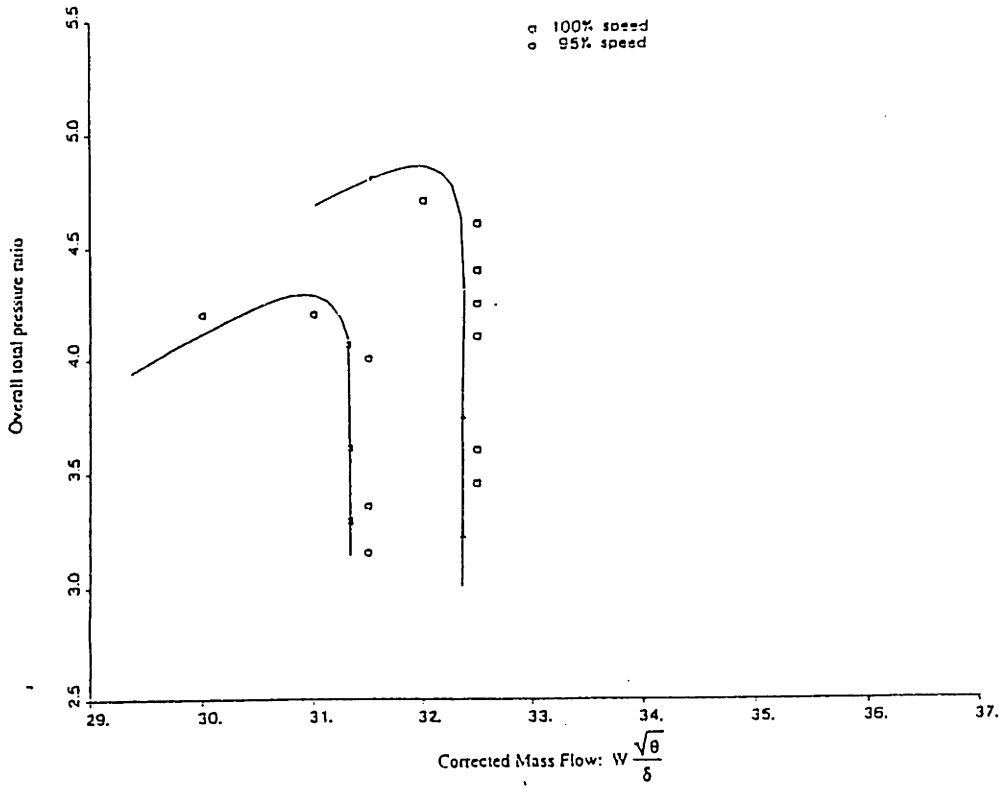

Figure 4.2.e NASA 5 stage compressor (74A design setting) first three stages

Pressure ratio characteristic

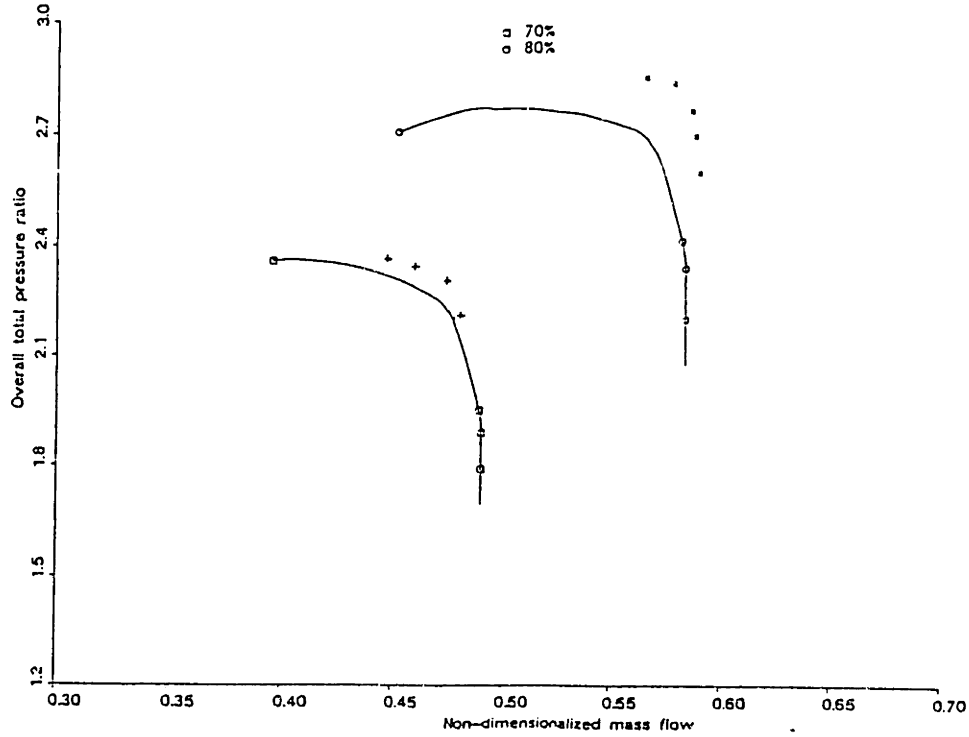

Figure 4.2.f NASA 5 stage compressor (74B design setting) first three stages

Pressure ratio characteristic

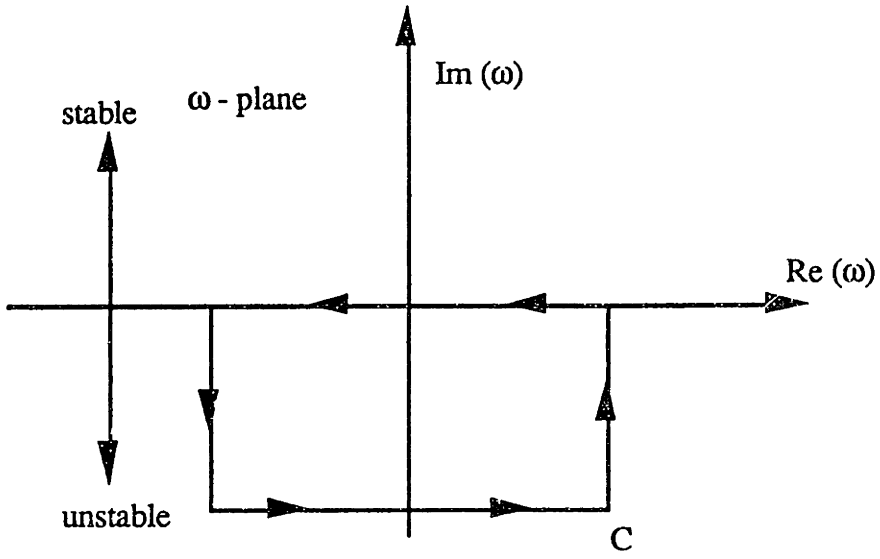

Figure 4.3.a ω - plane (Nyquist Criterion)

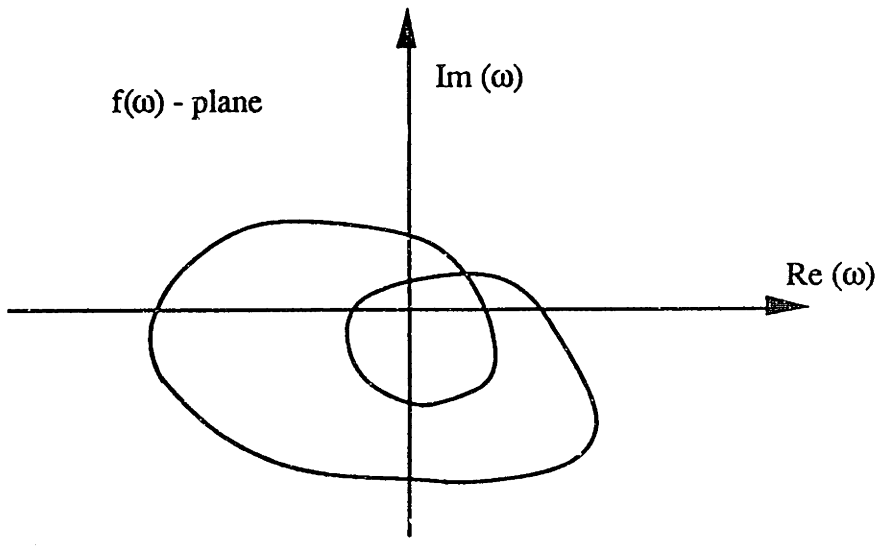

Figure 4.3.b f(ω) -plane (Nyquist Criterion)

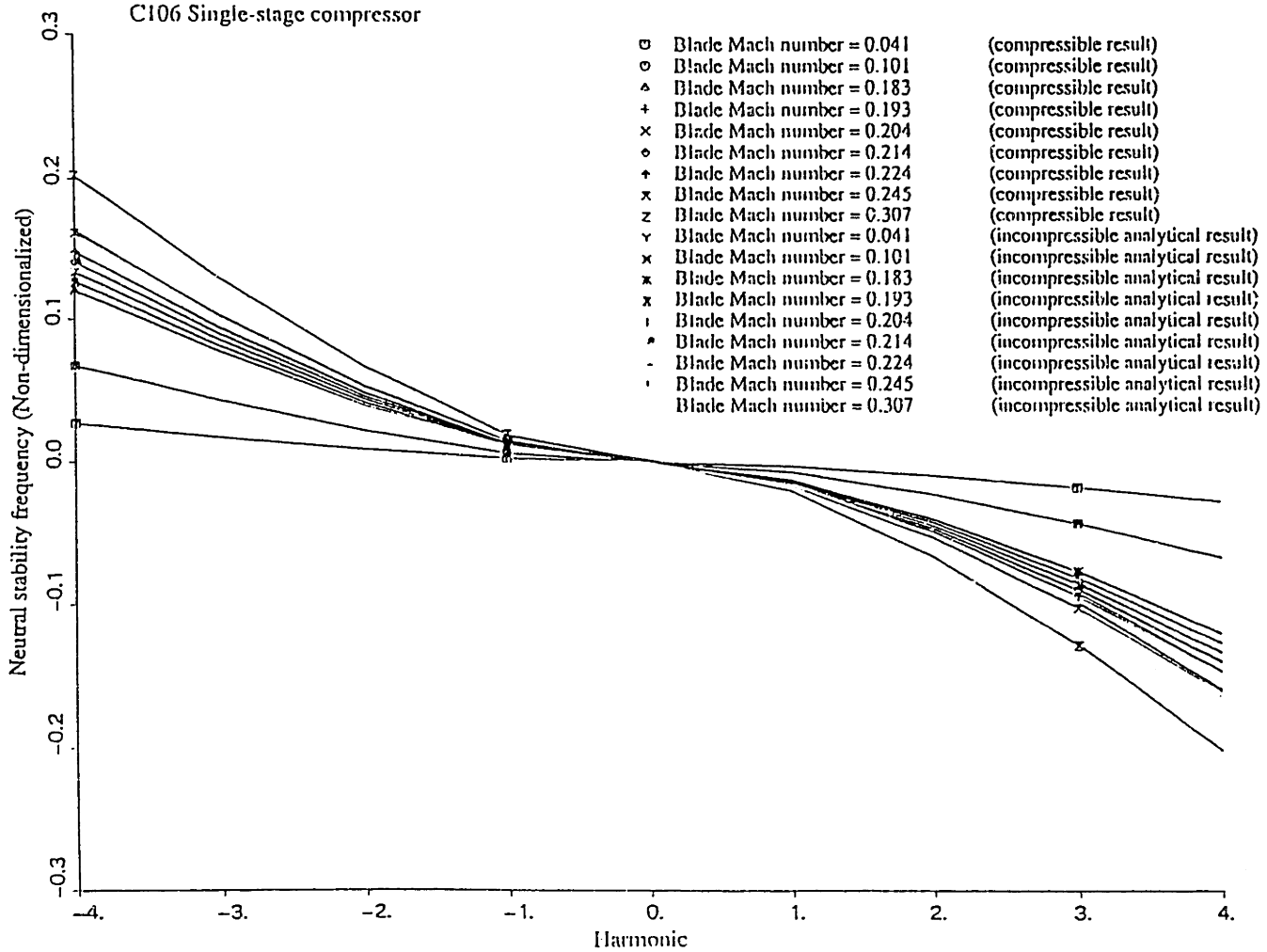

Figure 5.1: Neutral stability frequency results from the compressible and the incompressible models

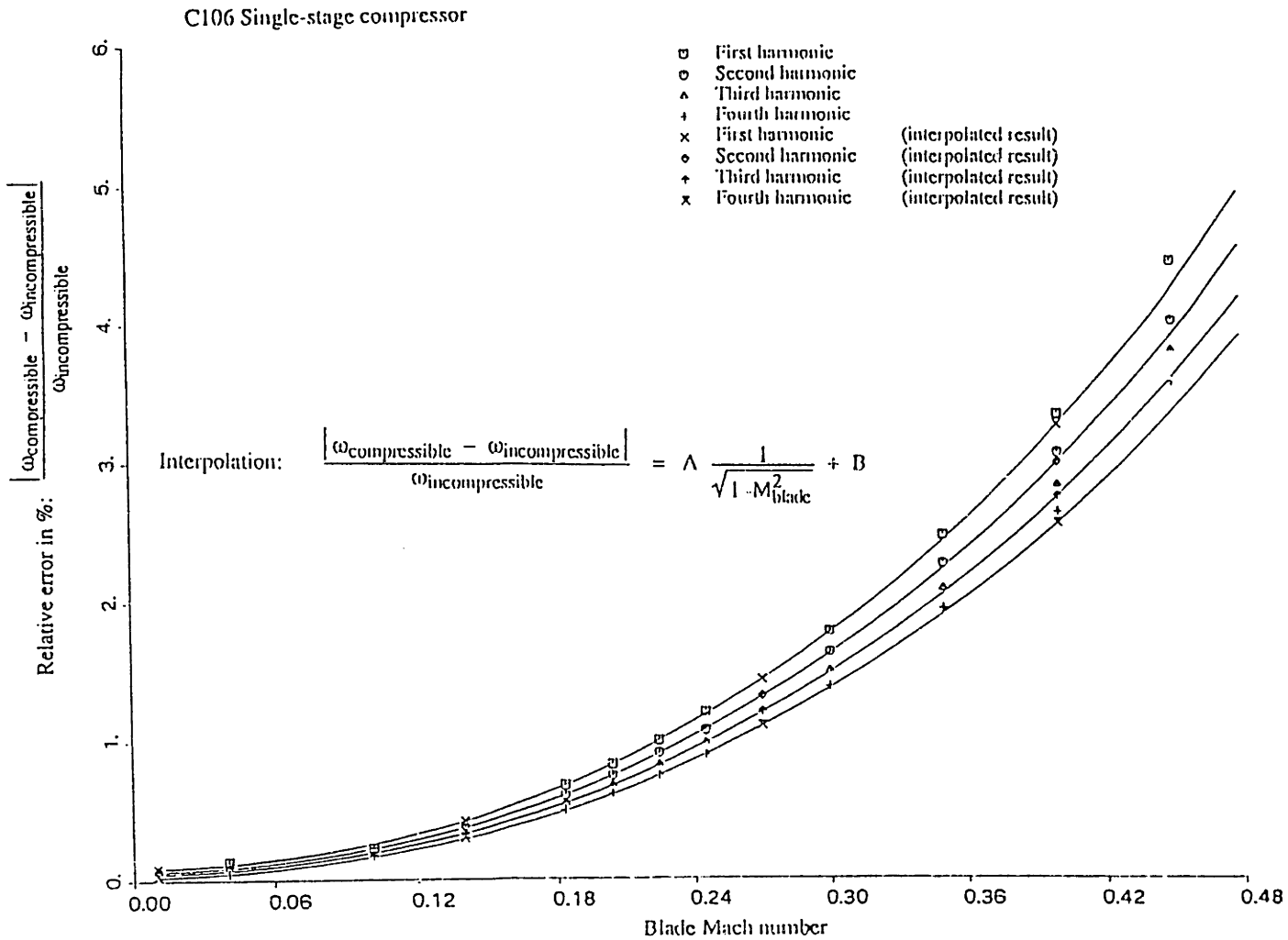

Figure 5.2: Relative error of the compressible and the incompressible models

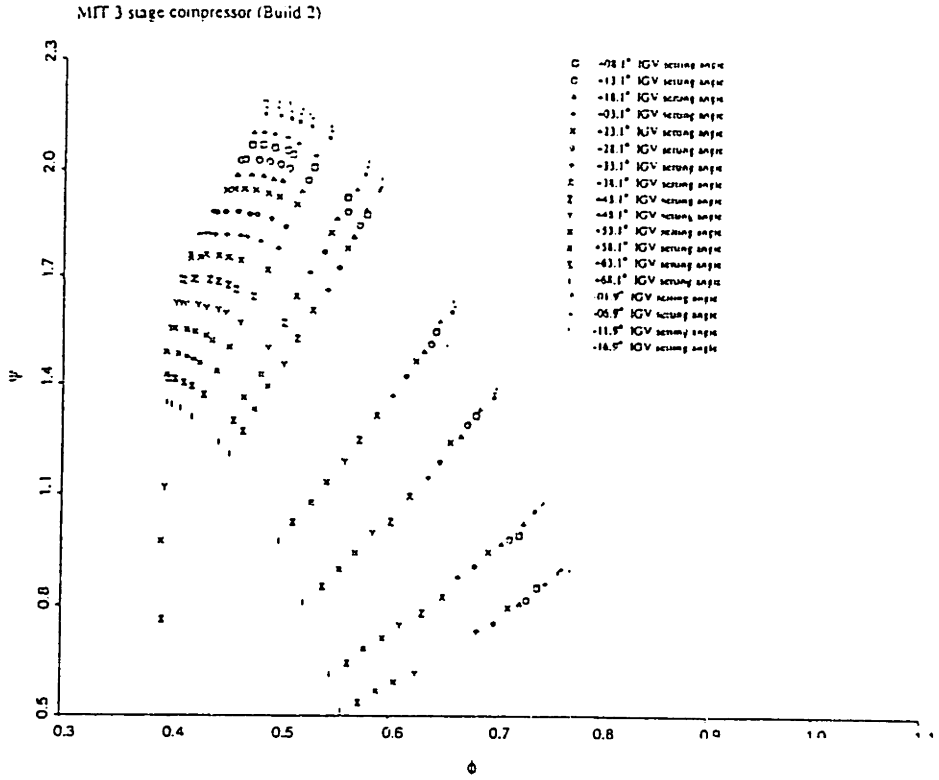

Figure 5.3: MIT 3 stage compressor - Experimental pressure rise characteristics

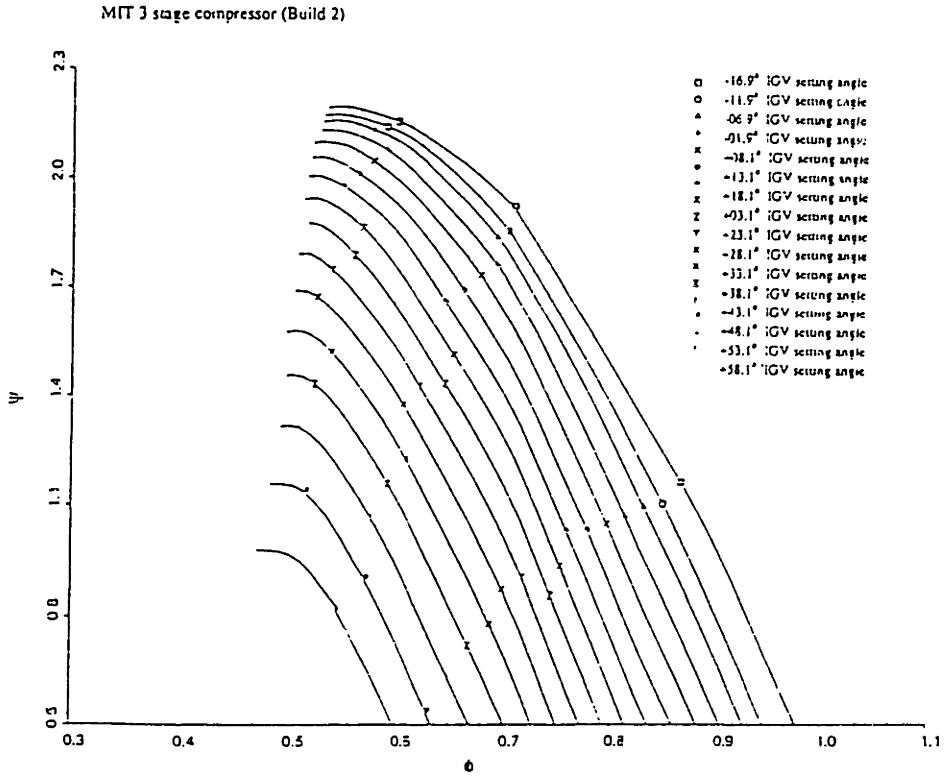

Figure 5.4: MIT 3 stage compressor - Predicted pressure rise characteristics and stall points

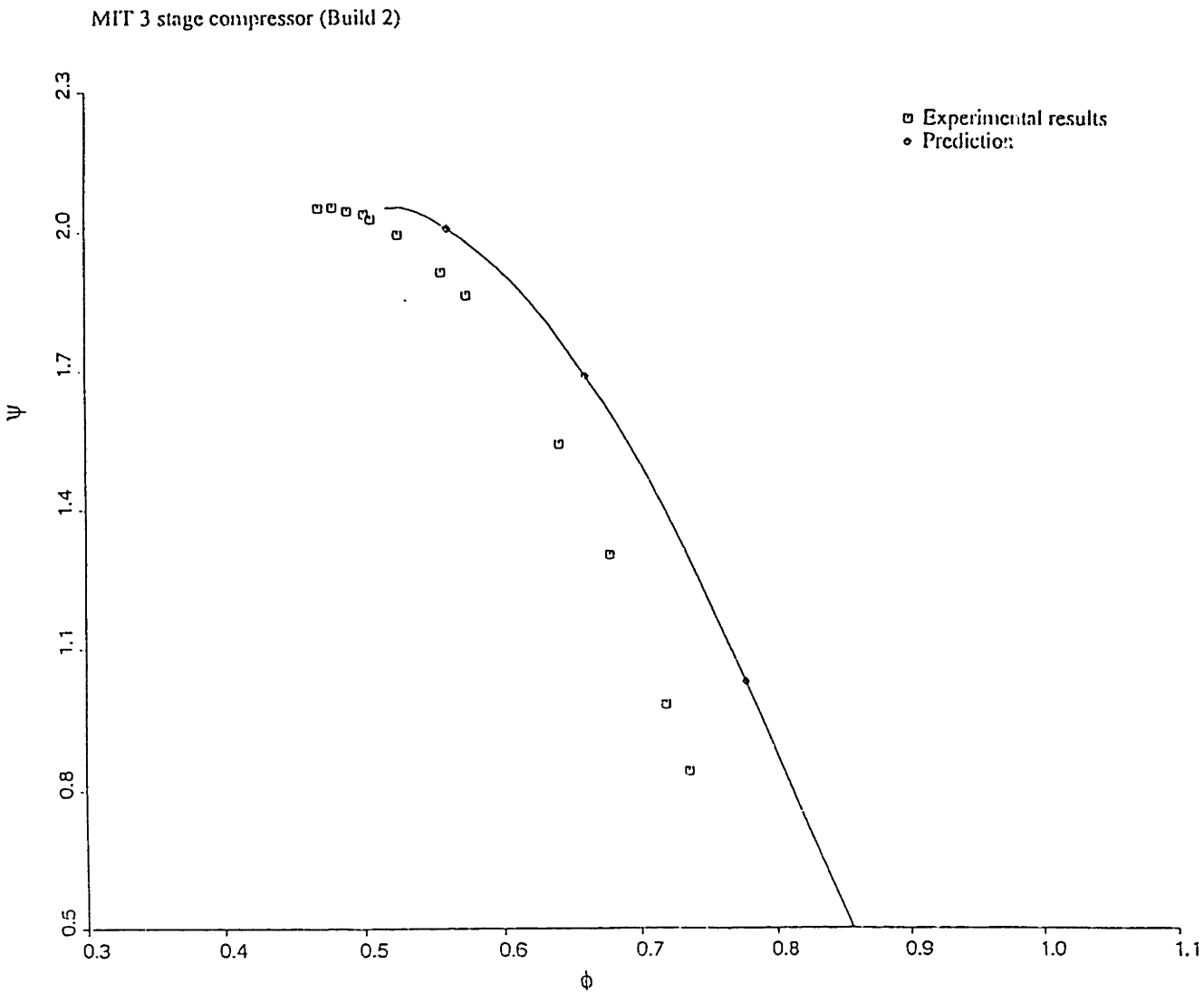

Figure 5.5: MIT 3 stage compressor -

Predicted and measured pressure rise characteristic at IGV= +8.1°

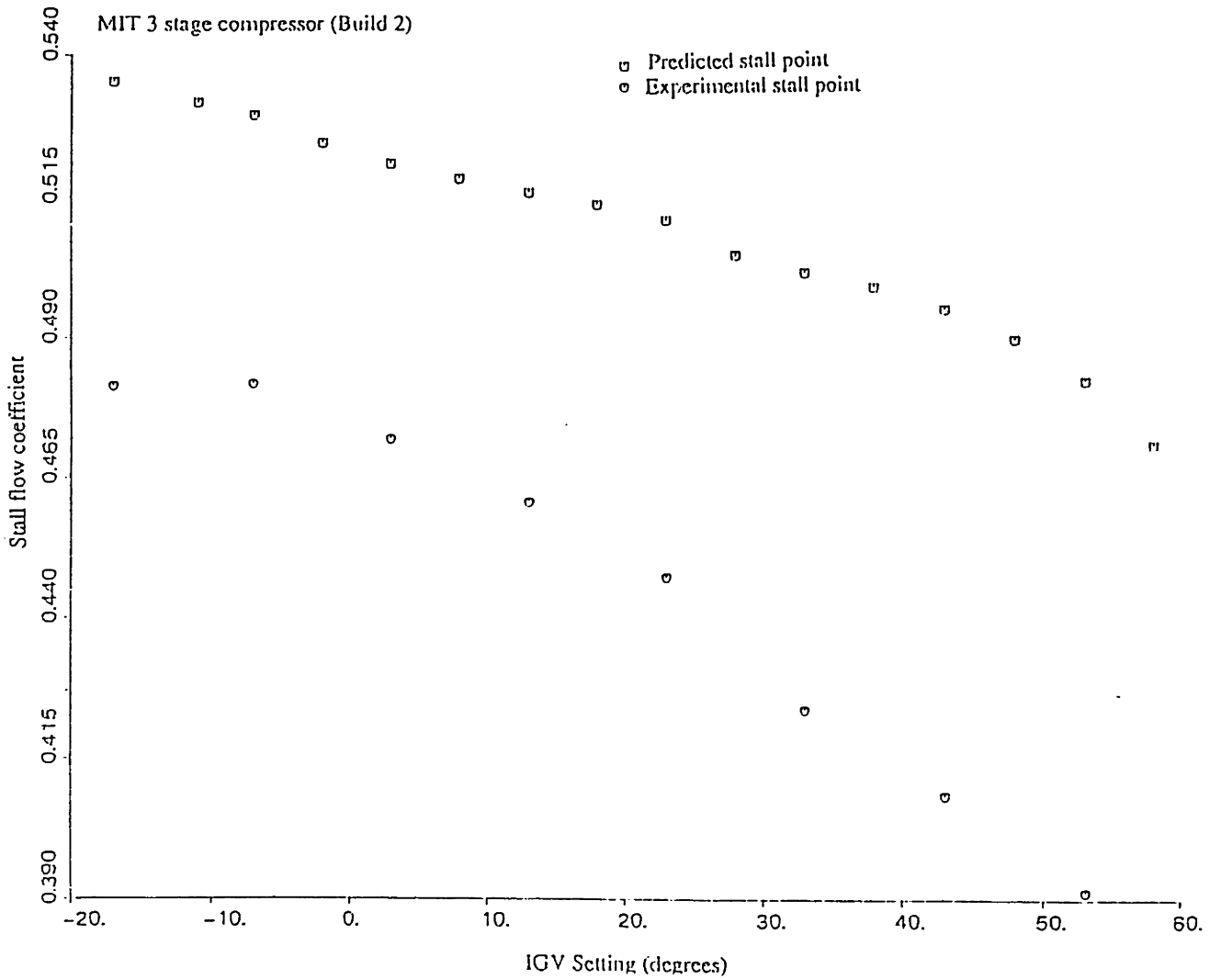

Figure 5.6: MIT 3 stage compressor - Predicted and experimental stall points

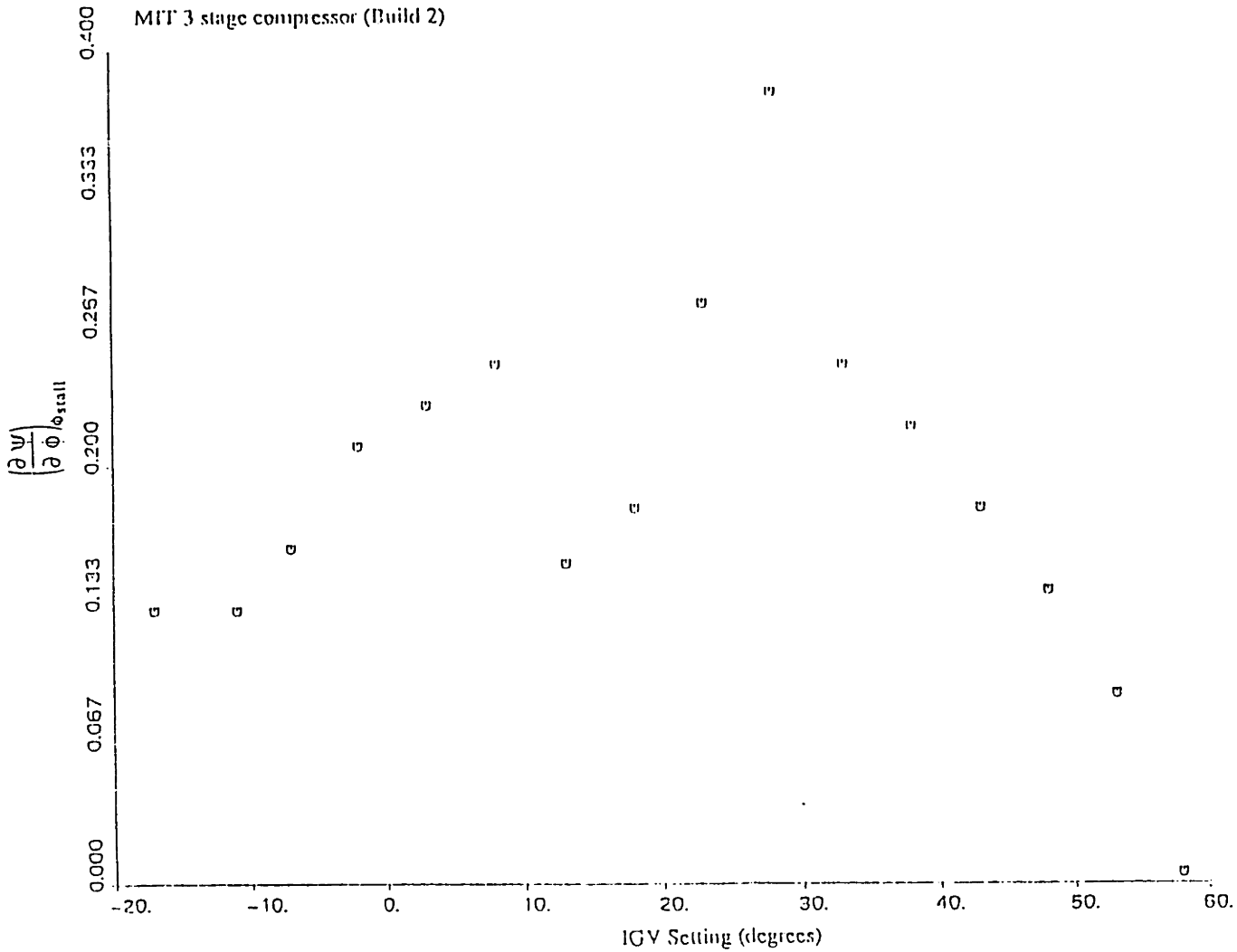

Figure 5.7: MIT 3 stage compressor -

Predicted slopes of the pressure rise characteristic at the predicted stall point

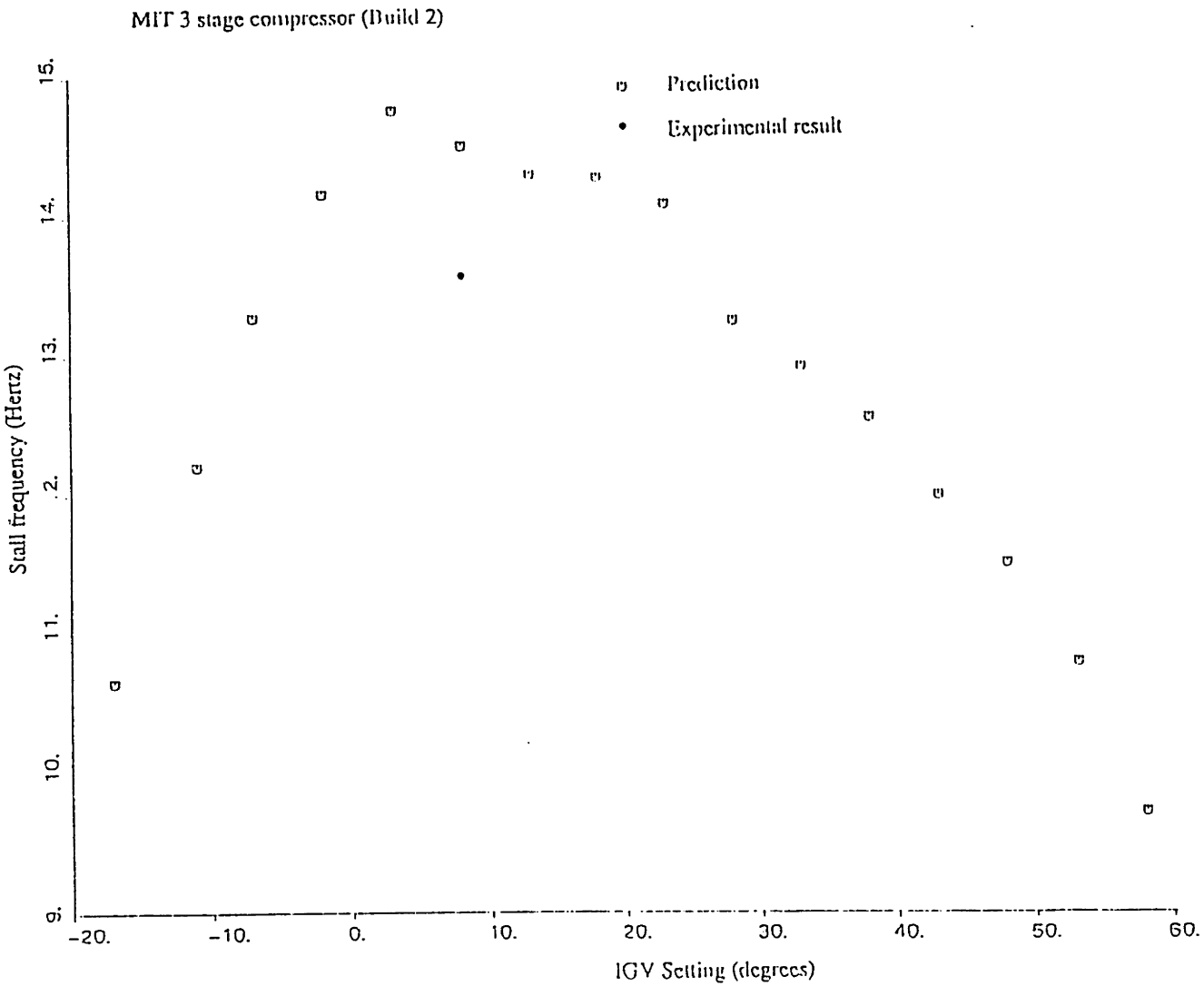

Figure 5.8: MIT 3 stage compressor - Predicted stall frequencies

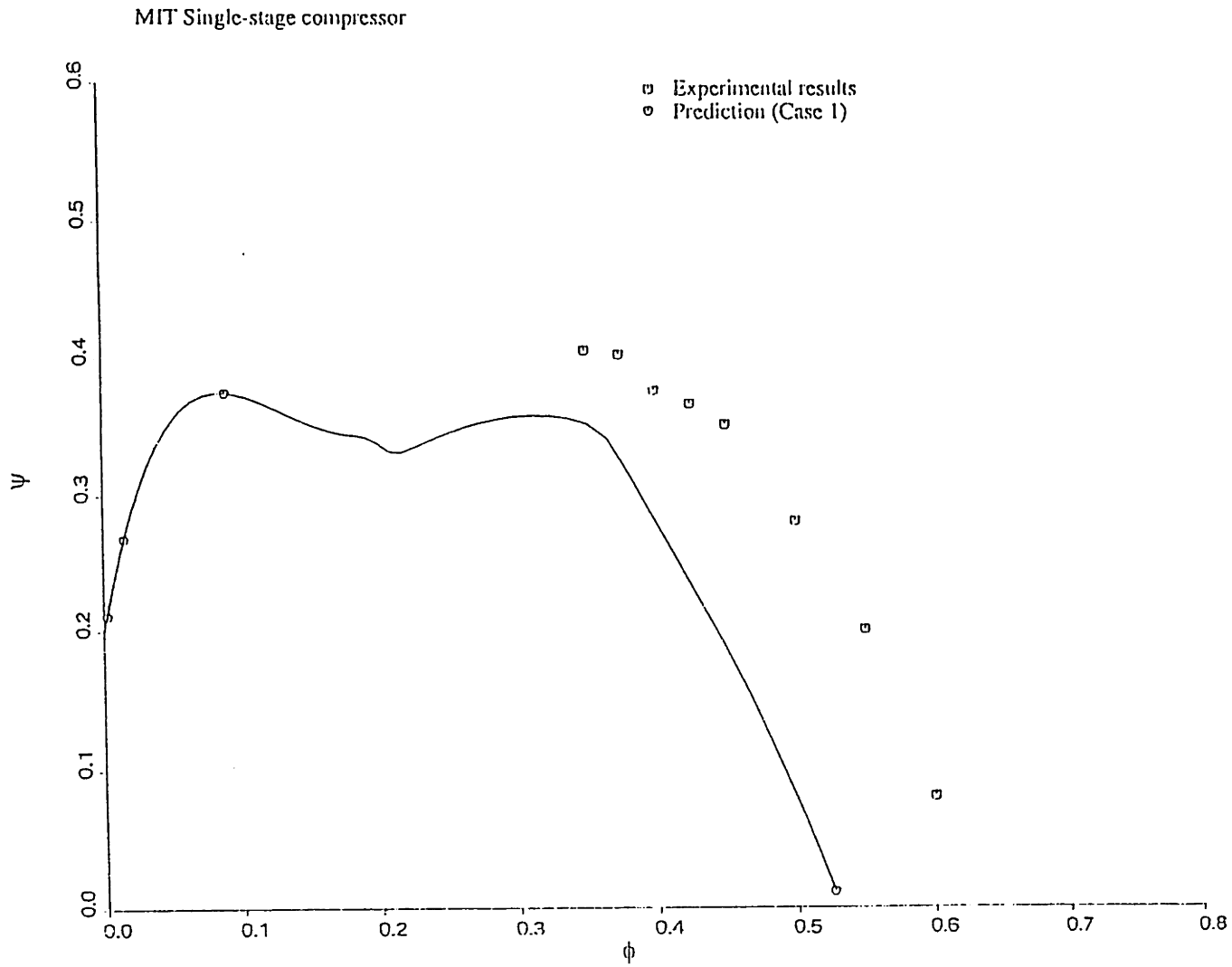

Figure 5.9: MIT Single-stage compressor - Pressure rise characteristic (Case 1)

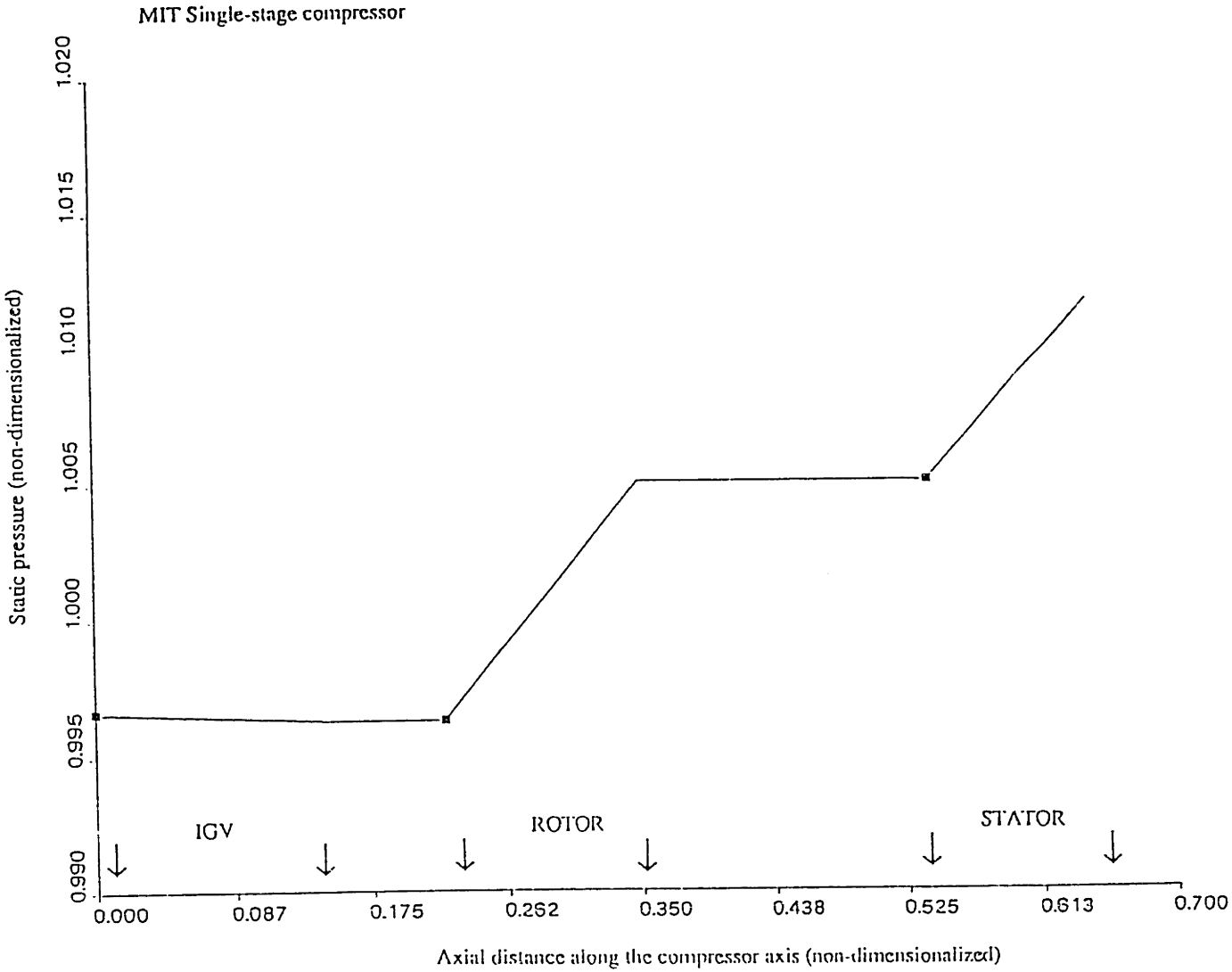

Figure 5.10: MIT Single-stage compressor - Static pressure distribution at neutral stability (Case 1)

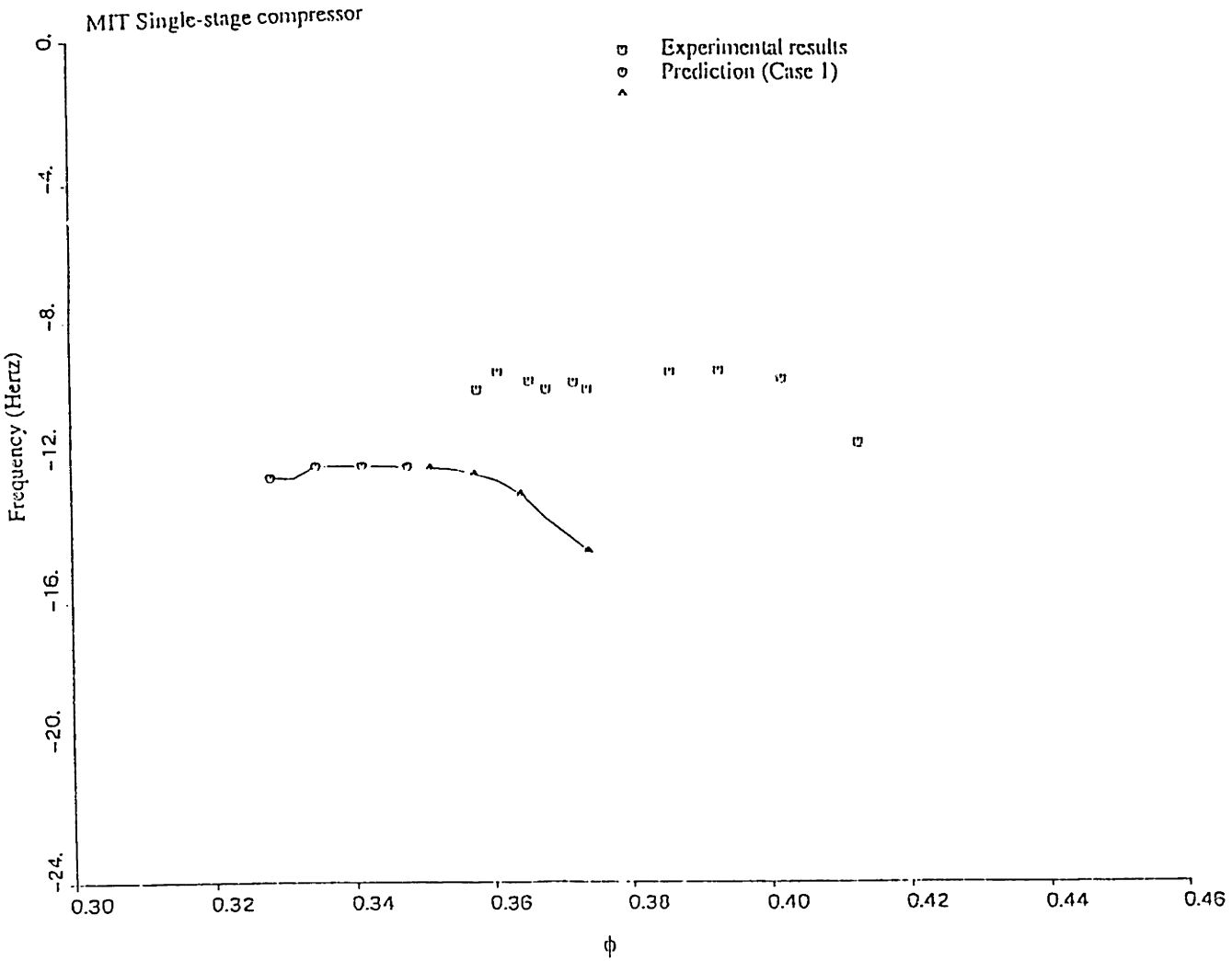

Figure 5.11: MIT Single-stage compressor - Travelling waves frequencies (Case 1)

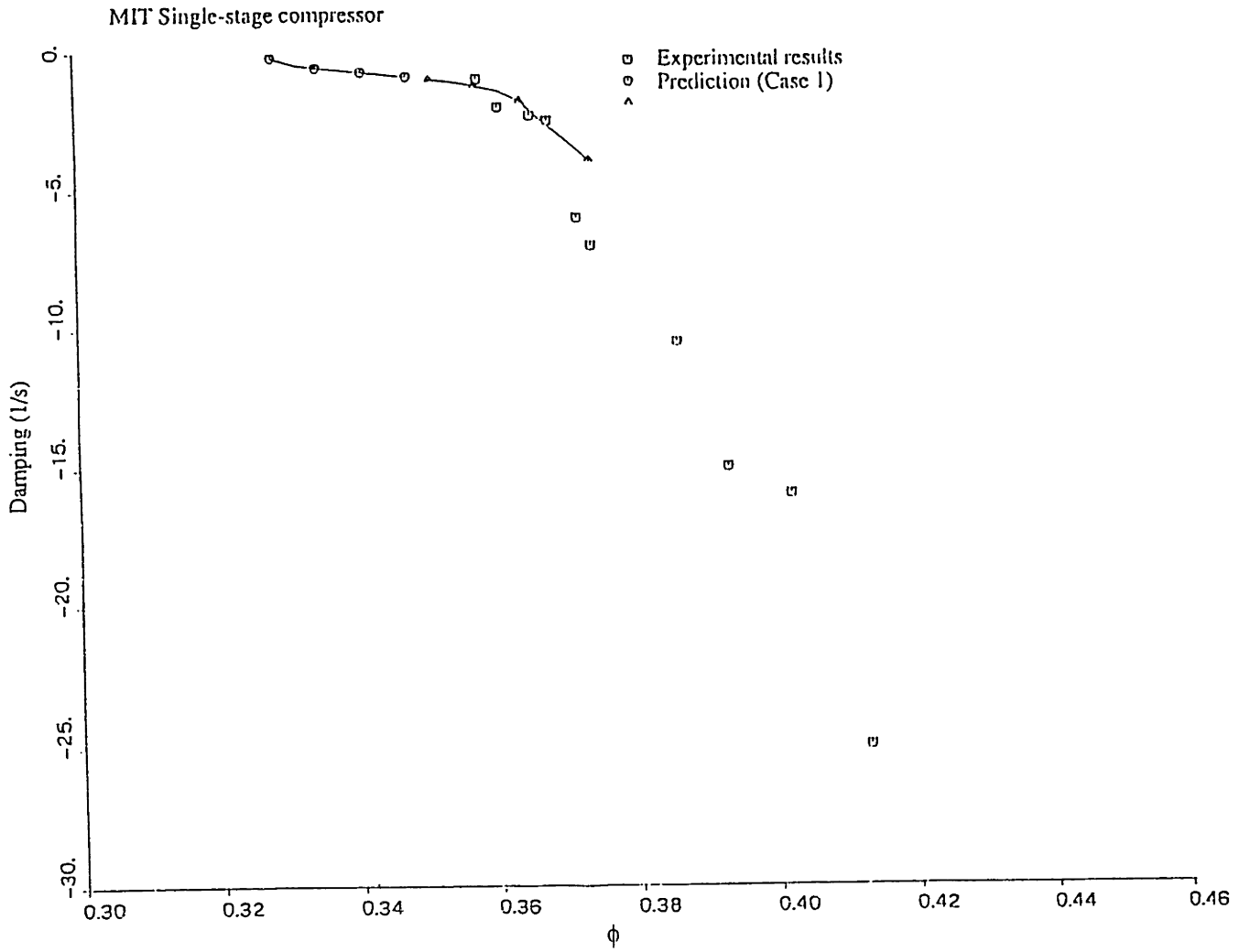

Figure 5.12: MIT Single-stage compressor - Travelling waves damping (Case 1)

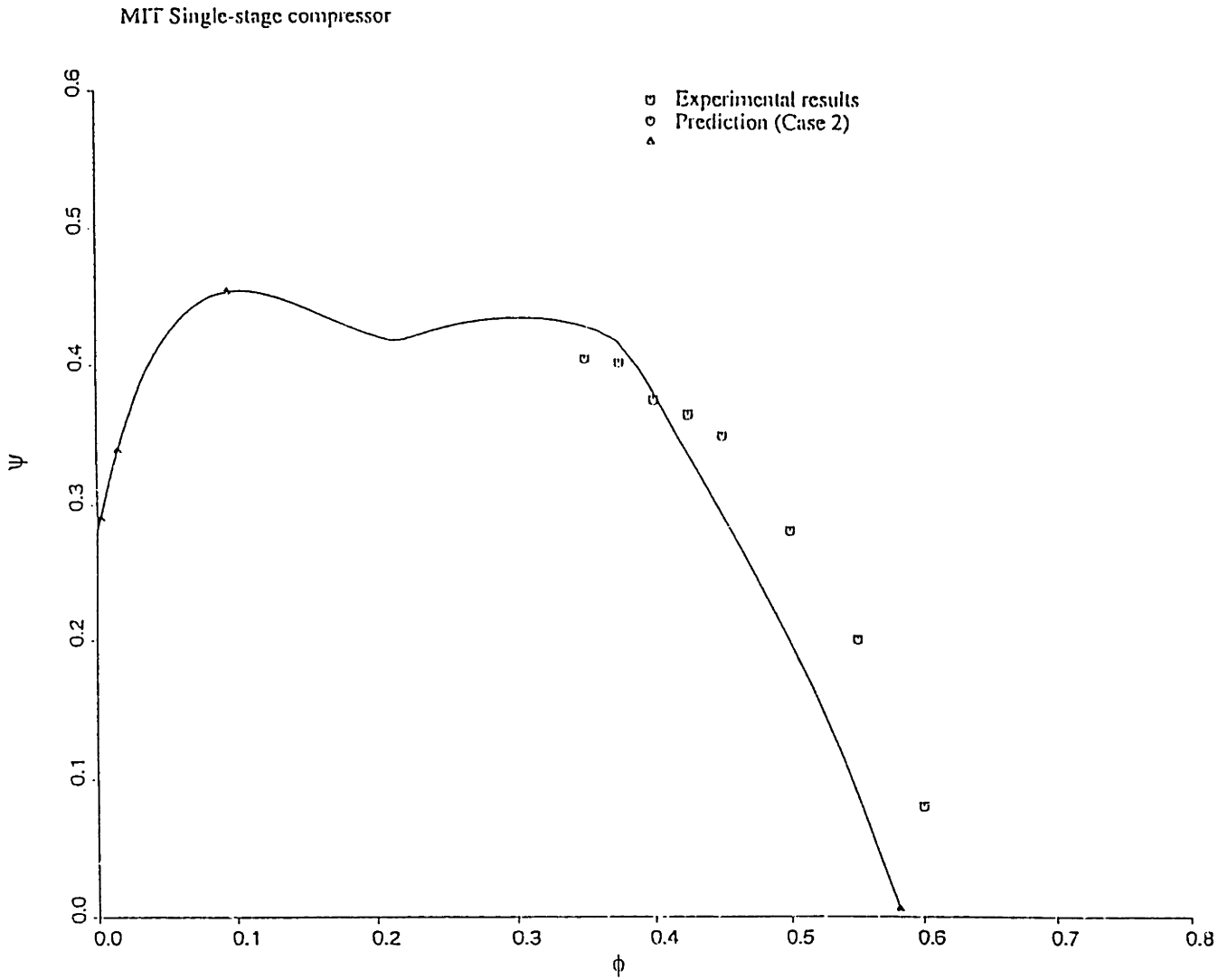

Figure 5.13: MIT Single-stage compressor - Pressure rise characteristic (Case 2)

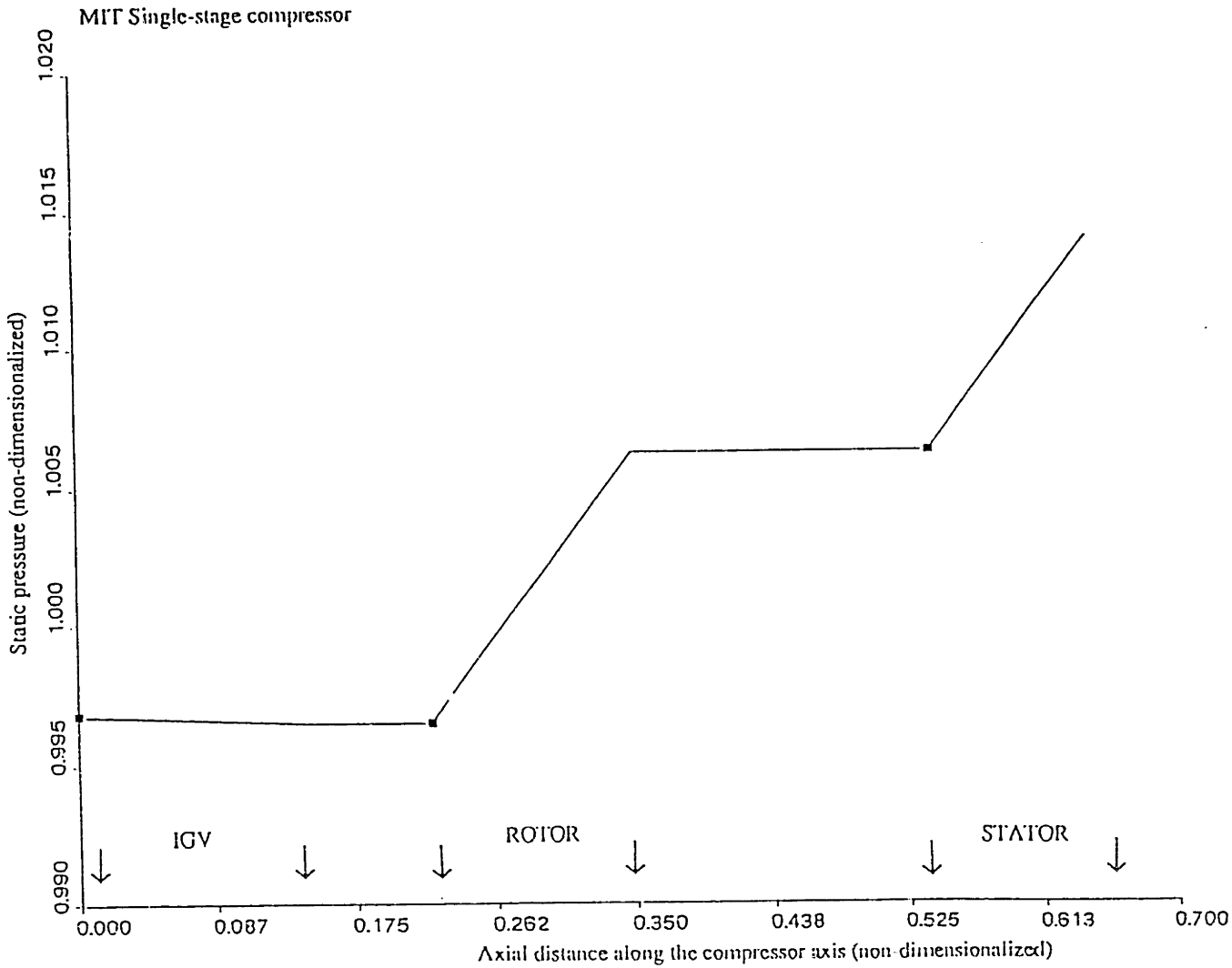

Figure 5.14: MIT Single-stage compressor - Static pressure distribution at neutral stability (Case 2)

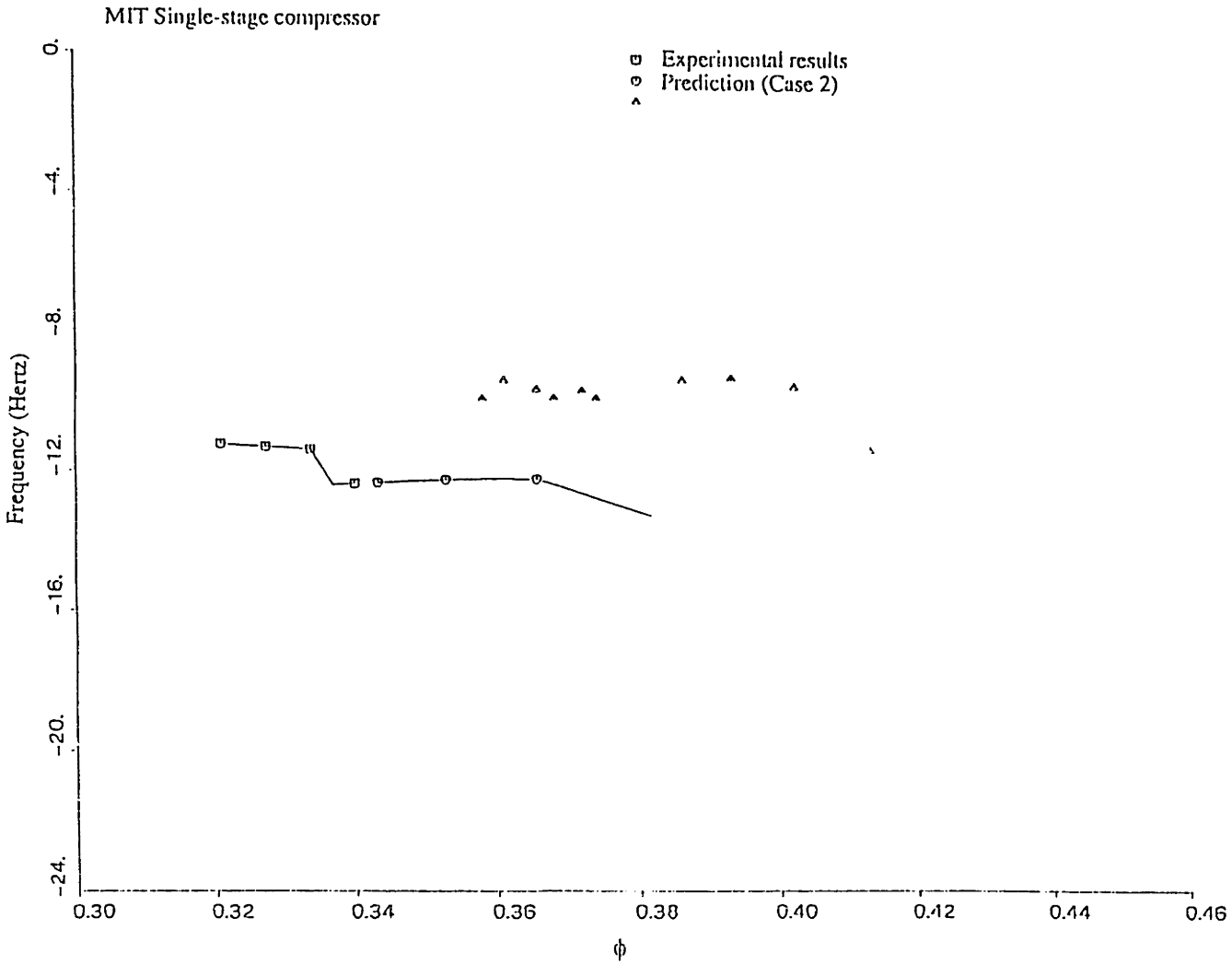

Figure 5.15: MIT Single-stage compressor - Travelling waves frequencies (Case 2)

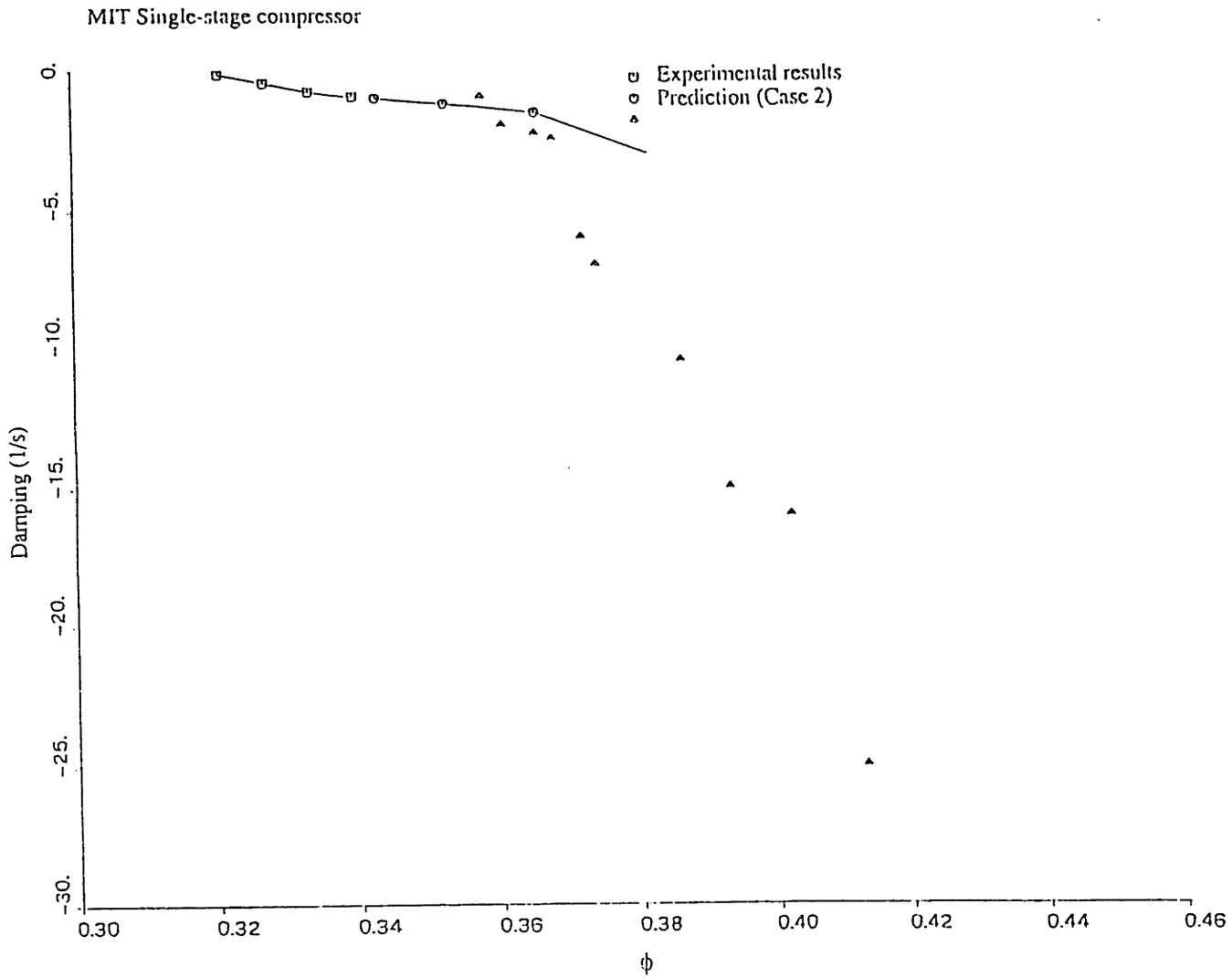

Figure 5.16: MIT Single-stage compressor - Travelling waves damping (Case 2)

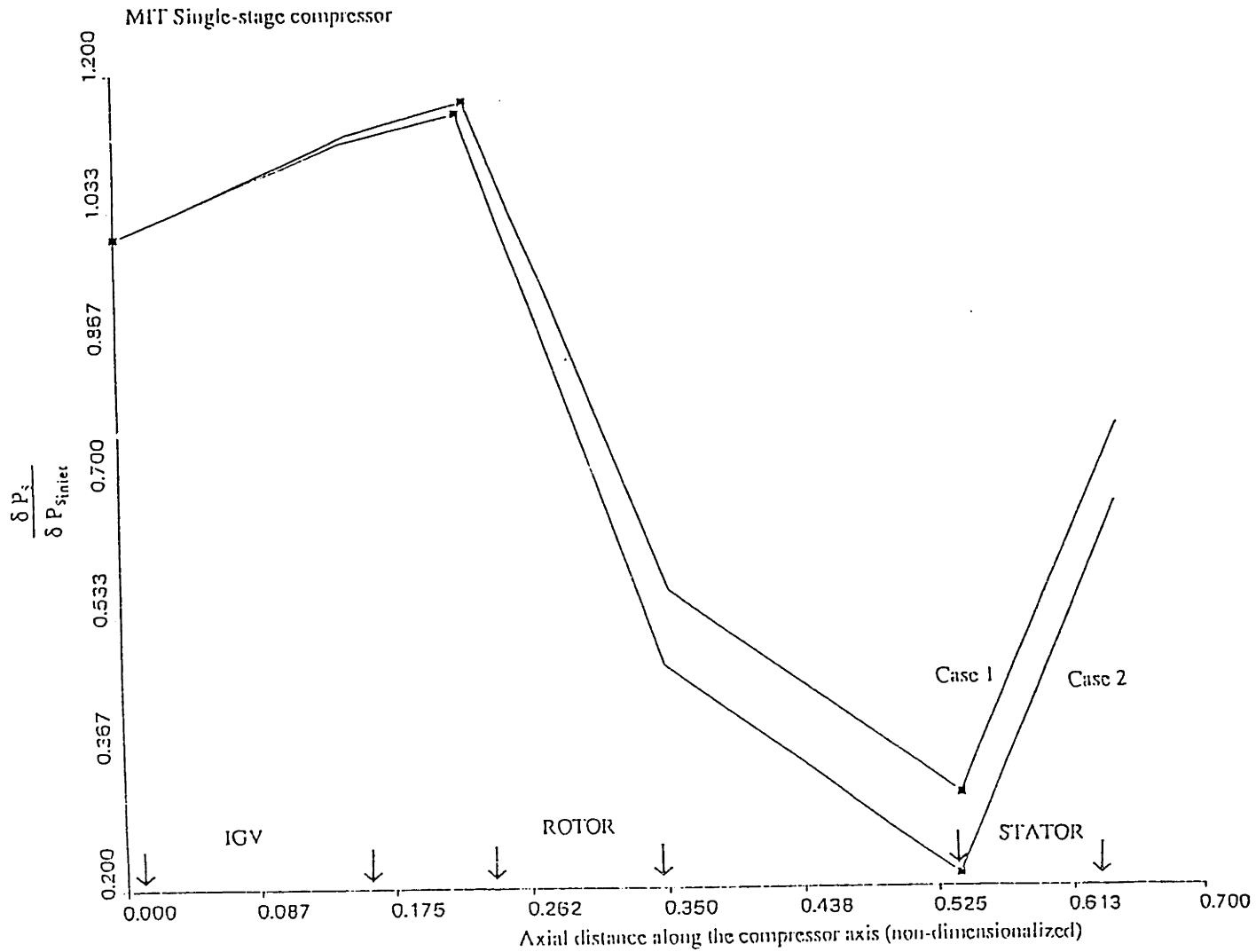

Figure 5.17: MIT Single-stage compressor -

First harmonic static pressure perturbations at 0.1% of stall

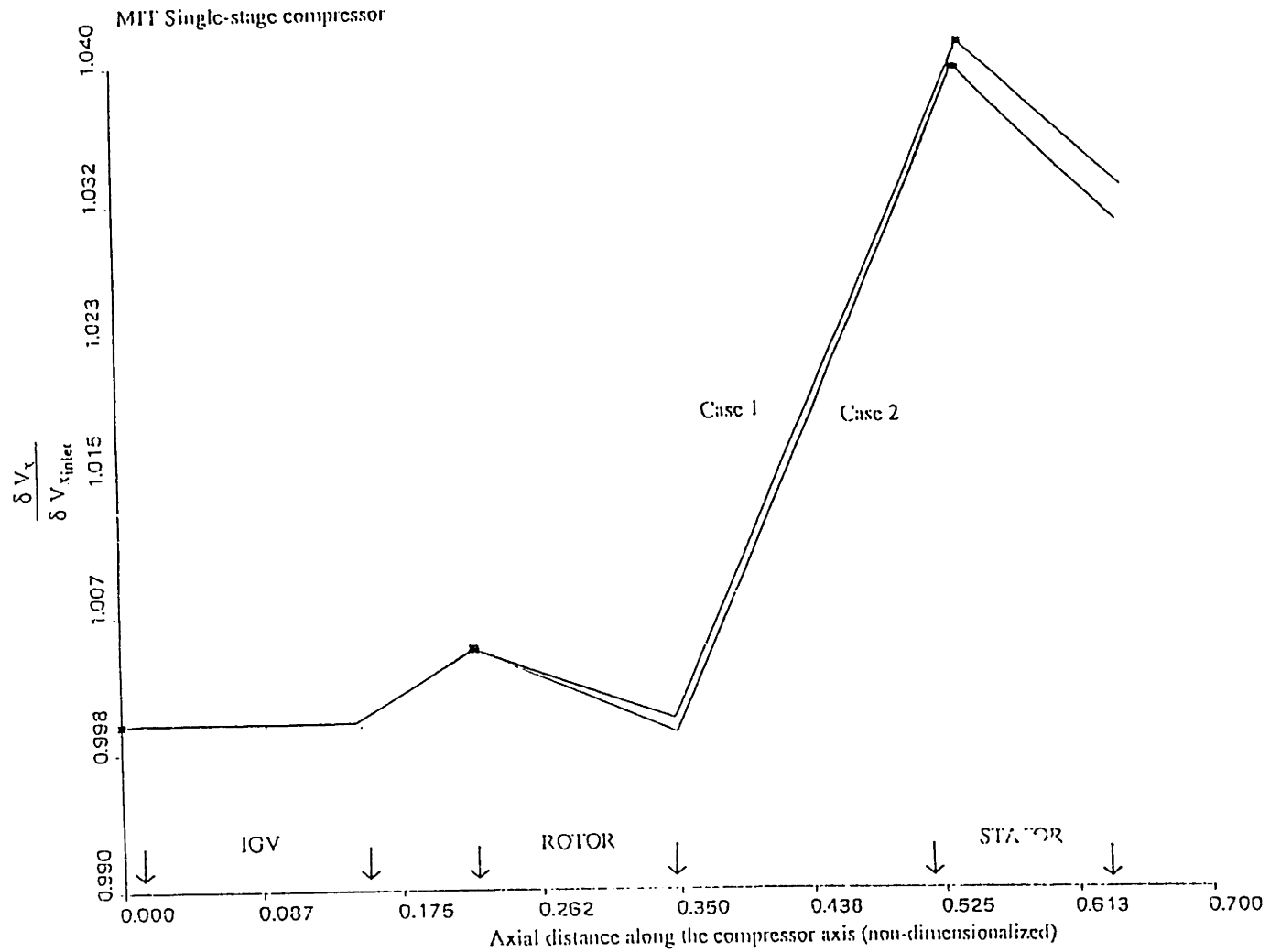

Figure 5.18: MIT Single-stage compressor - First harmonic axial velocity perturbations at 0.1% of stall

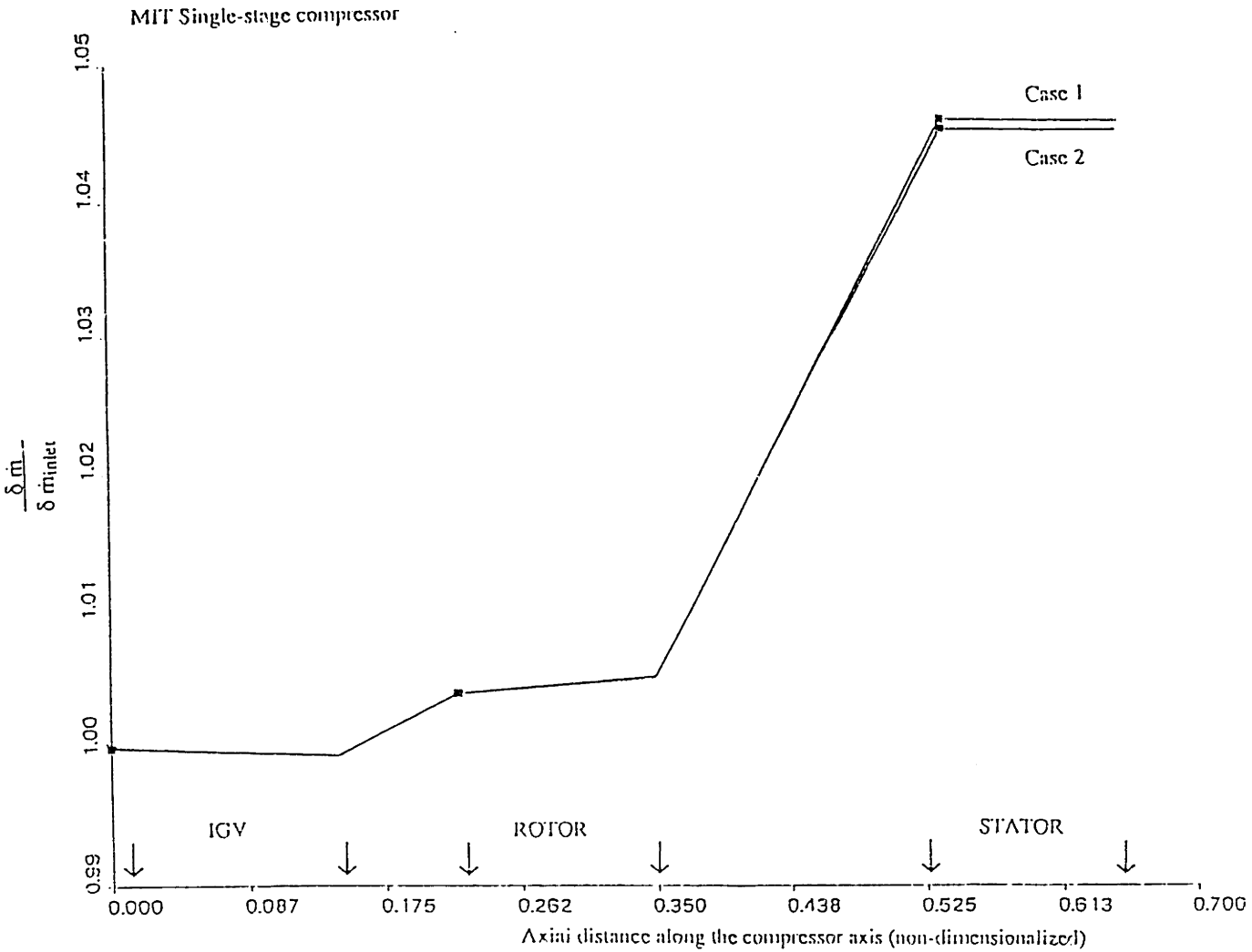

Figure 5.19: MIT Single-stage compressor -

First harmonic mass flow perturbations at 0.1% of stall

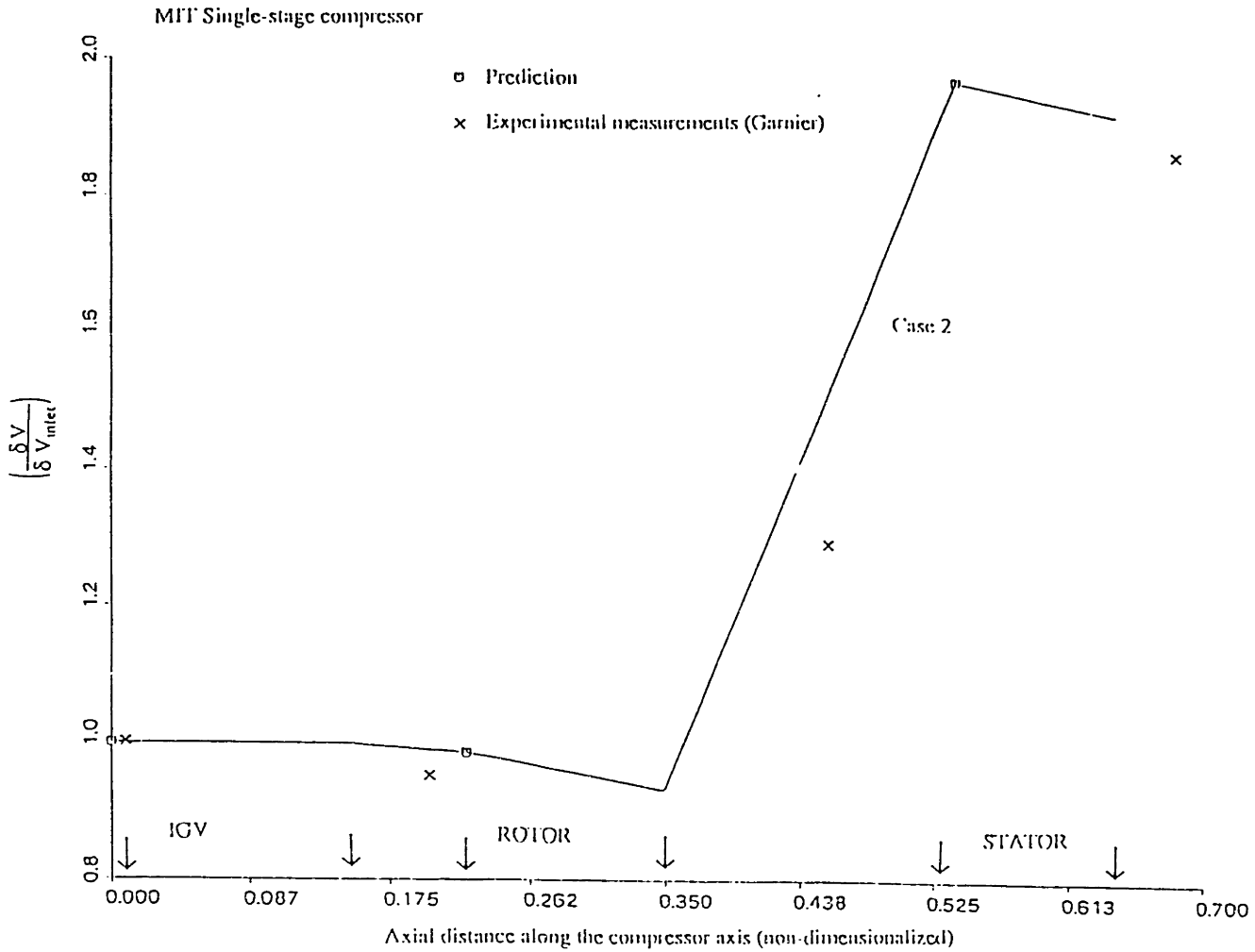

Figure 5.19.b: MIT Single-stage compressor -

First harmonic velocity perturbations at 0.1% of stall

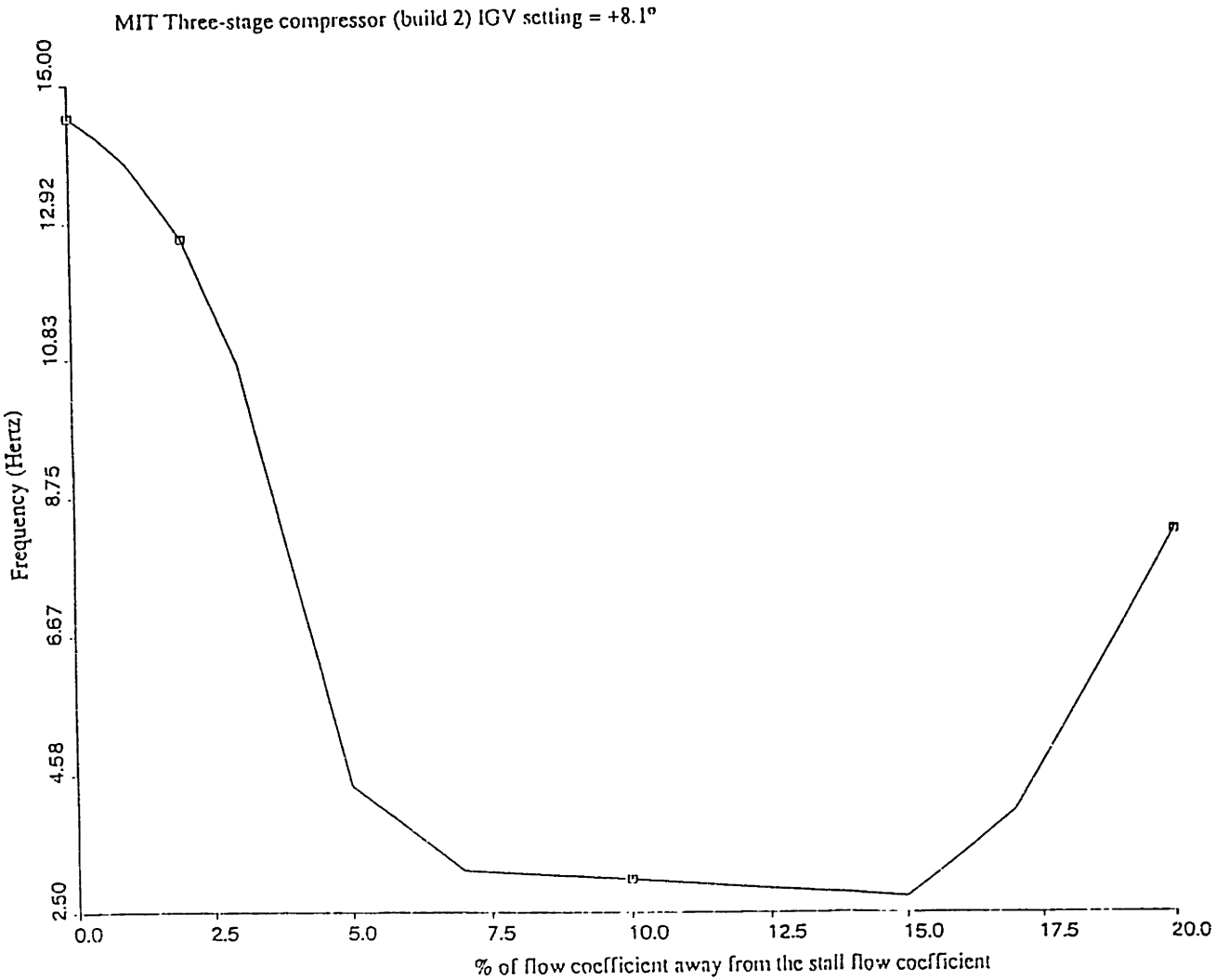

Figure 5.20: MIT Three-stage compressor (build 2) IGV setting = +8.1° - First harmonic travelling wave frequencies

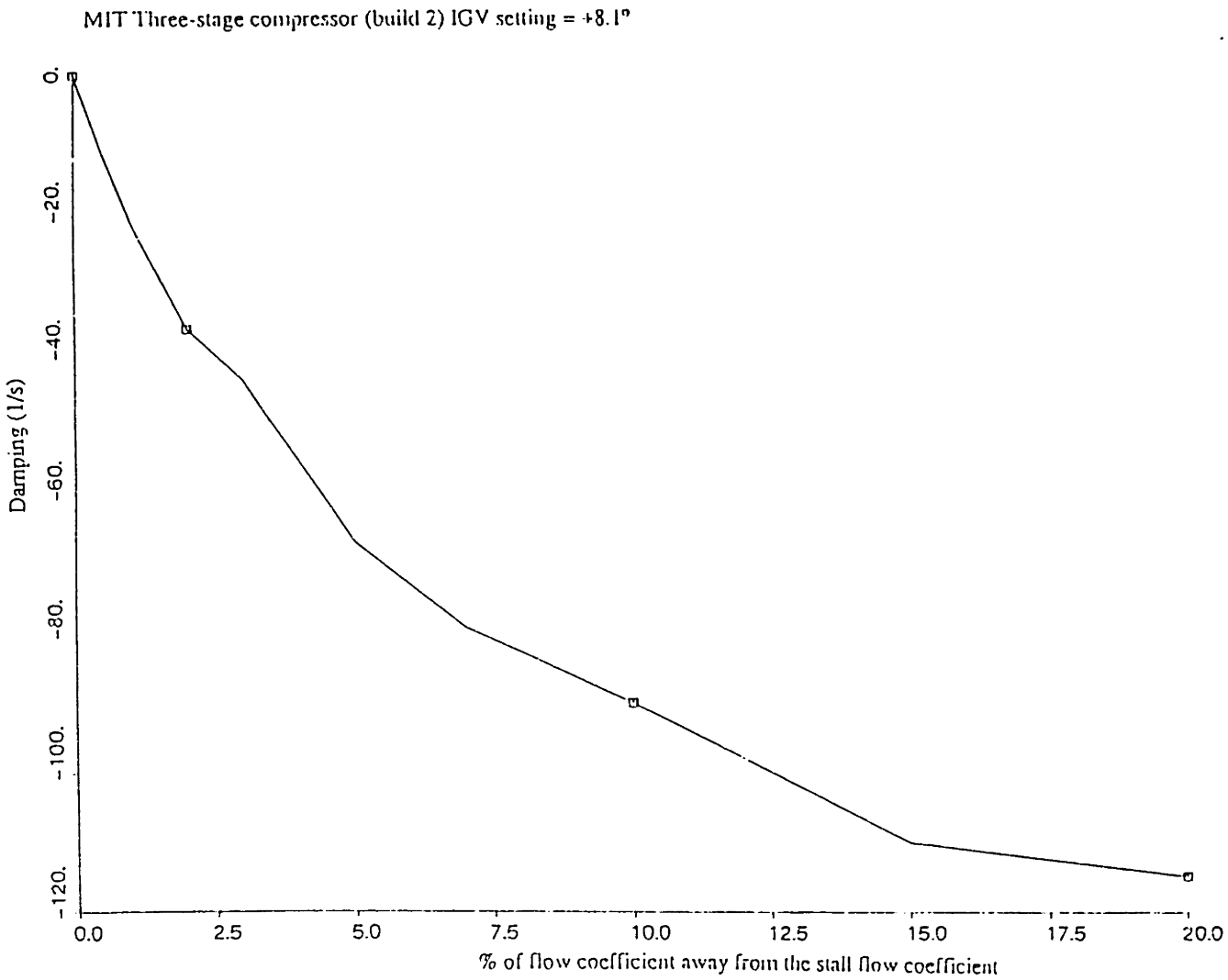

Figure 5.21: MIT Three-stage compressor (build 2) IGV setting = +8.1° - First harmonic travelling wave dampings

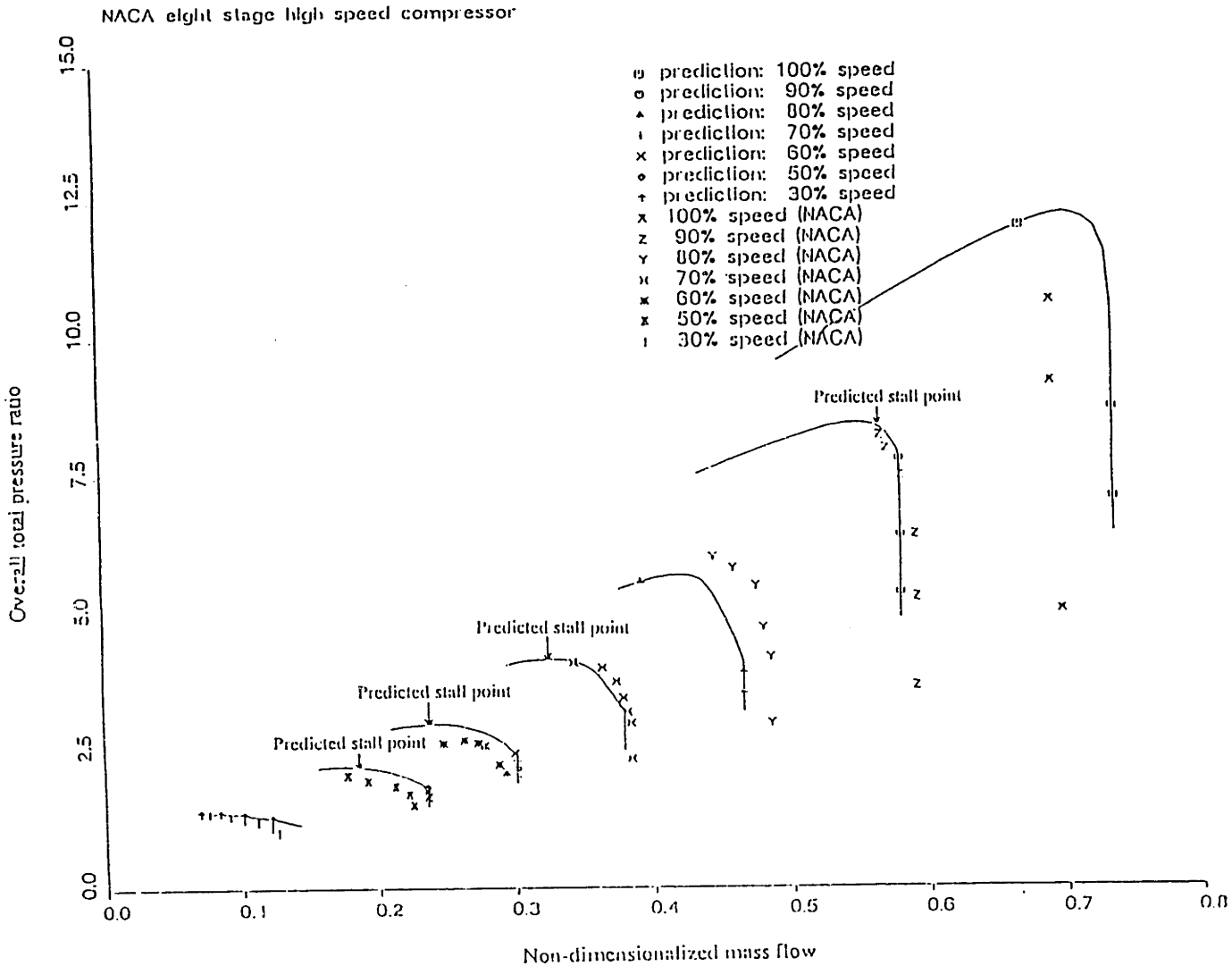

Figure 6.1 NACA Eight stage compressor -
Predicted and experimental pressure ratio characteristics and stall points

NACA *Eight-stage high-speed compressor*	n=1	n=2	n=3
Frequency at neutral stability (non-dimensionalized)	0.82	1.75	2.43
Percentage of rotor frequency	25 %	53 %	74 %
Mass flow function at each harmonic neutral stability operating conditions (non-dimensionalized)	0.146	0.185	0.123
Measured Stall/Surge Point Mass flow function: 0.175 *Rotor frequency: 111 Hz (50% design rotational speed)*			

Table 6.1: Predicted stall characteristics for the NACA 8 stage compressor (50%)

NACA *Eight-stage high-speed compressor*	n=1	n=2	n=3
Frequency at neutral stability (non-dimensionalized)	0.84	1.77	2.45
Percentage of rotor frequency	21 %	44 %	62 %
Mass flow function at each harmonic neutral stability operating conditions (non-dimensionalized)	0.183	0.239	0.160
Measured Stall/Surge Point Mass flow function: 0.25 *Rotor frequency: 133 Hz (60% design rotational speed)*			

Table 6.2: Predicted stall characteristics for the NACA 8 stage compressor (60%)

NACA *Eight-stage high-speed compressor*	n=1	n=2	n=3
Frequency at neutral stability (non-dimensionalized)	1.27	1.98	2.83
Percentage of rotor frequency	28 %	43 %	61 %
Mass flow function at each harmonic neutral stability operating conditions (non-dimensionalized)	0.220	0.324	0.322
Measured Stall/Surge Point Mass flow function: 0.34 *Rotor frequency: 156 Hz (70% design rotational speed)*			

Table 6.3: Predicted stall characteristics for the NACA 8 stage compressor (70 %)

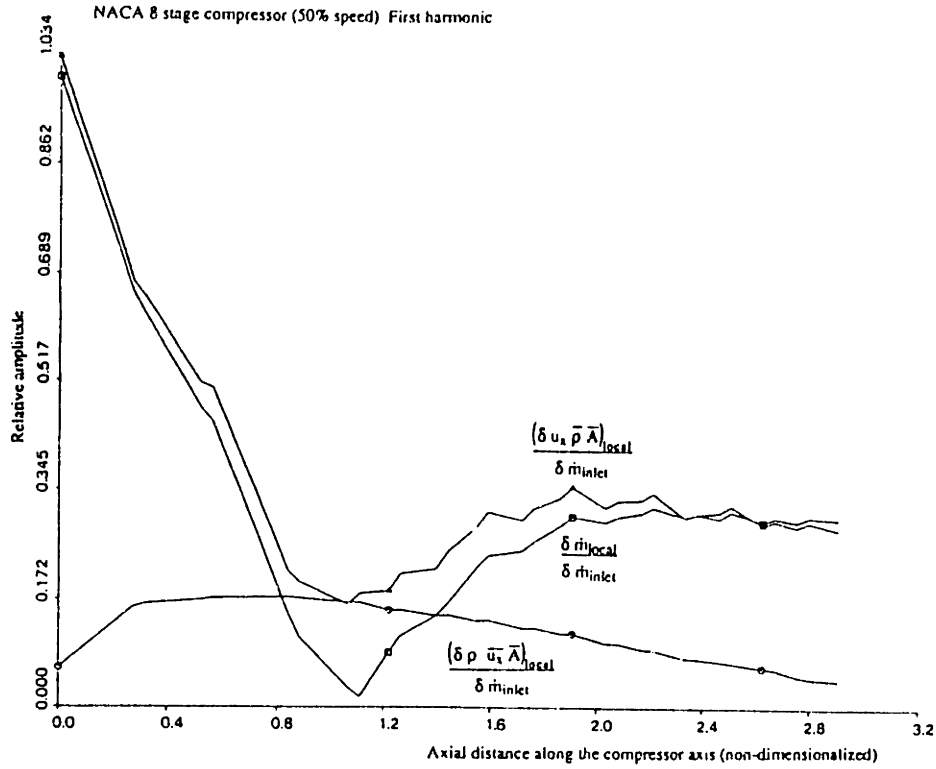

Figure 6.2.a NACA Eight stage compressor (50% speed) - Influence of the compressibility on the perturbations (first harmonic)

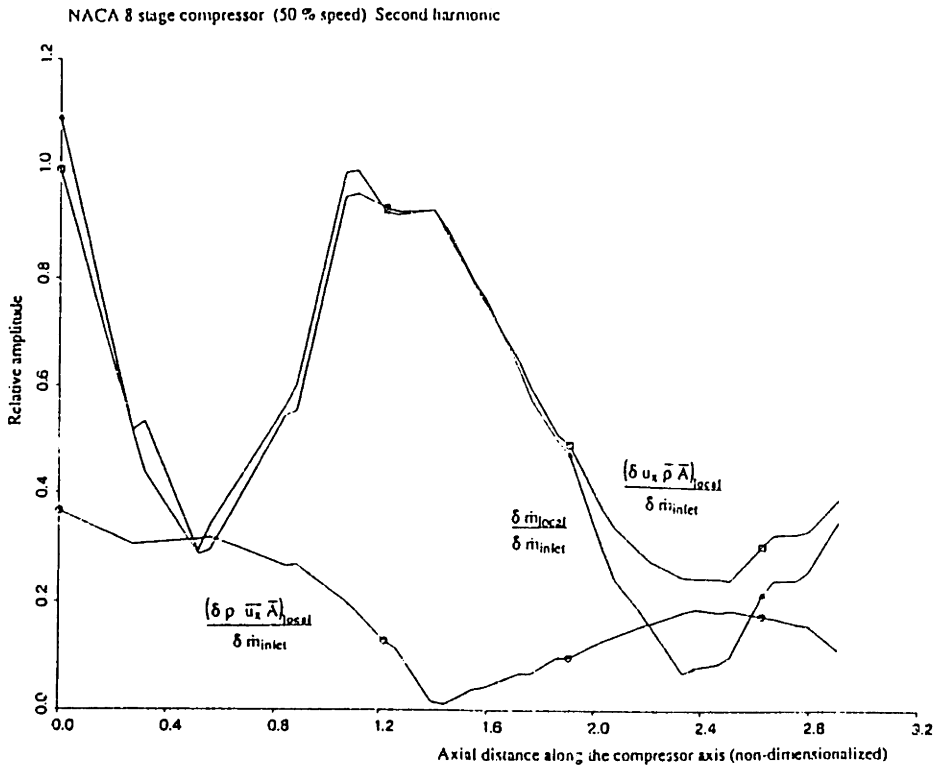

Figure 6.2.b NACA Eight stage compressor (50% speed) - Influence of the compressibility on the perturbations (second harmonic)

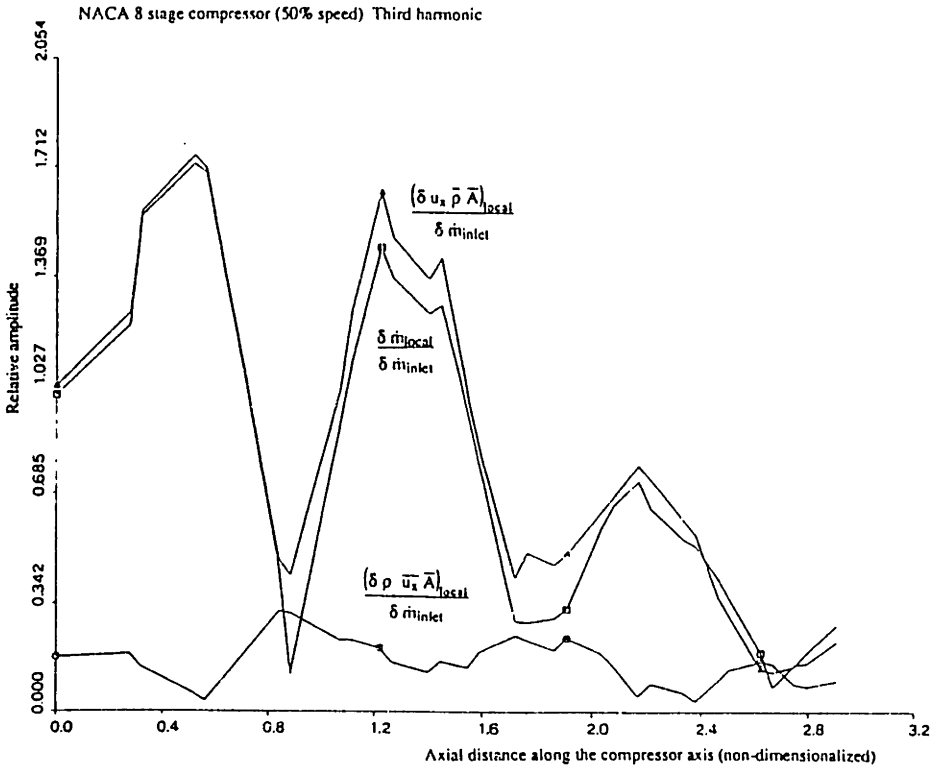

Figure 6.2.c NACA Eight stage compressor (50% speed) - Influence of the compressibility on the perturbations (third harmonic)

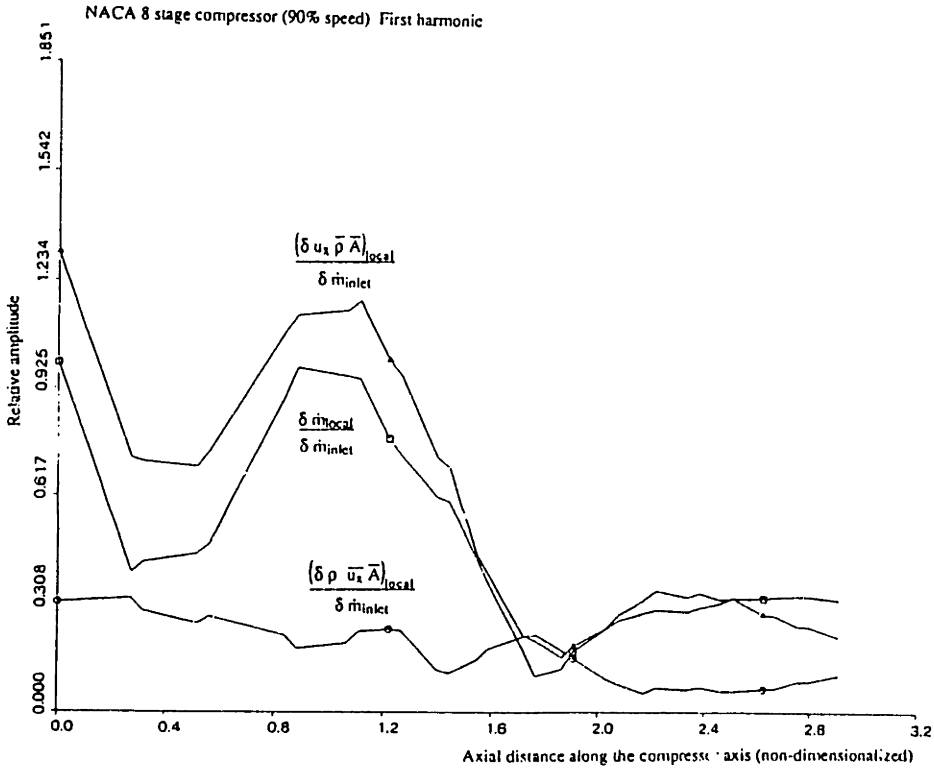

Figure 6.3.a NACA Eight stage compressor (90% speed) - Influence of the compressibility on the perturbations (first harmonic)

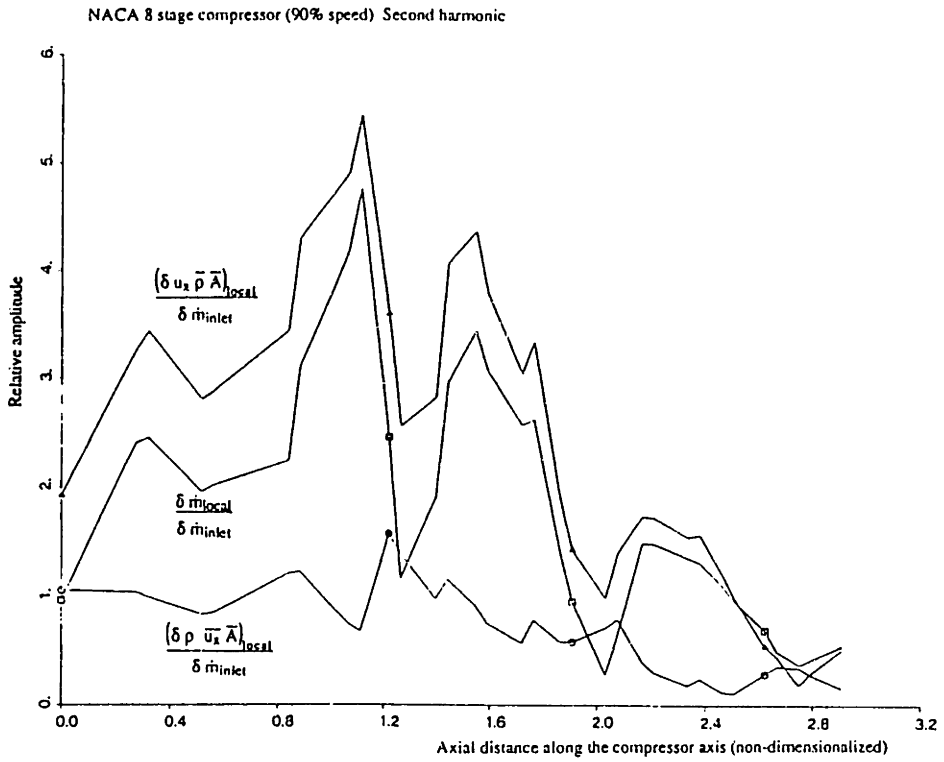

Figure 6.3.b NACA Eight stage compressor (90% speed) - Influence of the compressibility on the perturbations (second harmonic)

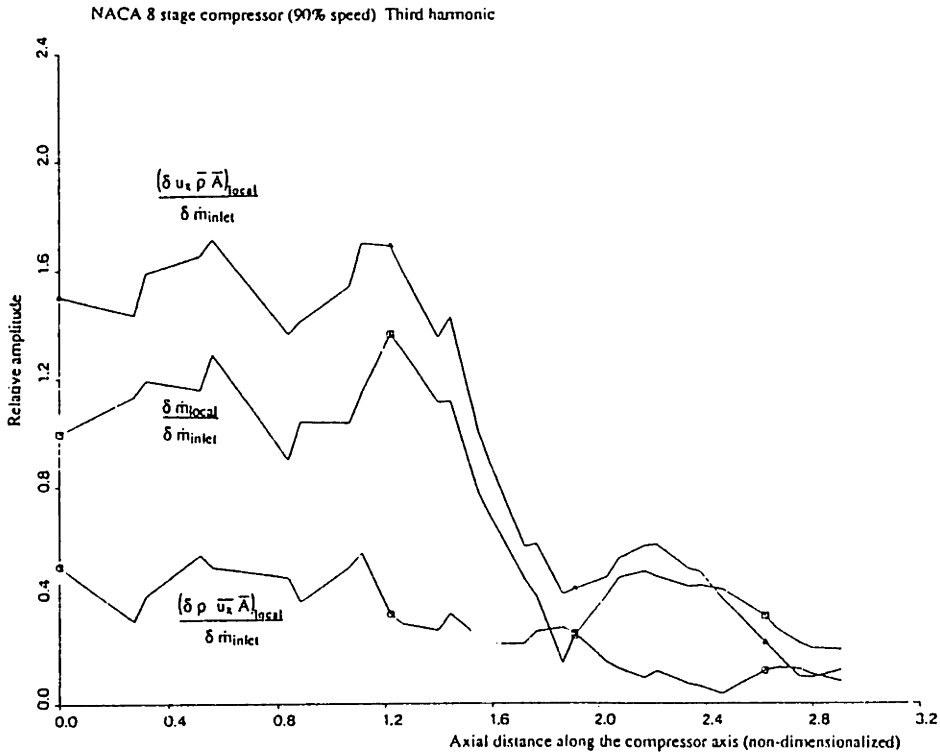

Figure 6.3.c NACA Eight stage compressor (90% speed) - Influence of the compressibility on the perturbations (third harmonic)

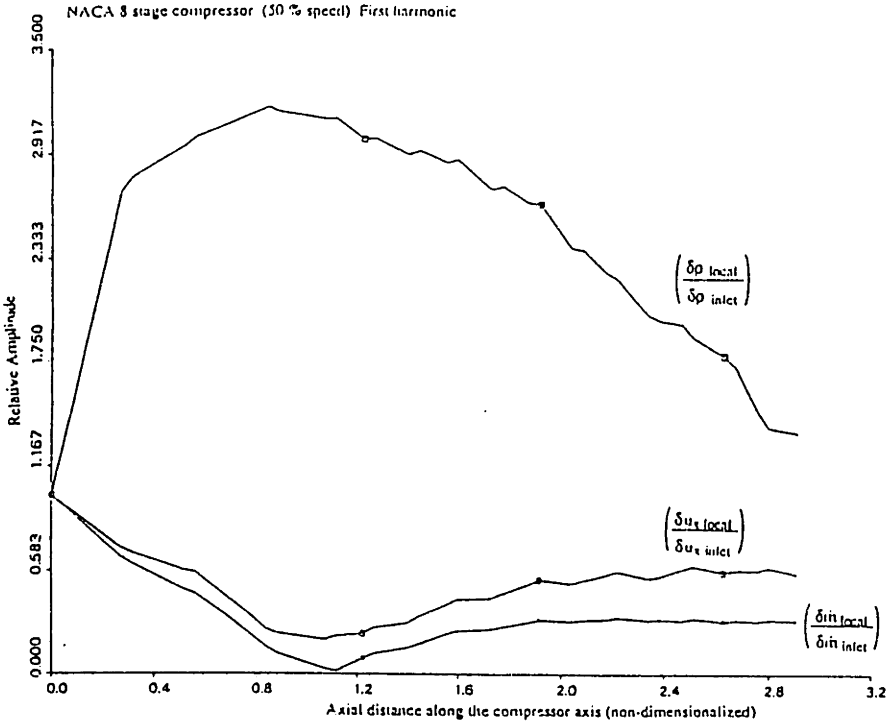

Figure 6.4.a NACA Eight stage compressor (50 % speed) - Perturbations distribution along the compressor axis (first harmonic)

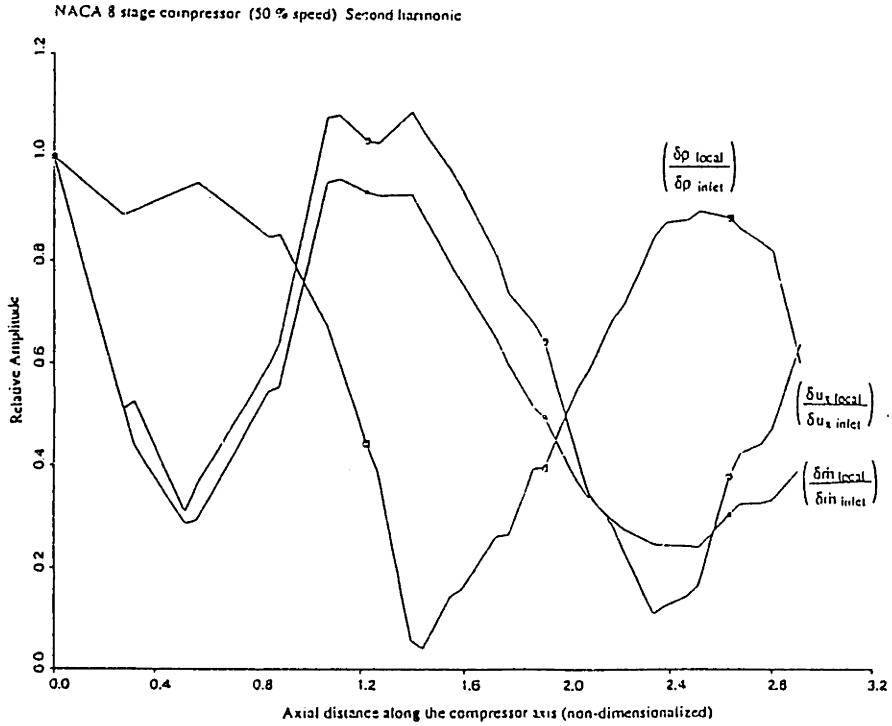

Figure 6.4.b NACA Eight stage compressor (50 % speed) - Perturbations distribution along the compressor axis (second harmonic)

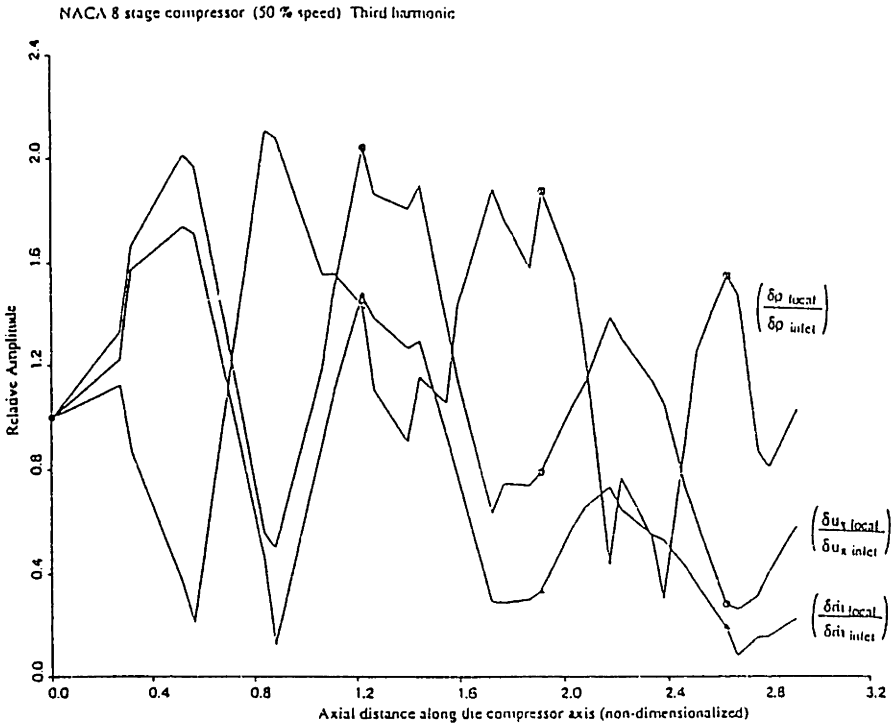

Figure 6.4.c NACA Eight stage compressor (50 % speed) - Perturbations distribution along the compressor axis (third harmonic)

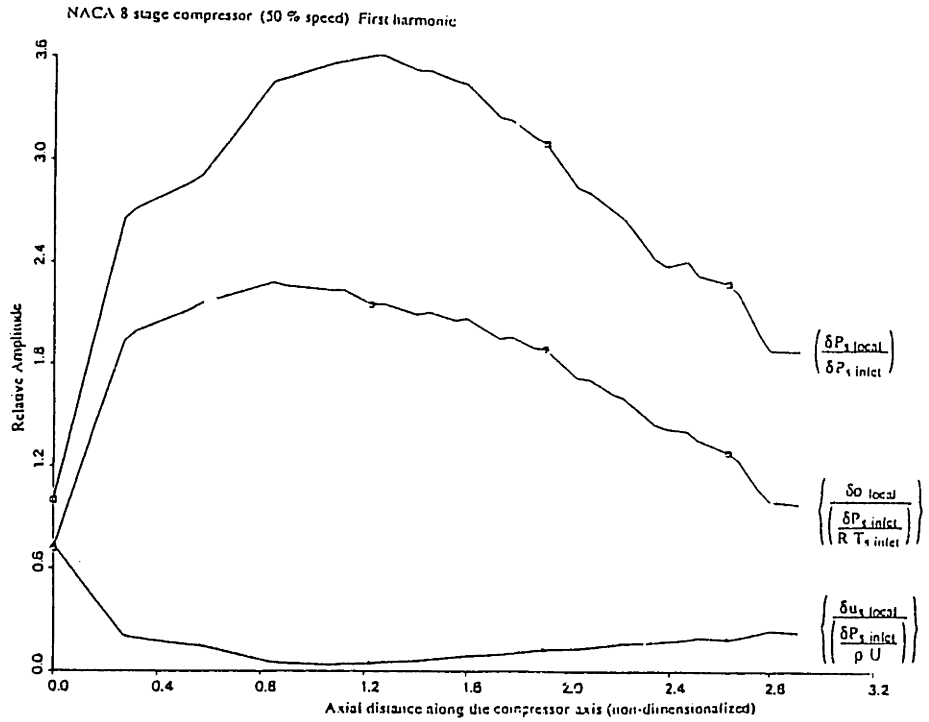

Figure 6.5.a NACA Eight stage compressor (50 % speed) - Relative perturbations distribution along the compressor axis (first harmonic)

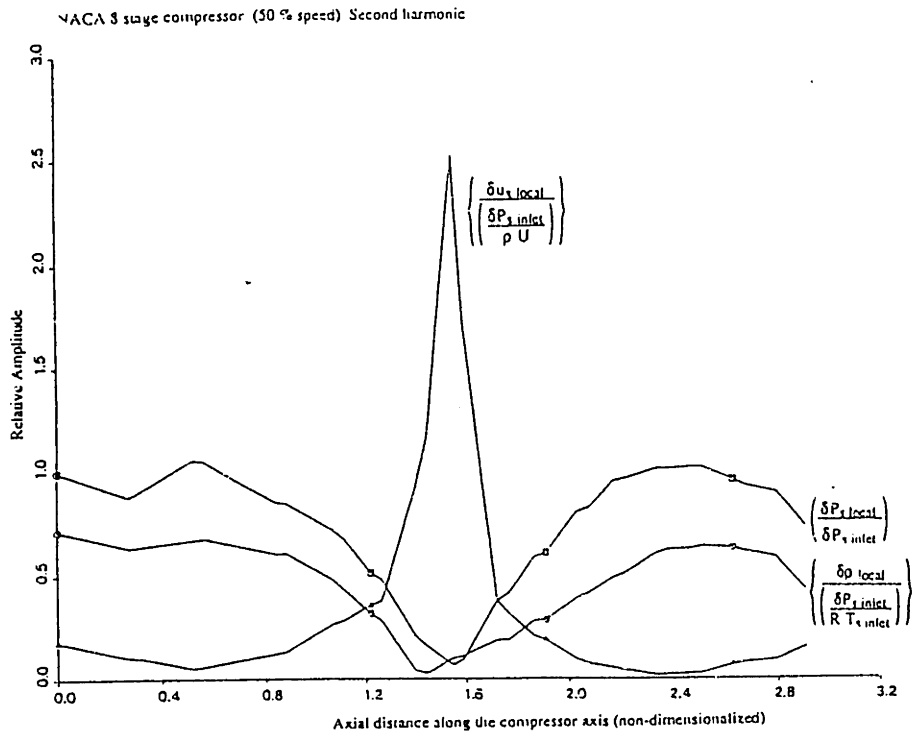

Figure 6.5.b NACA Eight stage compressor (50 % speed) -
Relative perturbations distribution along the compressor axis (second harmonic)

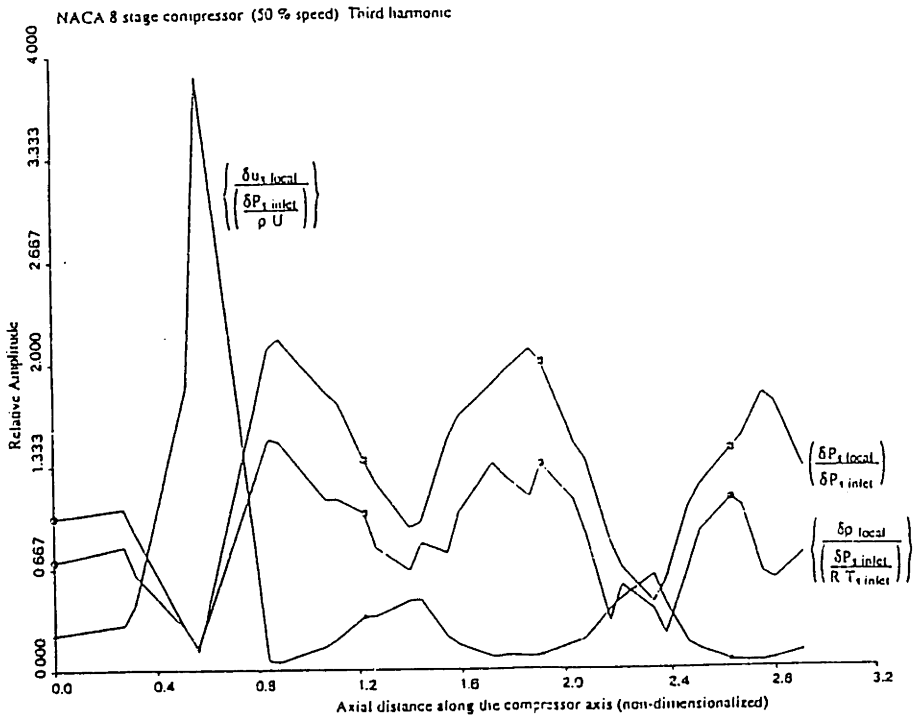

Figure 6.5.c NACA Eight stage compressor (50 % speed) -
Relative perturbations distribution along the compressor axis (third harmonic)

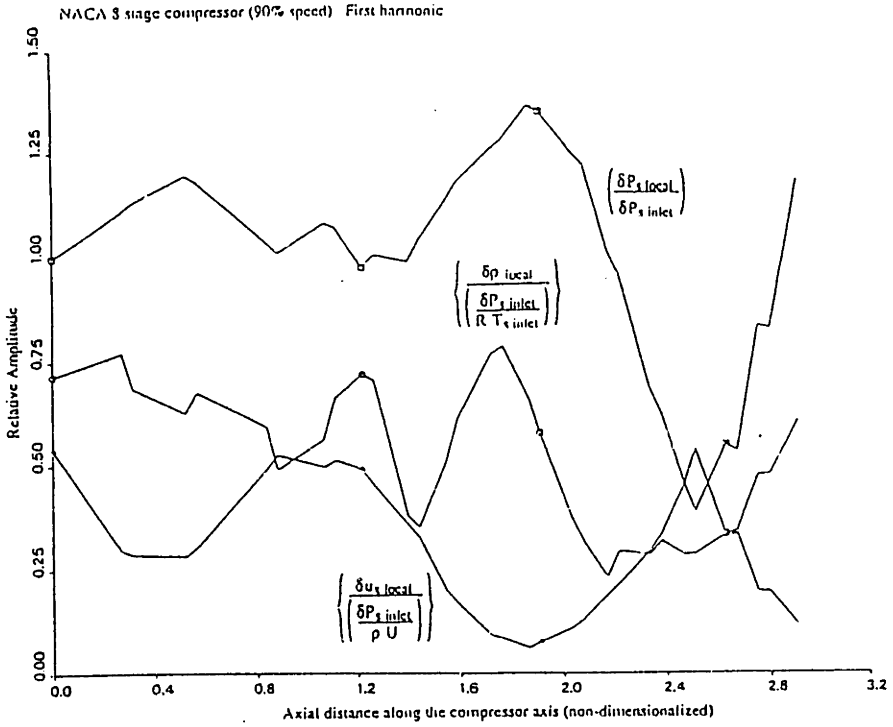

Figure 6.6.a NACA Eight stage compressor (90 % speed) - Relative perturbations distribution along the compressor axis (first harmonic)

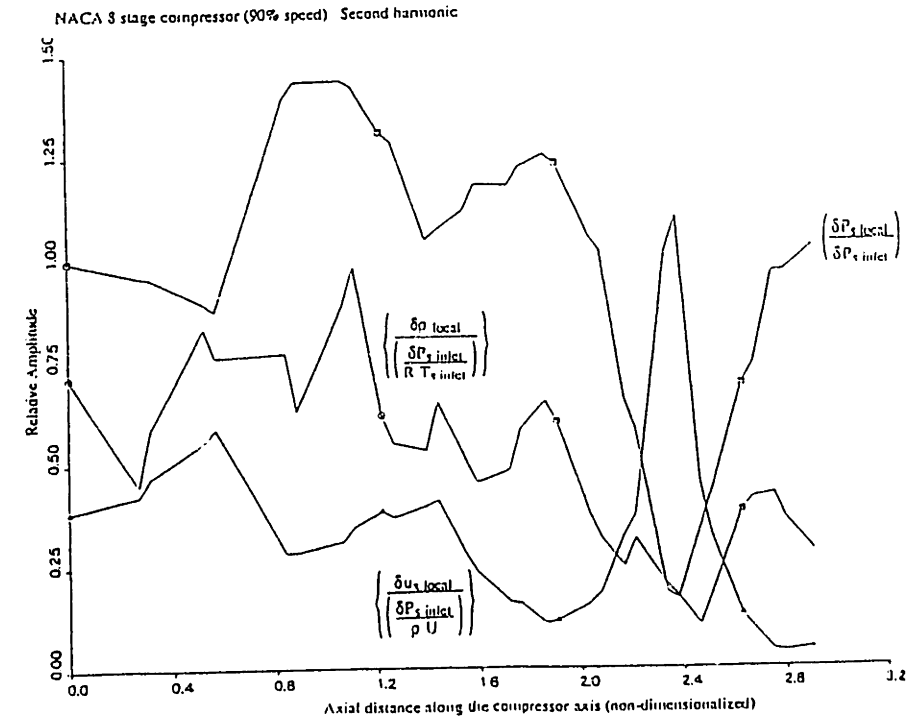

Figure 6.6.b NACA Eight stage compressor (90 % speed) - Relative perturbations distribution along the compressor axis (second harmonic)

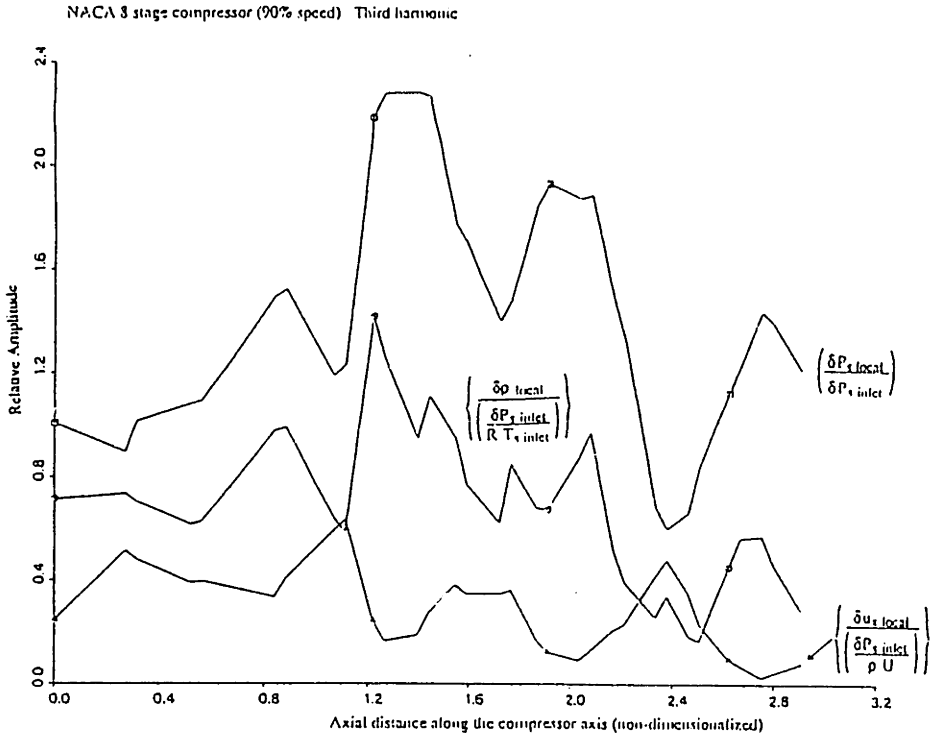

Figure 6.6.c NACA Eight stage compressor (90 % speed) -
Relative perturbations distribution along the compressor axis (third harmonic)

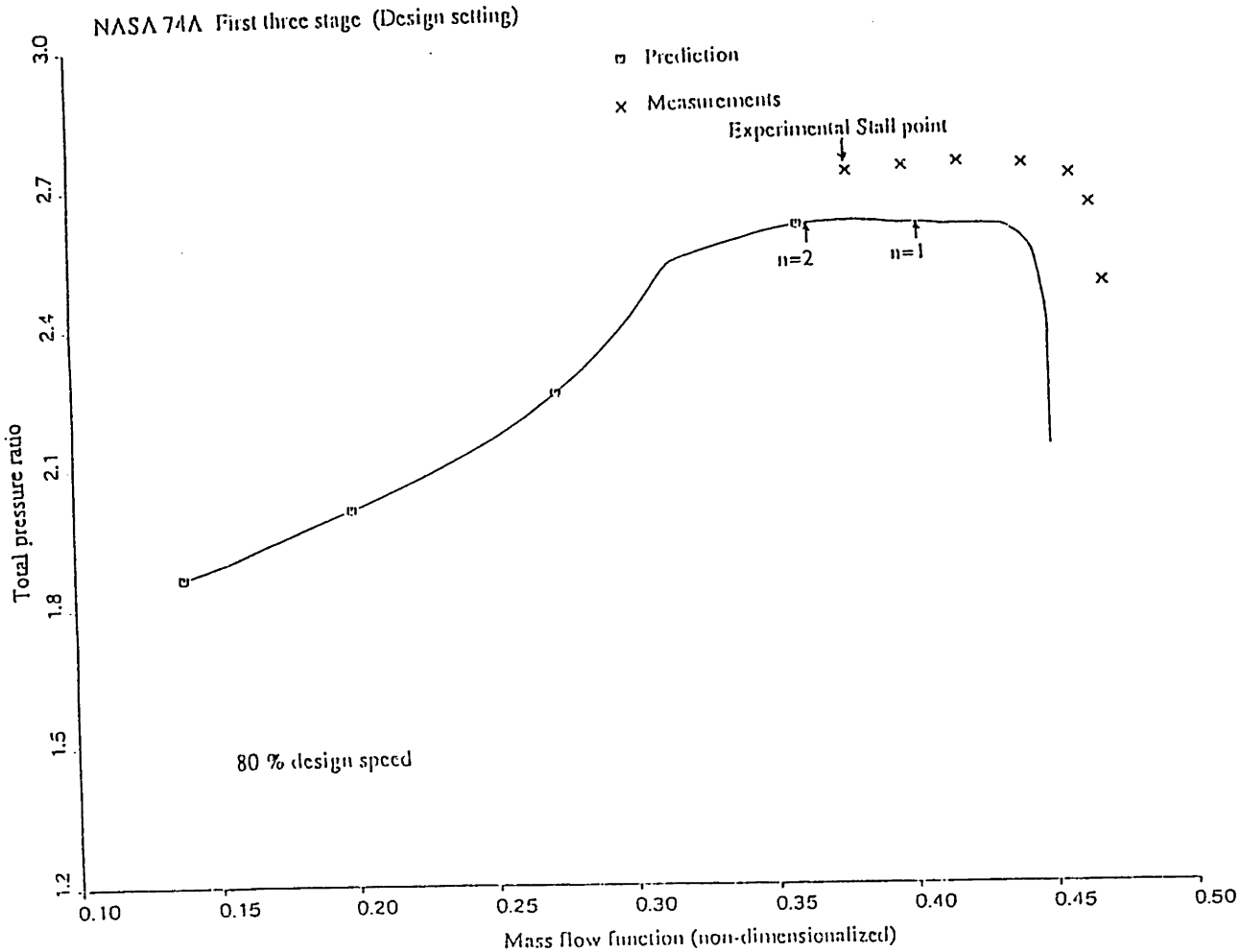

Figure 6.7 NASA Three-stage compressor (74 A) (Design setting) - Predicted and experimental pressure ratio characteristic and stall points at 80 % speed

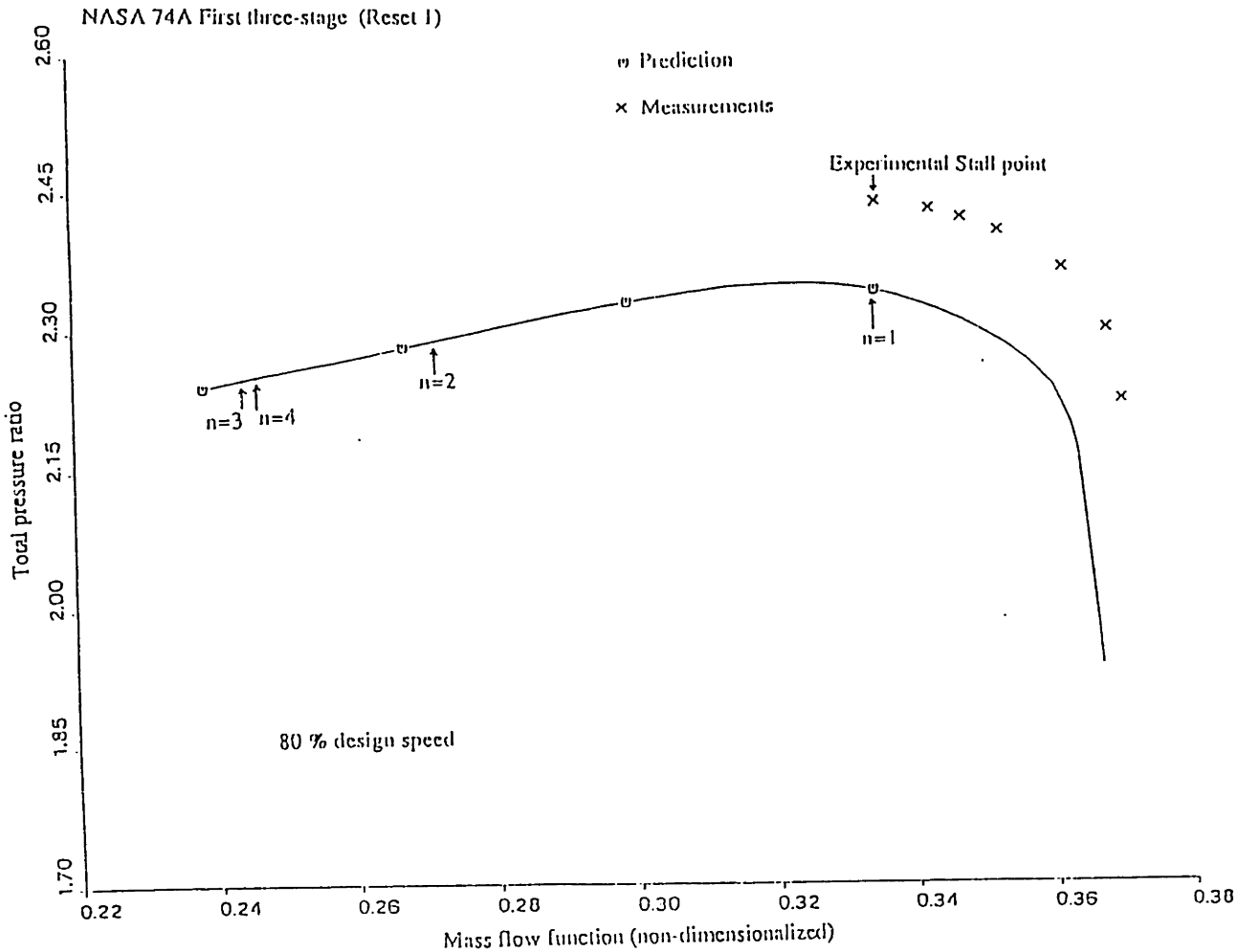

Figure 6.8 NASA Three-stage compressor (74 A) (Reset 1) -
Predicted and experimental pressure ratio characteristic and stall points at 80 % speed

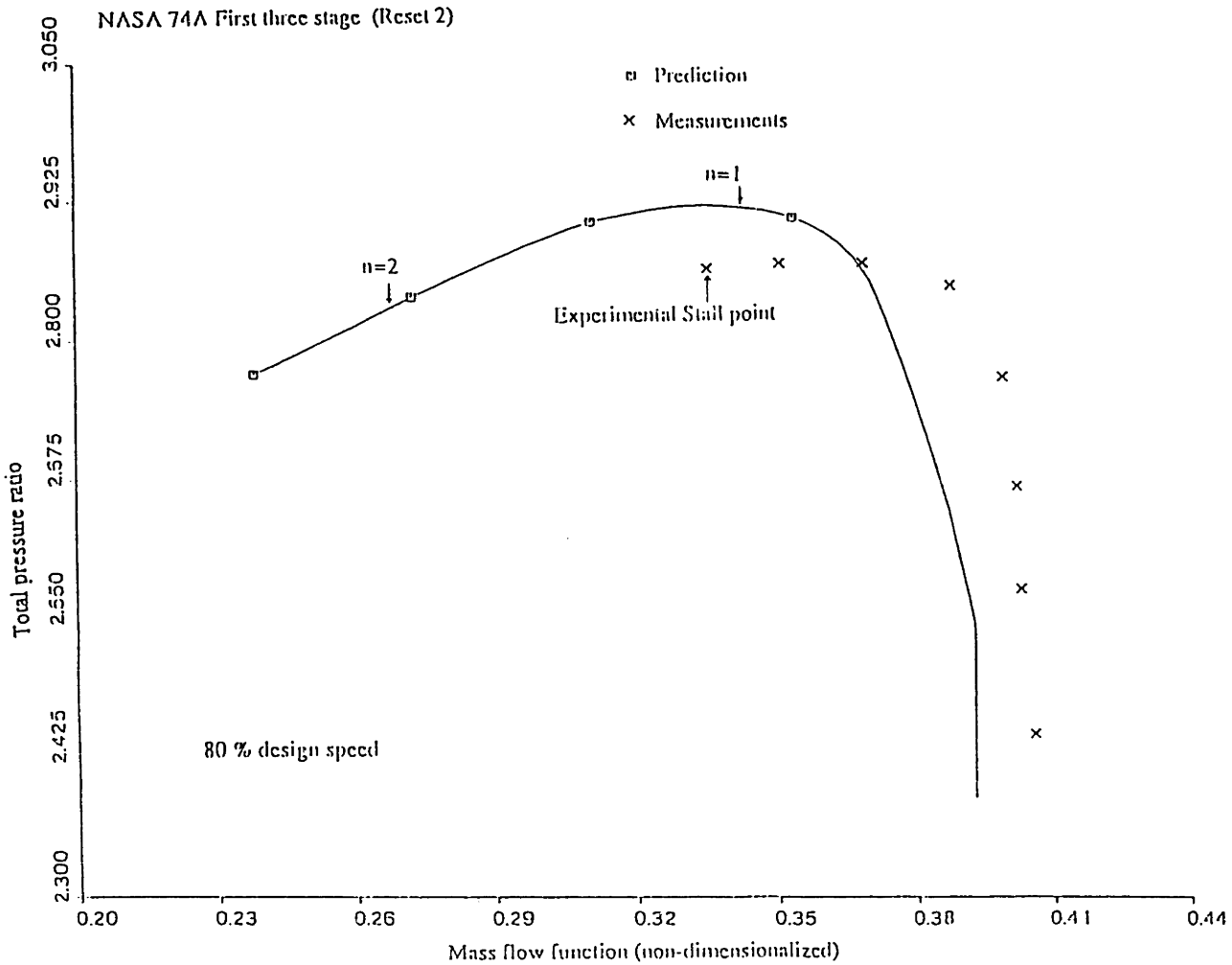

Figure 6.9 NASA Three-stage compressor (74 A) (Reset 2) -
Predicted and experimental pressure ratio characteristic and stall points at 80 % speed

NASA 74 A Design Setting *Three-stage high-speed compressor*	n=1	n=2
Frequency at neutral stability (non-dimensionalized)	0.53	1.1
Percentage of rotor frequency	65 %	118 %
Mass flow function at each harmonic neutral stability operating conditions (non-dimensionalized)	0.41	0.36
Measured Stall Point Mass flow function: 0.375 *Rotor frequency: 213 Hz (80% design rotational speed)*		

Table 6.4: Predicted stall characteristics for the 74A compressor at design setting

NASA 74 A Reset 1 *Three-stage high-speed compressor*	n=1	n=2	n=3	n=4
Frequency at neutral stability (non-dimensionalized)	0.802	1.607	2.453	3.270
Percentage of rotor frequency	15 %	32 %	48 %	64 %
Mass flow function at each harmonic neutral stability operating conditions (non-dimensionalized)	0.327	0.273	0.247	0.249
Measured Stall Point Mass flow function: 0.325 *Rotor frequency: 213 Hz (80% design rotational speed)*				

Table 6.5: Predicted stall characteristics for the 74A compressor at Reset 1

NASA 74 A Reset 2 *Three-stage high-speed compressor*	n=1	n=2
Frequency at neutral stability (non-dimensionalized)	0.815	1.622
Percentage of rotor frequency	16 %	32 %
Mass flow function at each harmonic neutral stability operating conditions (non-dimensionalized)	0.348	0.267
Measured Stall Point Mass flow function: 0.335 *Rotor frequency: 213 Hz (80% design rotational speed)*		

Table 6.6: Predicted stall characteristics for the 74A compressor at Reset 2

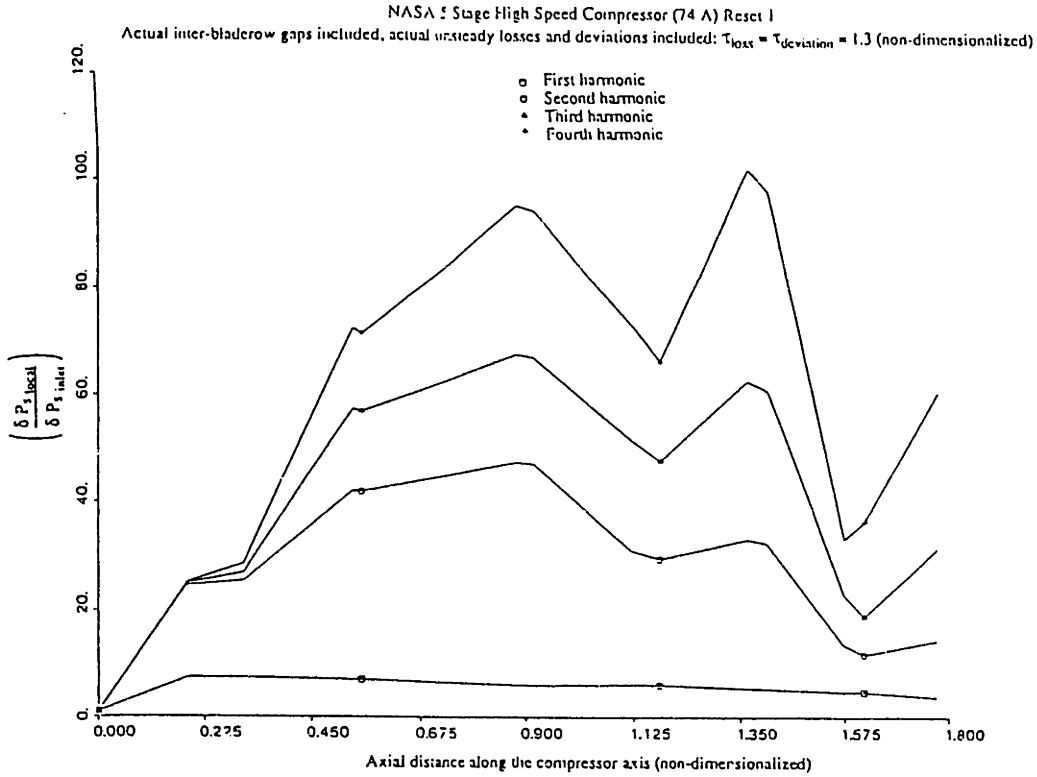

Figure 6.10.a NASA Three-stage compressor (74 A) (Reset 1) -
Static pressure perturbation distribution at each neutral stability for the first four harmonics

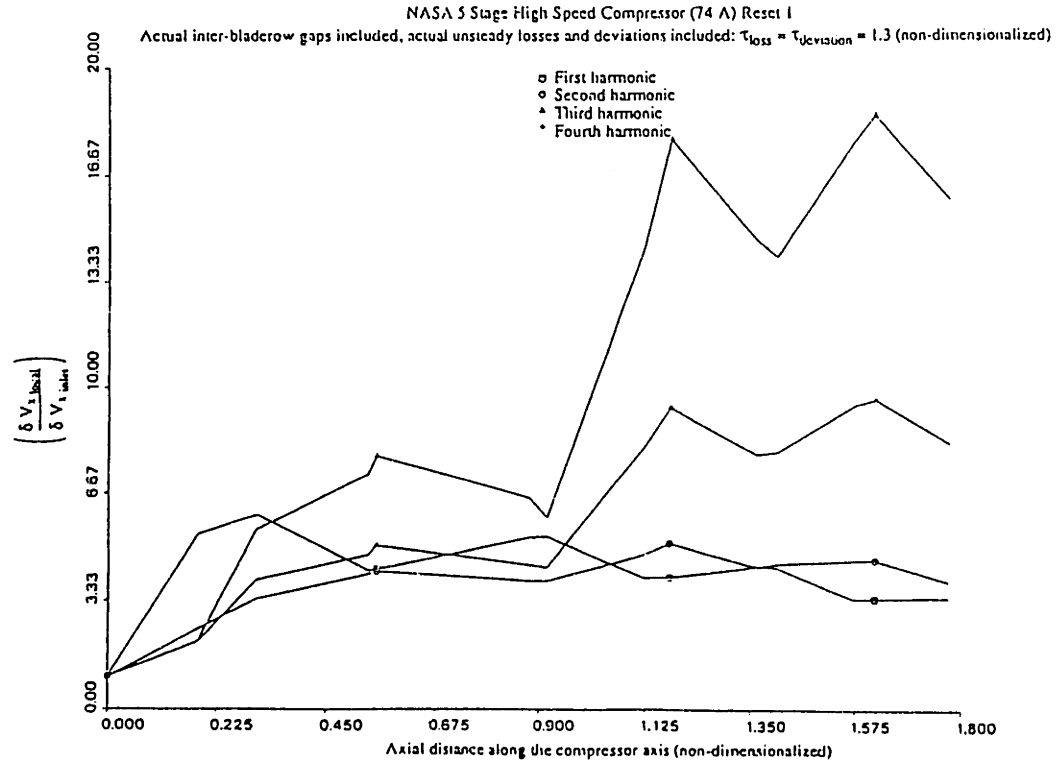

Figure 6.10.b NASA Three-stage compressor (74 A) (Reset 1) -
Axial velocity perturbation distribution at each neutral stability for the first four harmonics

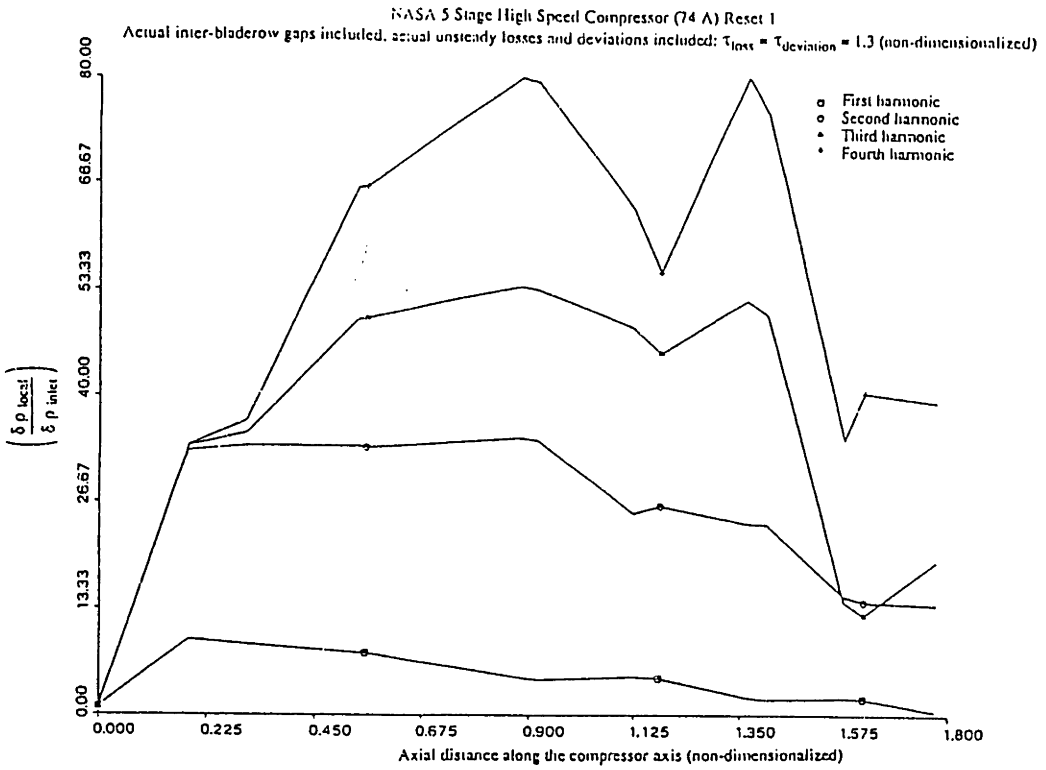

Figure 6.10.c NASA Three-stage compressor (74 A) (Reset 1) -
Density perturbation distribution at each neutral stability for the first four harmonics

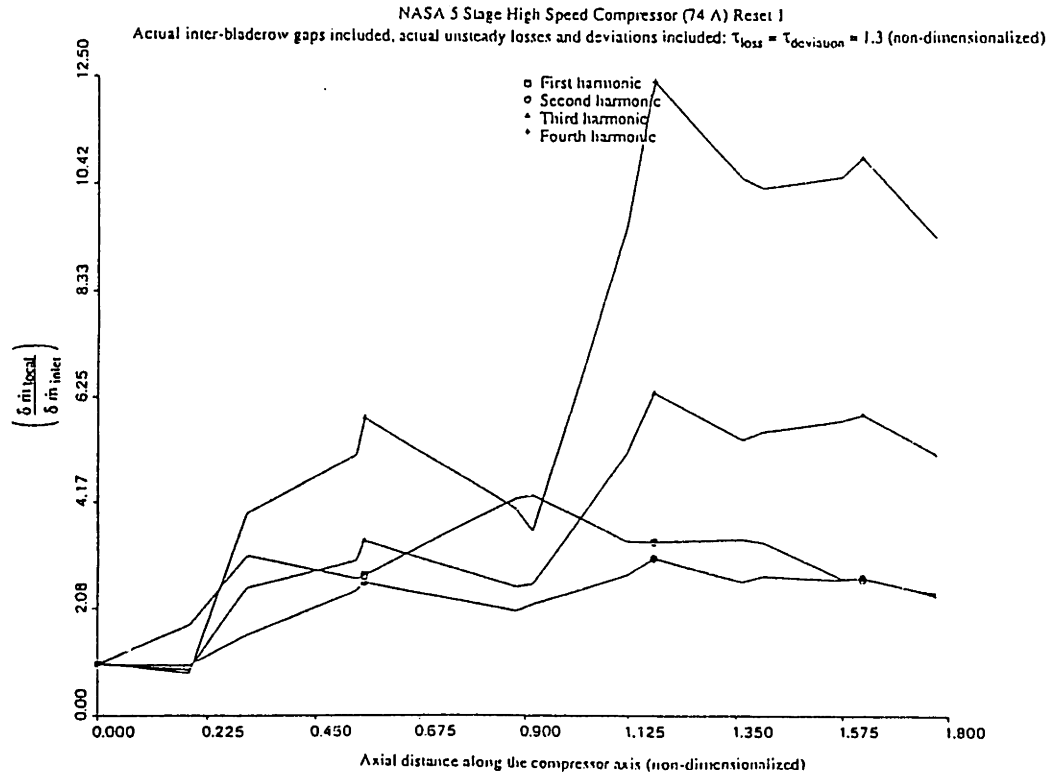

Figure 6.10.d NASA Three-stage compressor (74 A) (Reset 1) -
Mass flow perturbation distribution at each neutral stability for the first four harmonics

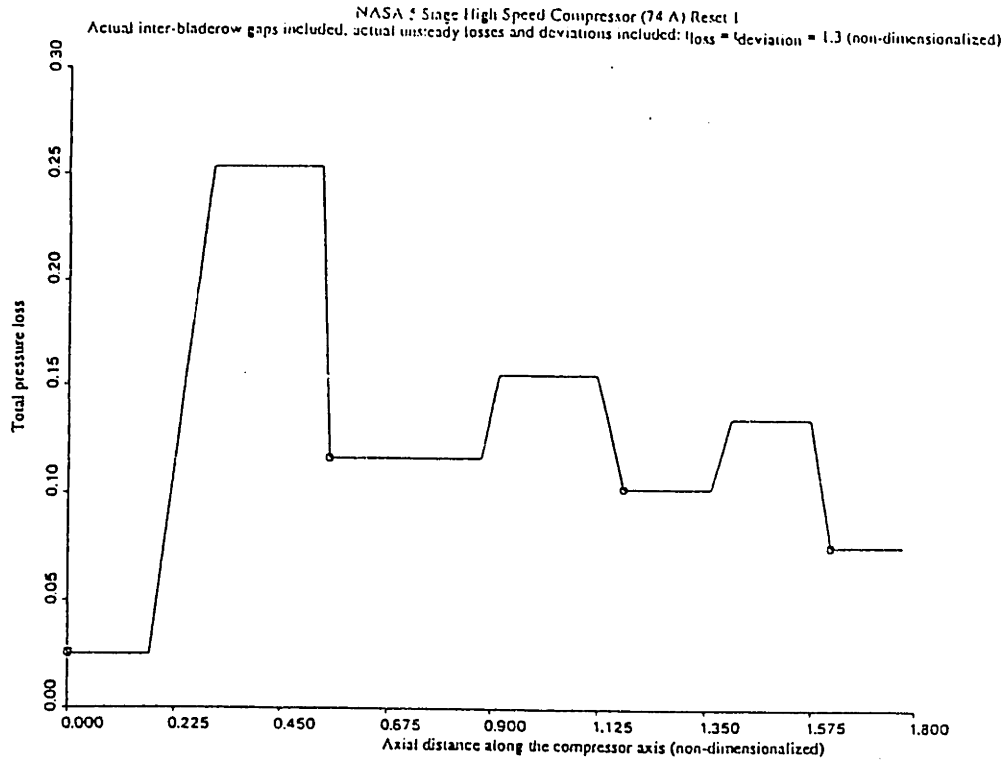

Figure 6.11.a NASA Three-stage compressor (74 A) (Reset 1 80% speed) - Total pressure loss distribution at 1 % of the stall point

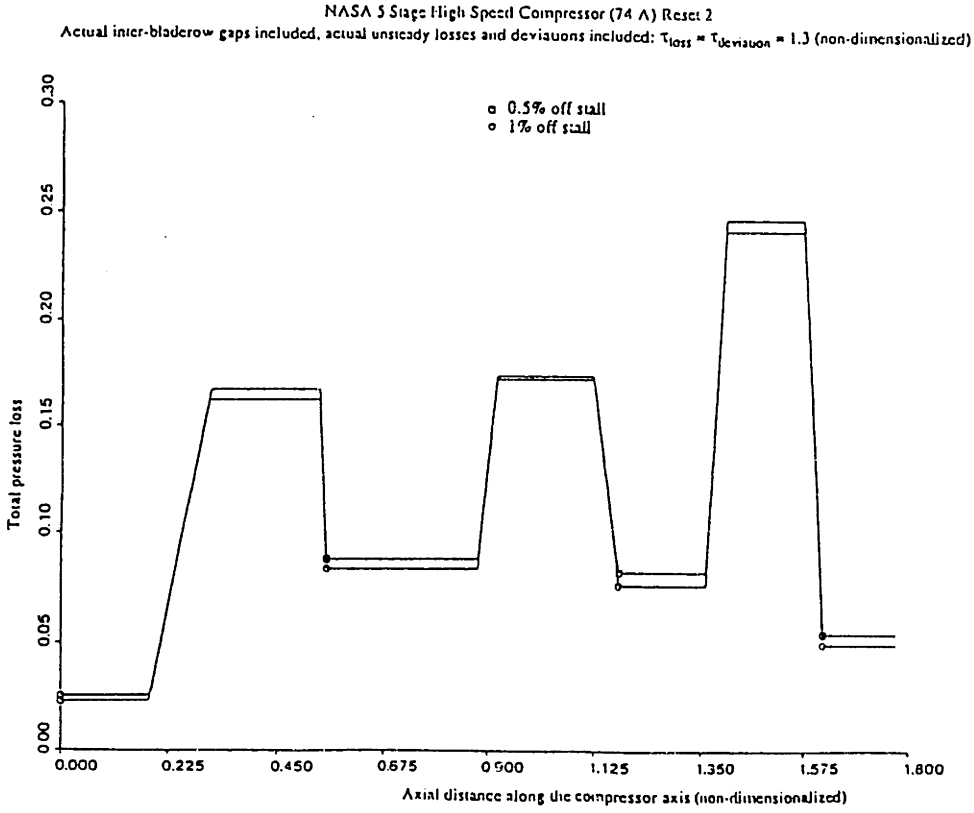

Figure 6.11.b NASA Three-stage compressor (74 A) (Reset 2 80% speed) - Total pressure loss distribution at 0.5% and 1 % of the stall point

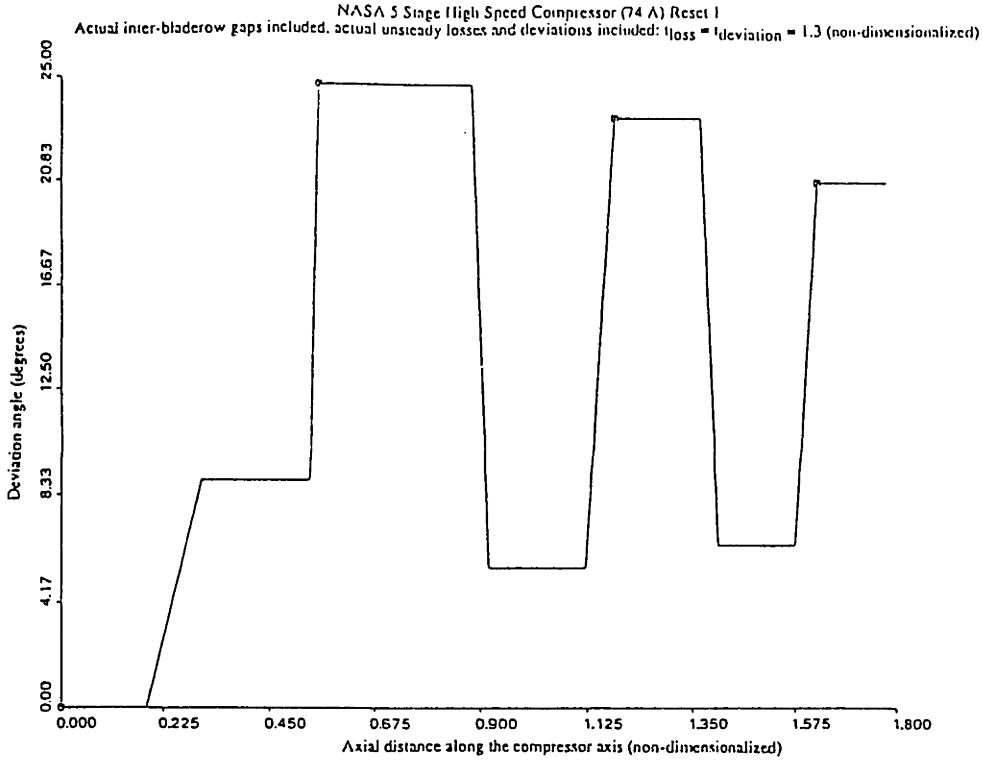

Figure 6.12.a NASA Three-stage compressor (74 A) (Reset 1 80% speed) - Deviationangle distribution at 1 % of the stall point

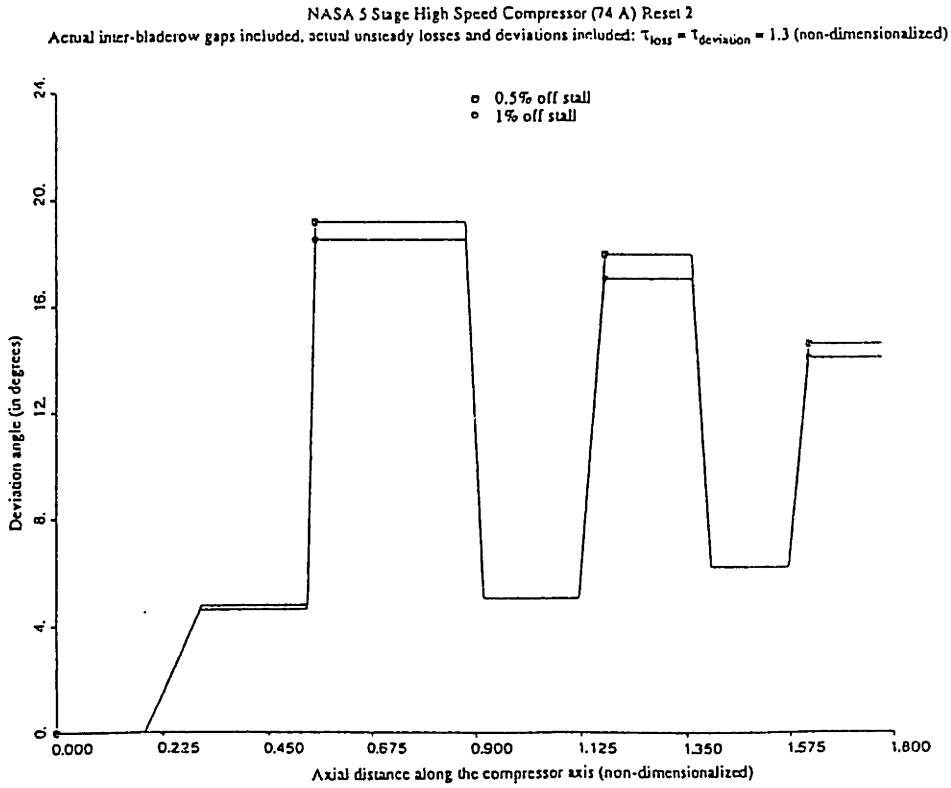

Figure 6.12.b NASA Three-stage compressor (74 A) (Reset 2 80% speed) - Deviation angle distribution at 0.5% and 1 % of the stall point

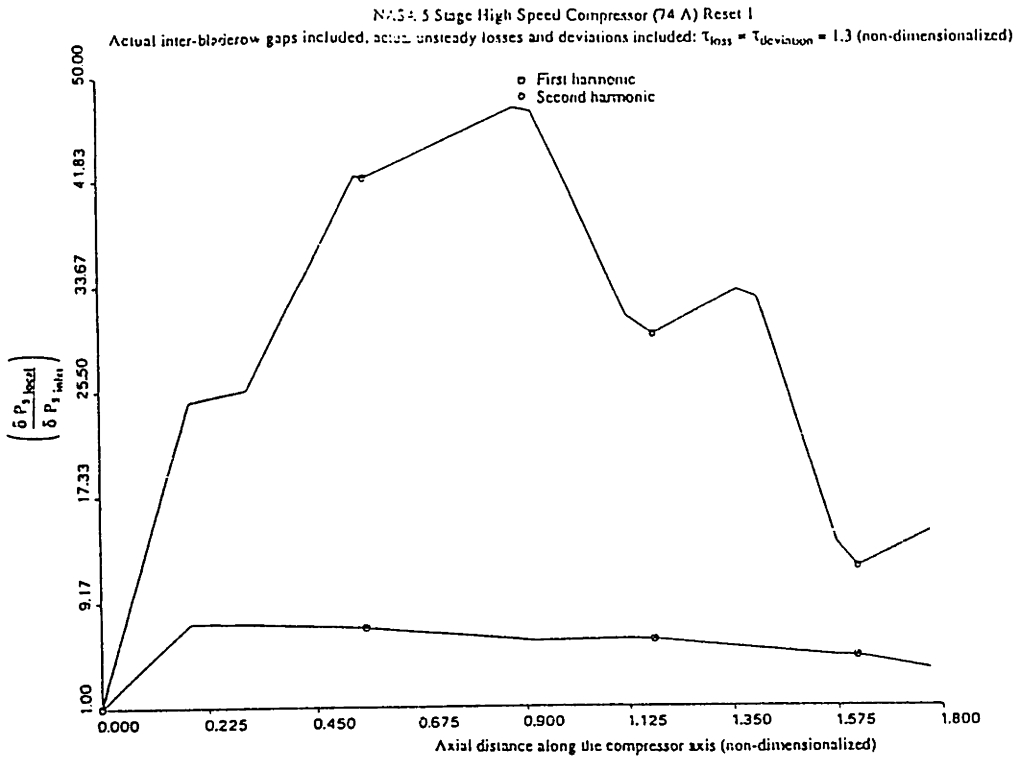

Figure 6.13.a NASA Three-stage compressor (74 A) (Reset 1 80% speed) -
Static pressure perturbation distribution at each neutral stability operating point for the first two harmonics

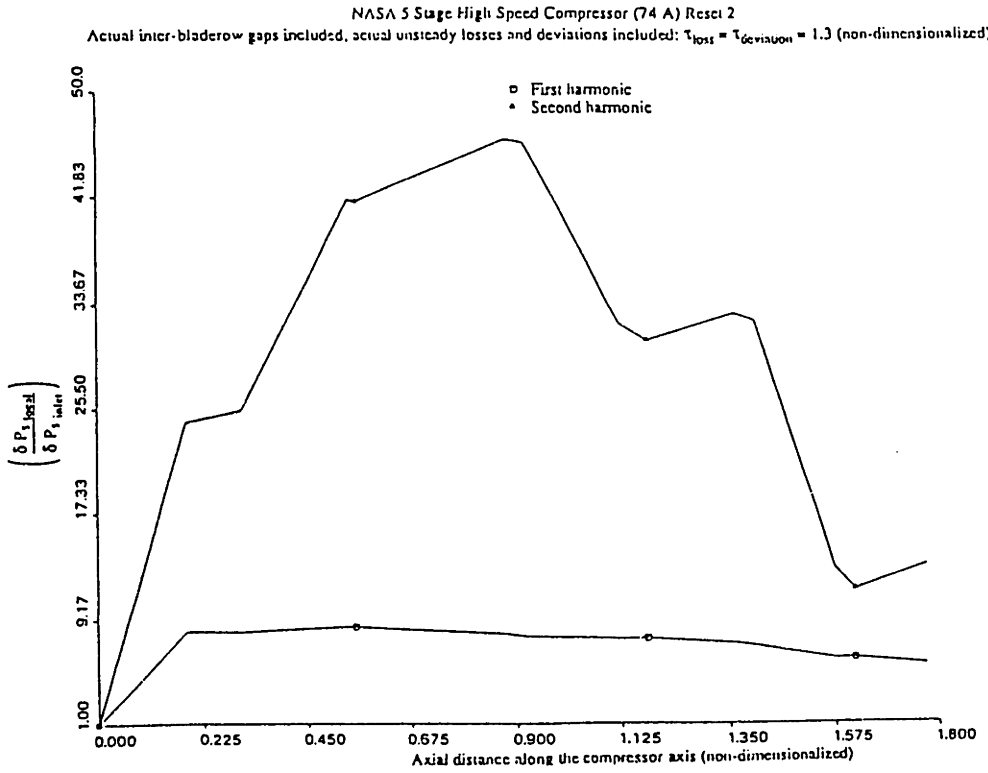

Figure 6.13.b NASA Three-stage compressor (74 A) (Reset 2 80% speed) -
Static pressure perturbation distribution at each neutral stability operating point for the first two harmonics

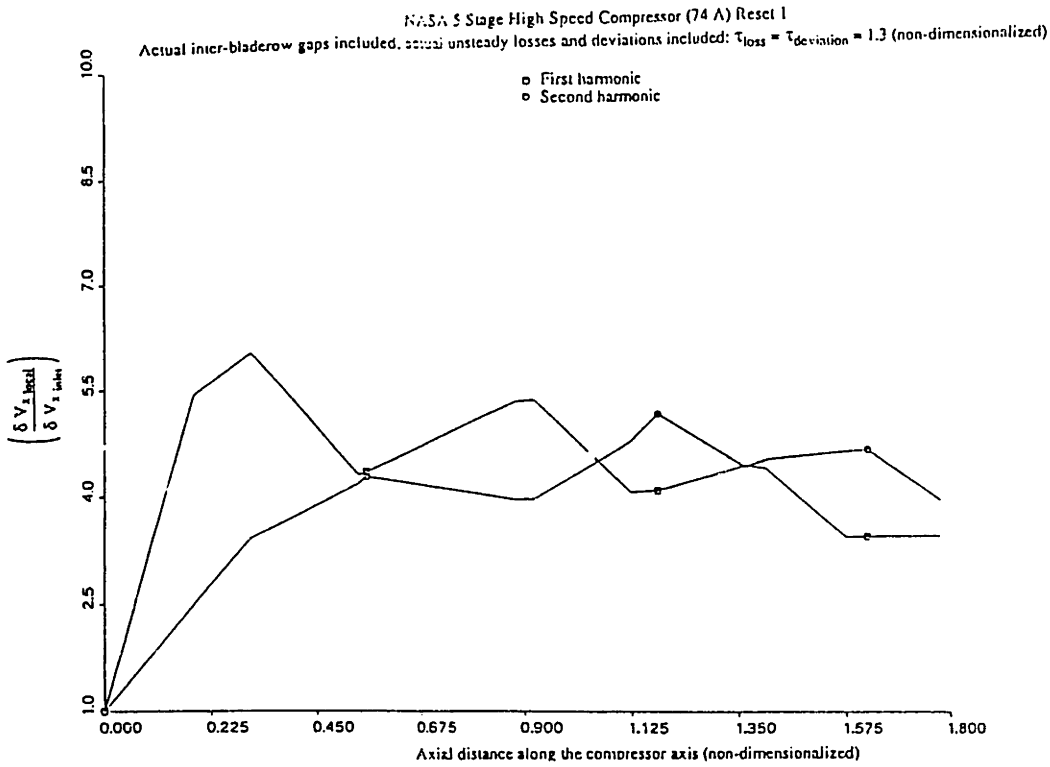

Figure 6.14.a NASA Three-stage compressor (74 A) (Reset 1 80% speed) -
Axial velocity perturbation distribution at each neutral stability operating point for the first two harmonics

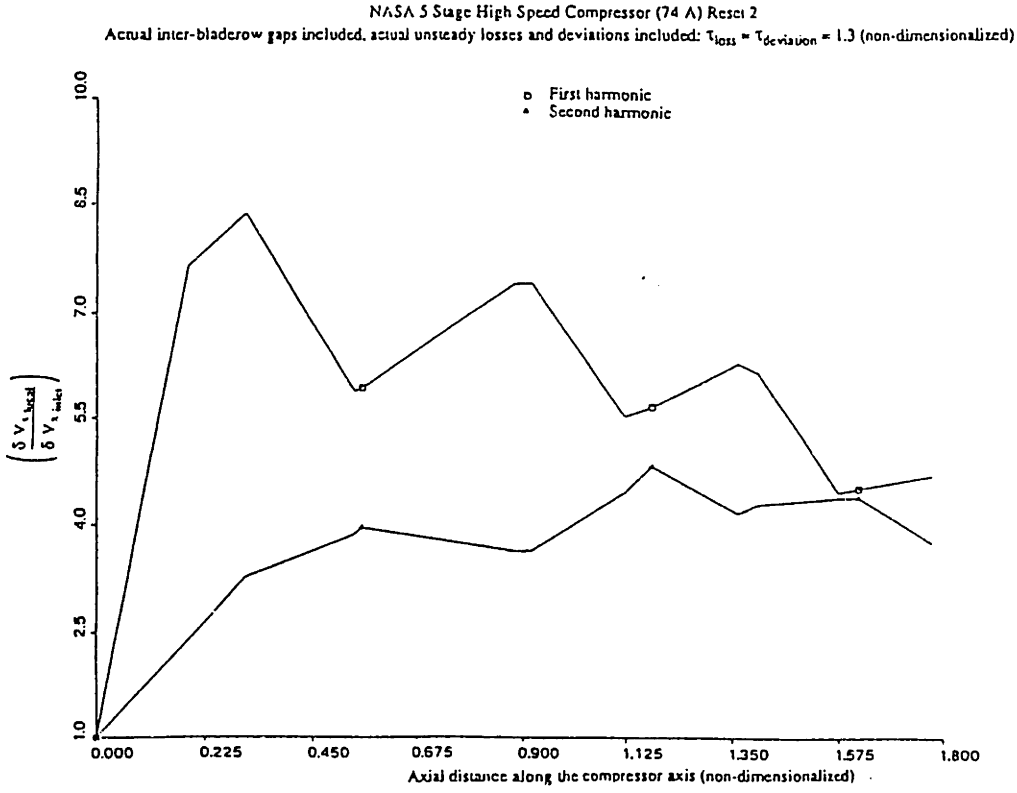

Figure 6.14.b NASA Three-stage compressor (74 A) (Reset 2 80% speed) -
Axialvelocity perturbation distribution at each neutral stability operating point for the first two harmonics

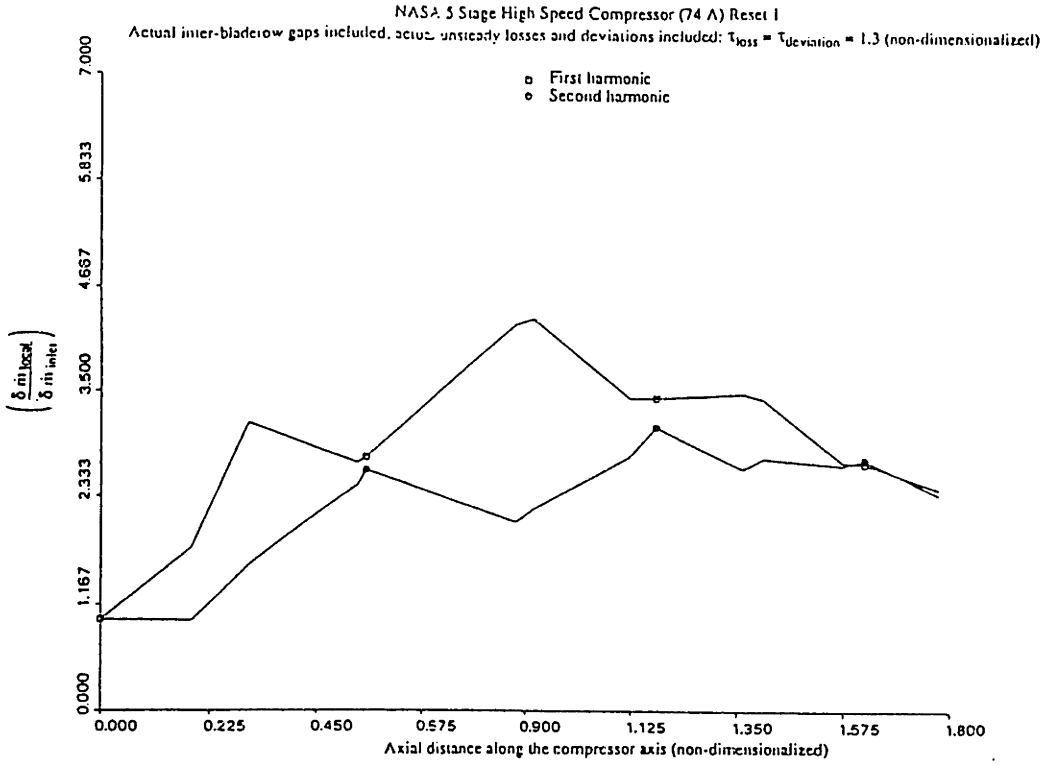

Figure 6.15.a NASA Three-stage compressor (74 A) (Reset 1 80% speed) -
Mass flowperturbation distribution at each neutral stability operating point for the first two harmonics

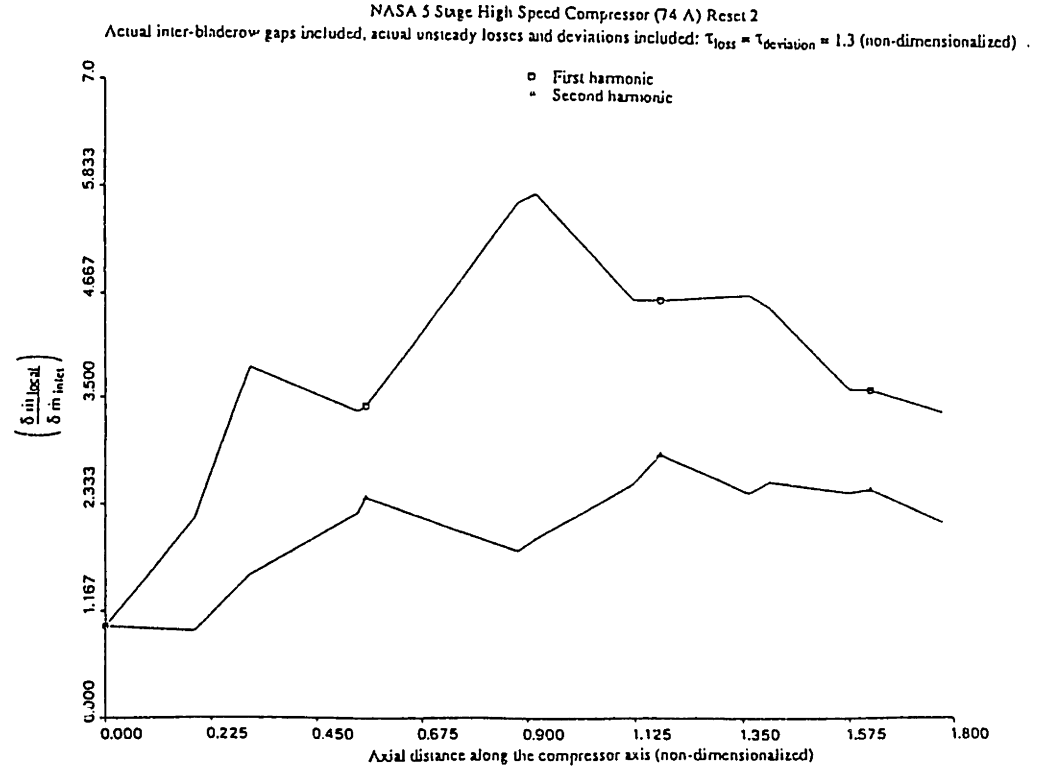

Figure 6.15.b NASA Three-stage compressor (74 A) (Reset 2 80% speed) -
Mass flowperturbation distribution at each neutral stability operating point for the first two harmonics

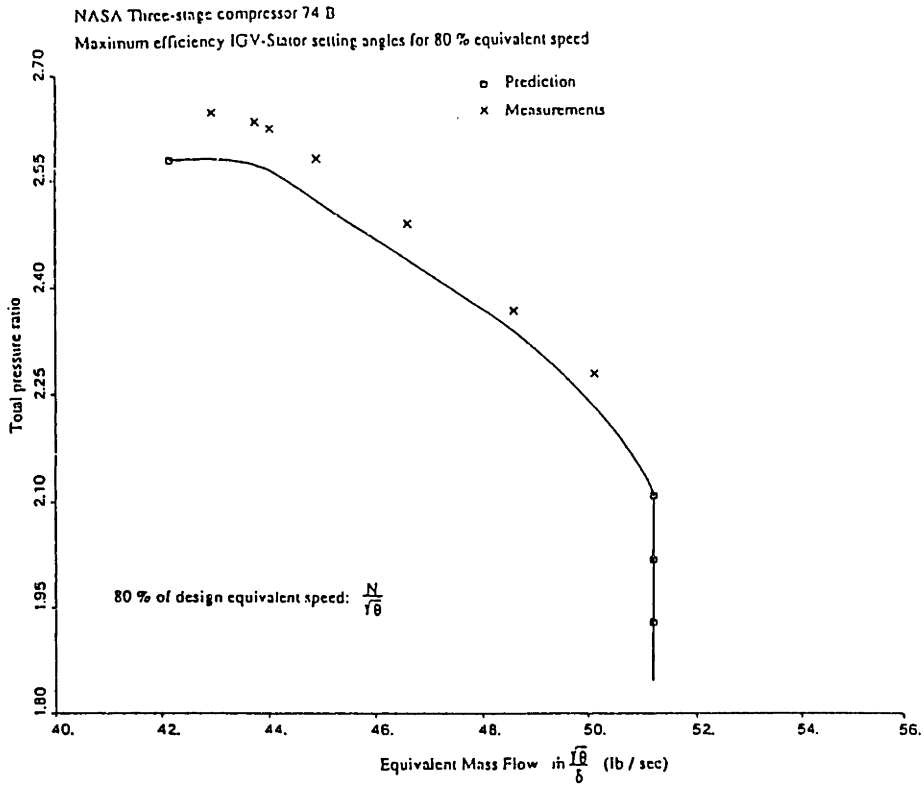

Figure 6.16.a NASA Three-stage compressor (74 B) (80/80) - Predicted and experimental pressure ratio characteristic and stall points

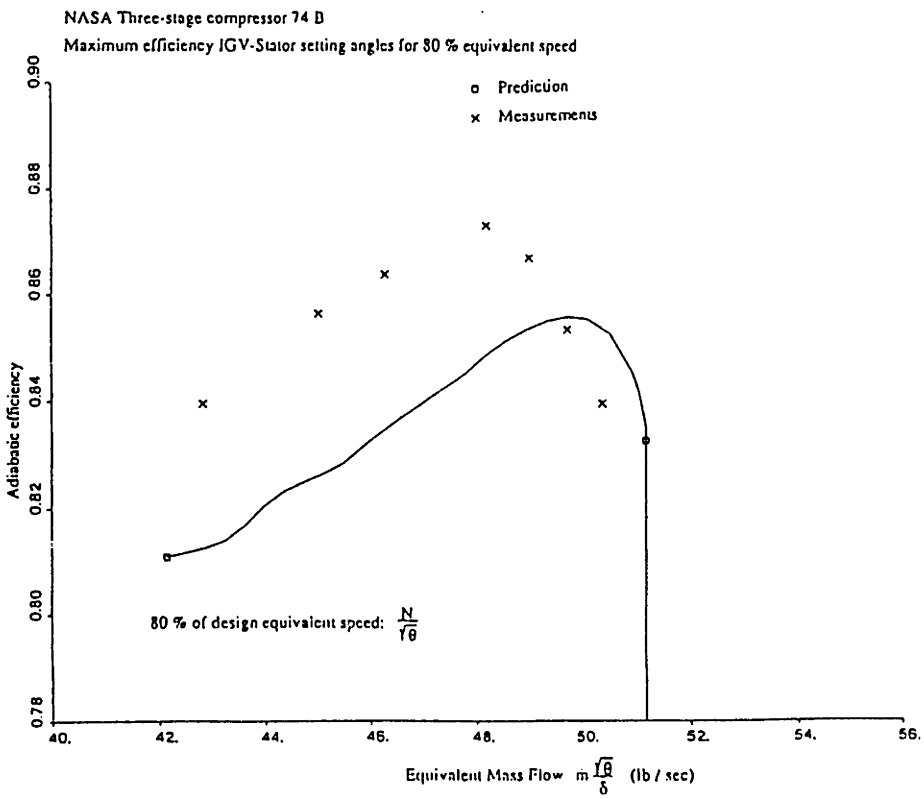

Figure 6.16.b NASA Three-stage compressor (74 B) (80/80) - Predicted and experimental adiabatic efficiency characteristic

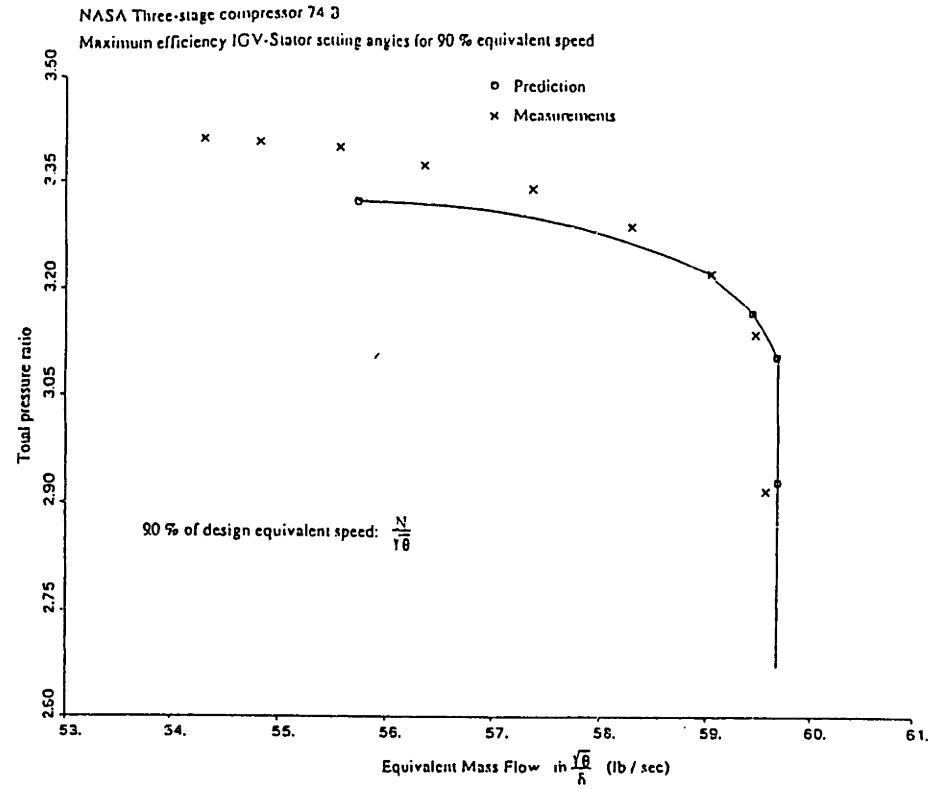

Figure 6.17.a NASA Three-stage compressor (74 B) (90/90) - Predicted and experimental pressure ratio characteristic and stall points

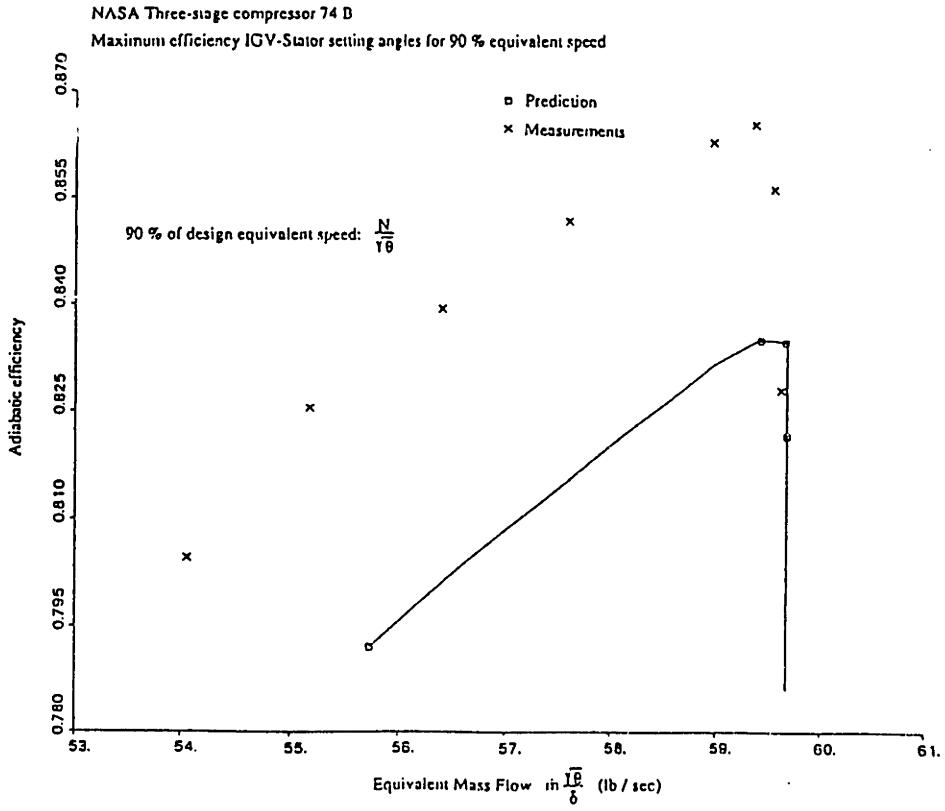

Figure 6.17.b NASA Three-stage compressor (74 B) (90/90) - Predicted and experimental adiabatic efficiency characteristic

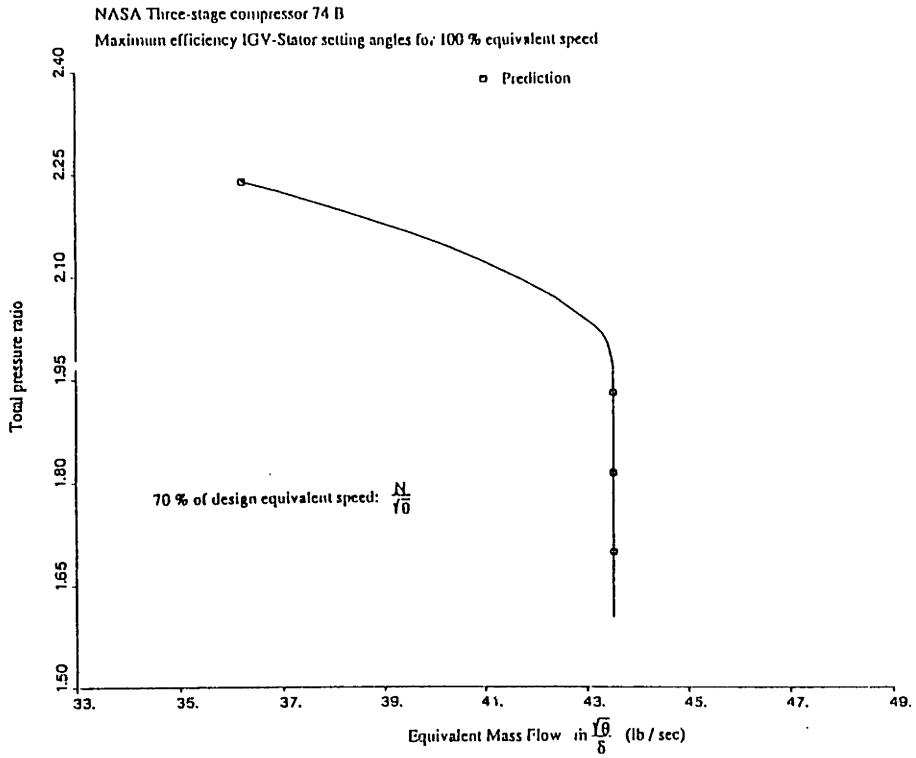

Figure 6.18.a NASA Three-stage compressor (74 B) (70/100) - Predicted pressure ratio characteristic and stall points

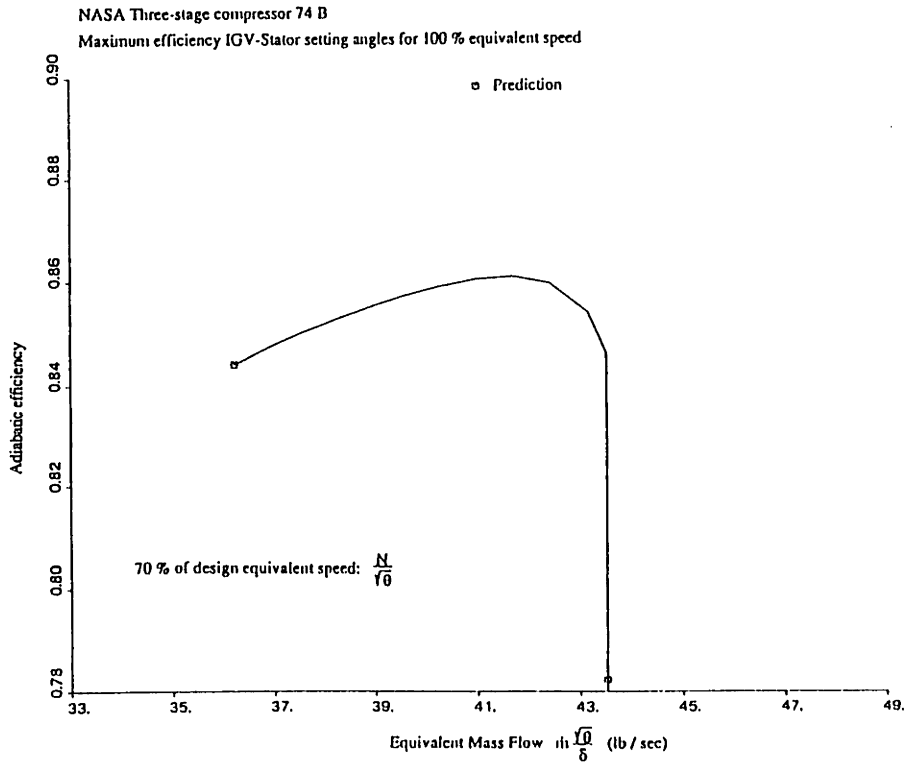

Figure 6.18.b NASA Three-stage compressor (74 B) (70/100) - Predicted adiabatic efficiency characteristic

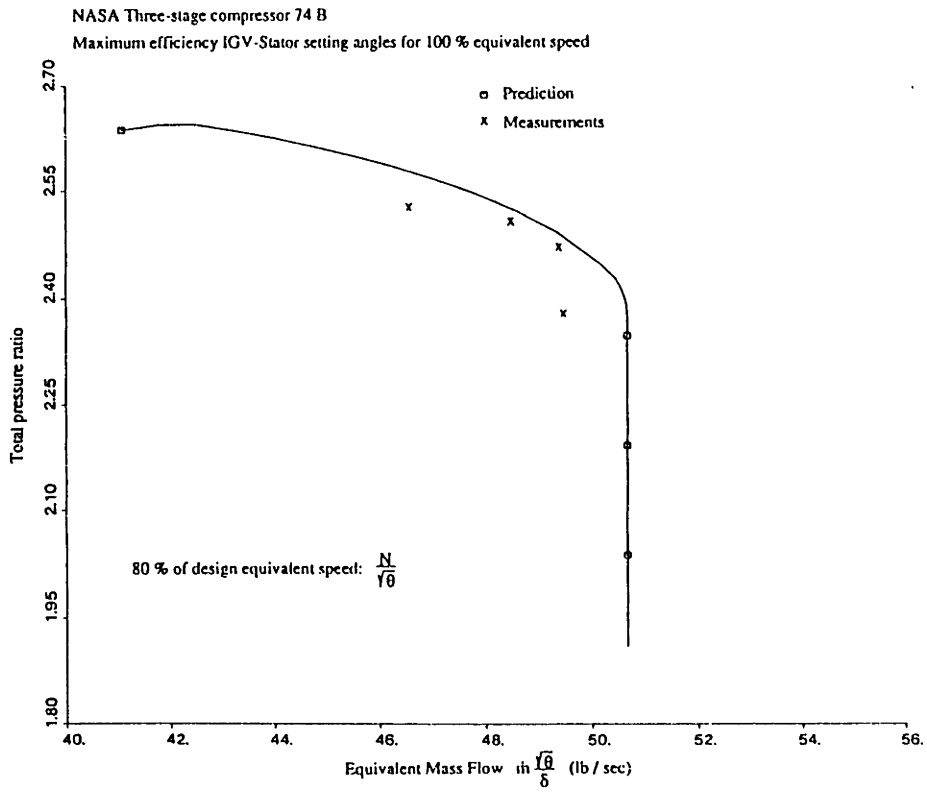

Figure 6.19.a NASA Three-stage compressor (74 B) (80/100) - Predicted and experimental pressure ratio characteristic and stall points

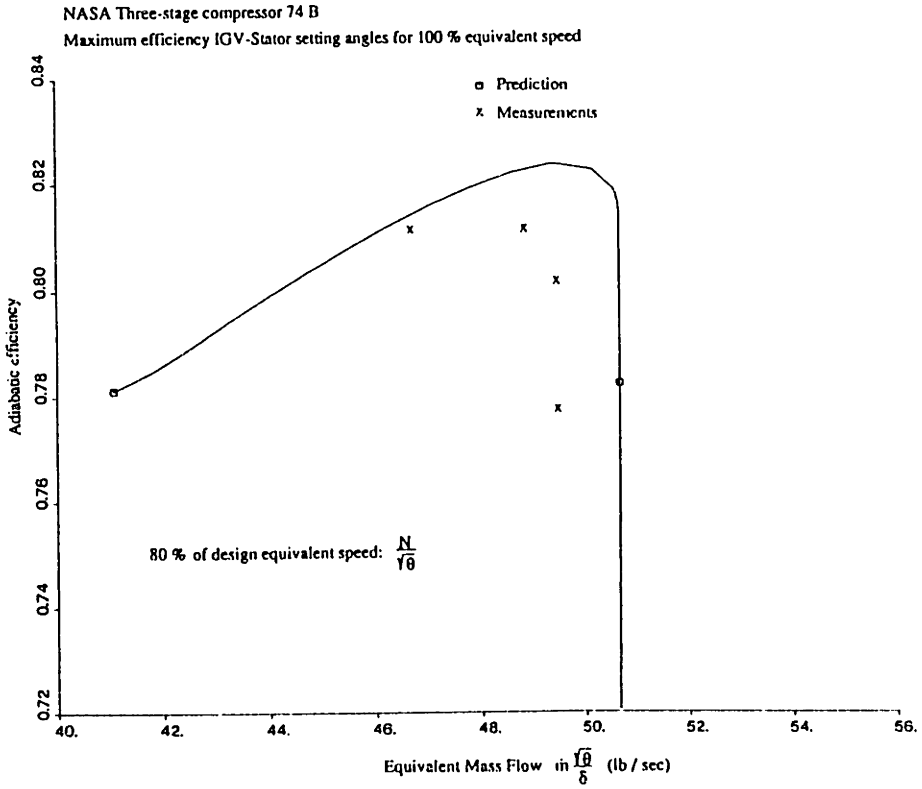

Figure 6.19.b NASA Three-stage compressor (74 B) (80/100) - Predicted and experimental adiabatic efficiency characteristic

NASA 74 B *Three-stage high-speed compressor*	90 % speed 90 % reset	80 % speed 80 % reset
$\left(\frac{\omega_{\text{rotating stall}}}{\omega_{\text{shaft}}}\right)_{\text{measured (post-stall behavior)}}$	0.40	0.55
$\left(\frac{\omega_{\text{rotating stall}}}{\omega_{\text{shaft}}}\right)_{\text{predicted (at stall behavior)}}$	0.35	0.49
Measured stall equivalent mass flow (lb/sec)	54.5	43
Predicted stall equivalent mass flow (lb/sec)	55.5	42

Table 6.7:

Comparison of the measured and predicted stall characteristics for the 74B compressor

NASA 74 B *Three-stage high-speed compressor*	70 % speed 100 % reset	80 % speed 100 % reset
$\left(\frac{\omega_{\text{rotating stall}}}{\omega_{\text{shaft}}}\right)_{\text{measured (post-stall behavior)}}$	0.56	0.68
$\left(\frac{\omega_{\text{rotating stall}}}{\omega_{\text{shaft}}}\right)_{\text{predicted (at stall behavior)}}$	0.44	0.57
Measured stall equivalent mass flow (lb/sec)	33	45
Predicted stall equivalent mass flow (lb/sec)	36	41

Table 6.8:

Comparison of the measured and predicted stall characteristics for the 74B compressor

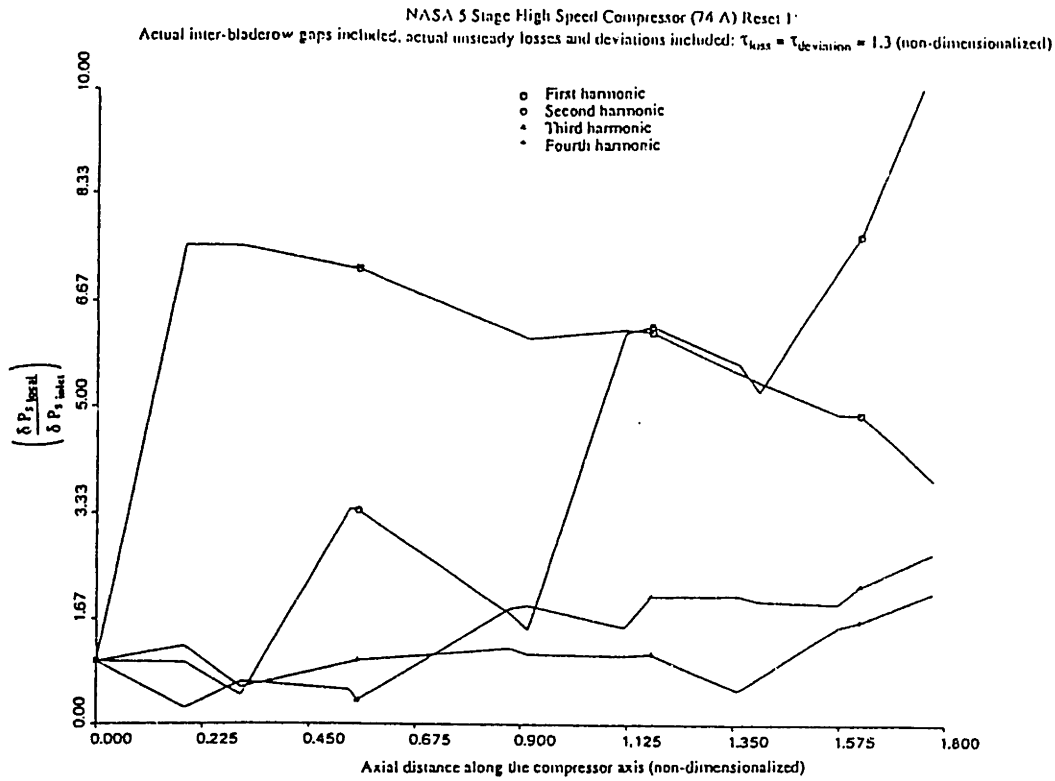

Figure 6.20.a NASA Three-stage compressor (74 A) (Reset 1 80% speed) - Static pressure perturbation distribution for the first four harmonics at 1% of the stall point

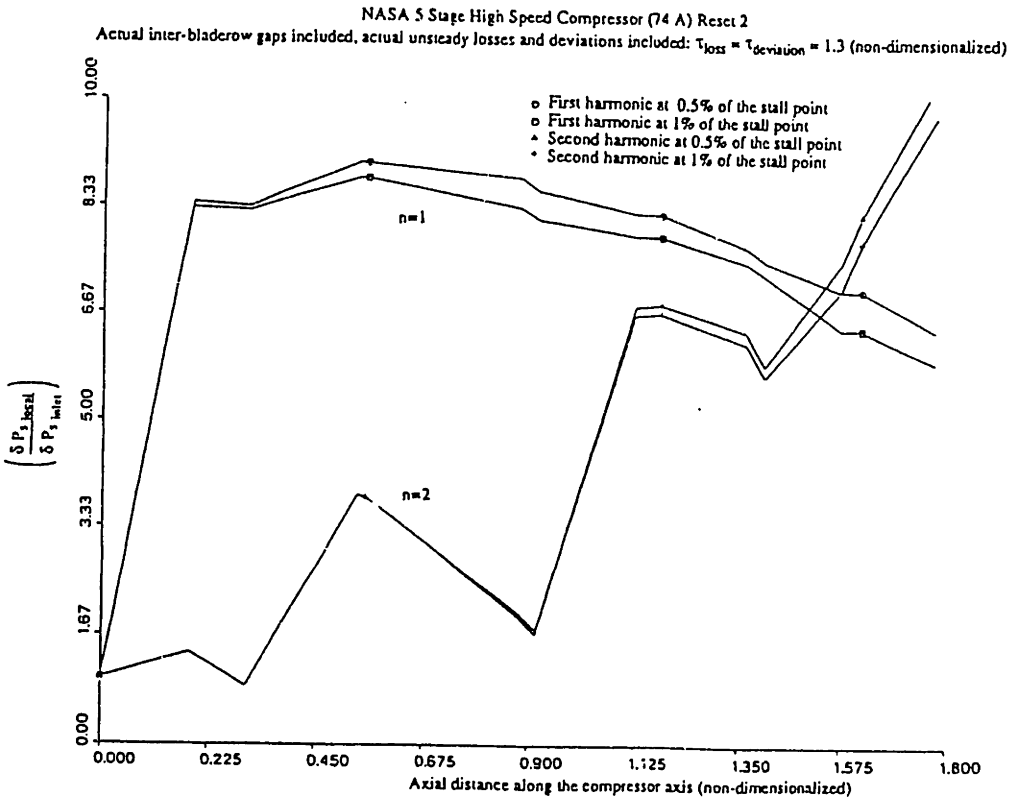

Figure 6.20.b NASA Three-stage compressor (74 A) (Reset 2 80% speed) - Static pressure perturbation distribution for the first two harmonics at 0.5% and 1% of the stall point

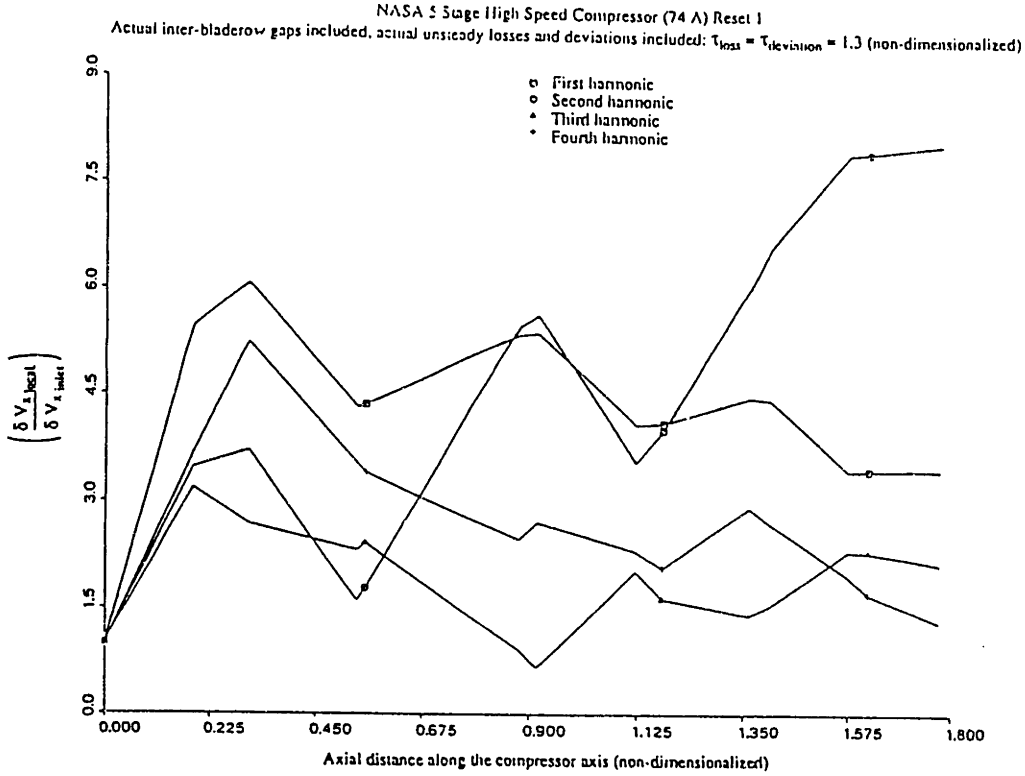

Figure 6.21.a NASA Three-stage compressor (74 A) (Reset 1 80% speed) - Axial velocity perturbation distribution for the first four harmonics at 1% of the stall point

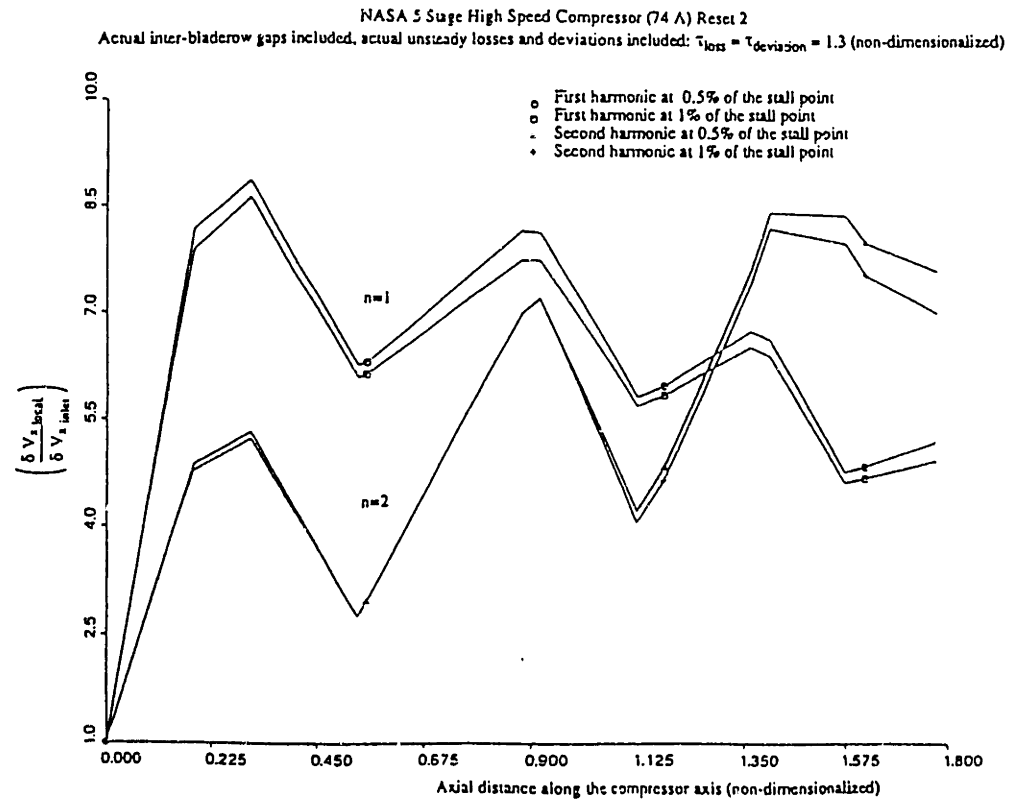

Figure 6.21.b NASA Three-stage compressor (74 A) (Reset 2 80% speed) - Axialvelocity perturbation distribution for the first two harmonics at 0.5% and 1% of the stall point

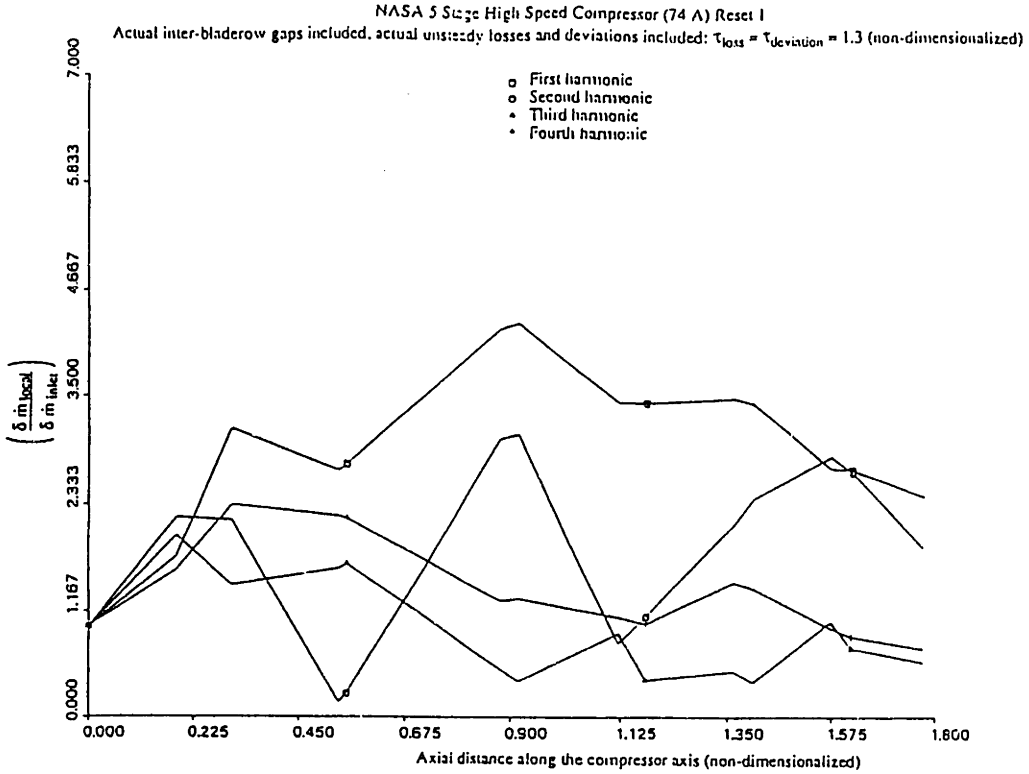

Figure 6.22.a NASA Three-stage compressor (74 A) (Reset 1 80% speed) - Mass flow perturbation distribution for the first four harmonics at 1% of the stall point

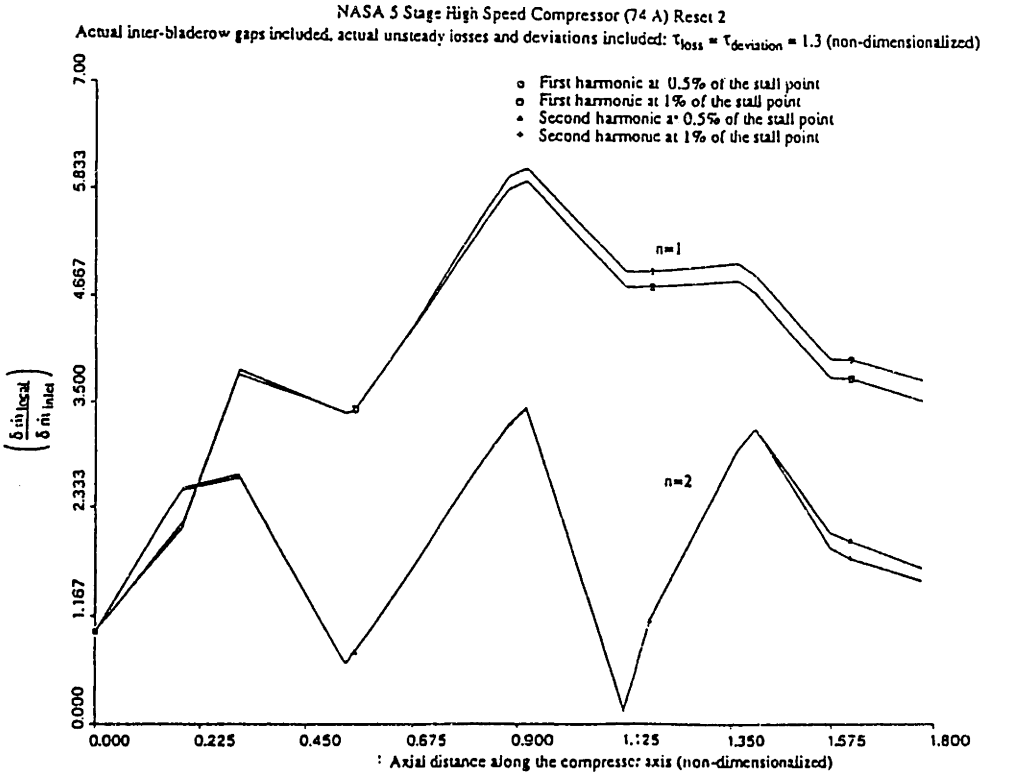

Figure 6.22.b NASA Three-stage compressor (74 A) (Reset 2 80% speed) - Mass flowperturbation distribution for the first two harmonics at 0.5% and 1% of the stall point

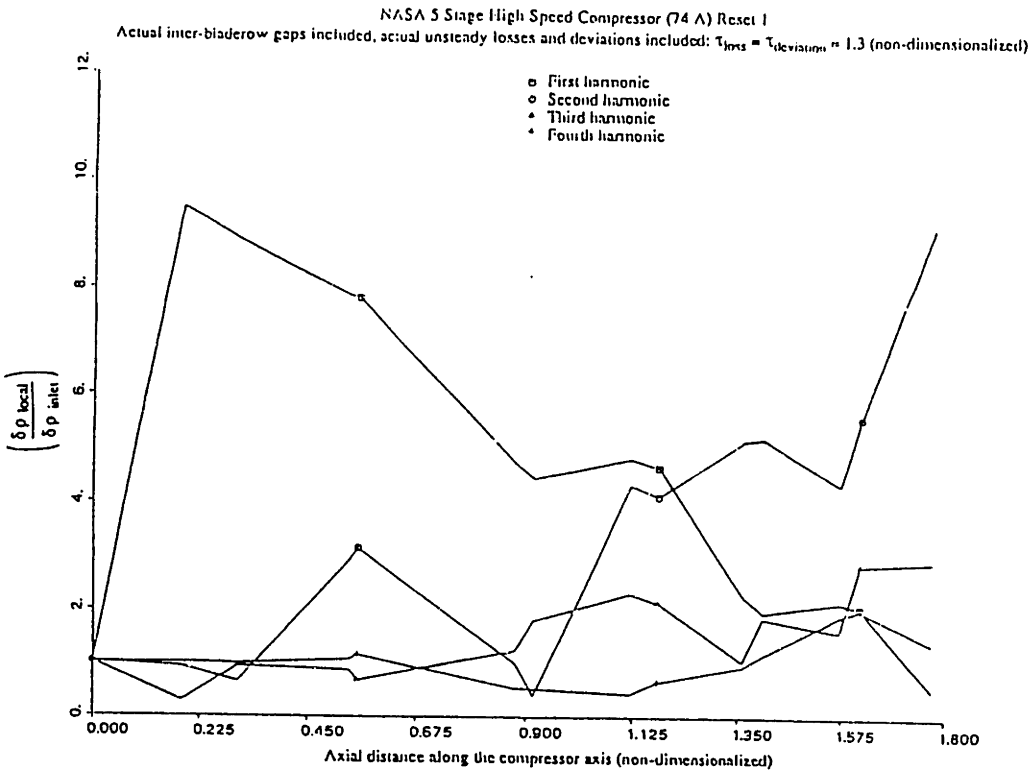

Figure 6.23.a NASA Three-stage compressor (74 A) (Reset 1 80% speed) - Density perturbation distribution for the first four harmonics at 1% of the stall point

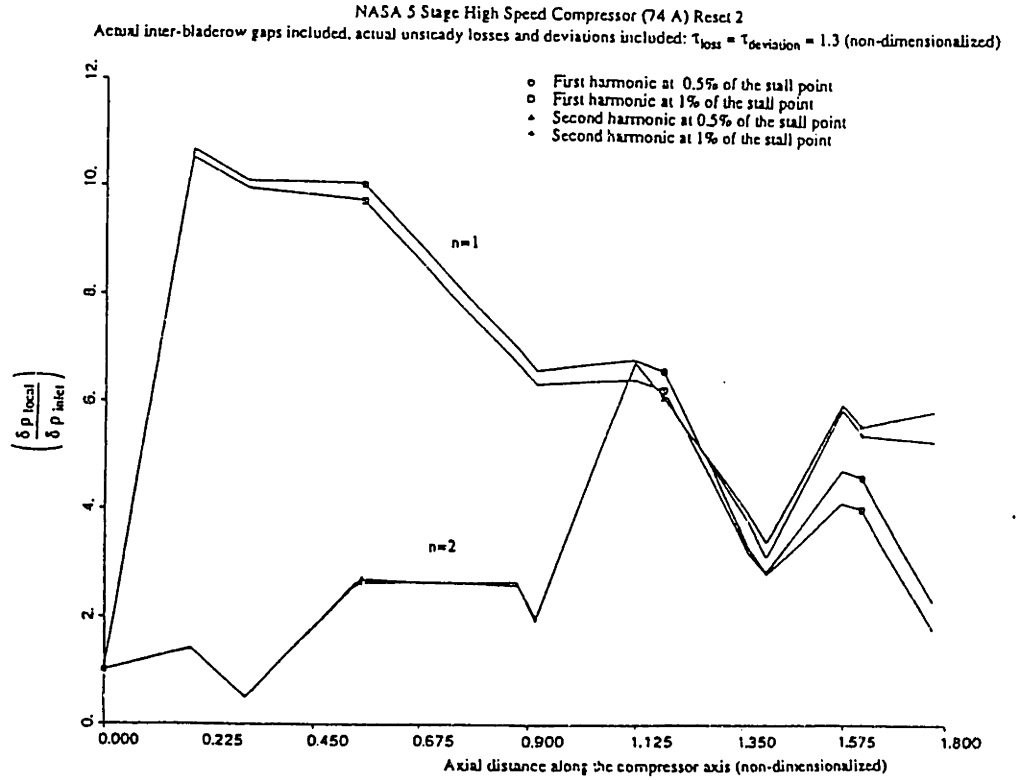

Figure 6.23.b NASA Three-stage compressor (74 A) (Reset 2 80% speed) - Density perturbation distribution for the first two harmonics at 0.5% and 1% of the stall point

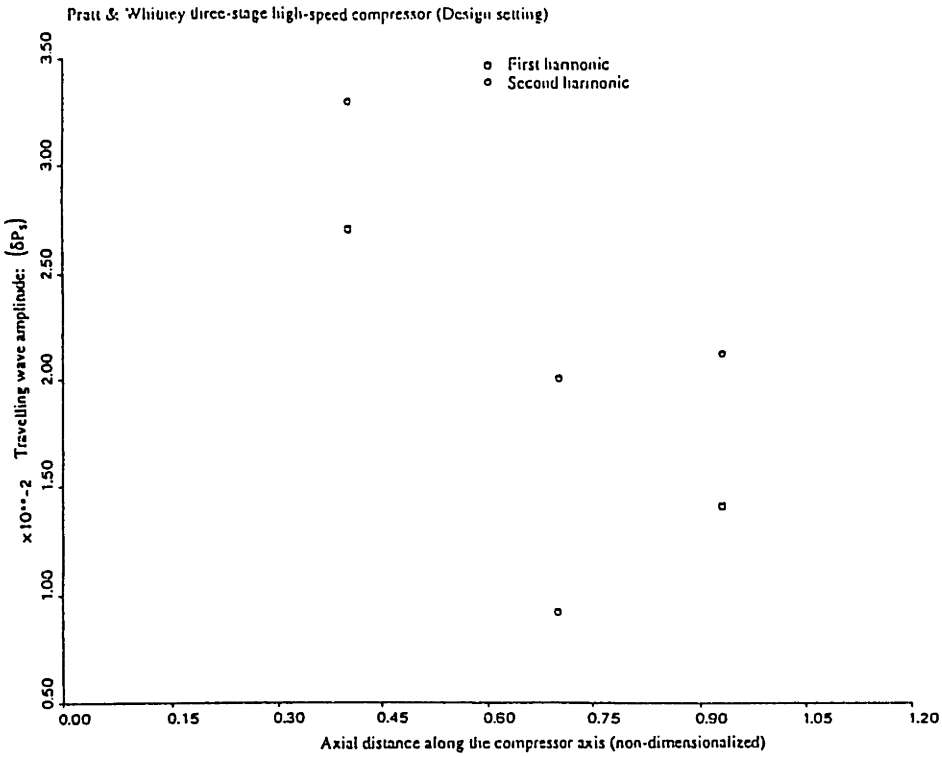

Figure 6.24 Pratt & Whitney Three-stage compressor (Design setting) - Experimental travelling wave static pressure perturbation distribution

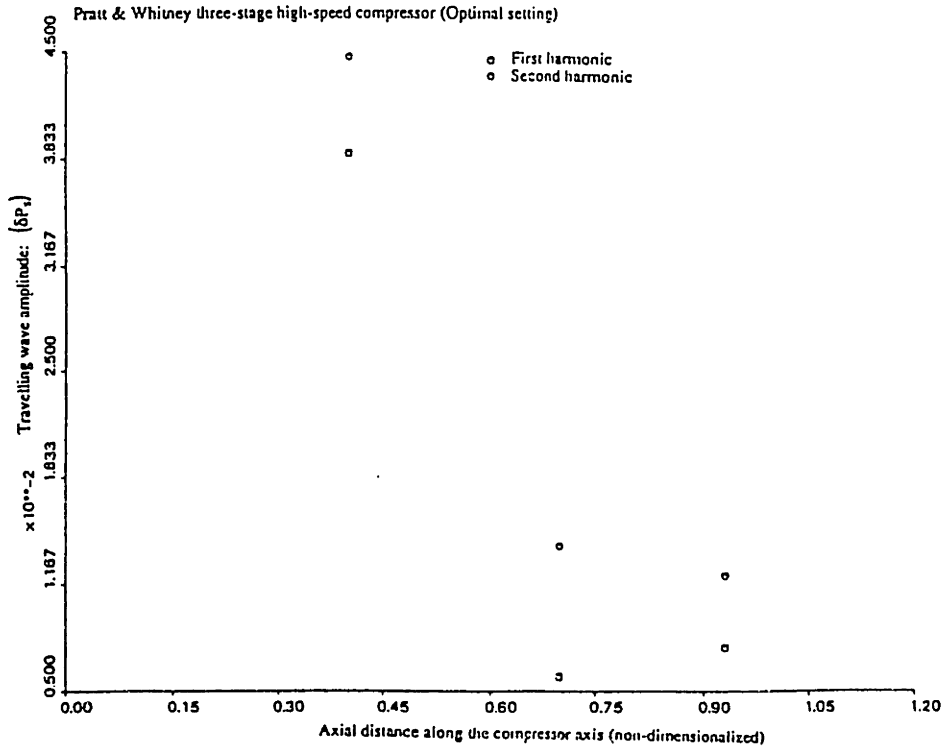

Figure 6.25 Pratt & Whitney Three-stage compressor (Optimal setting) - Experimental travelling wave static pressure perturbation distribution

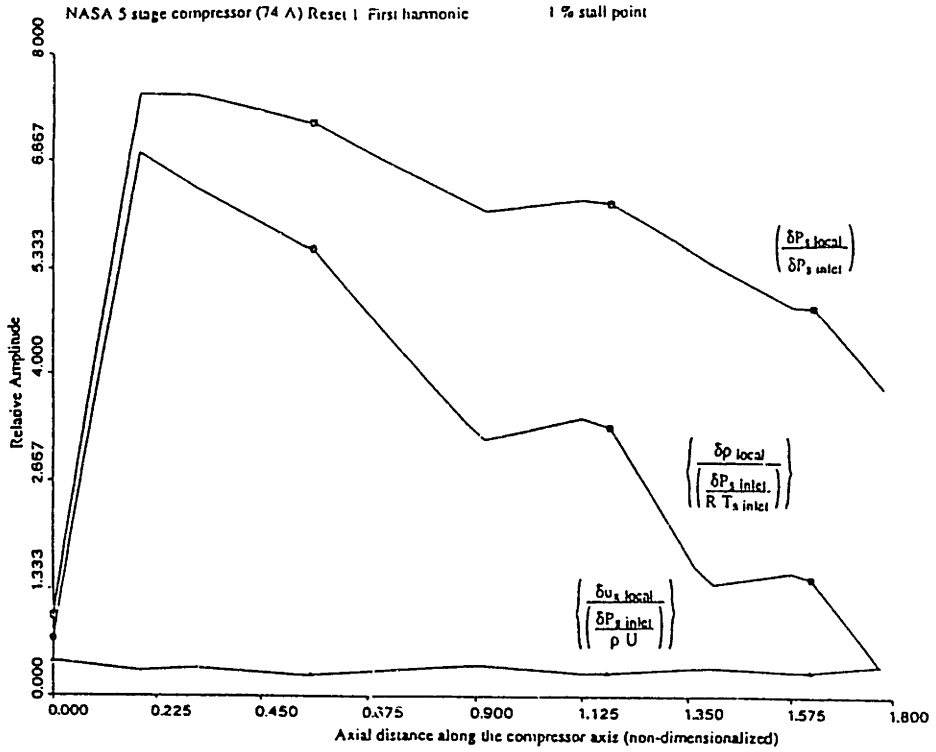

Figure 6.26.a NASA Three-stage compressor (74 A) (Reset 1 80% speed) - Relative amplitude of the flow field perturbations at 1% of the stall point (first harmonic)

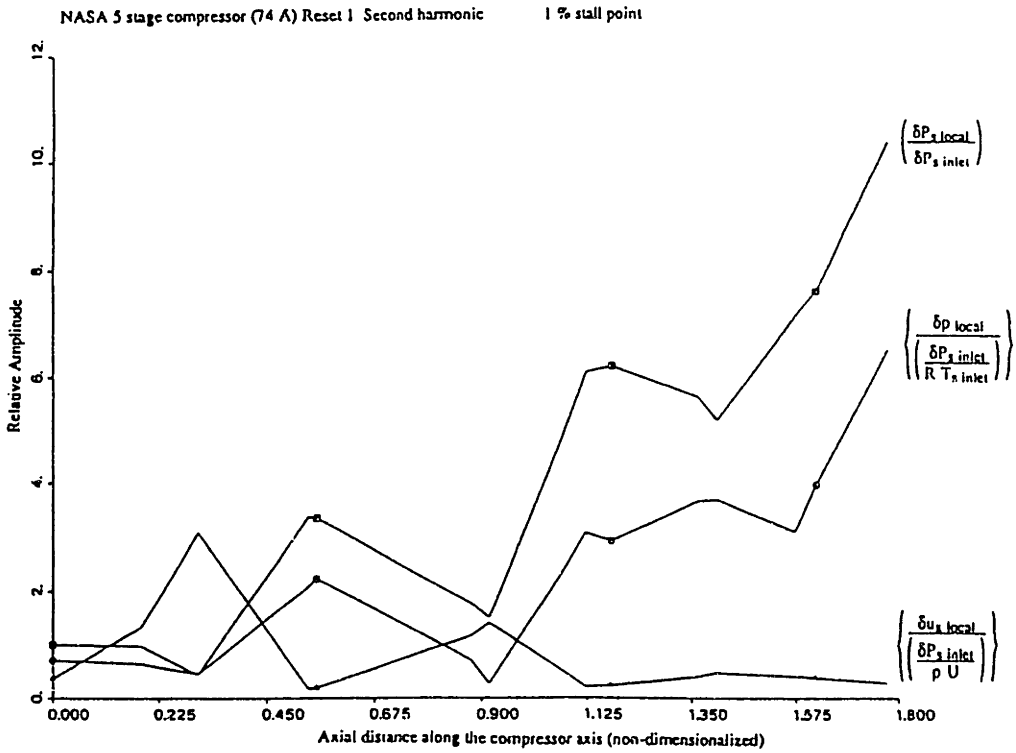

Figure 6.26.b NASA Three-stage compressor (74 A) (Reset 1 80% speed) - Relative amplitude of the flow field perturbations at 1% of the stall point (secondharmonic)

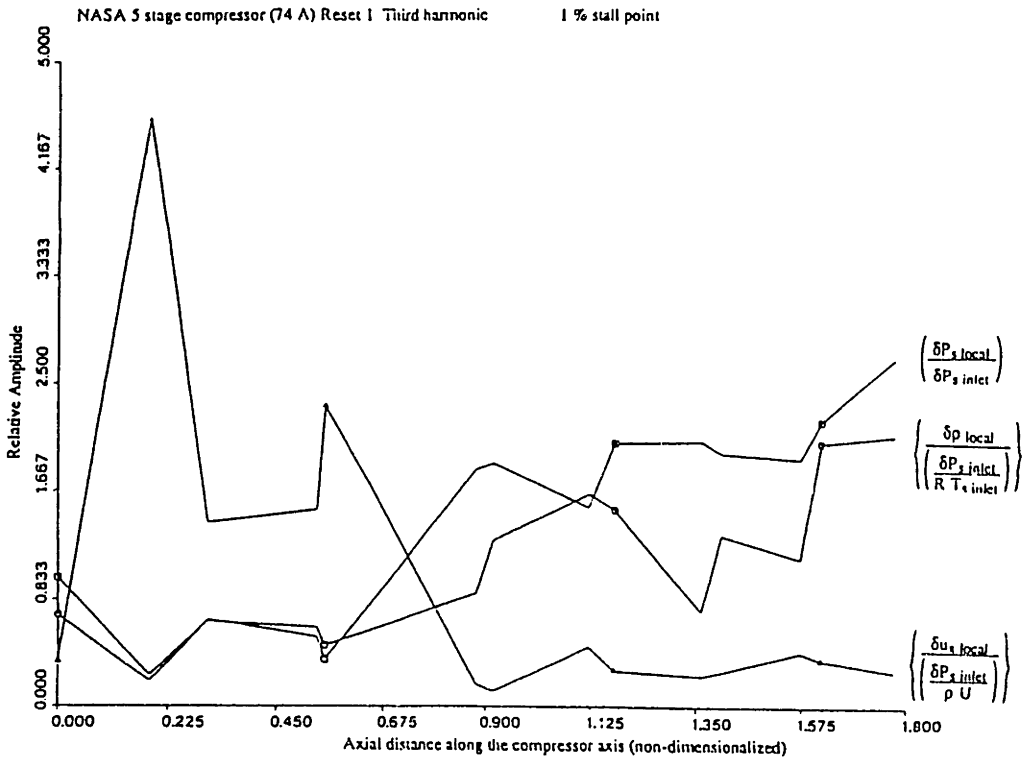

Figure 6.26.c NASA Three-stage compressor (74 A) (Reset 1 80% speed) - Relative amplitude of the flow field perturbations at 1% of the stall point (third harmonic)

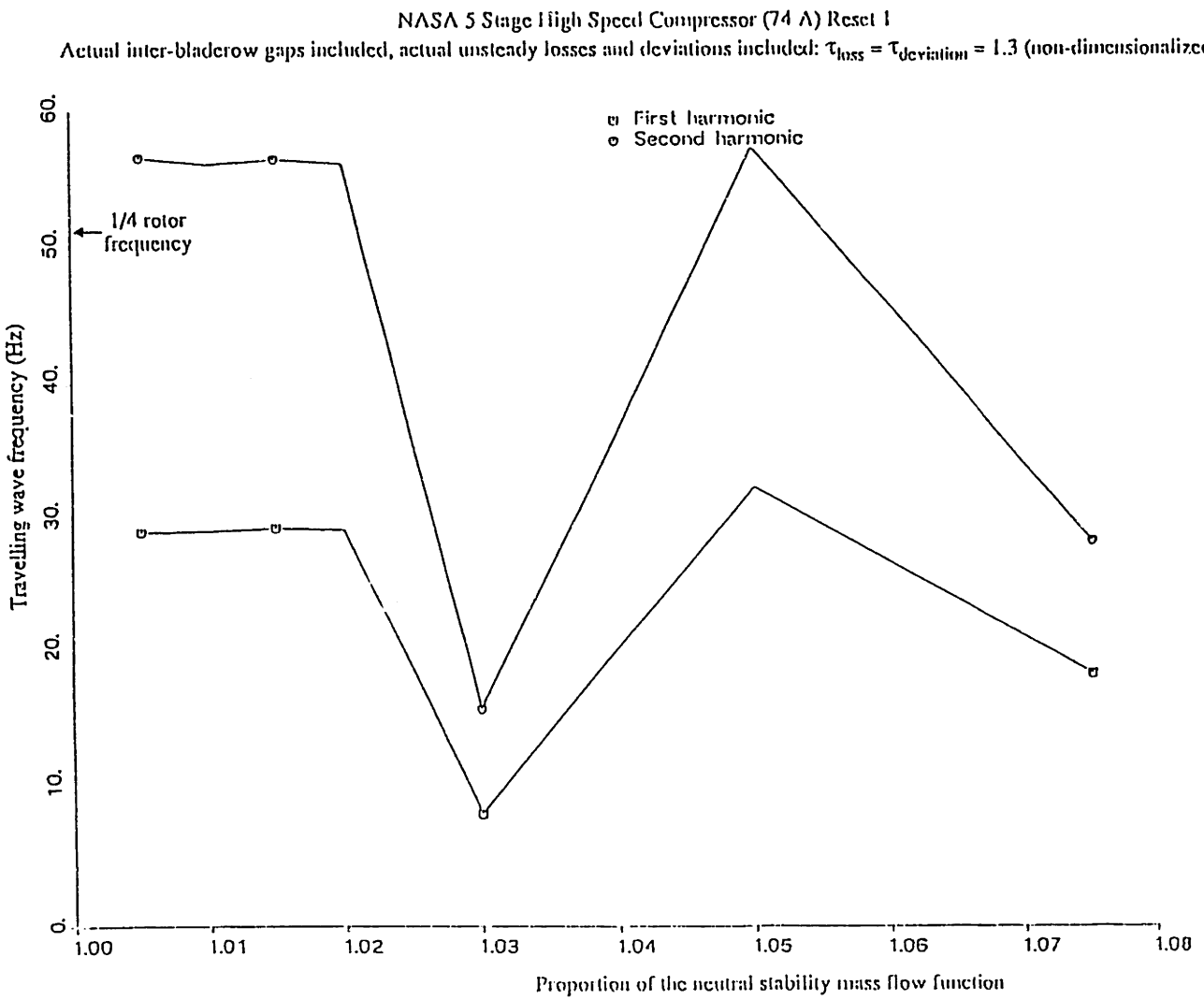

Figure 6.27 NASA Three-stage compressor (74 A) (Reset 1 80% speed) - Travelling waves frequencies

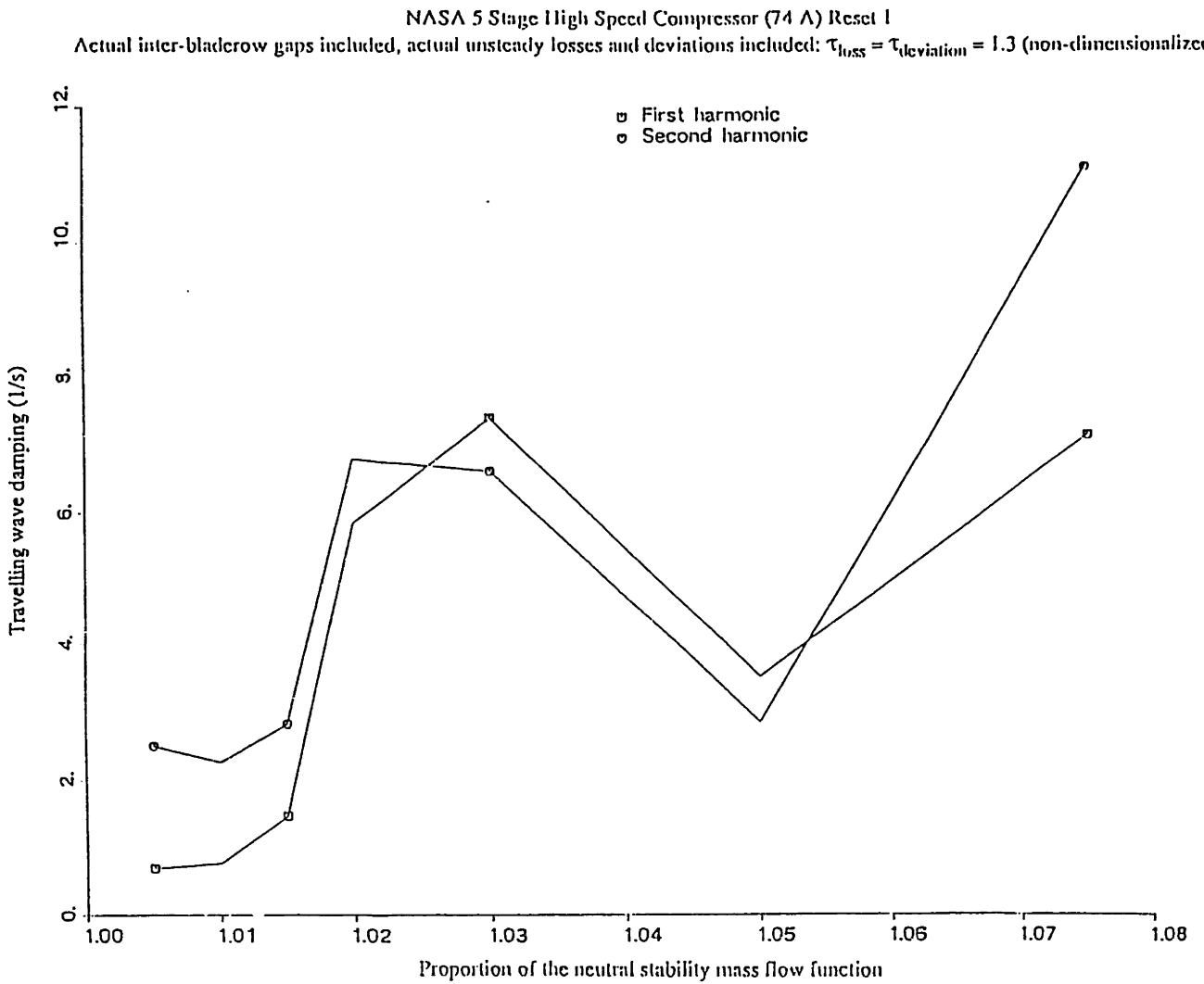

Figure 6.28 NASA Three-stage compressor (74 A) (Reset 1 80% speed) - Travelling waves damping

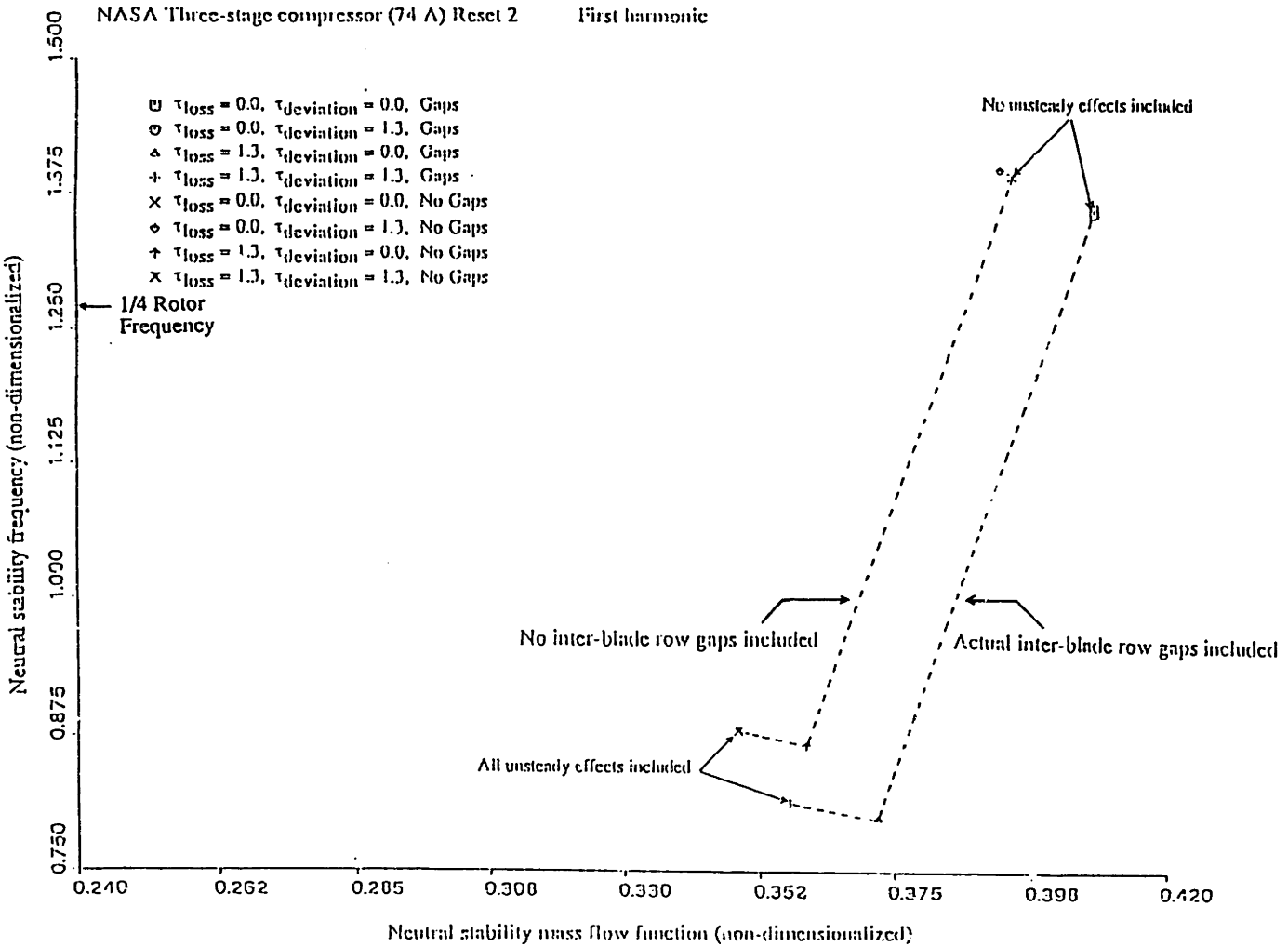

Figure 6.29 NASA Three-stage compressor (74 A) (Reset 1 80% speed) -
Influence of the unsteady losses, unsteady deviations and inter-blade row gaps on stability (first harmonic)

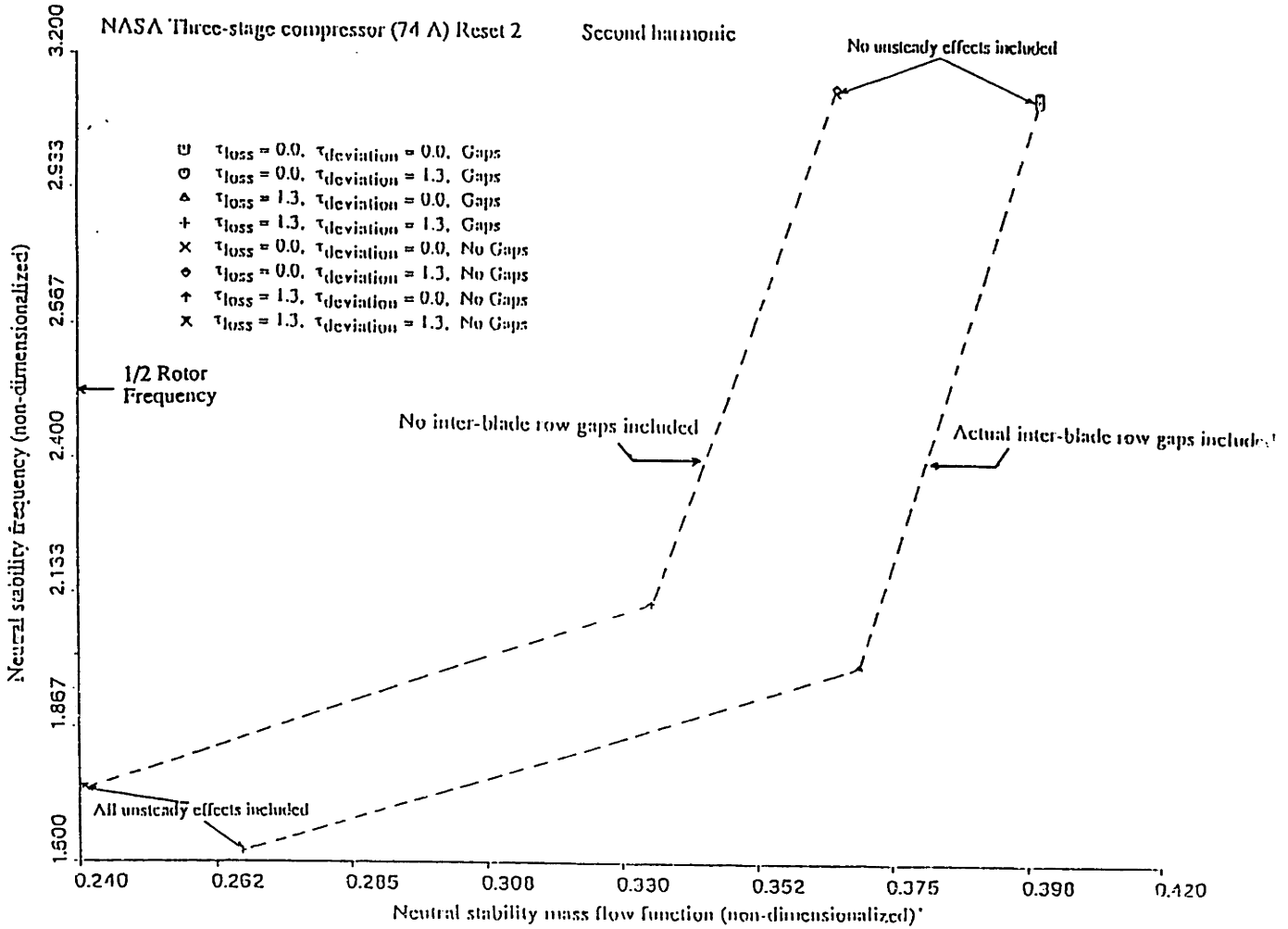

Figure 6.30 NASA Three-stage compressor (74 A) (Reset 1 80% speed) -
Influence of the unsteady losses, unsteady deviations and inter-blade row gaps on stability (second harmonic)